

Development of high-speed digital holographic shape and displacement measurement methods for middle-ear mechanics in-vivo

A Dissertation
submitted to the faculty of the

Worcester Polytechnic Institute

as a partial fulfillment of the requirements for the
Degree of Doctor of Philosophy
in
Manufacturing Engineering

By

Payam Razavi

19 March 2018

Approved:

Prof. Cosme Furlong, Advisor

Prof. John J. Rosowski, Advisor

Prof. Jeffrey T. Cheng, Member, Dissertation Committee

Prof. Loris Fichera, Member, Dissertation Committee

Prof. Douglas T. Petkie, Member, Dissertation Committee

Prof. Richard D. Sisson Jr., Director of Manufacturing & Materials Engineering

Copyright © 2018

By

CHSLT – Center for Holographic Studies and Laser micro-mechaTronics

Mechanical Engineering Department

Worcester Polytechnic Institute

Worcester, MA 01609-2280

All rights reserved

Abstract

The middle ear plays an integral role in the normal hearing process by transforming sound energy from the air inside the ear canal into vibrations of the inner-ear fluid, and a malfunction in any middle-ear component can lead to significant hearing loss. Despite decades of research on the Tympanic Membrane (TM or eardrum), the transformation of sound energy into ossicular mechanical vibrations is not yet well understood. Part of this is because the available clinical and research tools provide insufficient data to understand the complexities of this transformation. The data insufficiency arises due to methodological, technological, and physiological limitations such as required nanometer and microsecond spatio-temporal resolutions of the sound-induced TM motions. Although holographic methods provide nondestructive non-contact measuring capabilities that satisfy most of the constraints for TM measurements, the influence of large submillimeter scale physiological motions in live samples produced by heartbeat and breathing can result in near complete saturation of TM holograms. In this Dissertation, a new high-speed correlation interferometry holographic method is proposed that can compensate for the effects of physiological noise using an open-loop control configuration. Preliminary animal measurements with the proposed method demonstrate the necessary accuracy and precision to measure the motion of the entire TM produced by short-duration ($\geq 1 \text{ kHz}$) transient stimuli. Such rapid measurements reduce the effect of the longer and slower environmental and physiologic noises, and enable clinical applications.

In the second part of this Dissertation, a novel multiple wavelength high-speed holographic interferometric shape measurement method is incorporated into the high-speed displacement measurements. The method uses the imaging optics of the displacement measurement system to perform shape and orientation measurements. Displacement and shape measurements can be made in less than 200 msec and allow computation of true surface-normal displacements. The surface-

normal measurements are independent of the direction of observation, which helps comparisons of measurements made after changes in TM orientation or location. The results enable accurate and precise shape and displacement measurements for use in applications such as modal and finite element analyses, additive manufacturing of prosthetic TM grafts, clinical diagnosis, hearing rehabilitation, as well as optimization of hearing devices. In addition, measured shape parameters such as curvature, depth of cone etc., can help us understand TM mechanics and contribute to quantitative diagnostic assessments.

Acknowledgements

I would like to thank my supervisors, Professor Cosme Furlong and Professor John J. Rosowski, for their outstanding guidance and support during the PhD program. The lessons I learned from you are beyond the academia and they will always be with me for the rest of my life.

I would like to thank my committee members Professor Douglas T. Petkie, Professor Jeffrey T. Cheng, and Professor Loris Fichera for their comments and suggestions regarding my Dissertation. In addition, I gratefully acknowledge the support of the Center for Holographic Studies and Laser micro-mechanics (CHSLT) in the Mechanical Engineering Department of WPI, for the use of their facilities and equipment in my studies. I would like to thank Dr. Ivo Dobrev, Dr. Morteza Khaleghi, Mr. Peter Hefti, Mr. Koohyar Pooladvand, and Mr. Haimi Tang for their help and guidance in my work at the CHSLT. I would also like to thank Mr. Michael E. Ravicz and Dr. Nima Maftoon from the Eaton Peabody Laboratories (EPL) at Massachusetts Eye and Ear (MEE) for their help and guidance in my experimental work.

I would like to express my special gratitude to my wife and my best friend Maryam who always supported me, and our two beloved daughters, Nika and Melody, through all of the challenges we had. Without her constant encouragement, and support, I could not finish this chapter of my life. I would also thank my parents (Giti and Kamal), my wife's parents (Nezhat and Masoud), and my brother (Pedram) for their ongoing motivations, guidance, and support. Without you, I know I could not be where I am.

This Dissertation has been supported by funding from the National Institute of Health (NIH), National Institute of Deafness and other Communication Disorders (NIDCD), Massachusetts Eye and Ear (MEE), and the Mechanical and Manufacturing Engineering departments.

Table of contents

Abstract	i
Acknowledgements	iii
Table of contents	iv
List of Figures	vii
List of Tables	xv
Nomenclature	xvi
Objectives	xvii
Impact of this work	xviii
1 Introduction	xix
1.1 Problem statement	xix
1.2 Significance of the problem	xx
1.3 Dissertation outline	xxi
Part 1: Background	24
2 Physiology and anatomy of human ear	26
2.1 Middle-ear	27
2.2 Anatomy of the tympanic membrane	28
2.3 Ultrastructure of tympanic membrane	29
2.4 Available TM models	29
3 The need for TM measurements and constraints on such measurements	32
3.1 Benefits of full-field of view TM shape and transient response measurements	33
3.1.1 Full-field-of-view measurements	33
3.1.2 Transient response measurements	33
3.1.3 Shape measurements	34
3.2 TM measurement constraints	35
3.2.1 Anatomical and physiological constraints	35
3.2.2 Methodological constraints	36
3.2.3 High-speed Digital Holographic (HDH) method	38
3.2.4 Technological constraints of HDH	41
4 Holographic interferometry for displacements measurements and the need for TM shape	44
4.1 Sensitivity vector	44
4.2 TM displacements type	47
4.3 TM displacements measurements using surface normal vector	48
4.4 The effect of inaccuracies in the sensitivity vector and normal direction on measurements of the normal displacement	49
4.5 TM measuring specifications	51
4.5.1 Sample specifications	51
4.5.2 Optics and imaging sensor specifications	52
4.5.3 Setup specifications	52
4.6 Uncertainty due to sensitivity vector measurements	53
4.6.1 Variations in the angle and magnitude of the sensitivity vector across the field of view as a function of distance	54
4.6.2 Shape induced variations of the sensitivity vector across the field of view	56
4.6.3 Effects of shape resolution on the sensitivity vector	56
4.6.4 Coordinate of the illumination point P1 effects on the sensitivity vector	57
4.6.5 Sensitivity vector uncertainty: dominant parameters	58
4.7 Surface normal uncertainty	59

4.7.1	Analytical determination of surface normals	59
4.7.2	Surface noise effects on surface-normals	60
4.8	Preliminary estimation of required shape resolution	61
Part 2:	Developments	64
5	High-speed phase sampling methods using phase correlation interferometry.....	66
5.1	Challenges of high-speed phase sampling	66
5.2	Speckle pattern correlation interferometry	69
5.2.1	Effects of zero-order terms in speckle pattern correlation interferometry	72
5.2.2	Measurements of zero-order terms	74
5.2.3	High-speed phase Correlation Interferometry (HCI)	75
5.3	Uncertainty analysis on the HCI method	77
5.3.1	Zero order terms (DC)	77
5.3.2	Removal of zero order terms for high-speed transient measurements	79
5.3.3	Phase shifter resolution and precision	80
5.3.4	Speckle kernel size ratio	81
5.3.5	Phase unwrapping.....	85
5.4	Continuous phase shift in presence of spatiotemporal noises.....	86
5.5	High-speed Phase Correlation Calibration (HPCC) method	88
5.5.1	HPCC mathematical background	90
5.5.2	HPCC quantitative phase measurements	91
5.5.3	Automated phase detection algorithm	93
5.5.4	HPCC Requirements	93
5.5.5	Case 1 – high-speed continuous phase sampling in presence of temporal noises ($N(\mathbf{t})$) and phase shifter nonlinearities ($\delta\mathbf{t}$).....	95
5.5.6	Case 2 – High-speed phase sampling in presence of spatiotemporal motions	99
6	High-speed holographic shape measurements	106
6.1	Multiple Wavelengths Holographic Interferometry (MWHI)	108
6.1.1	MWHI in the presence of wavefront and optical distortions	112
6.1.2	Holographic flat surface calibration	113
6.1.3	Requirements of holographic flat surface calibration method	116
6.2	High-speed multi-resolution MWHI shape measurements.....	116
6.2.1	High-speed phase sampling in presence of wavelength and sample noises	118
6.2.2	Implementation of the high-speed MWHI method	121
6.3	High-speed combinatorial MWHI shape measurements	122
6.4	Shape and displacements measurement setup.....	124
6.5	Uncertainty analysis.....	126
6.5.1	Synthetic wavelength.....	127
6.5.2	Interference phase.....	128
6.5.3	Phase shifter error.....	129
6.5.4	Laser source Stability	129
6.5.5	Spatial resolution	130
6.6	Validation of the shape measurements	131
6.6.1	Shape resolution	131
6.6.2	Shape repeatability	133
Part 3:	Applications.....	135
7	High-speed holographic shape and transient response measurements of human tympanic membrane.....	136
7.1	Setup specifications	136

7.2	Timeline	137
7.3	Sample preparation	139
7.4	Multi-resolution MWHI shape measurements.....	140
7.5	Combinatorial shape measurements	143
7.6	Surface normal and sensitivity vector measurements.....	146
7.7	Determination of sensitivity multiplier.....	147
7.8	Displacements measurements results.....	148
7.9	Significance of surface-normal displacement measurements	152
8	Milestones.....	156
8.1	Continuous phase sampling and repeatability of the measurements	159
8.1.1	Transient response of the eardrum Excited by localized mechanical forces.....	160
8.1.2	Response of the human tympanic membrane to transient acoustic and mechanical stimuli: Preliminary results	167
8.2	In-vivo displacement measurements.....	177
8.2.1	High-speed holography for in-vivo measurement of acoustically induced motions of mammalian tympanic membrane	178
8.3	Robust high-speed temporal phase sampling.....	185
8.3.1	Noise immune high-speed holographic vibrometry	186
8.4	High-speed multi-resolution shape and displacement measurements	188
8.4.1	High-speed shape and transient response measurements of TM.....	189
8.5	High-resolution combinatorial MWHI shape measurements	195
8.5.1	Full-field surface profilometry using temporal domain high-speed multi- wavelength holography	196
	Conclusions and future work	198
	References.....	202
	Appendix A. Phase correlation interferometry: derivations of mathematics.....	210
	A.1 General speckle correlation case with intensity ratio r	211
	A.2 Equal intensity ratio ($r=1$).....	212
	A.3 Zero order terms were removed.....	213

List of Figures

Figure 2-1	The auditory periphery system in humans, (Flanagan, 2013; Geisler, 1998).....	26
Figure 2-2	Cross section of the human middle-ear showing the ear canal, the TM, the ossicles as well as middle-ear cavity.	27
Figure 2-3	(a) terminology of different components of the TM; and (b) typical shape and orientation dimensions of an adult human (Adapted from Ferrazzini, 2003).	28
Figure 2-4	Left, scanning electron microscope image of the surface of TM inferior to umbo showing the distribution of radial and circumferential fibers; and right, the internal structure of the TM tissue showing different categories of fibers and layers (Khaleghi, 2015; Lim, 1970).....	29
Figure 2-5	View of an electrical lumped model of the peripheral auditory system showing the model of tympanic membrane as a series of interconnected circuits: (a) lumped model representing the outer-, the middle- and inner-ear; and (b) detailed circuits representing the interconnected middle and inner ear. (Rosowski, 1996).....	30
Figure 2-6	FE model, distributions of the equivalent (von Mises) stress of the TM, adapted from (Rong Z Gan et al., 2016a);.....	31
Figure 3-1	Schematic representation of a scanning Laser Doppler Vibrometer for full field high-speed TM measurements. The laser Doppler Vibrometry measures the displacements by measurements of the beating frequency generated by superimposing a phase modulated test beam (i.e., with added frequency of fb by a brag cell crystal) and the reflected beam having a frequency shift due to the sample vibrations (i.e., fd due to Doppler frequency shift).....	37
Figure 4-1	Nomenclature for fringe analysis (adapted from Vest, 1979): (a) schematic representation of optical path length from observation to a point on the sample surface to point of observation on the CCD; and (b) variations in path-vectors and propagation vectors due to deformation vector L	45
Figure 4-2	Schematics of out-of-plane displacements measurements by the sensitivity vector K , and surface normal vector n	49
Figure 4-3	Schematic representation of the effects of variations of the measured interference phase as the angle between sensitivity vector and the surface normal vary across the field of view: (a) angles compared to sensitivity vector and surface normals; and (b) schematic representation of the interference phase measured at each location.	50
Figure 4-4	Schematic representation of maximum TM curvature located close to umbo. Umbo region is shown with (U).	52
Figure 4-5	(a) view of the model showing spatial variations of the sensitivity vector at distance $d=10$; and (b) the results of the numerical model. Blue line presents maximum rotation of the sensitivity vector across the field of view.	55
Figure 4-6	Spatial variations of sensitivity vector due to a TM-like shape oriented 45° with respect to camera axis. Shape induced rotations of the sensitivity vector	

	angle compared to a flat sample shows mean of $\sim 10^\circ$ rotation with standard deviation of 2.5°	56
Figure 4-7	(a) the sensitivity vector before and after an added noise when δzp is within $\pm 200\mu m$ using red and black vectors, respectively; and (b) standard deviation, mean and maximum rotation of the sensitivity vector of all points as a function of shape resolution $\pm \delta(zp)$ compared to the sensitivity vector without the noise.....	57
Figure 4-8	(a) schematic representation of the variations of the sensitivity vector due to uncertainty in the illumination rotation of the sensitivity vector due to the uncertainty in the coordinates of point $P1$ (i.e., $\delta(P1)$); and (b).....	58
Figure 4-9	Comparison of spatial filtering effects on αe for a fixed $\delta zp = \pm 50\mu m$ with $d = 10mm$. Red and blue vectors show the surface normals before and after the addition of the spatial noise. Gray vectors in the background represent the sensitivity vector at each point that are nearly immune to such level of surface discontinuities. The spatial distribution of surface normals in different window size of spatial filtering: (a) no spatial filtering mean of errors in α of about 40° ; (b) Gaussian spatial filter with window of 10 with mean of errors in α of about 20° ; and (c) Gaussian spatial filter with window of 100 with mean of errors in $\alpha < 10^\circ$	61
Figure 4-10	Results of numerical simulation under various uncertainties to determine maximum errors in the measured angle αe : (a) the sample shape and orientation with respect to illumination and observation angles together with spatial distribution of sensitivity vector and surface normals in ideal and uncertain conditions. Black and red arrows show the variations of the sensitivity vector while the green and magenta show the variations of the surface normal due to various parameters uncertainties; and (b) histogram of the parameter αe with Mean = 1.97° , and STD = 3.6°	62
Figure 5-1	Effects of high-speed phase stepping as the inter step time intervals decrease. Blue line shows the behavior of the phase shifter with longer inter-step with temporal intervals ($\Delta t1$) while the green line shows smaller interval $\Delta t2$. As Δt decreases, the phase shifting procedure is more affected by the transient ringing motions of the mechanical phase shifter.....	67
Figure 5-2	(a) Correlation coefficients between two extreme variations of the interference phase with respect to the reference speckle pattern due to the motions of the sample; and (b) schematic representation of formation of speckles and variations of the speckle pattern with respect to sample displacements. The figure show multiple coherent beams interfere constructively and destructively over the CCD of the camera to form a speckle pattern. Due to spatial periodicity of the light with a fixed wavelength, depending on the angle of observation, complete cycles of the interference phase harmonically generating the same pattern. The figure shows the relation between the displacements d and interference phase $\Delta\phi$ from the principles of holographic sensitivity vector.....	70
Figure 5-3	Correlation range schematic representation in terms of interference phase $\Delta\phi$	72

Figure 5-4	Timing of the events occurring during high-speed 2+N frame acquisition with the local correlation phase sampling method. N deformed frames are acquired at the maximum frame rate of the camera and referenced relative to frames captured during two periods prior to acoustic excitation. Acquisition takes into account the settling time of the piezoelectric (PZT) phase shifter, while minimizing the overall acquisition time. The PZT is returned to its original position at the end of the acquisition. Due to the distance between the sound source and the sample, there is an acoustic transmission delay (I. Dobrev et al., 2014b).	76
Figure 5-5	Wrapped interference phase estimated by the HCI method under various DC removal conditions: (a) DC not removed, holograms were intact; (b) DC was calculated using a group of randomly phase shifted references and removed from all holograms; and (c) DC was calculated using a complete cycle of phase-shifted references and removed from each hologram. Bottom panels show spatial distribution of modulo 2π wrapped phase across the blue line for each case.	77
Figure 5-6	Comparison of tangent function compared to partially removed zero order terms with $r = 1$.	78
Figure 5-7	Measured OPE with respect to phase shifter miscalibration at various phase angles. The error in the phase shifter in degrees is scaled on the x-axis. The y-axis is OPE the error in the optical length estimate in degrees. (The diamonded lines represent the negative errors). The calculations are performed around 4 potential values of phase shift (10, 30, 60 and 90 degrees). Minimum sensitivity to the phase shifter miscalibration occurs when the induced phase shift is at $\pm 90^\circ$. The largest errors in the estimated interference phase occur when the interference phase is near zero, but those errors are similar in magnitude to the error in the phase shift.	81
Figure 5-8	Correlation fringe patterns for a 10-mm in-plane translation calculated with correlation cells of dimensions: (a) 2×2 ; (b) 5×5 ; (c), 9×9 ; and (d) 19×19 pixels. Insets are the corresponding normalized correlation magnitude histograms with the independent axes ranging from -0.1 to 1, the range of correlation values for the pixels in the image. Panels beneath each correlation image are the intensities observed along the horizontal profile indicated by the dotted lines through the centers of the images. Adapted from (Schmitt & Hunt, 1997).	83
Figure 5-9	Schematic representation of one dimensional phase unwrapping procedure: (a) modulo 2π phase; (b) step function to trace the absolute value of the phase; and (c) unwrapped phase by addition of modulo 2π phase, panel (a), by the step function of panel (b). Adapted from (Ulf Schnars et al., 2015)	85
Figure 5-10	Off axis configuration parameters: (a) schematic representation of the setup; (b) enlarged pink area of panel (a), representing angle θ_{PZT} ; and (c) enlarged blue area of panel-a representing the spatially varying angle $\theta_s(x, y)$ due to shape and off-axis illumination.	87
Figure 5-11	Schematic representation of the effects of sample motions on the continuous phase shift. (a), random displacements of sample on top of linear motions of	

	the PZT positioner having faster motions compared to the sample; and (b) resultant applied shift affected by the sample motions having at least a complete cycle during the period of phase shift.	87
Figure 5-12	Schematic representation of the HPCC method initial steps. Red dashed lines represent the schematic timing of the center of repeated camera exposures, P refers to P_x, y, t_0, t_k with the range $1 - \epsilon, \rho_{min} - \epsilon$ as described in Eqn. (5-29), and P_{sc} is the scaled signal with the range $-1, 1$	92
Figure 5-13	Representation of the 2+N HCI measurements timeline using a continuous ramp. The high-speed exposures run continuously for the entire measurements while reference frames measurements, excitation, and transient response measurements are synchronized with the camera.	95
Figure 5-14	Results of HPCC method in determination of applied shift along a 2.8 msec continuous phase shift with about 1064 μ m displacements on a flat latex membrane: (a) the scan results of the correlation between the first and successive holograms averaged over all kernels over the spatial domain before and after automated corrections together with the normalized PZT input voltage. The location of the best frames determined by the algorithm are shown with colored shapes corresponding to $[0, \pi/2, 3\pi/2, 2\pi]$ shifted phase, P, P_{sc} are defined as in Figure 5-12 and $PDRC = P - a1$; (b) the correlation images before averaging for the chosen temporal instances and (c) histogram of each of the correlation images in panel (b) showing mostly normal distribution.	96
Figure 5-15	Applied shift signal P_{SC} in the frequency domain.	98
Figure 5-16	Representative results of application of HPCC algorithm on the 2+N HCI method: (a) wrapped phase; (b) wrapped and unwrapped phase of the line shown in (a); and (c) unwrapped phase.	98
Figure 5-17	Schematic representation of the effects of HPCC method application in Case 2: (a) schematic representation of differences in determined phase shift at different locations on the sample; and (b) a schematic map of spatially varied timings that yield a single uniform shifted phase. The schematic view does not represent the sensor resolution (e.g., 512 \times 512).	100
Figure 5-18	Steady state and transient acoustic excitation: (a) time domain; and (b) frequency domain. The frequency spectrum shows a sharp peak at 2 kHz.	101
Figure 5-19	Representative results showing the existence of a spatially varying phase shift during the ramp: (a) average correlation over all pixels in each image; (b) spatial distribution of the unscaled correlation maps showing patterns of sample displacements; and (c) histogram of each image showing non-Gaussian distribution (see similar graph of Case 1 in Figure 5-14).	102
Figure 5-20	Results of spatial calibration of the set of references for $\pi/2$ phase shift. The timing diagram of the events is shown schematically with the frames numbering as well as their location on the ramp.	103
Figure 5-21	Comparison of the results of temporal reference speckle pattern reconstruction: (a) speckle pattern reconstructed with $\pi/2$ applied shift compared to $t=0$ hologram; (b) intact speckle pattern from the hologram that	

	has the closest averaged value to $\pi/2$ phase shift; and (c) subtraction of (a) and (b) speckle patterns shown in percentile of the sensor depth (i.e., 2.5% of 212 is 100).	103
Figure 5-22	Comparison of the results of quantitative phase measurements using 2+1 HCI method for (a-c) with intact $\pi/2$ phase shifted reference hologram, and (d-e) with reconstructed reference frame using the HPCC method at each pixel: (a, d) wrapped phase; (b, e) wrapped and unwrapped phase plots along the lines shown in panel (a, d); and (c, f) unwrapped phase maps of each Case.	104
Figure 6-1	Three-dimensional geometrical representation of the two-wavelength optical setup. $P1$ is the point of illumination, $P2$ is the point of observation, P is an arbitrary point on the surface under investigation. Elliptical contours due to superposition of the two wavelength interferograms are shown that are intersecting the sample with contours of constant height.....	110
Figure 6-2	Schematic representation of the holographic flat surface calibration method. The uncalibrated shape of the flat surface is shown with the blue-bordered plane.	114
Figure 6-3	Two-dimensional schematic representation of the holographic flat surface calibration technique. Measuring the flat surface using the elliptical wavefronts, a non-flat distorted shape is determined and shown with dashed black lines. This is compared to a tilted coordinate system due to off axis illumination, which is shown with a thick black line. Subtraction of the black arrows (distorted shape of the flat sample) from any measurements result in removal of the distortions as well as the carrier from the measurements.	115
Figure 6-4	Off axis configuration parameters: (a) schematic representation of the setup; (b) enlarged pink area of panel (a), representing angle θ_{PZT} ; and (c) enlarged blue area of panel-a representing the spatially varying angle $\theta_s(x, y)$ due to shape and off-axis illumination.....	118
Figure 6-5	Representation of the spatially varied wavelength induced phase shifts: (a) correlation maps between two phase shifted holograms interfered by <0.02 nm wavelength variations captured in a period of $535\mu s$ during the wavelength tune; and (b) histogram of the gray scale values in panel (a) showing non uniform spatial phase shift. The sample is a human TM having a depth at the central region of $<2mm$	121
Figure 6-6	Schematic representation of the timeline of the events in a set of high-speed MWHI shape measurements. The blue diamond stem line in the top panel represent the initiation of a square pulse sent to the laser driver to alter the wavelength while the black line show the resultant wavelength variations having ~ 50 msec delay. Each of the circular stem lines indicate the initiation of a set of high-speed phase shifted frames as shown in the bottom panel. In each set a continuously linear phase shift (i.e., ramp) is performed by a duration of $<500 \mu s$ and amplitude of several wavelengths to generate a few cycles	122
Figure 6-7	Schematic view of the shape and displacement measurement setup. MS - Mechanical Shutter, VBS - Variable Beam Splitter, DM Dichroic Mirrors, M- Mirror, W - Wedge beam combiner, OL -Objective Lens.....	125

Figure 6-8	Schematic representation of the relation between the maximum quantifiable fringe density, maximum surface angle, and the minimum contour depth.	131
Figure 6-9	Spatial distribution of errors between the radius of the measured surface and the fitted sphere: (a) before the flat surface calibration; and (b) after the flat surface calibration. Top left of each panel is the modulo 2π interference phase before and after calibration respectively.	133
Figure 6-10	Custom made conical latex membrane to study the repeatability of the measurements: (a) the mechanism to make a 3D artificial membrane with adjustable depth; (b) side view for the measurements presented; and (c) isometric view showing the diameter of the sample.	133
Figure 6-11	(a) the wrapped modulo 2π phase corresponding to each of the five consecutive shape measurements; (b) spatial distribution of the standard deviation of wrapped phase in all trials; and (c) spatial distribution of standard deviation of unwrapped phase of all trials. All units are in radians....	134
Figure 7-1	Schematic view of the shape and displacement measurement setup. MS - Mechanical Shutter, VBS - Variable Beam Splitter, DM Dichroic Mirrors, M- Mirror, W - Wedge beam combiner, OL -Objective Lens.....	137
Figure 7-2	Timeline of the events in a set of shape and displacements measurements. The green and red background on the top panel represent the timing that each laser illuminate the sample. Green is for the 532 nm and red is for the infrared tunable laser. The round headed stems show the timing of camera triggers. The blue diamond stem represents the initiation of the laser tune, and the green diamond stem is the trigger to excite the sound source. The timing of the displacement measurement is shown with a dashed blue background. Bottom tight panel schematizes one of the continuous phase shifts to determine the phase of the wavefront sufficiently faster than laser wavelength variations.....	137
Figure 7-3	The sample, setup, and measuring instrumentations: (a) top view; (b) isometric view; and (c) the sample; a human post-mortem TM. The black contour shows the outline of the manubrium and umbo (shown with a U symbol).....	139
Figure 7-4	Representative phase maps showing the multiple resolution measuring capability: (a) timings of the wavelength variations with respect to the triggers. The wavelengths are numbered by their temporal sequence during the tuning ramp. There are no jumps in the actual wavelength tuning, the jumps observed in the wavelength readings are due to the low temporal resolution of the wavelength meter (<80 Hz); (b) wrapped and unwrapped phase maps taken with selected arbitrary combinations showing various number of fringes across the sample. Large synthetic wavelengths (i.e., $\lambda_{5,6}$) provide phase maps that are relatively immune to shape discontinuities as well they may not require phase unwrapping procedures (there are no wrapped discontinuities). The smaller synthetic wavelength phase maps (i.e., $\lambda_{1,10}$, $\lambda_{1,8}$) provide shorter contour depth with higher signal to noise ration to observe finer details of the surface, however they are more sensitive	

	to surface discontinuities as in panel of $\Lambda 1,10$, the unwrapping error artifacts at the umbo and annulus region were formed due to denser fringes.	141
Figure 7-5	Results of reconstructing the shape from the phase map having synthetic wavelength $\Lambda 1,8$ (shown in Figure 7-4): (a) 3D representation of the shape after slight spatial filtering (averaging 3 by 3 pixels). The peripheral regions of the shape (part of annulus and temporal bone) show unwrapping errors as a result of shadows and sharp discontinuities between the temporal bone and pars tensa; and (b) TM shape, masked and spatially filtered (averaging 15 by 15 pixels), suitable for determination of surface normals.	142
Figure 7-6	TM measured shape using the combinatorial MWHI method. Scaled and calibrated results are determined by fitting a normal distribution over >200 scaled measured shapes across the tuning ramp. The color bar represents the shape of the sample along the z-axis. The shape illustration in left and right view has a larger dimension along z-axis to show the shape at the umbo and annulus regions.	144
Figure 7-7	Distribution of 10 times down sampled surface normals (\mathbf{n}), and sensitivity vectors \mathbf{K} : (a) full-field surface normal distribution; (b) zoomed distribution of surface normals at the black line region of panel (a); (c) sensitivity vector distribution $\mathbf{K}(x,y)$ black dashed line region of panel (a); and (d) determined surface normals and sensitivity vector along the red line shown in panel (a). magenta vectors are the surface normals and black vectors are sensitivity vectors;	146
Figure 7-8	Schematics of out-of-plane displacements measurements by the sensitivity vector \mathbf{K} , and surface normal vector \mathbf{n}	147
Figure 7-9	Spatial distribution of sensitivity multiplier $\eta(x,y)$ determined for displacements measurements laser wavelength of $\lambda = 532 \text{ nm}$. The deep blue region has the multiplier equivalent to parallel observation and illumination.	148
Figure 7-10	The output of the HPCC algorithm showing the applied shift across the ramp using the methods described in Section 5.5.	149
Figure 7-11	Nine temporal instances of the full-field of view normal displacements of the TM due to an acoustic click excitation superimposed on its shape. The color bar represents the actual amplitude of the calculated normal displacements. The displacements in the 3D plots are 1000 times exaggerated to be able to show them on top of the millimeter-scale shape. The number on top right of each panel show the maximum absolute displacements at that instance.	151
Figure 7-12	Time waveforms of six selected regions across the sample out of more that 200,000 data points. The location of each point (the center of a spatial averaged window of 5 pixels) with respect to the shape of the TM is shown on the top right panel. Calibrated sound pressure readings are shown on top of the waveform of point 1 (umbo displacements).	152
Figure 7-13	The spatiotemporal absolute differences between surface-normal displacements and the displacements determined under PIO assumptions. The maximum differences occur at $387\mu\text{s}$ with an amplitude $\sim 138 \text{ nm}$	153

Figure 7-14 Temporal variations of errors induced by application of a PIO sensitivity vector with respect to the results obtain by application of spatially varied sensitivity vector and surface normals. The blue line shows the percentile between the two orange lines scaled on the right side of the panel in nanometers. The solid orange line shows the amplitude of maximum displacement errors at each hologram while the dashed orange line show the normal displacements measured at the same location.154

List of Tables

Table 3-1	Comparison of the performance of available HDH methods for the TM measurements application.	40
Table 4-1	Optical configuration specifications used for measurements in this Dissertation.....	52
Table 6-1	The results of sphere fitting for determination of shape resolution.	132

Nomenclature

TM	Tympanic Membrane
HPCC	High-speed Phase Correlation Calibration
HDH	High-speed Digital Holography
MWHI	Multiple Wavelengths Holographic Interferometry
CCD	Charge-Coupled Device
dB	Decibels
BS	Beam splitter
λ	Laser Wavelength
IR	Infrared
IL	Illumination point
OB	Observation Point
LDV	Laser Doppler Vibrometry
MEMS	Micro-Electro-Mechanical Systems
MWHI	Multiple Wavelengths Holographic Interferometry
SPL	Sound Pressure Level
K	Sensitivity vector
k_i	Illumination vector
k_o	Observation vector
τ	Exposure time
Λ	Synthetic wavelength
φ	Optical phase of the hologram
$\Delta\phi$	Interference phase
ω	Angular frequency
3D	Three dimensional
1D	One dimensional
PIO	Parallel Illumination Observation
LP/mm	Line-Pairs per millimeter
PZT	Piezoelectric or lead (Pb) zirconate (Zr) titanate (Ti)

Objectives

The primary objective of this work is to advance the performance of a full-field high-speed holographic system by development of shape and displacement measurement methods to increase precision and accuracy for better analysis of the complex spatiotemporal transient response of mammalian tympanic membrane (TM). The long-term objective is to develop a high-speed endoscopic shape and motion measurement system for in-vivo holographic measurements. In this Dissertation, the techniques applicable to this objective are described, which include:

1. Implementation and hardware developments together with control and synchronization procedures for high-speed shape and displacement acquisition,
2. characterization of measuring capabilities,
3. automation and improvements in acquisition and post-processing procedure,
4. representative measurements and analysis of TM motion and shape in cadaveric humans and live animals.

Impact of this work

Based on National Institute on Deafness and other Communication Disorder (NIDCD), >360 million people around the world suffer from some level of hearing loss and about 2 to 3 in 1000 US newborns (i.e., more than 12,000 newborns for 2015) are born with a level of hearing loss. Despite decades of research, the available clinical tools for the middle-ear are either qualitative (e.g., they require the response of patients or subjective observations) or they provide limited quantitative data based on acoustic reflectance. For better diagnosis and research on the complex structure of middle-ear in normal and pathological conditions, a bioinstrumentation capable of measuring the in-vivo full-field-of-view sound induced displacements of the Tympanic Membrane (TM, eardrum) is required. The methods developed in this Dissertation enable near instantaneous (<200 msec) and repeatable full-field-of-view measurements of the shape and acoustically induced transient displacements of the TM in live samples, that can directly benefit the lives of millions of people with hearing loss.

1 Introduction

1.1 Problem statement

Understanding the sound induced spatio-temporal displacements of the TM will provide valuable information about the performance of the TM and the rest of middle and inner ear. However, measurements of these displacements are very challenging due to required nanometer and microseconds spatial and temporal resolutions together with challenges such as millimeter-scale shape variations of the TM and its confined location within the ear canal. Furthermore, in-vivo TM measurements are adversely affected by submillimeter scale physiological motions (due to respiration, tremor, and heartbeat) which make measurements of the nanometer-scale sound-induced motions even more challenging.

A high-speed holographic system capable of performing transient full-field measurements of acoustically induced motions of the TM is in development. In many holographic interferometric cases, it is assumed to have a single sensitivity vector due to small variations of the optical path length (i.e., micrometers) with respect to the sample and setup dimensions (i.e., meters). However, due to millimeter-scale shape and orientation of the TM as well as close illumination/observation inside the ear canal, an assumption of single-sensitivity-vector can produce errors in the estimated normal motion as large as 50%.

1.2 Significance of the problem

Based on National Institute on Deafness and other Communication Disorder (NIDCD), about 2 to 3 in 1000 US newborns (i.e., more than 12,000 newborns for 2015) are born with a level of hearing loss and 5 out of 6 children may have middle-ear infection (otitis media) before the age of three. Diagnosis of hearing loss at early stages in child development (i.e., before 6 months) is critical for the initial development of the brain. However, detection of the type of the loss (conductive, sensorineural, or mixed) with the available clinical methods are very challenging and can lead to delays/errors in treatment. Efficient quantitative measurement tools are essential for early diagnosis of such diseases without relying on qualitative response of the patient. Such tools are needed for many other related areas such as modeling of the middle-ear, hearing devices (i.e., hearing aids and hearing protection), improvements in rehabilitation surgeries (i.e., tympanoplasty), and for additive manufacturing of biological grafts and artificial TMs.

1.3 Dissertation outline

This Dissertation has three main parts: Background, Developments, and Applications.

Chapter 2 of the Dissertation presents the literature and background information on anatomy and physiology of the middle-ear having the main focus on the Tympanic Membrane (TM) and complications in the characterization of TM function.

Chapter 3 specifically focuses on the TM measurements. First, the need for a viable and repeatable measuring instrument for the middle-ear is discussed followed by the methodological, technological and physiological constraints for the full-field shape and displacement measurements.

Chapter 4 presents the necessity of shape measurement in parallel with displacement measurements for higher accuracy by determination of surface-normals. First, the concept sensitivity vector in holography as well as the dominant theories governing the response of the TM are presented. In the next section, using a numerical simulation an uncertainty analysis is performed to determine the errors in an endoscopic configuration (which will be required for use in live patients) as well as TM shape and orientation. The last section of the uncertainty analysis uses the numerical model to answers the question of “What is the minimum shape and orientation measurements resolution (either axial or lateral) to accurately determine the surface-normal displacements?”

The developments part of the Dissertation (Chapters 5 and 6) presents the developments and improvements in high-speed holographic methodologies to enable rapid displacements and shape measurements in a short period (i.e., <200 msec) within one instrument.

Chapter 5 presents the methods developed to enable precision in the High-speed Digital Holography (HDH) displacement measurement methods. An uncertainty analysis was first performed with a detailed calculations about the basics of the correlation interferometry to

understand the effects of each parameter on the displacement resolution. A closed loop control mechanism using a continuous phase shift is proposed that can account for phase shifter positioner nanometer-scale inaccuracies, sample induced spatiotemporal motions, and wavelength variations. A novel method called High-speed Phase Correlation Calibration (HPCC) is developed to determine the applied phase shift during the reference holograms acquisition phase for the open-loop control mechanism. This method helps to robustly determine/reconstruct the desired phase shifted reference frames necessary for quantitative phase sampling. To show the robustness of the method in presence of various types of noises, the developments are tested by two experimental case studies resembling the two major possible measuring conditions (i.e., the post mortem and live TM measurements).

In Chapter 6, the proposed shape measurement method is presented based on multiple wavelength holography that utilizes the optimized HPCC method of Chapter 5 to extract high-resolution shape from the entire spatiotemporal bandwidth of the high-speed sensor. A simple but practical method to remove the wavefront distortions are presented called flat surface calibration. Representative measurements show the application of shape for determination of surface-normal displacements by accurate calculation of a spatially varying sensitivity of the holograms. Finally, the shape measurement resolution and precision is determined using standardized gauges.

The applications section consists of two chapters (Chapter 7 and 8).

Chapter 7 presents the representative results on a post mortem human TM together with preliminary analysis of the measurements to demonstrate the added shape and displacements measuring capabilities. It was determined that spatially varied sensitivity of holograms due to spatial variations of surface normal and sensitivity vector can produce spatially varied errors as large as 138 nm that indicate the added accuracy in HDH displacement measurements.

Chapter 8 presents the milestones in the developments of the HDH shape and displacement measurements methodologies mostly in the form of peer-reviewed publications. Each publication

addresses a step in the developments of the high-speed digital holography for the middle-ear research and clinical applications.

Appendix A holds the detailed calculations about stochastic probability analysis of the speckle patterns performed to verify and update the correlation interferometric methods in Chapter 5.

Part 1: Background

2 Physiology and anatomy of human ear

The role of the peripheral auditory system in humans and most terrestrial mammals is to convert the sound waves from the environment to nervous impulses sent to the brain. The auditory periphery consists of three main components: *the outer, the middle, and the inner ear* (Figure 2-1). The outer ear amplifies the sound waves using a funnel shape structure and guide the sound waves toward the *Tympanic Membrane* (TM, eardrum) at the inside (or medial) end of ear canal. The middle-ear is a miniaturized biomechanical transducer submerged in an air-filled cavity protected by the skull bone (temporal bone). The mammalian middle-ear consists of the TM, ossicles (three interconnected small bones called malleus, incus, and stapes), ligaments, and muscles. As sound stimuli reaches the TM, it vibrates the interconnected ossicles, which in turn vibrate the oval window located at the stapes footplate (Decraemer & Funnell, 2008; Rosowski, 1994, 1996).

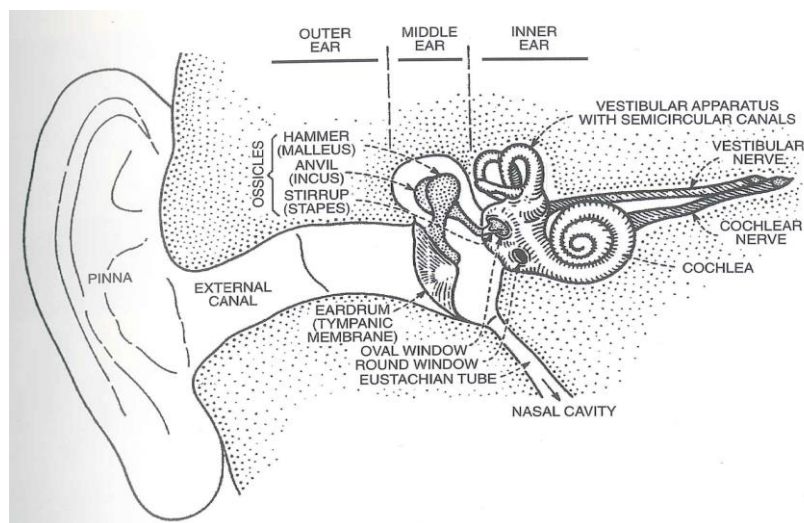


Figure 2-1 The auditory periphery system in humans, (Flanagan, 2013; Geisler, 1998)

The hearing related portion of the inner ear (cochlea) consists of three lymph-filled chambers rotating along an axis acting as a frequency filter. The pressure difference

between the Scala Vestibuli (chamber stimulated by ossicular vibrations of the oval window) and Scala Tympani (chamber connected to the round window) drive the hair cells sending impulses to the brain. While the major path to drive the cochlea is through the stapes footplate, the TM vibrations, which are the first step in the transformation of sound energy into the mechanical energy of ossicular motion, play an important role in driving the interconnected ossicles and inner ear (Geisler, 1998).

2.1 Middle-ear

The middle-ear is an air filled biomechanical system that consists of *Tympanic Membrane* (TM or eardrum), ossicles (three bones called *malleus*, *incus*, and *stapes*), ligaments, and muscles (Figure 2-2). Literature starting from the 19th century suggests the middle-ear is perfectly designed to match the low impedance of airborne sound waves, moving with high velocity and small mass, with the high impedance fluid (cochlear lymphs) inside the inner ear. The larger area of the TM ($\sim 70 \text{ mm}^2$ in adult human) compared to the stapes footplate ($\sim 3 \text{ mm}^2$ in adult humans) and the lever action of the ossicles are contribute to this transformer function.

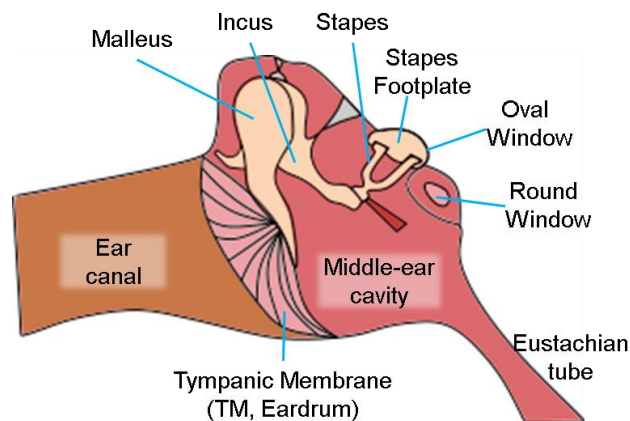


Figure 2-2 Cross section of the human middle-ear showing the ear canal, the TM, the ossicles as well as middle-ear cavity.

The response of the middle-ear to transients occur very rapidly (i.e., <2 msec) and there is no time for any active biological control system, therefore the literature suggests the middle-ear is under passive control. (Aernouts et al., 2012; T. Cheng et al., 2007; De Greef et al., 2015; Decraemer & Funnell, 2008; Fay et al., 2005; Feng & Gan, 2004; Geisler, 1998; Møller, 1963; Rosowski, 1994; Rosowski et al., 2009; Stasche et al., 1994; Volandri et al., 2011; F. Zhao et al., 2002).

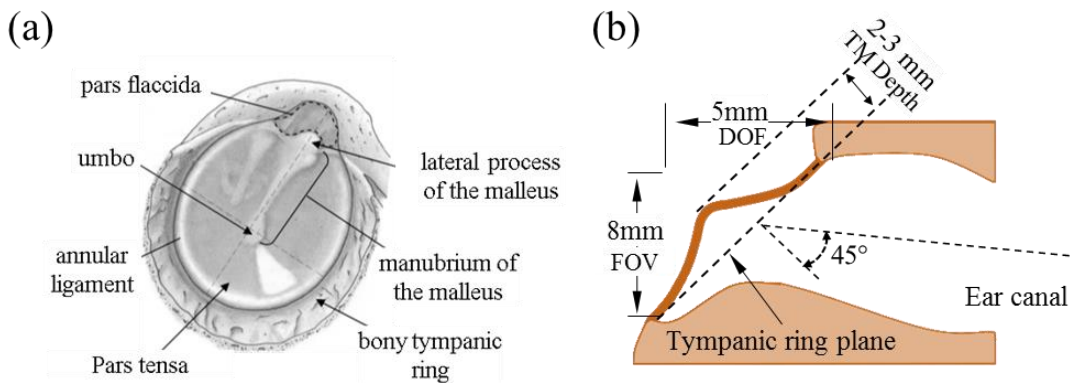


Figure 2-3 (a) terminology of different components of the TM; and (b) typical shape and orientation dimensions of an adult human (Adapted from Ferrazzini, 2003).

2.2 Anatomy of the tympanic membrane

The adult human TM has a conical shape with ~8-10 mm diameter and 2-3 mm depth compared to the Tympanic ring plane. The TM is typically positioned at an acute angle at the end of the ear canal (Figure 2-3). The amplitude of the sound induced displacements of the TM surface during normal daily conversation (40-70 dB SPL) ranges from sub-nanometers up to sub-micrometers (~0.1-700 nm). The human TM consists of two main parts, pars tensa, a thin multi-layer bio-composite with ~30-130 μm thickness, and pars flaccida, which is thicker and contributes little to the hearing process (Rosowski, 1996; Van der Jeught et al., 2013). Thickness measurements suggest that there are large variations with respect to age, and from person to person, however there is a high

correlation between spatial thickness variations across multiple samples showing a spatially varied thickness distribution of ~50 μ m to ~200 μ m (Kuypers et al., 2006; Volandri et al., 2011).

2.3 Ultrastructure of tympanic membrane

Ultrastructure observations on pars tensa (Figure 2-3-a) show three main layers with different structure. As shown in Figure 2-4, the middle lamina propria layer consists of two groups of collagenous fibers: radial ones connecting the annulus of the TM (tympanic ring) to the umbo and circumferential fibers holding the radial fibers in place. This layer is sandwiched between the epidermis and mucosal layer to form a thin and tough composite biological tissue (Decraemer & Funnell, 2008; Jackson et al., 2008; Lim, 1970).

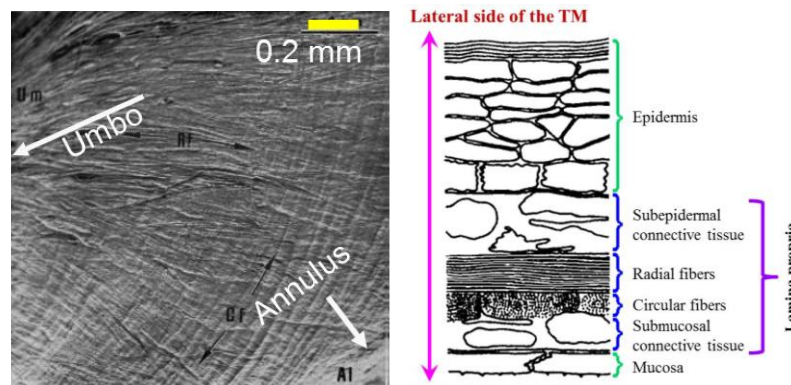


Figure 2-4 Left, scanning electron microscope image of the surface of TM inferior to umbo showing the distribution of radial and circumferential fibers; and right, the internal structure of the TM tissue showing different categories of fibers and layers (Khaleghi, 2015; Lim, 1970).

2.4 Available TM models

A viable model of the TM is required for many purposes such as rehabilitation (e.g., surgical reconstruction of the TM), diagnosis of middle-ear pathologies, production of better TM replacement grafts, and optimization of hearing aids (T. Cheng et al., 2007; Danti

et al., 2015; Deng et al., 2009; Fay et al., 2005 & Steele, 2005; Kozin et al., 2016). Overall, existing models can be classified into two main categories: Lumped-parameter (Feng & Gan, 2004; Zwislocki, 1962) and Distributed (De Greef et al., 2015; Funnell & Laszlo, 1978).

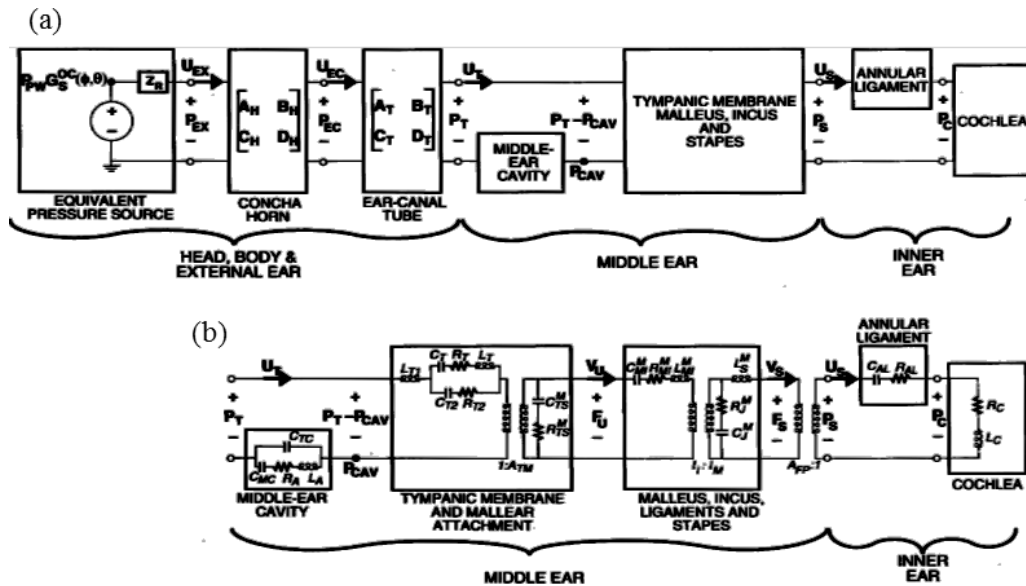


Figure 2-5 View of an electrical lumped model of the peripheral auditory system showing the model of tympanic membrane as a series of interconnected circuits: (a) lumped model representing the outer-, the middle- and inner-ear; and (b) detailed circuits representing the interconnected middle and inner ear. (Rosowski, 1996)

Lumped-parameter models are based on well-known impedance modeling of acoustical, mechanical systems by their equivalent circuits. Each part of the ear is modeled as a lumped linear/nonlinear time invariant system where the output of each connected element is the input to the other connected parts. Parameters of each part of the model are adjusted by experimental data to model the hearing process. These models are widely used to determine the performance of various hearing devices and to predict the hearing conditions in non-linear regions (i.e., due to high-amplitude sound). Figure 2-5 shows one of the lumped models used to model the complete human auditory periphery system.

Distributed models use Finite Element (FE) (De Greef et al., 2015; Funnell & Laszlo, 1978; Rong Z. Gan et al., 2016b) and continuum mechanics (Rabbitt & Holmes, 1986) to include more details to model the complex TM behavior. For instance, the TM distributed models try to include shape, thickness, ultrastructure, pre-stress, ligaments forces, etc. to simulate the hearing process. Figure 2-6 illustrates Von Mises stresses distribution across a chinchilla TM in response to tonal stimuli by use of FE modelling. The shape of all the middle ear components are determined by micro-CT scan (Rong Z Gan et al., 2016a).

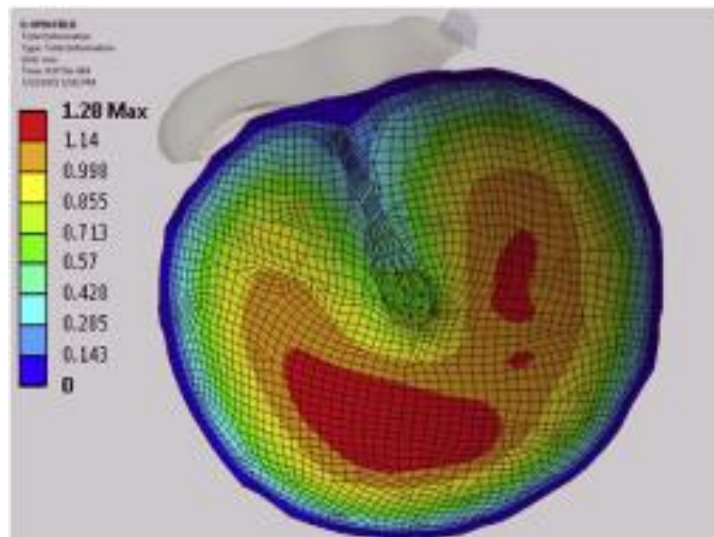


Figure 2-6 FE model, distributions of the equivalent (von Mises) stress of the TM, adapted from (Rong Z Gan et al., 2016a);

Both models have their own advantages. The lumped parameter models are suitable for easy analysis and prediction of the lower region of the hearing frequency range (i.e. <2 kHz) and distributed models can provide more fundamental information regarding the possible dynamic behavior of TM at higher frequencies. An issue with these distributed models, e.g. FE models, is the limited amount of data available for material characterization.

3 The need for TM measurements and constraints on such measurements

Modern TM models only partially explain the complex spatiotemporal behavior of the TM (especially in response to high-frequency sounds). Before models that are more accurate can be constructed, we need more detailed data about the spatial variations in TM properties that can best be determined from detailed spatial-temporal measurements of the TM's response to sound. While multiple measurements of TM mechanics (kinematics, shape, thickness, etc.) have been reported by multiple groups in multiple animals or post-mortem human samples, the available database does not fully predict TM behavior. In order to generate the necessary data a robust measurement tool is needed to quantify the response of TM to acoustical and mechanical stimulation, as well as its physical properties such as shape thickness, etc. in a stable environmental condition. Currently, there are limited available quantitative clinical and research tools to provide such a database. For instance, available clinical tools for research and diagnosis of the middle-ear still rely on qualitative response of patients (e.g., audiometry), or they provide qualitative information about the entire response of the TM (e.g., Reflectometry or wideband tympanometry), and/or quantitatively at a limited number of points across the TM (e.g., LDV¹).

¹ Laser Doppler Vibrometry (LDV) is not FDA approved for TM clinical use mostly due to the utility of reflective bids on the TM for better reflection.

3.1 Benefits of full-field of view TM shape and transient response measurements

As stated before, TM has a complex spatiotemporal response due to various parameters including but not limited to complex shape, spatially varied thickness, middle and inner ear load, and state of pre-stress by the middle ear muscles (tensor tympani). In this Section, the benefits of each capability of the proposed high-speed holographic shape and displacements in this dissertation are discussed separately.

3.1.1 Full-field-of-view¹ measurements

Full-field-of-view measurements are needed to spatially characterize the response at different regions of TM. For example, in a full-field measurement of displacements, the response at pars tensa, pars flaccida, manubrium, and umbo can be spatially separated and their interactions are studied separately to characterize the spatial and temporal response of the TM to sound.

3.1.2 Transient response measurements

TM acoustically induced transient response, due to a short broadband acoustic click², has unique advantages compared to conventional acoustically induce steady-state³ stimuli as follows:

¹ Full-field-of-view measurements refer to acquisition of the entire spatial domain of the sample without any lead or lag between the sample response and the measurements.

² Acoustic click is a short impulsive sound (similar to sound of a spark or the sounds a bat makes for echolocation) to rapidly excite the sample in a short period (e.g., <200 μ s).

³ Steady-state or tonal excitation refer to continuous excitation of the sample at a fixed frequency either by sound or other types of excitations.

1. Due to short impulsive type of excitation, the transient response can be temporally separated from the excitation. Unlike steady-state stimuli, the transient response let the sample freely move at superposition of its fundamental Eigen shapes. This can help to perform advanced experimental modal analysis.
2. Broadband excitation (i.e., 0.1-22 kHz) over a short period of time allows simultaneous estimation of the response of the TM to many frequencies,
3. The rapid time course of the measurements reduces the effects of low-frequency environmental and physiological noises that have confounded our efforts towards in-vivo measurements,
4. Negligible time-dependence of mechanical properties.

The main drawback of the transient response compared to steady state stimuli is that the interpretation and analysis is more complex due to superposition of multiple modal responses on top of each other.

3.1.3 Shape measurements

The shape measurements in parallel with the displacements measurements has the following unique advantages:

1. It compensates for shape induced spatial variation of the sensitivity vector to determine true surface normal displacements from interference phase data, which is the topic of Chapter 4.
2. Knowledge of shape and orientation with respect to the displacements makes the results independent of direction of observation, which enables the correlation of measurements (clinical examinations), in multiple subjects.

3. It helps to correlate the contributions of variations in shape and orientation from different TM's. For example, the speed of travelling waves maybe correlated with the curvature of the surface.
4. Since the area of TM is always larger than the area of the field of view, determination of surface-normal displacements increases the spatial resolution. Furthermore, the displacements that are observed from an angle has smaller projection compared to their real amplitudes, enabling quantification of larger displacements at maximum fringe density.
5. Knowledge of the shape of the TM highly benefits the interpretation of the transient measurements, by enabling accurate measurements of speed and trajectory of the travelling waves, as well as TM shape parameters such as curvature area etc.
6. Shape of the TM has many clinical diagnosis applications in tympanoplasty and manufacturing of personalized grafts adapted with the shape of the TM.

3.2 TM measurement constraints

As discussed before, the TM is the first observable stage in the response of the ear to sound stimuli and measurements of TM function are important for clinical and research applications. In this Section, three domains that constrain the required quantitative TM measurements are described:

3.2.1 Anatomical and physiological constraints

The TM acoustically induced displacements, in normal hearing conditions (<90 dB SPL) range from sub-nanometer to hundreds of nanometer requiring nanometer-scale displacement measuring resolution. The human TM has about 8 mm in diameter; therefore,

observing the nanometer-scale motions require maintaining a field of view of about five orders of magnitude larger than the displacements (i.e., centimeter vs. sub-micrometer). Furthermore, the conical human TM has a depth of about 2-3 mm together with an angled orientation relative to the ear canal results in a required depth of field of about half a centimeter (see Figure 2-3).

Rigid body motions due to heartbeat, muscle tremor, or respiration produce relatively slow (compared to sound frequencies) sub-millimeter displacements that accompanying the acoustically induced nanometer scale displacements making in-vivo measurements even more challenging (Razavi et al., 2017a). The confined location of the TM at the end of the ear canal together with its sensitive structure requires endoscopic and non-destructive measurements.

To satisfy the Nyquist criterion over the entire hearing frequency (i.e., 20 kHz) the measurements should have a temporal resolution of at least 40 kHz (i.e., $<25 \mu\text{s}$ sampling period). Furthermore, acoustically induced travelling waves forming on the surface of TM (will be discussed later in the applications part - Chapter 7) can have group velocities >50 m/s requiring even higher temporal resolution to track and quantify the wave parameters.

3.2.2 Methodological constraints

Currently, there are limited measurement methods with the capability of nanometer scale displacement resolution over a large field of view (i.e., $>10,000$ points) while maintaining microsecond temporal resolution. For instance, Laser Doppler Vibrometry (Buunen & Vlaming, 1981) and Optical Coherence Tomography (OCT) Vibrometry (Chang et al., 2011) can determine sub-nanometer to micrometer scale displacements with sufficient temporal resolutions but they require multiple scans and repetition for the full-field

measurements as shown in Figure 3-1. A complete scan take milliseconds up to minutes depending on the desired spatial resolution and type of scan; such scanning systems of repeated measurements are also more vulnerable to random physiological motions and other uncontrolled noises.

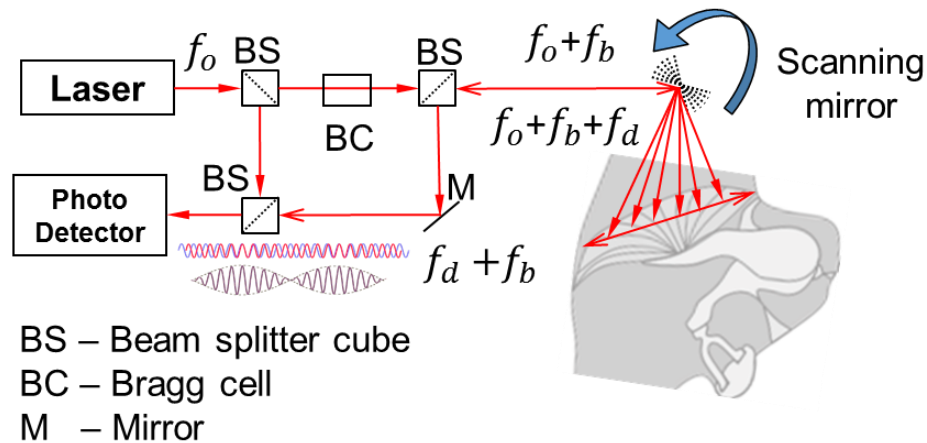


Figure 3-1 Schematic representation of a scanning Laser Doppler Vibrometer for full field high-speed TM measurements. The laser Doppler Vibrometry measures the displacements by measurements of the beating frequency generated by superimposing a phase modulated test beam (i.e., with added frequency of f_b by a bragg cell crystal) and the reflected beam having a frequency shift due to the sample vibrations (i.e., f_d due to Doppler frequency shift).

Holography is an optical-metrology method that can satisfy many of the TM measurement requirements such as nondestructive testing, nanometer-scale resolution, and large field of view. Holography has the capability to determine the phase and intensity of the scattered light that holds the information about the shape of the sample in nanometer scale. Holographic interferometry has the potential to determine various physical phenomena such as displacements, shape, variations in refractive index (i.e., due to fluid flow), etc. Khanna and Tonndorf were the first to utilize holography for TM measurements and their contributions opened a new path for other auditory researchers to explore this field (Dancer et al., 1975; Khanna & Tonndorf, 1972; Lokberg, 1980; Tonndorf & Khanna, 1972).

Rosowski and Furlong et al. demonstrated various significantly improved holographic methods to extract shape, and the acoustically induced one-dimensional and three dimensional displacements of the TM in response to continuous sinusoids (J. T. Cheng et al., 2010; Del Socorro Hernández-Montes et al., 2009; I. Dobrev et al., 2015; Khaleghi et al., 2015; Rosowski et al., 2009). In most of their publications, high-temporal resolution (either transient or continuous sinusoidal excitation) was achieved by stroboscopic imaging¹ relying on the repeatability of the motions. However, repetition of the measurements (i.e., synchronization of displacements cycle with respect to excitation cycle) is not usually possible in-vivo as the large physiological motions and time-dependent mechanical properties may alter the repeated measurements results. Dobrev et al. (2014) developed High-speed Digital Holography (HDH), which utilized the latest high-speed digital imaging technologies to extract transient full-field measurements of the TM. One of the main advantages of HDH is that a transient response of the TM could be measured with sufficient temporal resolution without repeating the excitation.

3.2.3 High-speed Digital Holographic (HDH) method

HDH is a branch of holographic methods that has can measure fast occurring phenomena happening over the course of milliseconds such as TM transient response. The first attempts in high-speed holography used chemical holograms and synchronization of a

¹ Stroboscopic illumination is a technique to acquire a high-speed steady state (having a fixed frequency) phenomenon using a slow acquisition device (i.e., a conventional camera <20 frames per seconds to measure > kHz motions). The method relies on synchronization of short exposures of illumination (with respect to period of excitation frequency) with a known phase-locked difference with respect to excitation to capture a full cycle of motions.

single or few instances of the high-speed phenomena (Abramson, 1983; Lauterborn & Ebeling, 1977). A milestone was achieved by the invention of faster and automated hologram capturing devices and pulsed lasers, which paved the way for techniques such as stroboscopic imaging of repeatable high-speed phenomena such as resonances in turbine blades in an industrial environment (Parker & Jones, 1988). The invention of Charge-Coupled Device's (CCD) revolutionized holographic methods by removing the chemical processes and later by development of digital holographic methods (e.g., numerical reconstruction of lens-less digital holograms) (U. Schnars, 1994; U. Schnars et al., 1995; U. Schnars & Juptner, 1994a; U. Schnars & Juptner, 1994b). HDH methods gained the capability of measuring non-repeatable transient phenomena by advancements in high-speed imaging technologies such that HDH methods now mostly refer to non-repetitive transient measurements (Pedrini et al., 2006; Pedrini et al., 1995; Pérez-López et al., 2006). Overall, the HDH advancements are constrained by two factors: available technology (as it will be discussed in Section 3.2.4) and methodology. Due to required high temporal resolution, most of the conventional methods available for quantitative phase estimation are not currently applicable for HDH.

The methods available for HDH can be classified as:

1. **Phase correlation speckle interferometry** (Davila et al., 2005; I. Dobrev et al., 2014b; Georgas & Schajer, 2012; Jones & Wykes, 1983; Pedrini et al., 2006; Schmitt & Hunt, 1997; Yu et al., 2004).
2. **Parallel phase shifting** (Akondi et al., 2016; Awatsuji et al., 2004; Kakue et al., 2017; Kakue et al., 2011; Millerd et al., 2004).

3. **Carrier frequency filtering phase sampling** (Pedrini et al., 1995; Pérez-López et al., 2006; Takeda et al., 1982).

Table 3-1 summarizes the advantages and disadvantages of each of the possible high-speed phase sampling methods for TM measurements. Phase correlation speckle interferometry relies on the pattern variations of laser speckles due to sample surface deformation, and estimates the interference phase by correlating the speckle patterns. The advantage of this method over the other two methods is its capability to temporally separate the phase sampling from the period of sample response to utilize the entire temporal bandwidth of a high-speed sensor. Since the spatial resolution in this method is related to speckle size and other factors, to be discussed later, the resolution is slightly lower than the maximum spatial bandwidth of the sensor. This drop in resolution can be minimized, and this method provides higher spatial resolution than the other available methods. In conclusion, the phase-correlation speckle interferometry provides the highest spatial resolution while it does not impose any complexities in hardware implementations.

Table 3-1 Comparison of the performance of available HDH methods for the TM measurements application.

	Major advantages	Drawbacks
Speckle phase correlation interferometry	Utilizing the highest spatial bandwidth of the sensor Simple setup (Off-axis holography with phase shifting) High intensity sensitivity	Stable reference holograms are required Speckle size has effects on resolution Spatially continuous phase
Parallel phase shifting	Spatial resolution of at most one third of the ones of sensor. No reference state is desired No mechanical phase shifts are required	Custom made polarizers Multiple stages of polarization Drop of spatial resolution Spatially continuous phase Lower light sensitivity
Carrier frequency	No mechanical phase shifts Simple setup High intensity sensitivity	Significant drop of spatial resolution About 1/9 th of the sensor spatial bandwidth

3.2.4 Technological constraints of HDH

Using holography as the method of measuring the TM displacements, the major technological constraints are spatial and temporal limitations of high-speed imaging sensors.

The performance of a high-speed imaging sensor is quantified by its Quantum Efficiency (QE), which is the measure of the effectiveness of an imager to produce electronic charge from incident photons. Conventional high-speed camera's use large pixels to increase the QE by absorbing more photons in each exposure. Because of limitations in the size of sensor arrays, the high-speed sensors have lower spatial resolution (i.e., <1 Megapixels >10 kHz) compared to a conventional cameras (i.e., >1 Megapixels, <500 Hz).

Only in terms of temporal resolution with respect to spatial resolution there are two types of high-speed camera's,

1. **Embedded high-speed memory on the sensor:** the sensor and memory are a single chip to maximize the frame readout rate enabling up to >1 GHz at a limited number of frames (i.e., smaller than few hundreds) (SIMD - Ultra High Speed Framing Camera)
2. **Separated sensor and memory:** Each image is processed and transferred onto a separate larger memory enabling higher recording duration (>0.5s). While the transfer rate between the sensor and the memory is constant, the camera trades spatial resolution to gain higher temporal resolution. For example, temporal resolution of one state of the art camera with this configuration varies from >20 kHz up to 2 MHz as the spatial resolution is decreased from full-resolution (1 megapixels) to 1024 pixels (Photron SA-Z High-speed camera).

Although current ultra-high-speed imaging technologies can provide sub nanosecond temporal resolutions (i.e., multi-million frames per seconds camera's), there are still many technological constraints. The spatial resolution of high-speed cameras are still far from the chemical holograms (i.e., ~5000 Line-Pairs LP/mm) or even high-resolution digital camera's (i.e., ~300 LP/mm at <100 Hz). Due to the 5 to 10 msec durations of TM transient response and current technological constraints, the second type of high-speed sensors (with separated sensors and memories) are most suitable for middle-ear measurements.

4 Holographic interferometry for displacements measurements and the need for TM shape

This Dissertation proposes developments in high-speed digital holography that measure shape, orientation, and acoustically induced transient response of TM in a fraction of a second. With such rapid acquisition, it is possible to maintain similar environmental and orientation conditions during sequential shape and displacements measurements. In this Chapter, the need for shape measurement and the related determination of holographic sensitivity vector for accurate measurements of the TM out-of-plane (normal) displacements is presented. The concept of sensitivity vector in holographic measurements together with the dominant theories governing the TM displacements are also explained. An uncertainty analysis is performed to understand the dominant factors affecting the spatially varied sensitivity vector as well as the determination of true surface-normal displacements. Such an analysis provides a basis for determining the shape resolutions.

4.1 Sensitivity vector

The displacements at each point of the surface in a holographic interferometric measurement of deformation, give rise to the optical path length difference. The optical path length in an off-axis configuration is shown in Figure 4-1-a as the sum of the blue vectors $\mathbf{r}_1, \mathbf{r}_2$. These vectors are called *path-vectors* in this context. The *propagation-vectors* (k_i) along each path-vector show the direction of the light array with an amplitude of $2\pi/\lambda$ (wave number, k) such that the dot product of each path-vector with its corresponding propagation-vector provides the optical path length in cycles of light (phase cycles). After a sample displaces, the optical path length is varied (shown with black path-vectors $\mathbf{r}_3, \mathbf{r}_4$ in Figure 4-1-b). The goal in this analysis is to determine the displacement

vector \mathbf{L} from the optical path length difference measured by the holographic interferometry.

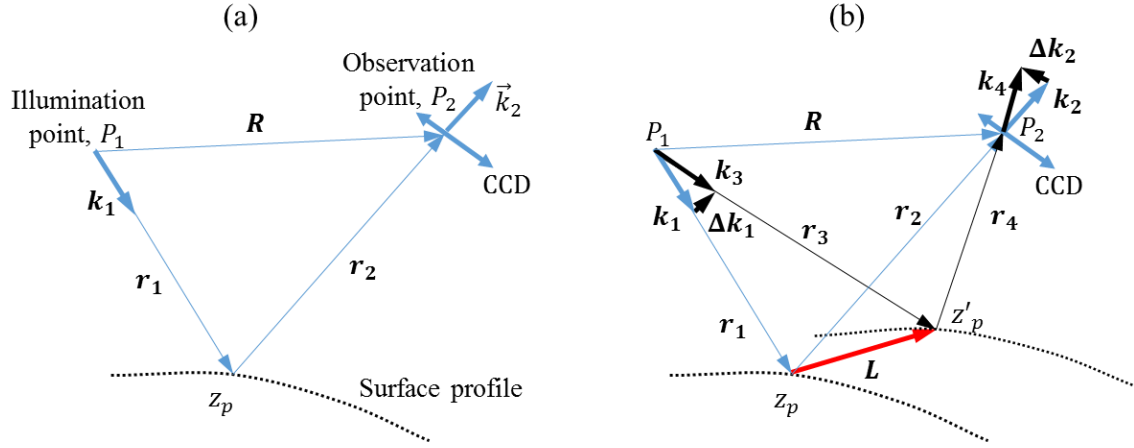


Figure 4-1 Nomenclature for fringe analysis (adapted from Vest, 1979): (a) schematic representation of optical path length from observation to a point on the sample surface to point of observation on the CCD; and (b) variations in path-vectors and propagation vectors due to deformation vector \mathbf{L} .

At the point z_p , using the vector equalities $r_2 = R - r_1$ and $r_4 = R - r_3$ the phase of the wavefront before and after displacement is described by the following equations,

$$\phi_1 = \mathbf{k}_1 \cdot \mathbf{r}_1 + \mathbf{k}_2 \cdot (\mathbf{R} - \mathbf{r}_1) + \phi, \quad (4-1)$$

$$\phi_2 = \mathbf{k}_3 \cdot \mathbf{r}_3 + \mathbf{k}_4 \cdot (\mathbf{R} - \mathbf{r}_3) + \phi, \quad (4-2)$$

where, ϕ_1 is the phase of the light reflected from the point z_p and observed at P_2 before the displacements, ϕ_2 is the phase of the light after the sample displaces, and ϕ is the random phase difference between the arms of the interferometer that is fixed by optics within the measurement system (Vest, 1979). The interference phase $\Delta\phi$ is the phase difference due to sample displacements,

$$\Delta\phi = \phi_1 - \phi_2. \quad (4-3)$$

Putting Eqn. (4-1) and Eqn. (4-2) in Eqn.(4-3) results in,

$$\Delta\phi = \mathbf{k}_1 \cdot \mathbf{r}_1 + \mathbf{k}_2 \cdot (\mathbf{R} - \mathbf{r}_1) - \mathbf{k}_3 \cdot \mathbf{r}_3 - \mathbf{k}_4 \cdot (\mathbf{R} - \mathbf{r}_3). \quad (4-4)$$

The differences between the propagation vectors before and after displacements can be written as,

$$\mathbf{k}_1 + \Delta\mathbf{k}_1 = \mathbf{k}_3, \quad \mathbf{k}_2 + \Delta\mathbf{k}_2 = \mathbf{k}_4, \quad (4-5)$$

Implementing Eqn. (4-5) in Eqn. (4-4) results in,

$$\Delta\phi = \mathbf{k}_1 \cdot \mathbf{r}_1 + \mathbf{k}_2 \cdot (\mathbf{R} - \mathbf{r}_1) - (\mathbf{k}_1 + \Delta\mathbf{k}_1) \cdot \mathbf{r}_3 - (\mathbf{k}_2 + \Delta\mathbf{k}_2) \cdot (\mathbf{R} - \mathbf{r}_3), \quad (4-6)$$

$$\Delta\phi = (\mathbf{k}_2 - \mathbf{k}_1) \cdot (\mathbf{r}_1 - \mathbf{r}_3) + \Delta\mathbf{k}_1 \cdot \mathbf{r}_3 + \Delta\mathbf{k}_2 \cdot (\mathbf{R} - \mathbf{r}_3), \quad (4-7)$$

The illumination and observation vectors (i.e., $|\mathbf{r}_i|$) are of lengths on the order of centimeters to meters while vibrations of the sample are in the order of nanometers to micrometers (i.e., $|\mathbf{L}| = |\mathbf{r}_1 - \mathbf{r}_3|$), therefore, we can approximate (Kreis, 2006; Vest, 1979),

$$\Delta\mathbf{k}_1 \perp \mathbf{r}_3, \quad \Delta\mathbf{k}_2 \perp \mathbf{r}_4, \quad (4-8)$$

Therefore, the second and third term in Eqn. (4-6) and (4-7) are negligible resulting in the well-known relation of,

$$\Delta\phi = (\mathbf{k}_2 - \mathbf{k}_1) \cdot \mathbf{L}, \quad (4-9)$$

which is widely used in holographic interferometry to determine displacements. For brevity, the holographic sensitivity vector is defined as,

$$\mathbf{K} = \mathbf{k}_2 - \mathbf{k}_1, \quad (4-10)$$

to simplify Eqn. (4-9) as,

$$\Delta\phi = \mathbf{K} \cdot \mathbf{L}. \quad (4-11)$$

It is important to note that the interference phase is the scalar result of a projection, and the information about the direction of the displacements are lost. Therefore, at least three independent sensitivity vectors are required to accurately determine the vector \mathbf{L} . In other words, measurements of displacements and/or deformations, from the interference phase $\Delta\phi$ require either multiple independent sensitivity vectors or the knowledge of the direction of displacements. In addition, in cases of close illumination and observation together with optical distortions, an inherent part of in-situ TM holographic measurements, the sensitivity vector varies along the TM surface. As we will see, the observation of the majority of TM surface in an endoscopic configuration has a few degrees tolerance in terms of rotation of the observation with respect to illumination vectors and having multiple independent sensitivity vectors is not possible. Therefore, the shape and orientation with respect to the illumination wavefront as well as a fundamental understating of the dominant direction of displacements are essential to determine displacements.

4.2 TM displacements type

The dominant type of acoustically induced displacements on the surface of the TM are investigated in this Section. The TM structure can be considered a thin shell because the ratios between its thicknesses and other relevant dimensions are small (Khaleghi, 2015; Khaleghi et al., 2016; Khaleghi et al., 2013; Lu, 2012; Rosowski et al., 2013; Timoshenko & Woinowsky-Krieger, 1959). Specifically,

$$\max\left(\frac{h}{R}\right) \leq \frac{1}{20}, \quad (4-12)$$

where, h is the TM thickness and R is the radius of curvature of the shell. As a result of the geometrical dimensions of the TM (i.e., $h \cong 30-120 \mu\text{m}$, and $R = 3-5 \text{ mm}$) together

with the small magnitude of the sound-induced motions (i.e., $<1 \mu\text{m}$ at 90-100 dB SPL), the TM can be approximated as a thin shell (Khaleghi et al., 2013, Rosowski et al., 2013; Lu, 2012). In a thin shell, the out-of-plane component of the displacements along the surface normal are dominant and in-plane components of these displacements are negligible. Our group has previously verified the thin shell theory by use of 3D holography (i.e., use of multiple sensitivity vectors) on post-mortem samples and observed that below 6 kHz the in-planes are negligible compared to out-of-plane component of displacements (Khaleghi et al., 2016). The dominance of the out-of-plane displacements, implies the surface normal direction is the direction of displacements in Eqn. (4-11). Knowledge of the shape, orientation and the displacement along any one angle allows us to compute surface normal displacement from our one-dimensional measurements of displacement.

4.3 TM displacements measurements using surface normal vector

From shape measurements made in sequence with displacement measurements, we determine the surface topology at each point on the sample. From this, we calculate the surface normal vector \mathbf{n} , which based on the thin shell theory is equivalent to the direction of the displacement vector (i.e., $\mathbf{L} = |\mathbf{L}|\mathbf{n}$), the magnitude of the normal displacement is determined by,

$$|\mathbf{L}| = \frac{\Delta\phi}{\mathbf{K} \cdot \mathbf{n}} = \frac{\Delta\phi}{|\mathbf{K}|\cos(\alpha)}, \quad (4-13)$$

where α is the angle between the sensitivity vector and the surface normal as shown in Figure 4-2.

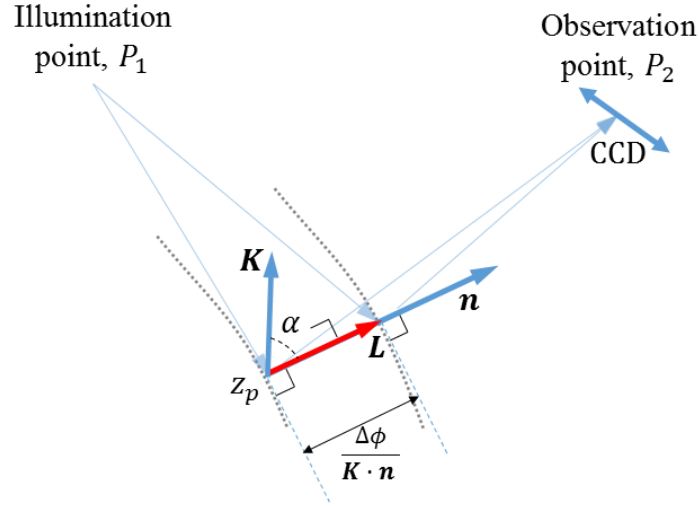


Figure 4-2 Schematics of out-of-plane displacements measurements by the sensitivity vector \mathbf{K} , and surface normal vector \mathbf{n} .

4.4 The effect of inaccuracies in the sensitivity vector and normal direction on measurements of the normal displacement

Based on Eqn. (4-13), magnitude of L is a function of,

$$|L| = l(\mathbf{K}, \mathbf{n}, \Delta\phi), \quad (4-14)$$

Therefore, any uncertainty in the displacement magnitude comes from three independent parameters and based on standard procedures (BIPM et al., 2008; Dobbert & Schrijver, 2014) the magnitude of uncertainty can be described by,

$$\delta(|L|) = \left\{ \left[\frac{\partial |L|}{\partial \mathbf{K}} \delta(\mathbf{K}) \right]^2 + \left[\frac{\partial |L|}{\partial \mathbf{n}} \delta(\mathbf{n}) \right]^2 + \left[\frac{\partial |L|}{\partial \Delta\phi} \delta(\Delta\phi) \right]^2 \right\}^{\frac{1}{2}}. \quad (4-15)$$

While each part of Eqn. (4-15) is independent of the others, the rest of this Chapter discusses the uncertainty in the first two parenthesis; the third parameter is discussed in Section 5.3 (Uncertainty analysis on the HCI method). To simplify the discussion we use the angle α (shown in Figure 4-2) to quantify uncertainties in the overall shape and setup geometries for determination of surface-normal displacements resolution.

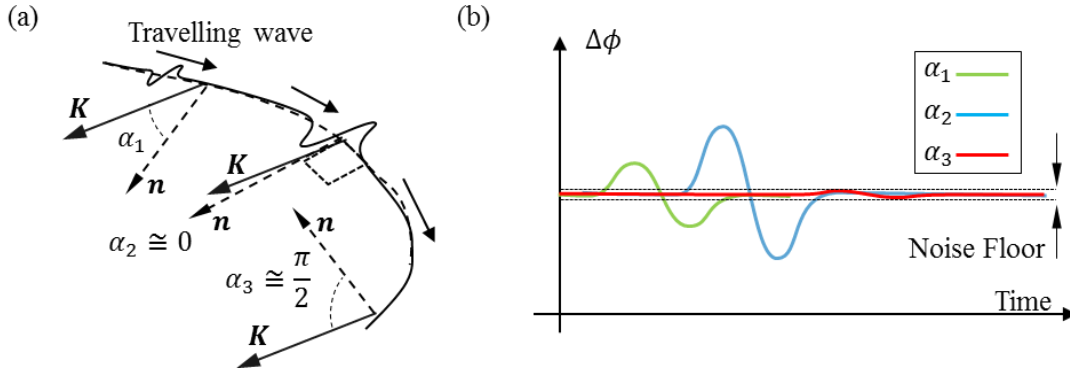


Figure 4-3 Schematic representation of the effects of variations of the measured interference phase as the angle between sensitivity vector and the surface normal vary across the field of view: (a) angles compared to sensitivity vector and surface normals; and (b) schematic representation of the interference phase measured at each location.

To illustrate the importance of how the shape affects the holographic measurements, a simple example is shown in Figure 4-3. Assume a lossless travelling wave on a curved one-dimensional thin-shell moving from one side of the field of view to the other. Since the wave is lossless, all the points on the shell will experience the same amplitude of motion at different times. However, as show in Figure 4-3-b, due to spatial variations of angle α , the holographic system is more sensitive at the central region compared to the other two regions where the surface normal vector differs significantly from the sensitivity vector. For α_3 (the red waveform in Figure 4-3-b) the information is completely lost as $\Delta\phi$, the displacement along the sensitivity vector, falls below the noise floor of the holographic system. Therefore, not compensating the measured phase difference for the relationship between the sensitivity and normal vectors may lead to misinterpretations of the 1D holographic displacement measurements, a simple phase measurement suggests the travelling waves faded out between α_2 and α_3 .

Now the next question is how significant are variations of the sensitivity vector to our estimates of surface-normal displacements. Specifically, what should be the required shape resolution for calculation of the surface normal as well as the sensitivity vector.

4.5 TM measuring specifications

In the following Sections: first the measurement parameters required for the TM displacements measurements are introduced, next the uncertainties in the surface normal measurement and sensitivity vector are each discussed separately, and finally a preliminary estimation of the required resolutions in determination of shape and setup coordinates are presented.

4.5.1 Sample specifications

Determination of the measurement parameters and resolution needed for our studies are based on previous measurements of TM shape. Figure 9 shows typical dimensions of an adult human TM. As discussed in Section 2.2, the TM has a tent like shape with up to 2-3 mm depth and 8-9 mm diameter. The umbo region (shown with a red square) is located at the tip of the manubrium and has $<1 \text{ mm}^2$ area. In humans, the umbo is eccentric toward the inferior side of the TM and inferior to the umbo are the highest spatial frequency in shape and the sharpest surface normal angles.

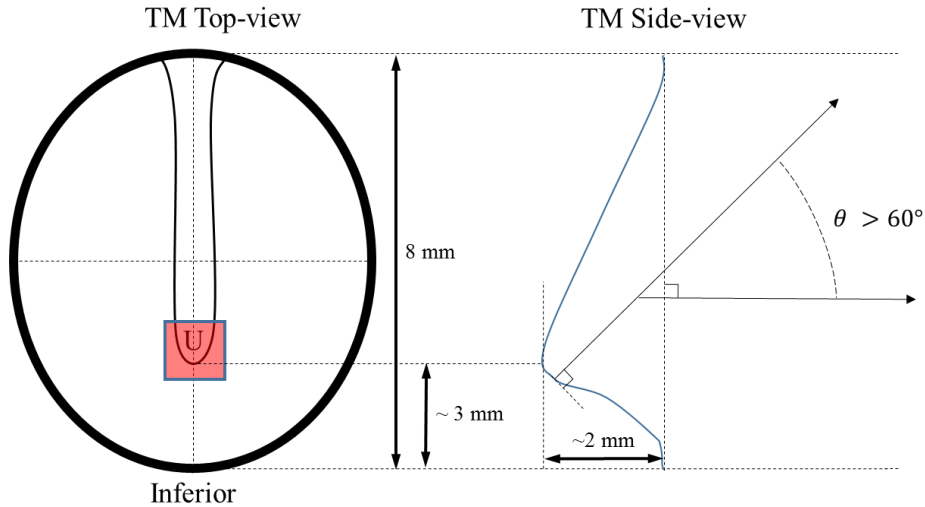


Figure 4-4 Schematic representation of maximum TM curvature located close to umbo. Umbo region is shown with (U).

4.5.2 Optics and imaging sensor specifications

The high-speed CCD cameras used for this study (Photron SA-5, SA-Z) have 1024 by 1024 pixels with 20 μm square pixel size. The number of pixels used in each image varies inversely with camera speed (see Section 3.2.4) (Photron, 2018). For the SA-Z camera, a framerate of 67.2 kHz reduces the square field of view by 512×512 pixels while for the SA-5 a frame rate of 42 kHz reduces the active field to 384×384 pixels (Photron, 2018).

4.5.3 Setup specifications

There were two different optical configurations used for TM measurements in this Dissertation as described in Table 4-1.

Table 4-1 Optical configuration specifications used for measurements in this Dissertation

Name	Mag	DOF, mm	Focal length	Resolution lp/mm	N.A	Lens type
Open optics	0.9-1	2-3	50 mm	10.08, ~100 μm	0.018	Fixed focal NIR coating
Otoscope	0.8-1.5	5	10 mm	5.04, ~ 200 μm	0.107	GRadient INdex (GRIN) 2.7mm

4.6 Uncertainty due to sensitivity vector measurements

This Section focuses on the first term in Eqn. (4-15): the effect of uncertainties in the sensitivity vector. Rewriting Eqn. (4-10) in terms of coordinates of: a point on the sample, $z_p(x, y)$ (as it will be discussed in Chapter 6), illumination point P_1 , and observation point P_2 (as shown in Figure 4-2 and Figure 4-1), the sensitivity vector can be rewritten in terms of shape and setup geometries as,

$$\begin{aligned} \mathbf{K}(x, y) &= \mathbf{k}_2(x, y) - \mathbf{k}_1(x, y) \\ &= \frac{2\pi}{\lambda} \left[\frac{(P_2 - z_p(x, y))}{\sqrt{(P_2^2 - z_p(x, y)^2)}} - \frac{(z_p(x, y) - P_1)}{\sqrt{(z_p(x, y)^2 - P_1^2)}} \right], \end{aligned} \quad (4-16)$$

where z_p is the measured shape along the z-axis for a point P on the sample. This equation has nine parameters and the solution of uncertainty is not traceable analytically. Therefore, to determine the uncertainty due to variations of the sensitivity vector due to shape, orientation, and setup geometries, a numerical simulation was developed to calculate the sensitivity vector for desired TM measuring specifications using Eqn. (4-16). This numerical analysis is later expanded to handle the surface normal determinations in Section 4.7.

To determine the uncertainty in measurements of the sensitivity vector for specific TM measurements, the following assumptions were made:

- 1- The magnitude of the sensitivity vector ($|\mathbf{K}|$) can be considered constant due to stability of the wavelength and the constancy of the large fraction of the path length fixed by the laser and measuring optics. Therefore, any uncertainty is due to rotation of the sensitivity vector, normal vectors, or the angle α .

- 2- It is assumed that illumination comes from a point source and the observation is performed with a point sensor.
- 3- The sample dimensions and setup geometries of in-vivo measurements (Section 8.1) was used while the TM was modeled using a set of curves that approximated its real shape. The surface was rotated 45° to mimic the orientation of TM at the end of ear canal. The curves and orientation were chosen to present a worst-case, scenario to determine maximum uncertainty.

4.6.1 Variations in the angle and magnitude of the sensitivity vector across the field of view as a function of distance

It is well known that the effects of spatial variations of the sensitivity vector across the field of view is smaller when the sample is farther away from the measurements and illumination point, but there is little data of the consequences of spatial variations at shorter distances.

From Eqn. (4-16), changes in the distance between the holographic system and the sample (d , shown in Figure 4-5-a) change the magnitude of the path-vectors (i.e., $|r_1| =$

$\sqrt{(P_2^2 - z_p^2)}$, $|r_2| = \sqrt{(z_p^2 - P_1^2)}$ as shown in Figure 4-1). Because the P_1 and P_2 are fixed,

and variations in z_p are constrained by the smaller dimensions of the sample, the contributions of such variations vanish as the distances between P_1 and z_p and P_2 and z_p become larger.

To quantify the uncertainty in sensitivity vector angle as a function of the distance between the sample and the illumination and measurement points the numerical simulation is used.

In this 2D analysis the sample was modeled by a horizontal line (representing a flat surface) to study the effects of variations in the distance between different points on the sample surface and P_1 and P_2 , without the complication of the shape. By comparing the vectors at

all locations, an estimation of the maximum rotation of the sensitivity vector across the field of view is determined. Figure 4-5-a schematizes the difference in sensitivity vector at different points along a 4 mm radius circle, with a measurement point positioned 10 mm from the circle plane and in line with the circle's center ($x = 0$), and a point illumination source that is positioned 10 mm from the circle plane, and 2 mm from the measurement point. With this configuration, we see variations in the sensitivity vector direction of more than 40 degrees (Figure 4-5-b). The blue curve in Figure 4-5-b illustrates how the variations in sensitivity vector angle decrease to nearly zero as the distance d between the planar sample and the illumination and measurement points increases to 100 mm.

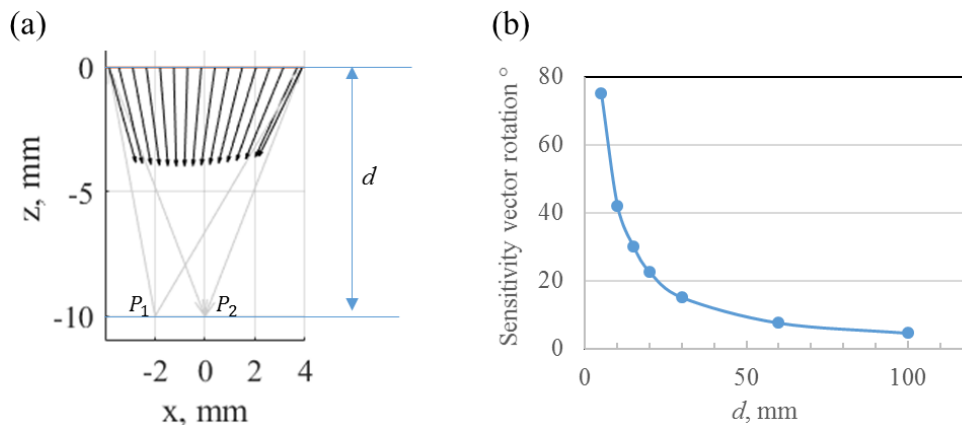


Figure 4-5 (a) view of the model showing spatial variations of the sensitivity vector at distance $d=10$; and (b) the results of the numerical model. Blue line presents maximum rotation of the sensitivity vector across the field of view.

The results indicate that the maximum rotations of the sensitivity vector is exponentially decaying as the distance d increases. As an example, to have a sensitivity vector rotation of smaller than five degrees across the field of view, the measuring system has to be at least 100 mm away from the sample. Furthermore, for the 10-15mm distance that will be used in the next Sections, a sensitivity vector rotation of about 30-40 degrees across the field of view is inevitable. Assuming errors in determination of angle α in Eqn. (5-13) are only

due to the sensitivity vector, these rotations can generate spatially varied errors in the measured amplitude of displacements as large as 24%.

4.6.2 Shape induced variations of the sensitivity vector across the field of view

This Section describes the effects of non-planar shape and orientation on spatial variations of the sensitivity vector. Figure 4-6 illustrates the spatial distribution of the sensitivity vector due to a TM-like shape and orientation with a distance d of about 10 mm. The results show a maximum rotation of $\sim 32^\circ$ across the field of view. Comparison of each point with the flat surface in Figure 4-5 with $d=10\text{mm}$ show a mean of 10° error with standard deviation of $\sim 2.5^\circ$.

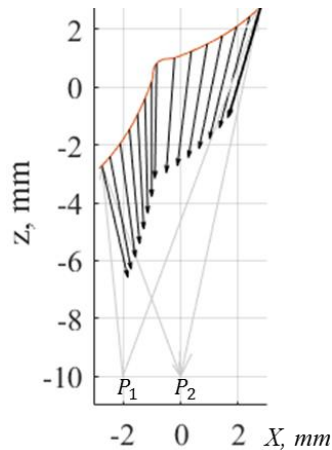


Figure 4-6 Spatial variations of sensitivity vector due to a TM-like shape oriented 45° with respect to camera axis. Shape induced rotations of the sensitivity vector angle compared to a flat sample shows mean of $\sim 10^\circ$ rotation with standard deviation of 2.5° .

4.6.3 Effects of shape resolution on the sensitivity vector

Assume the measured shape has a resolution within $\pm\delta(z_p)$ uncertainty along the z direction. We model such variations in the shape resolution, as a harmonic spatial noise with signal to noise ratio of $\delta(z_p)$ added to the curved and angled intersection of the TM as shown in Figure 4-7-a. The sensitivity vector rotation at each point due to the added

noise was measured for each $\delta(z_p)$. Figure 4-7-b shows the mean, maximum, and standard deviation of rotation of the sensitivity vector of all points as a function of shape resolution $\delta(z_p)$. Since the error is uniform across the sample and there are more than 750 points across the sample, the results of simulation show the effects of shape resolution on the sensitivity vector. The results indicate that a relatively large uncertainty within $\pm 700 \mu\text{m}$ has small effects on the sensitivity vector rotation (i.e., $< 1.5^\circ$). Therefore, in an endoscopic configuration we expect the shape resolution has small effects on the rotation of the sensitivity vector.

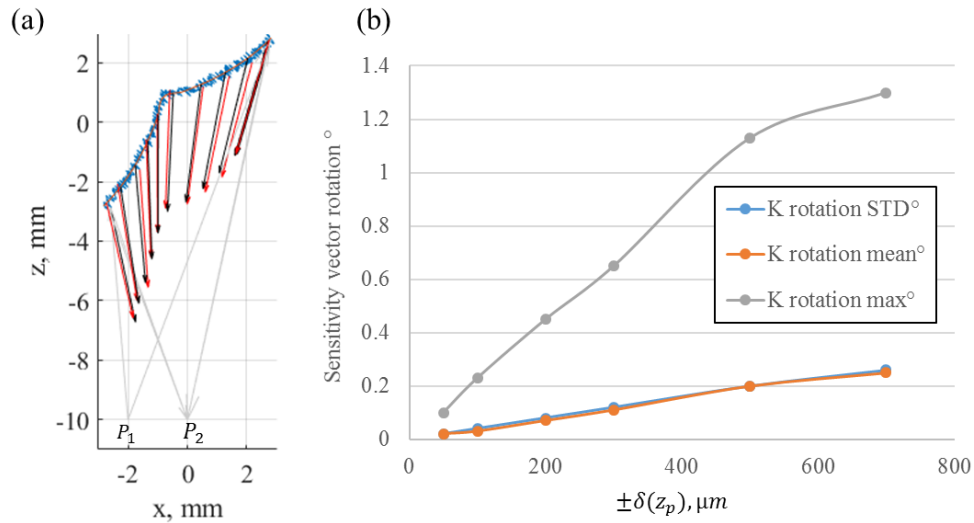


Figure 4-7 (a) the sensitivity vector before and after an added noise when $\delta(z_p)$ is within $\pm 200 \mu\text{m}$ using red and black vectors, respectively; and (b) standard deviation, mean and maximum rotation of the sensitivity vector of all points as a function of shape resolution $\pm\delta(z_p)$ compared to the sensitivity vector without the noise.

4.6.4 Coordinate of the illumination point P_1 effects on the sensitivity vector

The rotation of the sensitivity vector due to uncertainty $\delta(P_1)$ in measuring the coordinates of the illumination point is investigated using the same model configuration. It is assumed that the uncertainty in all dimensions are the same (i.e., $\delta(P_{1x}) = \delta(P_{1z}) = \delta(P_1)$). Mean,

max, and standard deviation are determined by the same method discussed in the previous Section and shown in Figure 4-8. The results suggest that in order to have $<1^\circ$ rotation in sensitivity vector the illumination coordinate need to be measured with a better than ± 100 μm accuracy.

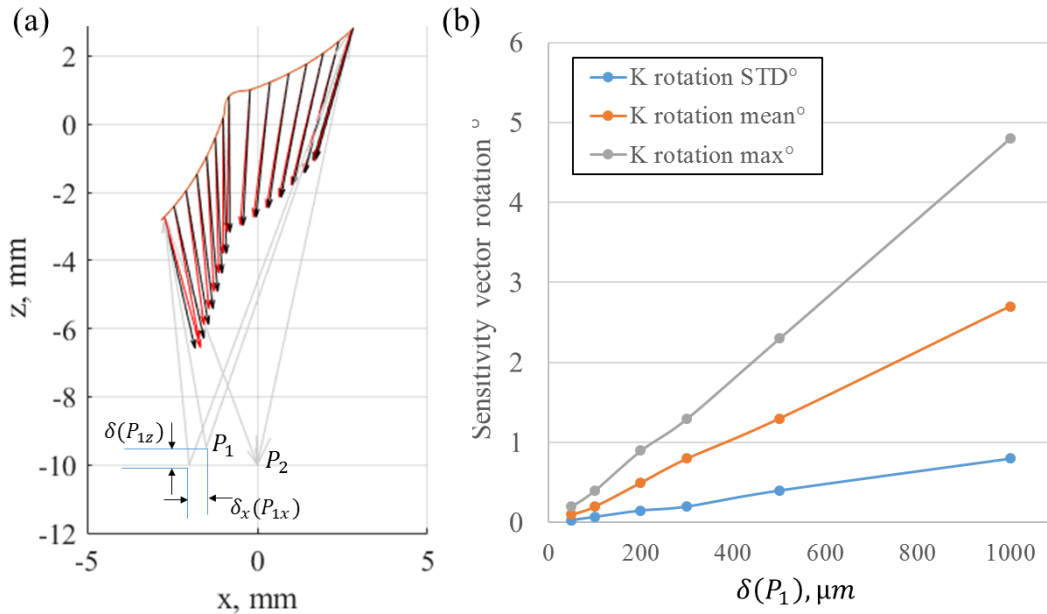


Figure 4-8 (a) schematic representation of the variations of the sensitivity vector due to uncertainty in the illumination rotation of the sensitivity vector due to the uncertainty in the coordinates of point P_1 (i.e., $\delta(P_1)$); and (b).

4.6.5 Sensitivity vector uncertainty: dominant parameters

The uncertainty in displacement measurement due to variations of sensitivity vector is depending mostly on the length of path vectors followed by the shape of the TM. The majority of errors due to shape and orientation of the sample is due to millimeter-scale variations of the depth, d , across the field of view, and not from small surface discontinuities. We also determined that the coordinates of the illumination point with respect to the observation point is important to accurately determine the sensitivity vector.

4.7 Surface normal uncertainty

In this Section, the effects of various parameters in surface normal uncertainty are discussed. First, a brief introduction on the mathematics and requirements of the calculations of the surface normals from a discrete 3D set of data are presented.

4.7.1 Analytical determination of surface normals

The second parameter affecting the uncertainty in measuring the displacements in Eqn. (4-15) is the uncertainty in surface normal. For a continuously differentiable function, the normalized gradient at each point provides the unit vector surface normals by,

$$\mathbf{n} = \|\nabla f_s(x, y, z)\| = \left[\frac{\frac{\partial(f_s)}{\partial(x)}}{\varrho}, \frac{\frac{\partial(f_s)}{\partial(y)}}{\varrho}, \frac{\frac{\partial(f_s)}{\partial(z)}}{\varrho} \right], \quad (4-17)$$

where f_s is the implicit form of shape (i.e., $f_s(x, y, z) = z_p(x, y) - z = 0$), while the denominator normalize the gradient vectors by the overall magnitude:

$$\varrho = \left\{ \left[\frac{\partial(f_s)}{\partial(x)} \right]^2 + \left[\frac{\partial(f_s)}{\partial(y)} \right]^2 + \left[\frac{\partial(f_s)}{\partial(z)} \right]^2 \right\}^{\frac{1}{2}}. \quad (4-18)$$

Therefore, the uncertainty of the measured surface normal $\delta(\mathbf{n})$ based on standard techniques (BIPM et al., 2008) is,

$$\delta(\mathbf{n}) = \left\{ \left[\frac{\partial n}{\partial x} \delta(x) \right]^2 + \left[\frac{\partial n}{\partial y} \delta(y) \right]^2 + \left[\frac{\partial n}{\partial z} \delta(z_p) \right]^2 \right\}^{\frac{1}{2}}, \quad (4-19)$$

where $\delta(x)$, and $\delta(y)$ are the uncertainty in experimental measurements of (x, y) coordinates (i.e., lateral shape resolution) and $\delta(z_p)$ is the uncertainty in the z direction (i.e., axial shape resolution).

Eqn. (4-19) indicates that the measured shape should have similar and minimum uncertainty in all three dimensions to minimize the overall uncertainty. Since the

holographic measurements have lateral resolution of $<200\mu\text{m}$ (see Table 4-1), it is desired to determine the sample depth (or the shape resolution) to have at least the same or higher resolution to not to have artifacts because of non-uniform derivations.

If $\delta(x) = \delta(y) = \delta(z_p)$, the derivatives of Eqn. (4-21) will be,

$$\frac{\partial n}{\partial x} = \varrho^{-1} \frac{\partial^2(f)}{\partial x^2}, \quad \frac{\partial n}{\partial y} = \varrho^{-1} \frac{\partial^2(f)}{\partial y^2}, \quad \frac{\partial n}{\partial z} = \varrho^{-1} \frac{\partial^2(f)}{\partial z^2}, \quad (4-20)$$

where, ϱ is defined in Eqn. (4-18). Therefore, Eqn.(4-21) takes the form of,

$$\delta(\mathbf{n}) = \delta(z_p) \left(\frac{\nabla^2 f}{\varrho} \right)^{\frac{1}{2}}, \quad (4-21)$$

where the numerator is the variance of gradient or the Laplacian ∇^2 of the shape function f . Eqn. (4-21) suggest that the uncertainty of the determined surface normal is related to the second order derivatives of the surface. This shows the uncertainty in determination of normals require measuring a sufficiently smooth function in all dimensions to provide uniform second order derivations and measuring the surface normals of a discrete set of measured data using the gradients require a continuously differentiable function free from any spatial discontinuities.

4.7.2 Surface noise effects on surface-normals

As it is illustrated using the numerical model in Figure 4-9-a and by use of the method discussed in Section 4.6.3, small spatial discontinuities with $\pm 50\mu\text{m}$ amplitudes result in large surface normal errors with mean of about 40° showing high sensitivity to spatial discontinuities. Since noise is inevitable, the measurement both axially and laterally should have sufficiently high resolution to allow for spatial filtering. As shown in Figure 4-9-b-c, using spatial filtering the effects of spatial noises can be reduced as long as the shape estimate is of a sufficiently high resolution.

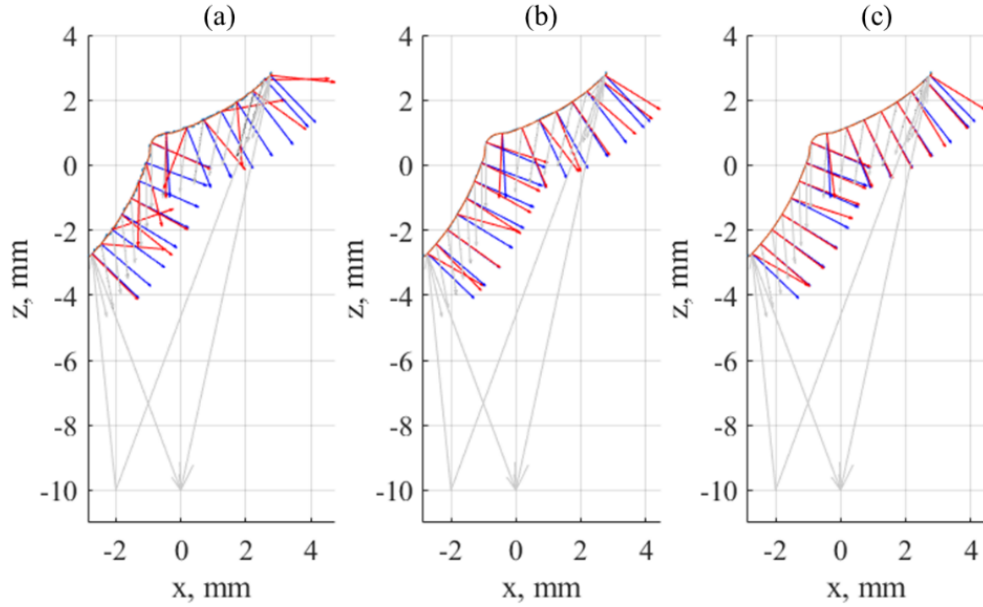


Figure 4-9 Comparison of spatial filtering effects on α_e for a fixed $\delta(z_p) = \pm 50\mu m$ with $d = 10mm$. Red and blue vectors show the surface normals before and after the addition of the spatial noise. Gray vectors in the background represent the sensitivity vector at each point that are nearly immune to such level of surface discontinuities. The spatial distribution of surface normals in different window size of spatial filtering: (a) no spatial filtering mean of errors in α of about 40° ; (b) Gaussian spatial filter with window of 10 with mean of errors in α of about 20° ; and (c) Gaussian spatial filter with window of 100 with mean of errors in $\alpha < 10^\circ$.

4.8 Preliminary estimation of required shape resolution

In this Section, using the numerical model used for determination of surface normal and sensitivity vector the overall combined uncertainty is measured. Both the sensitivity vector and the surface normal are needed to find α . To quantify the overall uncertainty the mean of α variations due to all parameters uncertainties for all points are used (called α_e).

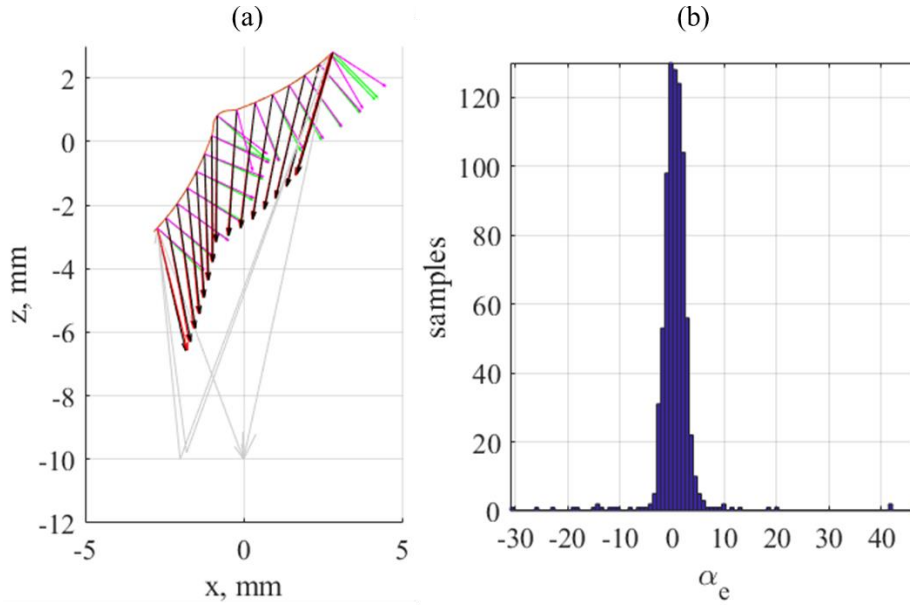


Figure 4-10 Results of numerical simulation under various uncertainties to determine maximum errors in the measured angle α_e : (a) the sample shape and orientation with respect to illumination and observation angles together with spatial distribution of sensitivity vector and surface normals in ideal and uncertain conditions. Black and red arrows show the variations of the sensitivity vector while the green and magenta show the variations of the surface normal due to various parameters uncertainties; and (b) histogram of the parameter α_e with Mean = 1.97°, and STD = 3.6°.

In order to measure the surface-normal displacements with smaller than $\pm 4\text{nm}$ uncertainty at 532nm, together with phase quantification within $\pm\pi/50$, using Eqn. (4-13) the angle α needs to be determined with $\pm 5^\circ$. Taking this angle range as a basis for the shape a preliminary estimation of the shape resolution is determined using the following specifications:

- Sample shape and orientation similar to TM 2D intersection with 8mm width, 3mm depth, rotated 45° , curvature of 1mm at umbo, and 3.5mm for two curvatures representing pars tensa,
- Distance $d=10\text{mm}$ from the observation point to the center of annulus plain,
- 2 mm off axis illumination with uncertainty of $\delta(P_1) = \pm 200\mu\text{m}$,

- Gaussian spatial filtering with window size of 50 samples for surface normal determination.

It was estimated that in order to determine α with uncertainty close to the desired range (i.e., $\alpha_e = \pm 5^\circ$) the shape needs to be measured with uncertainty of $\delta(z_p) = \pm 40 \mu m$.

Based on this analysis the main parameters governing the displacement resolution after the interference phase is the determination of surface normals that require sufficient shape resolution.

Part 2: Developments

5 High-speed phase sampling methods using phase correlation interferometry

Temporal phase sampling is cost effective and straightforward phase sampling method. The reference or object wavefront is phase shifted by altering the optical path using a nanometer-scale positioner (i.e., moving a mirror/tilting a glass plate). Despite the simplicity and ease of use, implementation of the temporal phase shift for high-speed holographic shape and displacement measurements on biological samples is a challenging task. This Chapter focuses on the developments of novel methods to measure the interference phase of a high-speed event in challenging conditions that are presented in the first section of this chapter. An uncertainty analysis is performed to determine the dominant factors affecting the displacement resolution determined by the $2+N$ HCI displacement measurement method. The uncertainty analysis also led to the development of the High-speed Phase Correlation Calibration (HPCC) method. The HPCC method together with a continuous high-speed phase sampling provide the necessary feedback to repeatedly and accurately recover the phase in post-processing phase of the measurements by compensating for sample spatiotemporal physiological motions.

5.1 Challenges of high-speed phase sampling

The challenges toward performing high-speed phase sampling for phase quantification in this dissertation include,

1- Live physiological motions and environmental vibrations

Live samples such as Tympanic Membrane undergo continuous rigid body motions (i.e., physiological motions due to heartbeat, respiration etc.) as well as spatially irregular deformations (i.e., due to environment acoustical excitation.) Although,

the transient response of the TM occurs at sufficiently larger temporal frequency compared to the physiological and environmental motions, the latter still interfere with the temporal phase shifting procedure resulting in low accuracy and precision.

2- Transient ringing and nonlinearities of the phase shifter actuator

The response of mechanical positioners used in phase shifting include hysteresis and nonlinearities that are especially prominent with rapid changes in position. In addition, due to the mechanics of the positioners and the phase shifting unit (e.g. mass, stiffness and damping), rapid accelerations/decelerations of the phase shifter (e.g., >1 kHz) result in ringing with time constants up to milliseconds. As the time intervals between the phase steps decreases, as shown in Figure 5-1, the effects of stepping results in overlapping undamped vibrations and random motions of the phase shifter positioner in nanometer-scale.

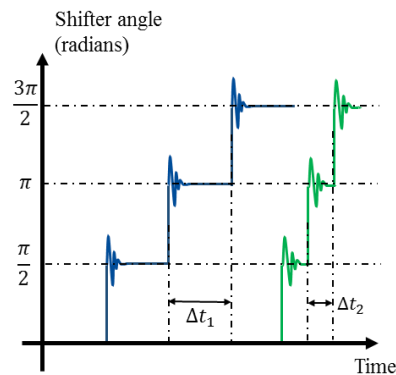


Figure 5-1 Effects of high-speed phase stepping as the inter step time intervals decrease. Blue line shows the behavior of the phase shifter with longer inter-step with temporal intervals (Δt_1) while the green line shows smaller interval Δt_2 . As Δt decreases, the phase shifting procedure is more affected by the transient ringing motions of the mechanical phase shifter.

3- Wavelength instabilities

In holographic interferometry, the sample displacements, shape, etc. are determined from measurements of the optical phase. The smallest motion or difference in shape

that can be resolved is directly related to the stability of the laser wavelength. In special cases (i.e., multiple wavelength holographic shape measurements), the laser source may undergo wavelength instabilities within the desired temporal resolutions for in-vivo measurements. These instabilities alter the optical path length spatiotemporally resulting in deficiencies in the phase sampling procedure.

4- Incompatible phase calibration methods

Temporal phase shifting methods require calibration of the phase-shift positioner (i.e., a piezoelectric actuator) to define the control voltage corresponding to a certain phase shift. Available phase shifter calibration methods require lengthy iterative acquisition of holograms with multiple averages in a stable environment (Creath, 1985; Hariharan, 1984). When it comes to shifting the optical phase on live samples in a noisy environment, sample motion and/or deformation add to the phase produced by the shifter, such that even if the phase shifter actuator is highly repeatable the applied shift is not repeatable. In this case, a method to determine the total shift in phase is needed.

One method to determine the optical phase in such challenging conditions is to control the piezo motions in a closed-loop fashion using real-time feedback from the shifted phase. However, such feedback requires a method for determining the motion produced by the shifter, and due to current technological limitations, real-time phase measurements from high-speed holograms are not possible. Furthermore, a single point high-speed photo detector only provides the desired feedback at a single location, which is not sufficient due to spatially varied phase shifts during the phase sampling process.

In this Chapter, it is demonstrated that high-speed phase sampling is the key to reduce the effects of environmental noises and laser instabilities. However, available methods are incapable of determining the applied shift without multiple iterations or significantly reducing the spatial resolution. In the following Sections, first the necessary background on the phase correlation method is presented. Next, the high-speed holographic displacement measurement method is presented followed by a sensitivity analysis to determine the dominant factors affecting its performance. Finally, the proposed High-speed Phase Correlation Calibration (HPCC) method is presented together with numerical simulation of the phase shift in various conditions.

5.2 Speckle pattern correlation interferometry

Measurements of the interference phase in the speckle correlation interferometric method relies on the statistical analysis of the spatial and temporal variations in a two beam (object and reference beam) speckle pattern. A speckle pattern is a complex constructive (bright spots) and destructive (dark spots) superposition of many spherical wave fronts reflected from a 'rough' surface with projections and indentations of depths larger than the laser wavelength. Due to this property, the speckle pattern depends upon variations in the optical path length. As shown in Figure 5-2, due to the periodicity of the light, as the sample undergoes continuous deformations equivalent to a complete cycle of phase, because the surface structure is stable during the displacements, the speckles vary harmonically between two independent patterns.

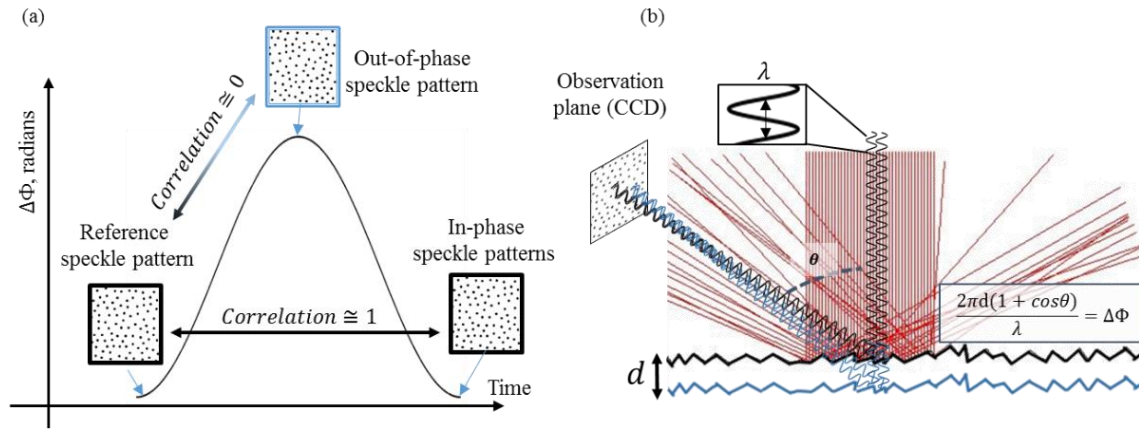


Figure 5-2 (a) Correlation coefficients between two extreme variations of the interference phase with respect to the reference speckle pattern due to the motions of the sample; and (b) schematic representation of formation of speckles and variations of the speckle pattern with respect to sample displacements. The figure show multiple coherent beams interfere constructively and destructively over the CCD of the camera to form a speckle pattern. Due to spatial periodicity of the light with a fixed wavelength, depending on the angle of observation, complete cycles of the interference phase harmonically generating the same pattern. The figure shows the relation between the displacements d and interference phase $\Delta\phi$ from the principles of holographic sensitivity vector.

Statistical analysis of in-phase speckle patterns using well-known methods (i.e., Pearson's correlations) show high correlation close to unity, while out-of-phase holograms in which the interference patterns are out-of-phase show near zero correlation values indicating different speckle patterns in the two phase conditions. The relationship between variations of speckle pattern with respect to the interference phase ($\Delta\phi$) is harmonic although the speckles are spatially random (Jones & Wykes, 1983). In a spatially discrete digital hologram, if sample displacements are spatially continuous, the phase variations along a small group of pixels centered at a pixel of interest are minimal. Therefore, superposition of a reference and object beam at the pixel of interest located at (x, y) , is described by,

$$I_{ref}(x, y) = I_r(x, y) + I_o(x, y) + 2\sqrt{I_r(x, y)I_o(x, y)} \cos(\phi), \quad (5-1)$$

where I_r and I_o represent the reference and object intensities, respectively, and ϕ is the random phase difference between the two interfered wave fronts (The off-axis

configuration generating such holograms is shown in Figure 5-10). After the sample displaces (or deforms), the optical path length between the two beams changes (see Figure 5-2-b) producing a phase difference $\Delta\phi$ in the deformed image that can be represented by,

$$I_{def}(x, y) = I_r(x, y) + I_o(x, y) + 2\sqrt{I_r(x, y)I_o(x, y)} \cos(\phi + \Delta\phi), \quad (5-2)$$

The correlation coefficient (i.e., Pearson's product moment coefficient) between a small kernel around the point of interest before and after sample deformation is (Appendix A), (Jones & Wykes, 1983; Schmitt & Hunt, 1997),

$$\rho(I_{ref}(x, y), I_{def}(x, y)) = \frac{\langle I_{ref}I_{def} \rangle - \langle I_{ref} \rangle \langle I_{def} \rangle}{\sqrt{(\langle I_{ref}^2 \rangle - \langle I_{ref} \rangle^2) \times (\langle I_{def}^2 \rangle - \langle I_{def} \rangle^2)}}, \quad (5-3)$$

where the operator $\langle \rangle$ approximates the weighted average of a random variable. The weighted average is defined for discrete and for continuous random variables such as X as follows (Jones & Wykes, 1983):

$$E(X) = \langle X \rangle = \sum_{all\ x} x P(x = X) = \sum_{all\ x} x P(x), \quad (5-4)$$

$$E(X) = \langle X \rangle = \int_{all\ x} x f(x) dx$$

where functions P and f represent the probability of a certain value. The correlation coefficient of Eqn. (5-3) can be evaluated by noting that,

- I_{ref} , I_{def} and ϕ are independent variables, which means $\langle XY \rangle = \langle X \rangle \langle Y \rangle$, $\langle X + Y \rangle = \langle X \rangle + \langle Y \rangle$.
- $\phi + \Delta\phi$ and ϕ are assumed to be uniformly distributed within the kernel, meaning the probabilities of ϕ and $\phi + \Delta\phi$ are $\frac{1}{2\pi}$ within $[-\pi, \pi]$. Therefore, $\langle \cos\phi \rangle = \langle \cos(\phi + \Delta\phi) \rangle = 0$, $\langle \cos^2\phi \rangle = \langle \cos^2(\phi + \Delta\phi) \rangle = \frac{1}{2}$, and $\langle \cos\phi \cdot \cos(\phi + \Delta\phi) \rangle = \frac{\cos\Delta\phi}{2}$.
- $\langle I^2 \rangle = 2\langle I \rangle^2$

If we use the beam ratio $r = I_o/I_r$ to substitute $I_o = rI_r$ in Eqn. 1 and Eqn. 2, the correlation coefficient can be calculated as

$$\rho(I_{ref}(x,y), I_{def}(x,y)) = \frac{(r+1)^2 + 4r \cos(\Delta\phi)}{(r+1)^2 + 4r},$$

$$\text{if } \Delta\phi = 0 \rightarrow \rho_{max} = 1 \tag{5-5}$$

$$\text{if } \Delta\phi = \pm\pi \rightarrow \rho_{min} = \frac{(r-1)^2}{(r+1)^2 + 4r}$$

This process is explained in detail in the Appendix A.1.

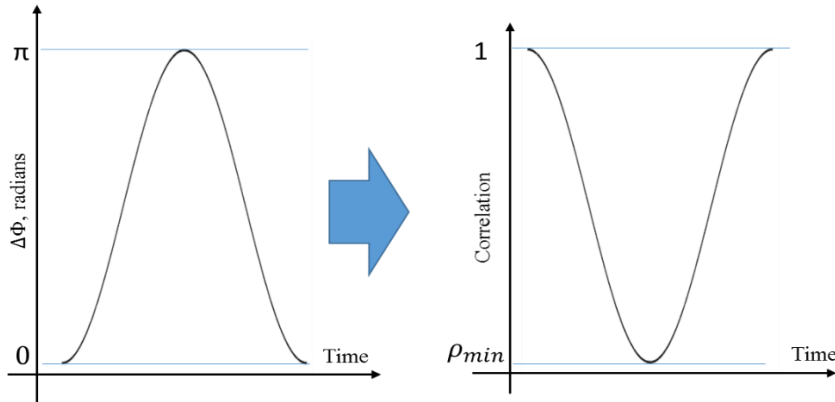


Figure 5-3 Correlation range schematic representation in terms of interference phase $\Delta\phi$

As it is shown in Figure 5-3, the range of $\rho(I_{ref}, I_{def})$ is $[\rho_{min}, 1]$. Based on Eqn. (5-5), correlations coefficients smaller than ρ_{min} theoretically do not exist, but in practice, due to the spatial noise of the speckles as well as sensor electronic noise, the correlation range shifts with a value of ϵ (i.e., $[\rho_{min} - \epsilon, 1 - \epsilon]$)(Schmitt & Hunt, 1997).

5.2.1 Effects of zero-order terms in speckle pattern correlation interferometry

Based on Eqn. (5-5), the beam intensity ratio r (i.e., $r = I_o/I_r$) limits the minimum correlation coefficient attainable by the correlation. Experimental investigations by Dobrev et al. (2014) show the removal of the zero order terms (i.e., $I_r + I_o$ terms in Eqn.

(5-1) and (5-2)) improves the performance of the correlation in detection of the interference phase (I. Dobrev et al., 2014b). Here, we present, to the best of our knowledge for the first time, the statistical mathematics behind the effects of the zero order terms on the quality of the measurements. Assuming that the zero order terms are completely removed, the modified reference and deformed intensities of Eqn. (5-1) Eqn. (5-2) become,

$$I'_{ref} = 2\sqrt{I_r I_o} \cos(\phi), \quad (5-6)$$

$$I'_{def} = 2\sqrt{I_r I_o} \cos(\phi + \Delta\phi). \quad (5-7)$$

In this case, the correlation coefficient of Eqn. (5-3) is,

$$\begin{aligned} \rho(I'_{ref}, I'_{def}) &= \frac{\langle \cos(\phi) \cos(\phi + \Delta\phi) \rangle}{\sqrt{\langle \cos^2(\phi) \rangle \langle \cos^2(\phi + \Delta\phi) \rangle}} \\ &= \frac{\frac{1}{2\pi} \int_{-\pi}^{\pi} \cos(\phi) \cos(\phi + \Delta\phi) d(\phi)}{\sqrt{\frac{1}{2\pi} \int_{-\pi}^{\pi} \cos^2(\phi) d(\phi) \cdot \frac{1}{2\pi} \int_{-\pi}^{\pi} \cos^2(\phi + \Delta\phi) d(\phi + \Delta\phi)}} = \cos(\Delta\phi). \end{aligned} \quad (5-8)$$

The details of this calculation is presented in Appendix A.3 (Eqn. (A-30)).

These calculations are a proof of the relation between the zero order terms and the shift of the correlation range, which is the basis of the HPCC method discussed later in this Chapter (Section 5.5). These results also show the necessity of removal of zero order terms to extract the cosine of the interference phase. The next Sections presents a brief description of how the zero order terms can be removed by temporal averaging under some conditions, while later in the HCI method's sensitivity analysis Section (Section 5.3.2), an enhanced method for temporal removal of zero order terms for high-speed correlation interferometry is presented.

5.2.2 Measurements of zero-order¹ terms

In conventional digital holography, removal of the zero-order terms is performed by spatial averaging over all pixels of a single hologram or using frequency domain filtering (Ulf Schnars et al., 2015; I. Yamaguchi & Zhang, 1997). These methods are not of interest since they provide the zero-order terms at a low spatial resolution compared to the actual hologram, and cannot be used with speckle correlation interferometric methods. In this Section, a temporal averaging technique is presented that maintains the spatial resolution of the zero-order terms within the actual holograms. In detail, a phase shifted hologram obtained by temporal phase stepping is described by,

$$I(x, y, \phi_i) = I_r + I_o + 2\sqrt{I_r I_o} \cos(\phi_i) \quad (5-9)$$

where ϕ_i is the phase shift introduced by the phase shifter device. Averaging over n holograms produces,

$$\frac{1}{n} \sum_{i=1}^n I(x, y, \phi_i) = I_r + I_o + \frac{1}{n} \sum_{i=1}^n 2\sqrt{I_r I_o} \cos(\phi_i). \quad (5-10)$$

The higher-order terms, can be describe by a series (S_n) of the form,

$$\frac{1}{n} \sum_{i=1}^n 2\sqrt{I_r I_o} \cos(\phi_i) = S_n = \frac{1}{n} (a \times \cos(\phi_n)), n \in \mathbb{N}, \quad (5-11)$$

where, $a = 2\sqrt{I_r I_o}$. The sum of this series will converge to zero as long as n is sufficiently large,

$$S = \lim_{n \rightarrow \infty} \left(\frac{1}{n} (a \times \cos(\phi_n)) \right) \cong 0, \quad (5-12)$$

¹ The zero-order terms are also called DC-terms or constant background intensity.

therefore, averaging over many holograms using Eqn. (5-10) provides the DC terms,

$$\frac{1}{n} \sum_{i=1}^n I(x, y, \phi_i) \cong I_r + I_o. \quad (5-13)$$

Subtraction of this term from all holograms is equivalent to removal of the zero order terms. This is the general case of averaging over many holograms. Since there may not always be a sufficiently large number of holograms in a series, temporal averaging over a small number of holograms is proposed later on in this Chapter (Section 5.3.1)

5.2.3 High-speed phase Correlation Interferometry (HCI)

Because cosine is an even (or symmetric) function (i.e., $\cos(-\theta) = \cos(\theta)$), the sign of the phase cannot be quantified by a single correlation between the reference and deformed holograms. To solve this problem, an additional $\pi/2$ phase shifted reference is acquired to provide the modulo 2π phase map. (Georgas & Schajer, 2012; Pérez-López et al., 2006). Again, we remove the zero order terms due to their known effects on the correlation.

$$I_{ref}(x, y) = 2\sqrt{I_r(x, y)I_o(x, y)} \cos(\phi) \quad (5-14)$$

$$I_{ref+\pi/2}(x, y) = 2\sqrt{I_r(x, y)I_o(x, y)} \cos(\phi + \pi/2)$$

Given the $\pi/2$ shift in the second reference state, the relationship between the phase change produced by deformation ($\Delta\phi$) and the ratio of the correlations of the deformed and two reference states is simplified,

$$\frac{\rho\left(I_{ref+\frac{\pi}{2}}, I_{def}\right)}{\rho\left(I_{ref}, I_{def}\right)} = \frac{\sin(\Delta\phi)}{\cos(\Delta\phi)} = \tan(\Delta\phi), \quad \Delta\phi = \text{atan2}\left[\frac{\rho\left(I_{ref+\frac{\pi}{2}}, I_{def}\right)}{\rho\left(I_{ref}, I_{def}\right)}\right] \quad (5-15)$$

Since this method requires one phase shift prior to sample deformation without any requirement of phase shifting during the sample response, it is ideal for high-speed acquisition by utilizing the entire temporal bandwidth during the sample response time.

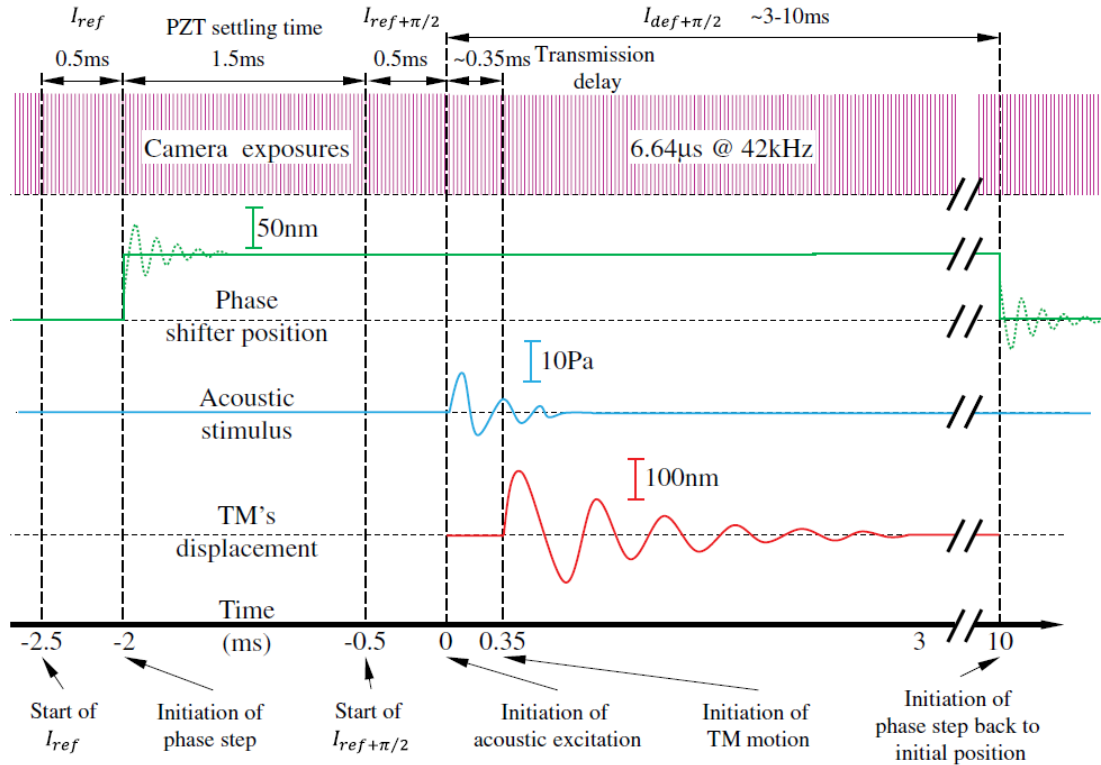


Figure 5-4 Timing of the events occurring during high-speed 2+N frame acquisition with the local correlation phase sampling method. N deformed frames are acquired at the maximum frame rate of the camera and referenced relative to frames captured during two periods prior to acoustic excitation. Acquisition takes into account the settling time of the piezoelectric (PZT) phase shifter, while minimizing the overall acquisition time. The PZT is returned to its original position at the end of the acquisition. Due to the distance between the sound source and the sample, there is an acoustic transmission delay (I. Dobrev et al., 2014b).

Taking a burst of highly stable deformed holograms, instead of a single one, the method is capable of determining the continuous kinematics of the high-speed events. Dobrev et al. (2014b) implement this method to adapt high-speed imaging technologies and applied it to measurements of human TM. Since this method requires 2 reference frames, and “N” consecutive deformed frames it is called “2+N” and since it require high-speed we call it 2+N High-speed Correlation Interferometry (HCI) method. Figure 5-4 shows the timing diagram of the events during the measurements of acoustically induced transient response of TM together with the timing required for the single stepped phase shift in a set of 2+N HCI measurements.

5.3 Uncertainty analysis on the HCI method

To understand the dominant factors affecting the performance of the HCI method a sensitivity analysis is described in this Section. The accuracy of the method is investigated compared to the resolution of the phase shifter, proper removal of the zero order terms, speckle to kernel size ratio, and phase unwrapping errors on the accuracy of the method are described.

5.3.1 Zero order terms (DC)

Figure 5-5 shows the effect of removal of the zero order terms on the modulo 2π phase obtained by the HCI method using the same set of holograms under condition of complete, partial, or no removal. It is clearly visible from the phase maps and line intersections of Figure 5-5 that without the removal of the zero order terms, the phase contrast is severely reduced. Thus, the HCI method is highly sensitive to proper estimation of zero order terms. The focus of this part is to demonstrate how the zero order terms interfere with the process of phase quantification of the $2+N$ HCI method.

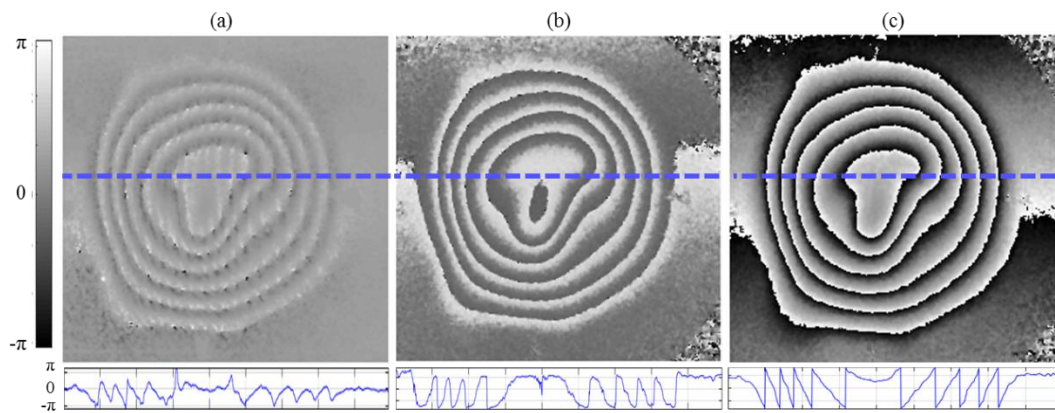


Figure 5-5 Wrapped interference phase estimated by the HCI method under various DC removal conditions: (a) DC not removed, holograms were intact; (b) DC was calculated using a group of randomly phase shifted references and removed from all holograms; and (c) DC was calculated using a complete cycle of phase-shifted references and removed from each hologram. Bottom panels show spatial distribution of modulo 2π wrapped phase across the blue line for each case.

Using Eqn. (5-5) If the zero order (DC) terms are not, or only partially removed in each of the measured frames (the deformed as well as the reference frames), the remaining DC term results in a non-zero ratio r across the hologram and complicates the ratio of the correlation functions.

$$\frac{\rho(I_{ref+\pi/2}, I_{def})}{\rho(I_{ref}, I_{def})} = \frac{1 + r^2 + 2r \sin(\Delta\phi)}{1 + r^2 + 2r \cos(\Delta\phi)} = f(r, \Delta\phi) \neq \tan(\Delta\phi), \quad (5-16)$$

where $f(r, \Delta\phi)$ is a function related to both the interference phase and the value of intensity ratio $r(x, y)$ at the desired kernel. Since the correlation ratio no longer equals the tangent of the phase change, the use of the inverse tangent to obtain $\Delta\phi$ from the correlation ratio provides a spatially corrupted phase with varied spatial frequency.

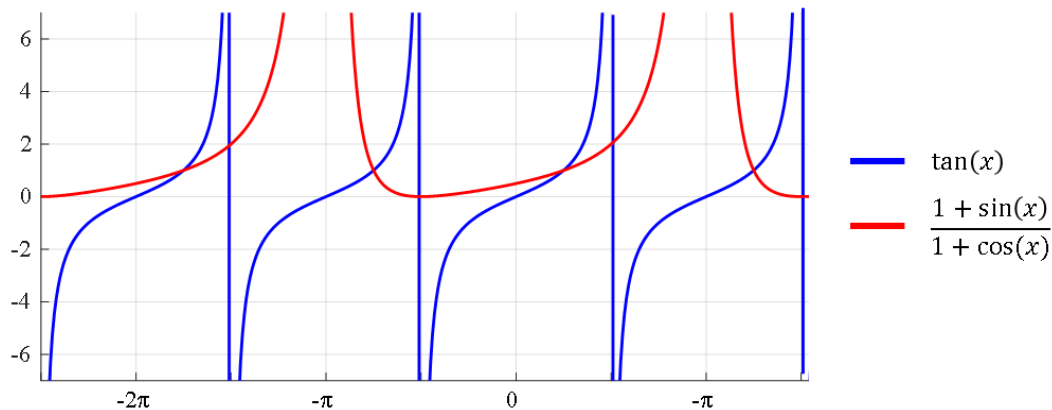


Figure 5-6 Comparison of tangent function compared to partially removed zero order terms with $r = 1$.

For example if the DC is not removed and¹ $r = 1$, the range and domain of the ratio of the correlation function is different compared to that of the tangent (Figure 5-6). The range of the resultant function without proper DC removal has a non-symmetric form with a period

¹ object and reference has the same intensity at the pixel of interest

double the tangent function. In addition, the required jumps for most of the unwrapping algorithms should be between $\pm\infty$ however in this case the ratio only jumps between 0 and $+\infty$, which limits the application of available unwrapping algorithms. Since the ratio $r(x, y)$ is spatially varying, the behavior of the resultant function varies in space leading to corrupted phase data as shown in Figure 5-5-c.

Another important effect of the partial removal of the zero order terms (e.g., by temporal DC removal using a biased number of phase shifter reference frames) results in spatially continuous but different correlation function compared to the tangent. This phenomena is shown in Figure 5-5-b, where it produces difference in the number and location of interference fringes¹ leading to errors in the location and number of the jumps in the modulo 2π phase. The removal or compensation for the presence of the zero order terms is an essential part of the HCI method and is required to accurately measure the modulo 2π phase.

5.3.2 Removal of zero order terms for high-speed transient measurements

In the previous Section, it was explained that temporal averaging over many phase shifted holograms can provide the zero-order terms of the holograms of interest. However, as Figure 5-4 suggests, the phase shifter is incremented nearly instantaneously and remains at its stepped position during the rest of the measurement. The induced transient motions of the sample alters the measured phase over a longer period of time but for most of the

¹ Interference fringe, a bright or dark band caused by beams of light that are in phase or out of phase with one another.

averaging time the cosine term in Eqn. (5-12) is constant. Therefore, blind temporal averaging over a set of high-speed holographic measurements does not guarantee a good estimate of the zero order terms. To better define these terms without extending the length of the experiment, only a small number of holograms (4 or more), that describe a complete and symmetric cycle of the phase shifted reference are needed. More precisely, temporal averaging of a holographic image series can provide an accurate estimate of zero-order terms when the following criteria are met,

$$\frac{1}{n} \sum_{i=1}^n 2\sqrt{I_r I_o} \cos(\phi_i) = 0, \text{ iff } \{|\phi_1 - \phi_i| = 2\pi i \text{ and } \sum_{i=1}^n \phi_i = 0, \quad (5-17)$$

$$i = 1, 2, \dots \}.$$

By changing from a reference phase step to a phase ramp of sufficient duration and amplitude, it is possible to perform one symmetric and complete cycle of phase shift prior to sample excitation. However, a remaining challenge is detection of the complete cycle in the presence of the spatiotemporal noise.

5.3.3 Phase shifter resolution and precision

In order to estimate the accuracy of the phase shifter required to produce an acceptable error in the interference phase, a sensitivity analysis to errors around the imposed $\pi/2$ phase shift in Eqn. (5-15) was performed. Assuming the error in phase measurement, using the 2+N method () is caused only by the phase shifter, the Optical Path length Error in degrees (OPE $^\circ$) is,

$$OPE^\circ = \left| \Delta\phi - \tan^{-1} \left[\frac{\sin(\Delta\phi + e)}{\cos(\Delta\phi)} \right] \right|, \quad (5-18)$$

where, e denotes the error in the phase shifter and $\Delta\phi$ is the interference phase computed from the shifted and unshifted references and the deformed states (Eqn. (5-15)). Figure

5-7 shows the relation between OPE and e across constant positive and negative interference phases away from the singularities ($\Delta\phi = \pm \frac{\pi i}{2}, i = 1, 2, \dots$). The analysis demonstrate OPE° is largest when $\Delta\phi$ is close to 0° , where OPE approximates e .

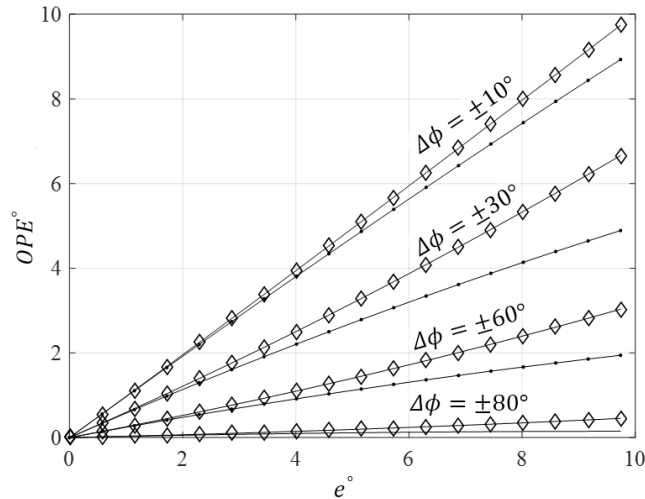


Figure 5-7 Measured OPE with respect to phase shifter miscalibration at various phase angles. The error in the phase shifter in degrees is scaled on the x-axis. The y-axis is OPE the error in the optical length estimate in degrees. (The diamonded lines represent the negative errors). The calculations are performed around 4 potential values of phase shift (10, 30, 60 and 90 degrees). Minimum sensitivity to the phase shifter miscalibration occurs when the induced phase shift is at $\pm 90^\circ$. The largest errors in the estimated interference phase occur when the interference phase is near zero, but those errors are similar in magnitude to the error in the phase shift.

5.3.4 Speckle kernel size ratio

Speckles are the core of the phase correlation method and the quality of their correlation governs the measuring resolution. Speckle¹ size (d_{sp}) is directly related to the lens to CCD distance (z), wavelength (λ) and aperture diameter (D) of the imaging objectives (Kreis, 2006).

¹ Subjective speckles

$$d_{sp} = \frac{2.44\lambda z}{D}. \quad (5-19)$$

Speckle kernel size ratio S is equivalent to the pixel size of the HCI method, which is defined by

$$S = \frac{d_{sp}}{k_s}, \quad k_s = n_k \times p_s, \quad (5-20)$$

where, k_s is the kernel size, n_k is the discrete width of the square kernel ($n_k \in \mathbb{N}, n_k > 3$) and p_s is the pixel size of the camera. The speckle kernel size ratio S is an important parameter that governs the range of resolvable displacements for a given spatial resolution (i.e., minimum/maximum detectable phase at various spatial resolutions).

Speckle size is adjusted by changing the aperture diameter (see Eqn. (5-19)). However, in high-speed holography, due to illumination limitations, the aperture diameter is usually near its maximum, and there is limited room for change. While wavelength is little varied, the design of the optics should be carefully performed to accommodate the desired speckle size. This task can be performed by adjusting the sample to CCD distance, variations in numerical aperture, and/or choosing the wavelength with respect to sample surface roughness.

For a fixed kernel size n_k , if speckle size is small compared to the pixel size ($d_{sp} < p_s \rightarrow S < 1$), the correlation measures the superposition of many speckles. Since averaging of many speckles reduces the range of the probabilities of having full constructive and destructive interference, the sensitivity of the correlation technique to the interference phase is reduced. On the other hand, if the speckles are large compared to the pixels (e.g., $d_{sp} > p_s \rightarrow r_{sp} > 1$), larger kernel sizes (n_k) are required to detect the interference phase and the spatial resolution is reduced. Therefore, averaged speckle size of the entire hologram should be about one pixel with standard deviation of a few pixels to ensure

adequate sensitivity of the correlation to phase changes to obtain maximum spatial resolution.

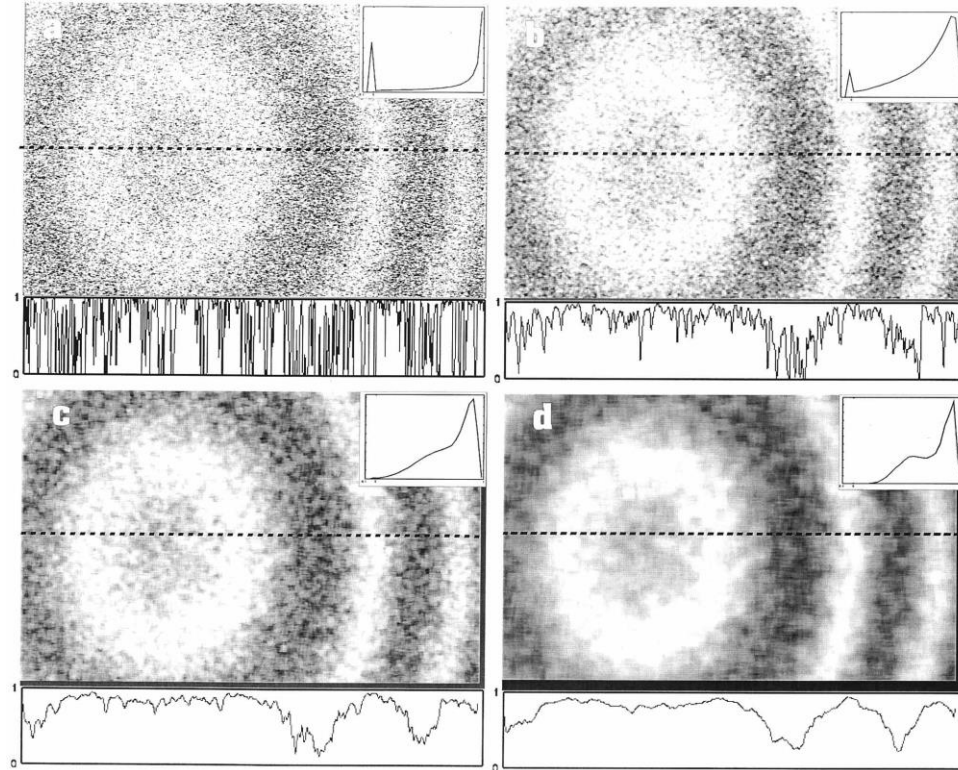


Figure 5-8 Correlation fringe patterns for a 10-mm in-plane translation calculated with correlation cells of dimensions: (a) 2×2 ; (b) 5×5 ; (c), 9×9 ; and (d) 19×19 pixels. Insets are the corresponding normalized correlation magnitude histograms with the independent axes ranging from -0.1 to 1, the range of correlation values for the pixels in the image. Panels beneath each correlation image are the intensities observed along the horizontal profile indicated by the dotted lines through the centers of the images.

Adapted from (Schmitt & Hunt, 1997).

While in most of the HCI measurements the speckle size is fixed, the adjustments of the kernel size (k_s) adjusts the spatial resolution with respect to the displacement resolution. Schmitt et al. experimentally verified that the kernel size acts as a spatial averaging filter which has inverse relationship with displacement resolution (Schmitt & Hunt, 1997). This phenomenon is shown in Figure 5-8, which compares two-frame correlation calculations (i.e., Eqn. (5-5)) of the same set of data reconstructed using different kernel sizes. Overall,

based on the experimental verifications performed by the author, an increase in the kernel size results in:

- **Increased displacement resolution.** As the kernel size increases, the interference phase is averaged over more pixels, which has the effect of reducing the noise in the phase estimate. The decrease in noise leads to an increase in the signal-to-noise ratio and the ability to detect reliably smaller changes in phase.
- **Decreased spatial resolution.** Since the spatial resolution of the sensor is fixed, larger kernels lead to an increase in the size of resolvable spatial differences.
- **Increase the computational load.** As the kernel size increases, the number of computations for each kernel cubically increases.

As an example, in some applications high displacement resolution measurements (i.e., a small fraction of a wavelength) are needed but high spatial resolution is not. In this case, large kernels can increase the displacement resolution of the system to observe smaller displacements with the price of an increase in the smallest resolvable spatial distances. In most TM measurements, large displacements (i.e., multiples of wavelengths) occur that require full bandwidth of the sensor, in this case the smallest possible kernel should be used to increase the spatial resolution and provide maximum number of quantifiable fringes across one hologram. It should be noted that the effects of kernel size are relatively immune to temporal noises.

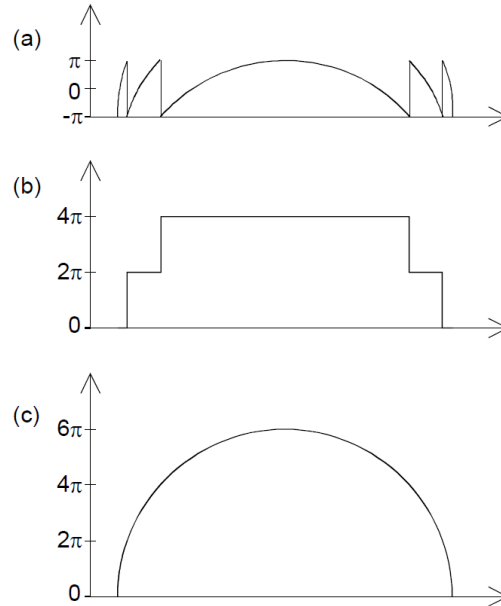


Figure 5-9 Schematic representation of one dimensional phase unwrapping procedure: (a) modulo 2π phase; (b) step function to trace the absolute value of the phase; and (c) unwrapped phase by addition of modulo 2π phase, panel (a), by the step function of panel (b). Adapted from (Ulf Schnars et al., 2015)

5.3.5 Phase unwrapping

Phase quantification in HCI is performed by removal of spatial discontinuities of the modulo 2π phase using well-developed available unwrapping methods (Herráez et al., 2002). The topic of efficient and robust phase unwrapping algorithms for multi-dimensions is beyond the scope of this thesis and is well described in multiple references (Ghiglia & Pritt, 1998; Herráez et al., 2002). Here we briefly describe the process and its requirements as well as its effect on HCI performance. The procedure of simple one-dimensional unwrapping along a single line is shown in Figure 5-9. The phase unwrapping algorithm uses multidimensional search methods to detect discontinuous regions within the phase map.

Due to the complexities that arise when using experimental data in two dimensions, the wrapped phase has to meet certain criteria to ensure the algorithms can remove the jumps

between $\pm\pi$. Analysis of experimental data shows that inefficiency in removal of zero-order terms as well as phase shifter miscalibration generate spatial errors as large as 2π in the unwrapped phase. This phenomenon is shown later in Figure 5-22, panel (a-c), by depicting the results of unwrapping errors due to spatial miscalibration of the phase shifter. Since high-speed holography deals with thousands of holograms for each measurements, the generation of accurate and precise modulo 2π phase maps reduces the need for computationally intensive unwrapping algorithms.

Overall, the ability of an unwrapping algorithm to remove spatial discontinuities is directly related to the contrast of the modulo 2π phase map which is related to phase shifter calibration, removal of zero order terms as well as the kernel size.

5.4 Continuous phase shift in presence of spatiotemporal noises

If the phase shifter temporal steps (as shown in Figure 5-1 and Figure 5-4) is changed to a temporally continuous phase shift (i.e., due to a ramp or continuous motions of a sample as shown in Figure 5-17), each camera exposure observes the integration of the captured intensity over the exposure period described as,

$$I(x, y, t_i) = \frac{1}{\tau} \int_{t=t_i-\frac{\tau}{2}}^{t_i+\frac{\tau}{2}} I_{DC}(x, y) + I_M(x, y) \cos(\delta(t) + \phi) dt, \quad (5-21)$$

where τ is the duration of the camera exposure, $\delta(t)$ is a known temporally varying phase shift generated by the mechanical phase shifter device, I_{DC} and I_M are the zero-order terms and the modulation, respectively, and x and y are the coordinate of the center of the kernel (i.e., a box of $n_k \times n_k$ pixels). Function $\delta(t)$ is the “*phase shifter function*” and it is described by,

$$\delta(t) = D_{pzt}(t) \frac{2\pi}{\lambda(t)} (1 + \cos \theta_{pzt}), \quad (5-22)$$

where $D_{pzt}(t)$ describes the motion of the mirror in time, $\lambda(t)$ is the wavelength, and θ_{pzt} is the constant angle shown in Figure 5-10-b.

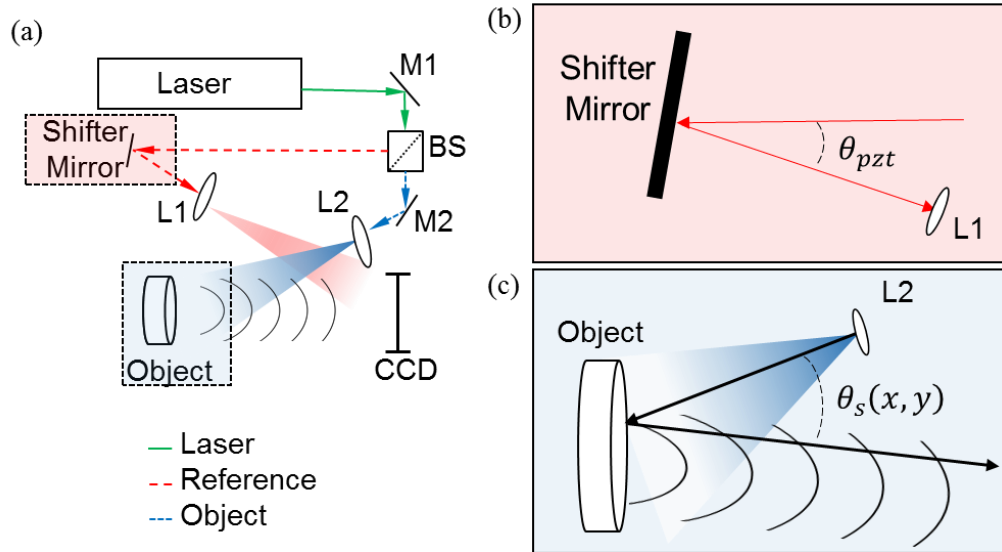


Figure 5-10 Off axis configuration parameters: (a) schematic representation of the setup; (b) enlarged pink area of panel (a), representing angle θ_{pzt} ; and (c) enlarged blue area of panel-a representing the spatially varying angle $\theta_s(x, y)$ due to shape and off-axis illumination.

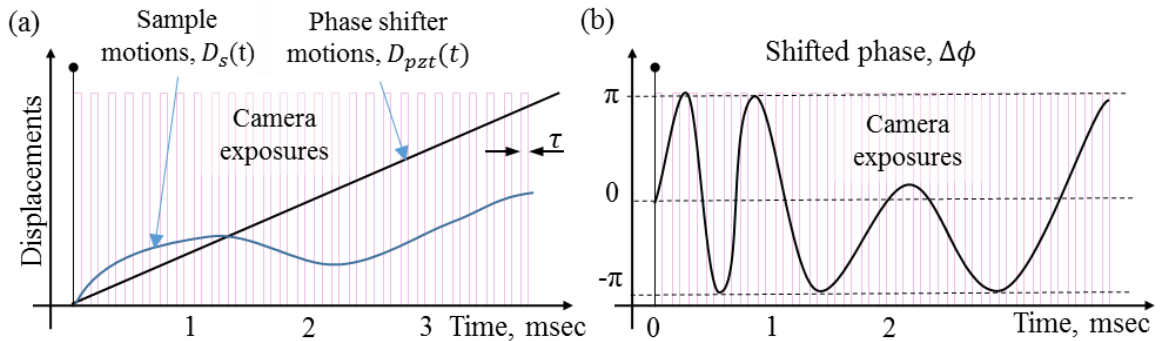


Figure 5-11 Schematic representation of the effects of sample motions on the continuous phase shift. (a), random displacements of sample on top of linear motions of the PZT positioner having faster motions compared to the sample; and (b) resultant applied shift affected by the sample motions having at least a complete cycle during the period of phase shift.

If the sample, imaging sensor, optical components, etc. move during the phase shift, they introduce noise-like spatiotemporal variations of the optical path length that constructively and destructively add to the phase shifter function, represented as,

$$I(x, y, t_i) = \frac{1}{\tau} \int_{t=t_i-\frac{\tau}{2}}^{t_i+\frac{\tau}{2}} I_{DC} + I_m \cos[\delta(t) + N(x, y, t) + \phi] dt, \quad (5-23)$$

where, $N(x, y, t)$ is the “**shifter noise**” the non-shifter induced spatial and temporal variations in the interference phase. Variations in the spatial domain are mostly due to sample displacements and/or as a result of off-axis illumination along the sample shape and orientation that produce a spatially varying angle $\theta_s(x, y)$ shown in Figure 5-10. The relation between this angle to the sensitivity vector and wavelength variations will be explained in Chapter 6 Section 6.2.1.

5.5 High-speed Phase Correlation Calibration (HPCC) method

In the previous Section, it was demonstrated how the temporal phase shifting process is affected by the spatiotemporal displacements of the sample such that the applied phase shift may completely differ from the shifted phase. To solve this problem we need to overcome two challenges:

- 1- Generate the desired temporal phase shift in presence of constructive or destructive phase shifts introduced by sample motions.
- 2- Measure the applied shift produced by all processes in the spatiotemporal hologram domain to select the appropriate phases.

The ideal case to overcome both of these challenges is to actively quantify the applied shift across the ramp for each point on the hologram and adjust the PZT positioner motions to account for motions of the sample. However, current technological limitations in high-

speed cameras does not allow live process of images. To solve this problem, an open loop temporal phase sampling method is presented that can resolve the problem of unknown applied shift using the same high-speed sensor without the need for any additional hardware (e.g., multiple photo detectors).

Current available methods to quantify the phase either reduce the spatial or temporal resolutions of high-speed cameras (Section 3.2.4). In this Section, a method is presented based on principles of correlation interferometry to determine the state of relative shifted phase. While this method passively determines the applied shift from calculations of the time-varying correlation between successive image frames, it is called High-speed Phase Correlation Calibration (HPCC). The results of this calibration is to detect the desired applied shift between any two desired frames without the loss of temporal resolutions of the high-speed camera.

Although this method has the capability to determine the interference phase (i.e., deformations of the sample), as it will be discussed later the requirements of this method are not fully satisfied for the transient response of TM. Therefore, in this Dissertation HPCC method is used as a complementary process for repeatability and accuracy of the HCI 2+N method and later the temporal phase sampling for the shape measurement method (i.e., multiple wavelength holographic interferometry 6).

To illustrate the performance of the HPCC method, two representative cases studies are presented that cover different applications. The implementations focus on high-resolution accuracy of the phase shift with pure temporal noise as well as reconstruction of the desired phase shifted hologram in the presence of spatiotemporal noises, that to the best of our

knowledge it was performed for the first time. Each case is evaluated by experiments under controlled conditions to demonstrate the capabilities of the proposed method.

5.5.1 HPCC mathematical background

By performing a continuous phase shift, with sufficient amplitude and speed we can guarantee the existence of a complete cycle of phase shift during the reference acquisition phase. This complete cycle is necessary for the open loop control mechanism of the HPCC method to provide the desired frame having the shifted phase.

The spatially varying intensity from two temporally phase shifted holograms (at t_0 and t_1) with a known phase shifter function $\delta(t)$ and unknown spatiotemporal shifter noise function $N(x, y, t)$ without removal of zero order terms are:

$$\begin{aligned} I(x, y, t_0) &= I_{DC} + I_m \cos[\delta(t_0) + N(x, y, t_0)], \\ I(x, y, t_1) &= I_{DC} + I_m \cos[\delta(t_1) + N(x, y, t_1)]. \end{aligned} \quad (5-24)$$

The correlation between two small regions of these holograms using Eqn. (5-5) is,

$$\rho(I(x, y, t_0), I(x, y, t_1)) = \frac{(1+r(x,y))^2 + 4r \cos(\Delta\phi(x,y,t_0,t_1))}{(1+r(x,y))^2 + 4r}, \quad (5-25)$$

where,

$$\Delta\phi(x, y, t_0, t_1) = \delta(t_1) - \delta(t_0) + N(x, y, t_1) - N(x, y, t_0), \quad (5-26)$$

The absolute value of the phase is not of interest; instead, we concentrate on the periodic nature of the phase shift, where the time t_0 is taken as the reference and $\Delta\phi$ is represented as,

$$\Delta\phi(x, y, t_0, t_1) = \delta(t_1) + N(x, y, t_1), \quad (5-27)$$

which is the relative phase shift at time t_1 with respect to the original phase at time t_0 .

5.5.2 HPCC quantitative phase measurements

Quantification of the applied shift $\Delta\phi$ from the correlation of Eqn. (5-25) requires,

- The knowledge of spatially varying beam intensity ratio $r(x, y)$
- Resolving the sign ambiguity problem of the even cosine function (i.e.,
 $\cos(-x) = \cos(x)$)

Based on sensitivity analysis of the zero order terms (Sections 5.3.1 and 5.3.2) we demonstrated that the main factor that spatially alter the correlation range is the beam intensity ratio $r(x, y)$. As it was stated previously in the correlation interferometry Section (Section 5.2), the effects of the intensity ratio r on the correlation is on its range of correlation values from $[-1, 1]$ to $[\rho_{min} - \epsilon, 1 - \epsilon]$. The exact estimation of ratio r from the holograms is not straight forward, due to its relation to the spatial variations in the superposition of real and complex parts in a two-beam speckle pattern that is affected by sensor noise. By temporal analysis of the complete cycles of shifted phase, it is possible to experimentally determine this range and scale the correlation output independent of zero-order terms removal or determination of the ratio $r(x, y)$. Specifically, the interference phase between any two frames at the desired location is determined by,

$$\cos(\Delta\phi(x, y, t_0, t_i)) = \left[\frac{\rho(I(x, y, t_0), I(x, y, t_i))}{a_2} - a_1 \right], \quad (5-28)$$

where a_1 and a_2 are two parameters that map the observed correlation range of $[\rho_{min} - \epsilon, 1 - \epsilon]$ to $[-1, 1]$ without the need for DC compensation. To describe the temporal variations of the correlation a new parameter is introduced,

$$\begin{aligned}
P(x, y, t_0, t_k) = \{ & \rho(I(x, y, t_0), I(x, y, t_i)), i = 1, 2, \dots, k \} = \\
& (\rho(I(x, y, t_0), I(x, y, t_1)), \rho(I(x, y, t_0), I(x, y, t_2)), \dots, \\
& \rho(I(x, y, t_0), I(x, y, t_k))) ,
\end{aligned} \tag{5-29}$$

where, P is a set we call “*correlation signal*”, derived from consecutive correlation measurements between a desired reference frame at t_0 (usually before the measurements) and the rest of the reference frames. From such a set a_1 and a_2 can be defined as,

$$\begin{aligned}
a_1 &= \frac{1}{2} [\max(P) - \min(P)] = \frac{1}{2} \left[1 - \left[\frac{1-r}{1+r} \right]^2 \right] = \frac{2r}{(1+r)^2} \\
a_2 &= \max(P - a_1) \\
P_{SC}(x, y, t_0, t_k) &= a_2^{-1} (\rho(I(x, y, t_0), I(x, y, t_k)) - a_1)
\end{aligned} \tag{5-30}$$

where, \min and \max are functions to determine global minimum and maximum values of P and P_{SC} is the scaled correlation signal. This process is shown schematically in Figure 5-12.

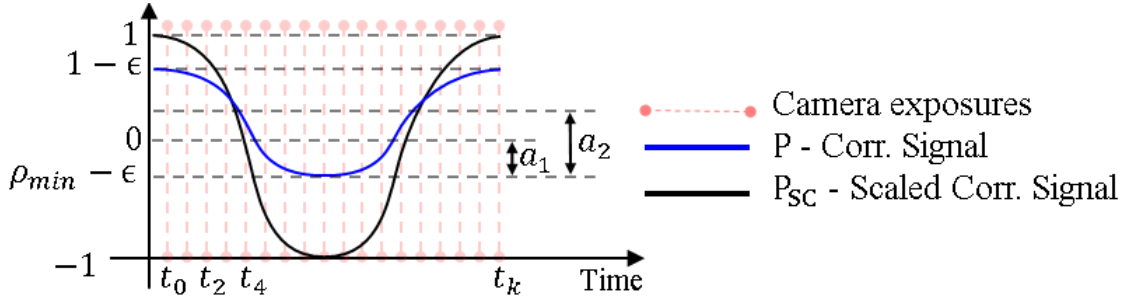


Figure 5-12 Schematic representation of the HPCC method initial steps. Red dashed lines represent the schematic timing of the center of repeated camera exposures, P refers to $P(x, y, t_0, t_k)$ with the range $[1 - \epsilon, \rho_{min} - \epsilon]$ as described in Eqn. (5-29), and P_{SC} is the scaled signal with the range $[-1, 1]$.

To resolve the sign ambiguity problem: If the high-speed hologram exposures (i.e., τ) are small compared to the period of the correlation signal produced by the shifted phase, the temporal phase increments between two consecutive holograms are always smaller than π

(see Figure 5-12 red dashed lines with respect to P.) Therefore, the sign ambiguity is resolved by temporal scanning of the holograms using the signal P while making sure that there are no rapid phase variations larger than π .

5.5.3 Automated phase detection algorithm

In the next step, we describe an automated phase detection algorithms that identifies the specific temporal frames corresponding to the applied phase shift of interest (i.e., $P_{sc} = [1, 0, -1, 0]$ equivalent to $\Delta\phi = [0, \frac{\pi}{2}, \pi, 3\pi/2, 2\pi]$ respectively) without the use of inverse trigonometric functions. To distinguish between the cycles and to remove the sign ambiguity, the algorithm scans the sign of the P_{sc} signal to detect the locations where the sign changes. For example, the difference between ($P_{sc} = 0$) $\rightarrow \pi/2$ compared to ($P_{sc} = 0$) $\rightarrow 3\pi/2$ is the sign becoming negative or becoming positive, respectively. It should be noted that if the sample is stable and the positioner acts linearly, a continuous phase shift using a ramp, generates a sinusoidal correlation signal P_{sc} of a frequency determined by the velocity of the phase shifter in wavelengths per second. However, in practice, due to the effects of noises that contribute to the detected signal, the phase correlation signal may not be sinusoidal (see Figure 5-19 later in Section 5.5.6). Therefore, in the design of the current phase detection algorithm the use of curve fitting or estimation of a single frequency for detection of the desired applied shift was put aside.

5.5.4 HPCC Requirements

Since this method determines the applied shift without direct measurements of zero order terms, and without the need for multiple phase shifting repetitions, it is highly suitable for

any holographic interferometry applications. The method is highly robust as long as the following criteria are met:

1. Acquisition frequency must be sufficiently larger than the frequency of the scaled correlation signal in order to detect the sign and global extrema of the signal without uncertainties (i.e., >8 frames per cycle).
2. The amplitude of the phase shift should be sufficiently large to generate at least one complete cycle of shifted phase. This is to ensure the algorithm can determine the global minima for its calculations as well as accurate estimation of zero-order terms.
3. Kernel size must be sufficiently large to remove the spatial speckle and sensor noise effects in determination of the shifted phase.

As stated before, although it is possible to use the HPCC method for quantification of displacements without the need for phase shifting or DC removal, current measuring temporal resolution is not yet sufficient to observe the entire TM transient response without $> \pi/2$ temporal jumps. The HPCC method is to provide the information regarding the state of the phase shifted reference in the 2+N HCI algorithm (Section 5.2.3) as well as high-speed shape measurements method (Chapter 6 Section 6.2.1).

The following two Sections present two cases where this method can be used. These two cases depict the results of using this method for improved accuracy and precision of HCI methods for displacement measurement applications. The application of this method for shape measurements is demonstrated in the next Chapter after proper explanations of the basics of multiple wavelengths holographic interferometry.

5.5.5 Case 1 – high-speed continuous phase sampling in presence of temporal noises ($N(t)$) and phase shifter nonlinearities ($\delta(t)$).

For the measurements of TM motions performed on post-mortem samples in a quiet and stable environment, nonlinearities of the PZT actuator, together with vibrations in the setup, camera, and sample can cause temporal variations of the optical path length during temporal phase shifting. With minimal spatial variations of the optical path length, it can be assumed that the entire hologram has a single applied shift for each timing t (e.g., in Eqn. (5-23), $\delta(t) + N(t) = const.$) In this Case, the averaged correlation signal is determined by,

$$\bar{P}(x, y, t_0, t_k) = \frac{1}{n^2} \sum_{x=1}^n \sum_{y=1}^n \rho(I(x, y, t_0), I(x, y, t_i)), \quad i = 1, 2, \dots \quad (5-31)$$

To enhance the resolution and precision of the 2+N method, the step of the phase shift is replaced by a continuous linear ramp as shown in Figure 5-13. The measurement sequence start by acquiring 200 reference frames during the continuous phase ramp. The growth rate and amplitude of the ramp is adjusted to ensure the existence of at least one complete cycle of applied shift in the presence of noises. In case of noisy environment, usually >1.5 cycles is acquired to account for constructive/destructive effects of the noise.

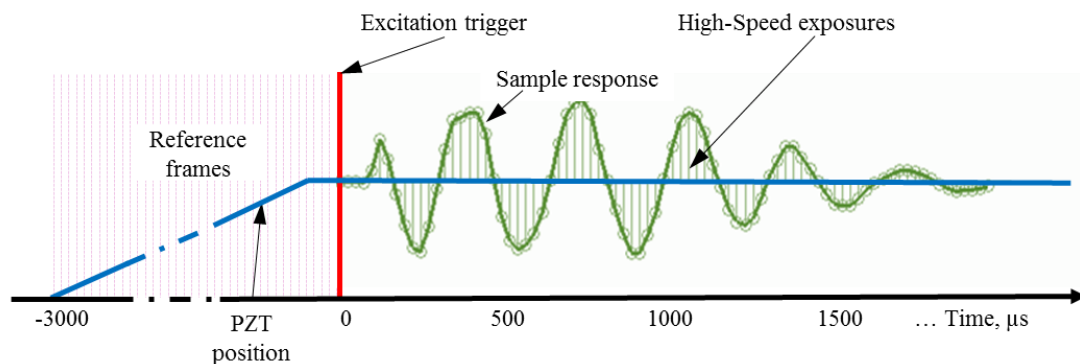


Figure 5-13 Representation of the 2+N HCI measurements timeline using a continuous ramp. The high-speed exposures run continuously for the entire measurements while reference frames measurements, excitation, and transient response measurements are synchronized with the camera.

A flat latex membrane was used as a sample while all the environmental conditions were controlled to have minimal effects on the sample motion. The measurements were performed with a frame rate of 67.2 thousand frames per second. A set of reference holograms are first acquired during a linear continuous ramp with a duration of 3ms and an amplitude sufficiently large to generate slightly larger than one complete cycle (slightly larger than 2λ at 532nm). In the next step, the sample is excited by a short acoustic click (50 μ s square pulse) that elicits a series of deformed holograms corresponding to the motions of the excited sample. The deformed frames are captured while the PZT phase shifter is fixed at the maximum position of the ramp.

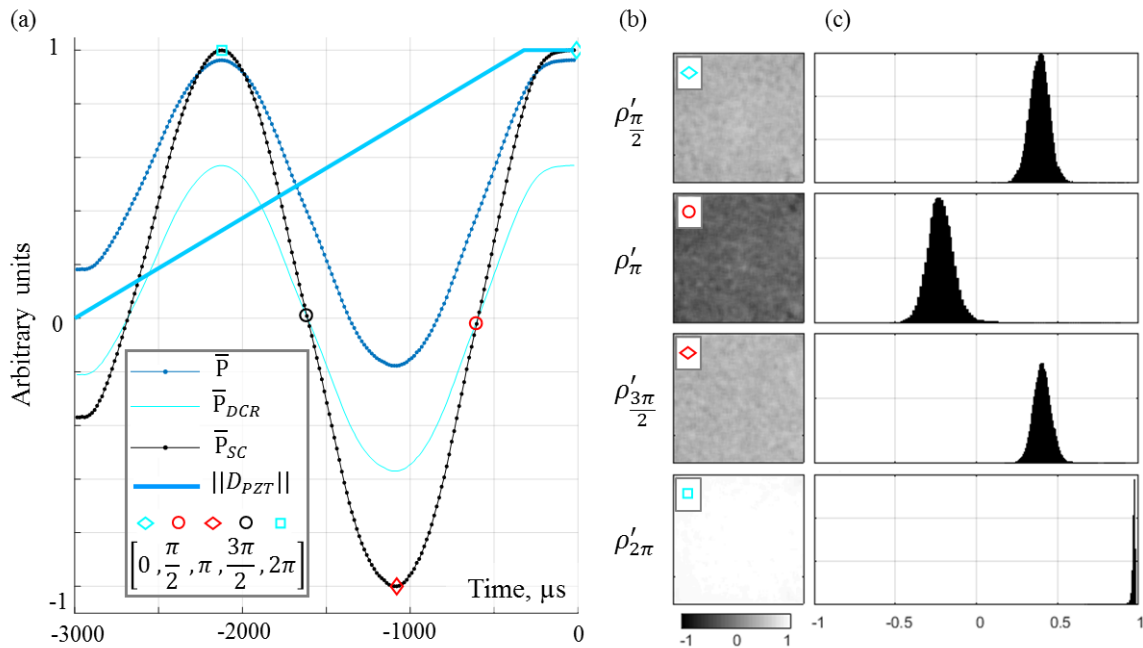


Figure 5-14 Results of HPCC method in determination of applied shift along a 2.8 msec continuous phase shift with about 1064 μ m displacements on a flat latex membrane: (a) the scan results of the correlation between the first and successive holograms averaged over all kernels over the spatial domain before and after automated corrections together with the normalized PZT input voltage. The location of the best frames determined by the algorithm are shown with colored shapes corresponding to $[0, \pi/2, \pi, 3\pi/2, 2\pi]$ shifted phase, P, P_{SC} are defined as in Figure 5-12 and $P_{DRC} = P - a_1$; (b) the correlation images before averaging for the chosen temporal instances and (c) histogram of each of the correlation images in panel (b) showing mostly normal distribution.

The results of scanning the set of reference holograms taken during the ramp with the HPCC method are shown in Figure 5-14-a. The normalized voltage input to the piezo phase shifter is shown by a thick blue line. The ramp input to the piezo starts at $t=-3000 \mu\text{s}$, and has a duration of $\sim 2.8 \text{ msec}$. The excitation is triggered 3 msec after the initiation of the piezo motions to ensure the piezo reaches its stable position. The dark blue dotted line shows the measured correlation signal by averaging over the signals P acquired from the entire surface of each hologram where each dot represents a new correlation value.

To ensure the HPCC algorithm determines the applied shift relative to the set of deformed frames, the calculation is performed backwards in time (i.e., $\bar{P}(x, y, t_0, t_{-3000 \mu\text{s}})$). The black dotted line shows the scaled symmetric applied shift with the range of $[-1,1]$. Feeding the scaled correlation signal to the automated phase detection algorithm, the best frames corresponding to repeated $\pi/2$ phase shift intervals are determined. These frames are shown by \diamond \circ \diamond \circ \square in Figure 5-14-a. Spatial distributions of the unscaled correlation of each hologram at the four selected phases are shown in Figure 5-14-b. The background intensity turns to near gray at $\pi/2$ and $3\pi/2$, while it turns to a darker gray corresponding to $\rho \cong \rho_{min} - \epsilon$ at π , as well as nearly white at 2π corresponding to $\rho \cong 1 - \epsilon$. Since the correlation images of Figure 5-14-b are obtained without the DC removal of the holograms, the resultant correlation patterns show a minimum value corresponding to spatial distribution of ρ_{min} across the holograms. Histograms of the value of the raw correlation values over the surface of each image in Figure 5-14-c show Gaussian distribution of the correlation at a constant value illustrating that the holograms have a spatially uniform applied shift consistent with minimal spatial noises.

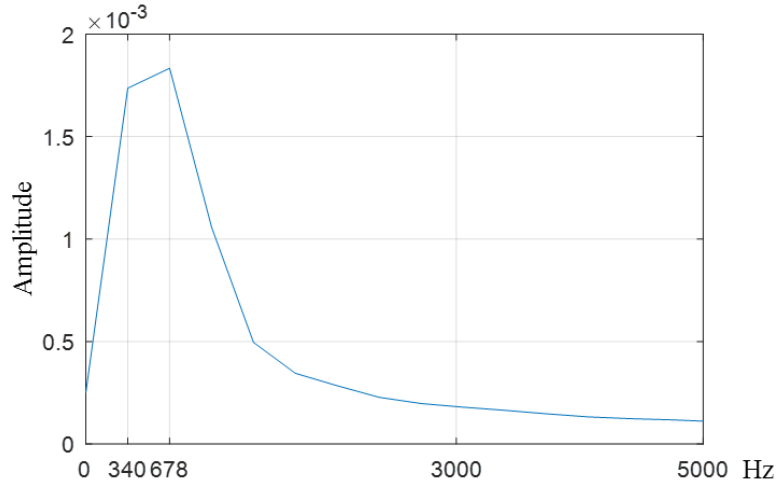


Figure 5-15 Applied shift signal \bar{P}_{SC} in the frequency domain.

Analysis of the \bar{P}_{SC} signal in the frequency domain (Figure 5-15) shows a peak centered at 550 Hz (a period of ~ 1.82 msec) with Full Width at Half Maximum (FWHM) of about 1 kHz that demonstrates the detected signal is not completely described by a sinusoid. This suggests the existence of acceleration/deceleration or nonlinear behavior of the PZT positioner across the ramp (Figure 5-14-a). Analysis of the time domain signal also shows ~ 100 μ s delay in the initiation of the applied shift as well as the settling compared to the input signal to the PZT positioner.

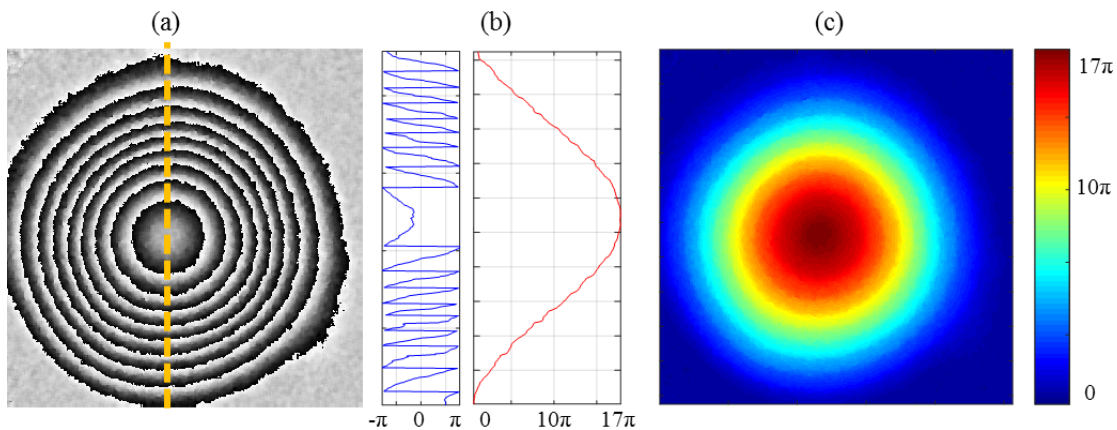


Figure 5-16 Representative results of application of HPCC algorithm on the 2+N HCI method: (a) wrapped phase; (b) wrapped and unwrapped phase of the line shown in (a); and (c) unwrapped phase.

Figure 5-16 shows the results of the measured modulo 2π phase map using the HPHC algorithm. The blue diamond and red circle frames (Figure 5-14) were chosen as the reference while a deformed frame at a time point of near maximal displacement ($t=255 \mu\text{s}$) was selected as the deformed frame.

5.5.6 Case 2 – High-speed phase sampling in presence of spatiotemporal motions

In-vivo measurements of TM motions are accompanied by sub-millimeter scale physiological motions due to heartbeat, respiration etc. These motions may be a combination of rotation and translation with respect to the measuring coordinate system, and generate spatially varied phase shifts during the phase sampling period. Furthermore, airborne noise may acoustically excite the membrane during the phase sampling procedure, contributing to the uncontrolled spatiotemporal motions. The superposition of such artifactual motions and the shifter induced temporal nonlinearities of Case 1 results in spatiotemporally varied noise during the phase shifting procedure (i.e., $N = N(x, y, t)$ in Eqn. (5-23)).

Because of spatial variations in the imposed phase shift produced by the addition of spatially varying artifactual noise and motions, the holograms does not have a spatially uniform applied shift and, the approach of Case 1 in averaging over the entire hologram, using Eqn. (5-31), results in erroneous detection of the applied shift. The effects of such noise on the performance of the HPCC method are shown later in Figure 5-19-b. Furthermore, the use of such spatially non-uniform phase shifted holograms, as a reference frame, in the $2+N$ HCI method results in spatially corrupted phase as well as large unwrapping errors (Figure 5-22-a -b -c Section 5.5.6). Prior to the method proposed in this

Section, it was recommended to use parallel phase shifting (Kakue et al., 2011) or carrier frequency (Takeda et al., 1982) methods rather than temporal phase shift to remove the temporal dependency of phase sampling (For more explanation see Appendix A). However, these methods greatly reduce the spatial resolution of the high-speed cameras, which is inconsistent with the requirement of full-resolution high-speed digital holography.

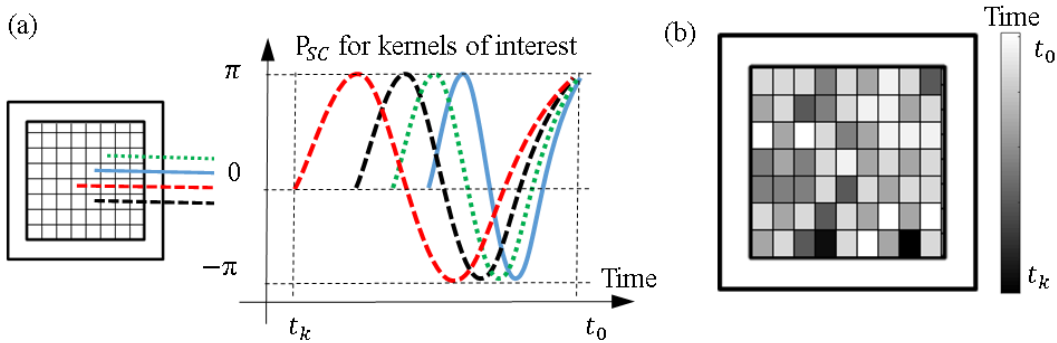


Figure 5-17 Schematic representation of the effects of HPCC method application in Case 2: (a) schematic representation of differences in determined phase shift at different locations on the sample; and (b) a schematic map of spatially varied timings that yield a single uniform shifted phase. The schematic view does not represent the sensor resolution (e.g., 512×512).

As shown schematically in Figure 5-17-a, if the correlation signal of a smaller region is used (a pixel or a neighborhood of pixel sufficiently small compared to the fringes induced by the noise) the applied phase shift during the ramp can be determined without the effects of the noises. In a smaller region, the spatial variations of the applied shift due to spatiotemporal motions of the sample alter the frequency of the P_{sc} signal. Using the HPCC method applied to each pixel, a map of the best frames corresponding to the phase shift of interest is detected (e.g., $\frac{\pi}{2}$). As shown schematically in Figure 5-17-b (and later in Figure 5-20 for actual measurements), this map has the information of the frames that each point on the hologram reaches the desired phase shift.

In the next step, using the map of each desired shifted phase, the speckle patterns from different timings are used to form a reconstructed reference hologram (see Figure 5-21). The reconstructed reference hologram has a uniform single angle phase shift compared to the desired reference hologram (i.e., t_0), eliminating the effects of the spatiotemporal phase shifts due to the noises.

To demonstrate this method, we performed the following experiment: The measurements were performed on a flat latex membrane similar to Case 1 with the difference of an extra 2 kHz steady state acoustic excitation. The steady state tone is generated using a second speaker to produce a noise that is interfering with the transient induced response over the entire length of the experiment. The additional steady state excitation ensures the sample is always moving spatiotemporally during the reference acquisition period to mimic in-vivo physiological motions. Figure 5-18 shows the acoustic sound pressure signal in time and frequency domains illustrating the presence of a continuous low level tone on top of the broadband acoustic click (Figure 5-18-a), which produces a narrow-band peak at 2 kHz in the averaged spectrum (Figure 5-18-b).

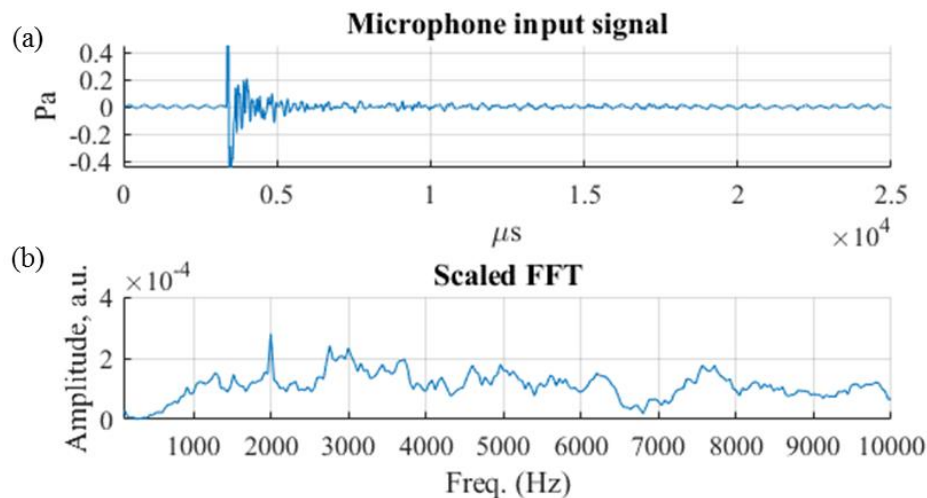


Figure 5-18 Steady state and transient acoustic excitation: (a) time domain; and (b) frequency domain. The frequency spectrum shows a sharp peak at 2 kHz.

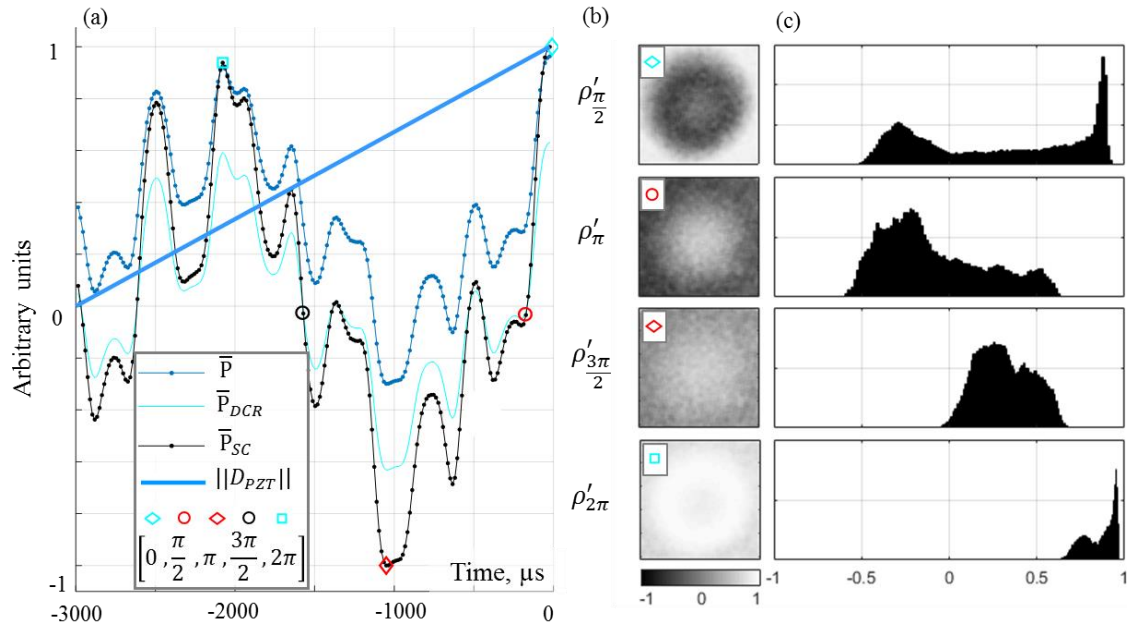


Figure 5-19 Representative results showing the existence of a spatially varying phase shift during the ramp: (a) average correlation over all pixels in each image; (b) spatial distribution of the unscaled correlation maps showing patterns of sample displacements; and (c) histogram of each image showing non-Gaussian distribution (see similar graph of Case 1 in Figure 5-14).

To illustrate the problem of using a single temporal hologram as a calibration reference, without compensating for spatial variations in the calibration phase, the same spatial averaging technique of Case 1 was used to generate the results shown in Figure 5-19. Spatial variations of the applied shift across the selected reference frames are evident in Figure 5-19-b, which shows the unscaled correlation maps between the reference frame at time zero (blue diamond frame) and the frames picked by the algorithm. Figure 5-19-c shows the histograms of the same correlation maps. Due to the spatiotemporal motions, they do not have the Gaussian distribution of the correlation patterns of Figure 5-14.

Applying the HPCC method independently to all pixels with kernel size of 5 pixels and applying the automated phase determination algorithm, the frames corresponding to $\pi/2$ phase shift at each pixel were detected as shown in Figure 5-20 to be used for the 2+N HCI method.

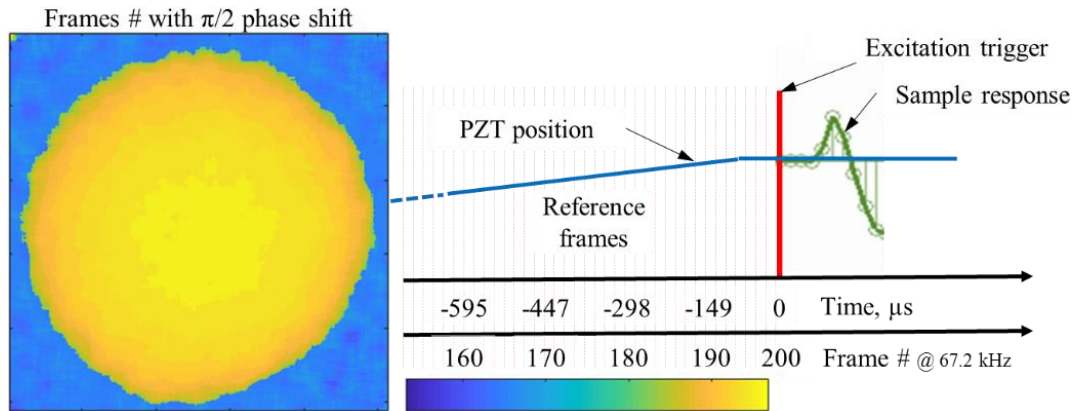


Figure 5-20 Results of spatial calibration of the set of references for $\pi/2$ phase shift. The timing diagram of the events is shown schematically with the frames numbering as well as their location on the ramp.

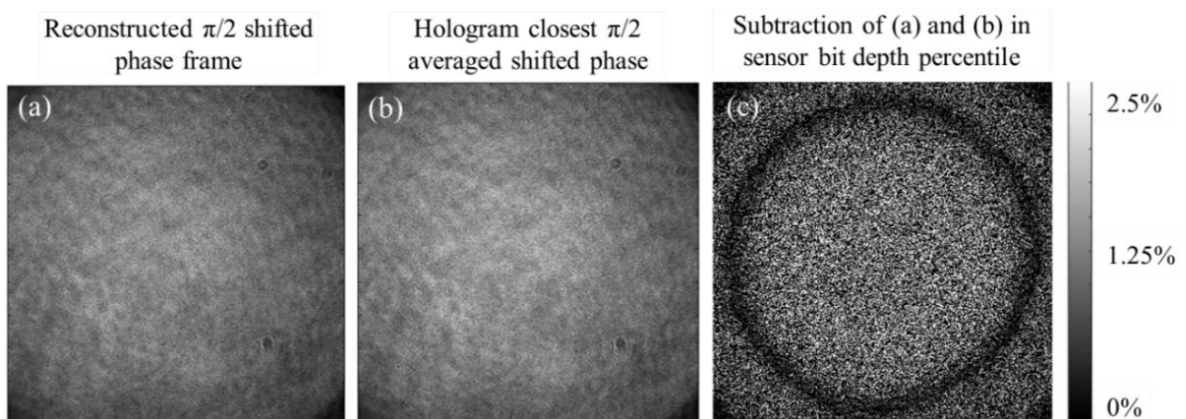


Figure 5-21 Comparison of the results of temporal reference speckle pattern reconstruction: (a) speckle pattern reconstructed with $\pi/2$ applied shift compared to $t=0$ hologram; (b) intact speckle pattern from the hologram that has the closest averaged value to $\pi/2$ phase shift; and (c) subtraction of (a) and (b) speckle patterns shown in percentile of the sensor depth (i.e., 2.5% of 2^{12} is 100).

Using the information from the frames map of Figure 5-20, where each pixel describes the frame number where the applied shift is $\pi/2$ relative to the desired reference frame (i.e., frame 200), we can reconstruct a new $\pi/2$ reference 'frame' in which the intensity of each pixel equals that of the corresponding pixel determined by the map of Figure 5-20. Figure 5-21 shows the comparison between such reconstructed $\pi/2$ phase shifted reference speckle pattern and the speckle pattern from a single temporal instance that has an average shifted angle closest to a $\pi/2$ phase shift (red circle in Figure 5-19). Figure 5-21-c shows the

difference in intensity between the two holograms with a maximum differences as small as 2.5% of the hologram bit depth¹ (i.e., 2^{12} for Photron SA-Z).

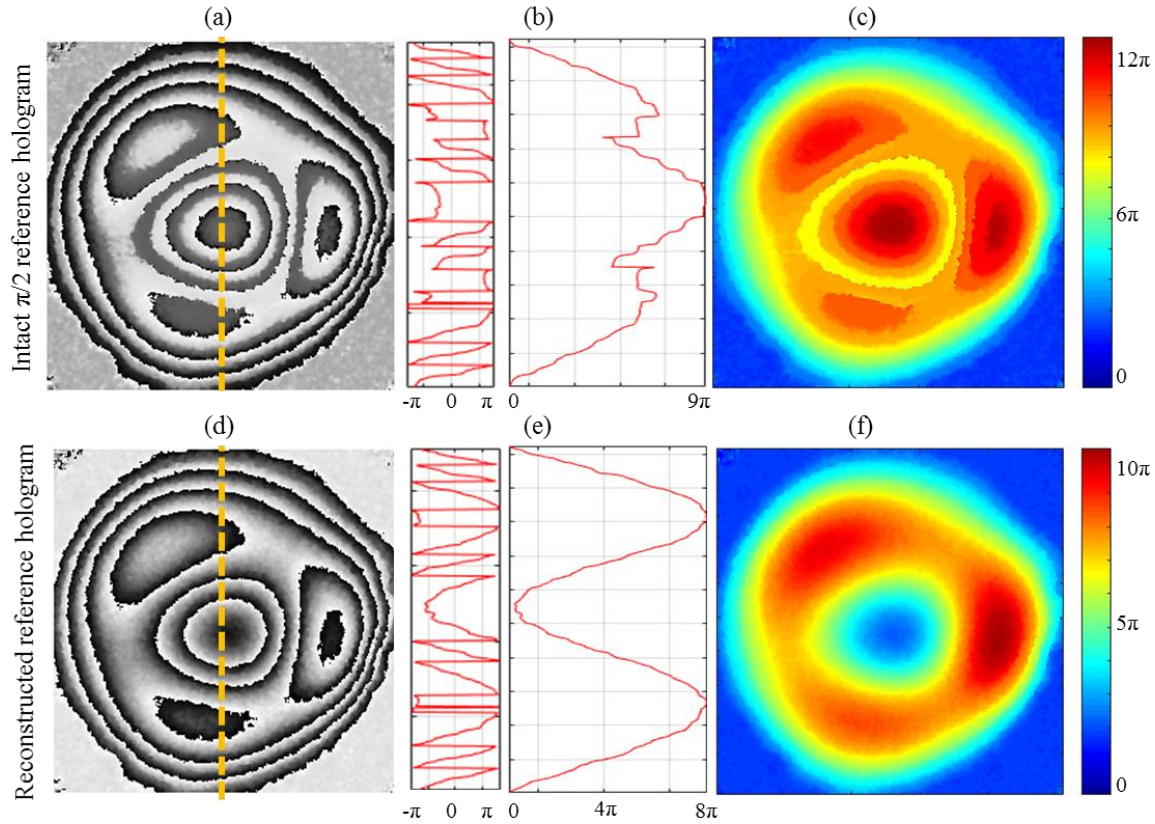


Figure 5-22 Comparison of the results of quantitative phase measurements using 2+1 HCI method for (a-c) with intact $\pi/2$ phase shifted reference hologram, and (d-e) with reconstructed reference frame using the HPCC method at each pixel: (a, d) wrapped phase; (b, e) wrapped and unwrapped phase plots along the lines shown in panel (a, d); and (c, f) unwrapped phase maps of each Case.

In the next step, using the 2+1 HCI method with the reconstructed reference frame and the reference frame at $t=0$ together with an arbitrary deformed frame at the timing of about 1 msec after excitation, the interference phase was measured. Figure 5-22 shows the wrapped modulo 2π phase map as well as the corresponding unwrapped maps obtained

¹ Bit depth, is the number of bits used to indicate the color of a single pixel.

from the 2+1 HCI using the reconstructed reference and best average reference holograms. Comparing the wrapped phase of the two cases, the central regions in Figure 5-22-a show significantly lower phase contrast compared to its peripheral regions, while in Figure 5-22-d the phase contrast is relatively constant across the image. The variation in phase contrast in Figure 5-22-a generates significant unwrapping errors as shown in Figure 5-22-b and Figure 5-22-c. The high-contrast wrapped phase image of Figure 23-d allows error-free phase unwrapping, as shown in Figure 5-22- e and Figure 5-22-f.

These results show the superiority of the proposed method, compared to the other holographic methods with significant spatial resolution reduction, for quantitative phase measurements in the presence of steady state spatiotemporal noises using the cost effective and non-complex temporal phase shifting procedure. The effects of such noises were nearly completely removed by reconstruction of the single $\pi/2$ phase shifted reference hologram. Results show highly repeatable phase quality across all the deformed holograms after replacing the $\pi/2$ phase shifted reference hologram with the reconstructed one. Temporal reference reconstruction enables transient measurements in the presence of large continuous spatiotemporal noises. Spatial calibration of the speckle pattern using the HPCC method, relaxes most of the requirements of the temporal phase shifting such as highly controlled environmental conditions, as well as sample/setup stability. This method can also be used for double exposure shape and displacements measurement methods by reconstructing four reference and deformed holograms to be used for multiple wavelengths holographic interferometry.

6 High-speed holographic shape measurements

Holographic measurements of Tympanic Membrane (TM, eardrum) motion and shape at the confined location of the ear canal require at least a centimeter square field of view and half a centimeter depth of field to observe the nanometer scale acoustically induced displacements. Furthermore, to observe the TM inside the ear canal, an endoscopic configuration to illuminate and observe the TM from about a centimeter working distance is needed. This short distance does not allow for beam collimation resulting in elliptical rather than planar wavefronts. As a result, the resultant holograms will have spatially varying sensitivity vectors that unless compensated for, can result in large errors (>50%) in determination of the absolute value of the displacements.

Determination of the spatially varying sensitivity vector requires knowledge of TM shape and orientation along with well-defined setup geometries such as illumination/observation coordinates. In this section, the development of a High-speed Digital Holographic Shape measurement method are presented, which can determine the shape and orientation of the TM just prior to displacements measurements. A flat surface calibration technique is proposed that enables the detection of the shape of the wavefront as well as the angle of the sensitivity vector with respect to the camera axis. In the next Chapter, we apply our High Speed methods of shape and motion measurements to provide accurate determination of the true surface normal displacements on a tympanic membrane.

The design and implementation of the shape measurements system is performed by taking into account the following functional requirements on the surface of a tympanic membrane:

1. The small ($<1 \text{ cm}^3$) triangulation volume inside the ear canal,

2. The imaging optics of the High-speed Digital Holographic (HDH) displacement measurements system,
3. the need to adjust shape resolution to account for different TM depths and angles of observation,
4. Short intervals (<200 msec) between shape and displacements measurements,
5. High-speed shape measurements to minimize the effects of in-vivo physiological motions and to maintain the shape coordinate system for the displacement measurements.

Meeting these functional requirements in one method is not a trivial task. Many of the methods that have been previously applied to TM shape measurements are not suitable. For example, structured light projection (Dirckx & Decraemer, 1997; Van der Jeught & Dirckx, 2017) requires large triangulation angles compared to the ear canal's confined volume and projection of a pattern, while others that are capable of single shot in-vivo endoscopic measurements (Bedard et al., 2017) require high-resolution sensors (>10 Megapixels) and specialized optics that are incompatible with the HDH system. Multiple-Wavelength Holographic Interferometry (MWHI) is capable of providing the shape under small triangulation volumes (Khaleghi, 2015; Khaleghi et al., 2016; Lu, 2012; Rosowski et al., 2013), and like HDH is based on holography, which minimizes necessary hardware modifications. The main drawback of MWHI is its nanometer scale sensitivity to sample vibrations in order to measure sub-millimeter scale resolution shape. MWHI can provide varying shape resolution, but this is achieved either by repeated lengthy (> seconds) laser tunes, or multiple lasers that complicate the system optics and geometry. MWHI

endoscopic shape measurements would also suffer from any near-field elliptical distortions and require compensatory calibration for these effects.

In this Chapter, a high-speed MWHI system that can satisfy the five functional requirements is described, and a practical calibration method to remove the elliptical wavefront distortions to enable endoscopic MWHI shape measurements.

6.1 Multiple Wavelengths Holographic Interferometry (MWHI)

The interference pattern of two linearly polarized wavefronts (i.e., object and reference) with the same wavelength but different propagation directions (i.e., wave vector) in the complex form is described by,

$$E_r(\mathbf{r}, t) = A_r e^{i(\omega t - \mathbf{k}_r \cdot \mathbf{r} - \phi_r)}, \quad (6-1)$$

$$E_o(\mathbf{r}, t) = A_o e^{i(\omega t - \mathbf{k}_o \cdot \mathbf{r} - \phi_o)}, \quad (6-2)$$

where, A_o and A_r are the wavefront amplitudes, \mathbf{k} is the wave vector (i.e., $\mathbf{k} = (\mathbf{k}_x, \mathbf{k}_y, \mathbf{k}_z)$, $|\mathbf{k}| = 2\pi/\lambda$), \mathbf{r} is the space vector describing the point of interest with respect to the observation coordinate system, and ϕ_r and ϕ_o are the phases of each wavefront. The superposition of these two wavefronts forms a holographic interference pattern with a spatially varying intensity that can be acquired by a CCD. In this Chapter the 3D global coordinate system uses the x, y, z letters (i.e., a Cartesian reference frame) while the local coordinate system of the holograms use u, v letters (in other Chapters only (x, y) coordinates are used since local and global coordinates were linearly related). The intensity is described by,

$$\begin{aligned}
I(u, v, t) &= |E_r(u, v, t) + E_o(u, v)|^2 \\
&= (E_r(u, v, t) + E_o(u, v))(E_r(u, v, t) + E_o(u, v))^*, \\
&= I_r + I_o + 2\sqrt{I_r I_o} \cos(\mathbf{K} \cdot \mathbf{r} + \phi),
\end{aligned} \tag{6-3}$$

where * denotes the complex conjugate, $\phi = \phi_r - \phi_o$ is the phase difference between the two beams, $I_r = A_r^2$, $I_o = A_o^2$, the intensities of the two beams, and $\mathbf{K} = \mathbf{k}_r - \mathbf{k}_o$. Since Eqn. (6-3) depends on \mathbf{K} , any change in the wavelength can alter the phase difference. Combinations of the interference patterns produced by two slightly different wavelengths produces intensity contours that describe the shape of the sample.

The holograms measured before and after variations in the wavelength while other conditions of the sample and setup are steady are described by,

$$\begin{aligned}
I_j(u, v, \lambda_0) &= I_r + I_o + 2\sqrt{I_r I_o} \cos(\phi + \delta(j)) \\
I_j(u, v, \lambda_i) &= I_r + I_o + 2\sqrt{I_r I_o} \cos(\phi + \Delta\gamma_i(u, v) + \delta(j)),
\end{aligned} \tag{6-4}$$

where, u, v are the coordinates of the point of interest on the hologram, λ_0 is the initial wavelength, λ_i is a set of discrete secondary wavelengths of interest, and $\Delta\gamma_i$ is the interference phase as a result of desired variations of the wavelength. Small wavelength induced variations of I_r and I_o intensities change the zero order terms at each wavelength. While the phase recovery method (i.e., using Eqn. (6-5)) automatically removes the zero order terms for each wavelength these parts of the intensity variations effects on the interference phase are negligible.

The term $\delta(j)$ is a set of n discrete phase shifts (i.e., $\delta(j) = 0, \frac{\pi}{2}, \dots, \frac{n\pi j}{2}$) with respect to each wavelength to quantify the interference phase $\Delta\gamma_i$. For simplicity the sub index of $\Delta\gamma_i$ represent the value of the second wavelength (i.e., $\Delta\gamma_i(u, v) = \Delta\gamma(u, v, \lambda_i)$ with

respect to λ_0). For example, if four phase shifted frames are used (i.e., $j = 1, \dots, 4$ in Eqn. (6-4)) at each wavelength, for any two desired wavelengths there are at least 8 phase shifted holograms that can provide the interference phase by,

$$\Delta\gamma_i(u, v) = \tan^{-1} \left[\frac{(I_3(\lambda_0) - I_1(\lambda_0))(I_4(\lambda_i) - I_2(\lambda_i)) - (I_4(\lambda_0) - I_2(\lambda_0))(I_3(\lambda_i) - I_1(\lambda_i))}{(I_3(\lambda_0) - I_1(\lambda_0))(I_3(\lambda_i) - I_1(\lambda_i)) - (I_4(\lambda_0) - I_2(\lambda_0))(I_4(\lambda_i) - I_2(\lambda_i))} \right], \quad (6-5)$$

where (u, v) arguments of each intensity are not shown for clarity (Furlong & Pryputniewicz, 2000).

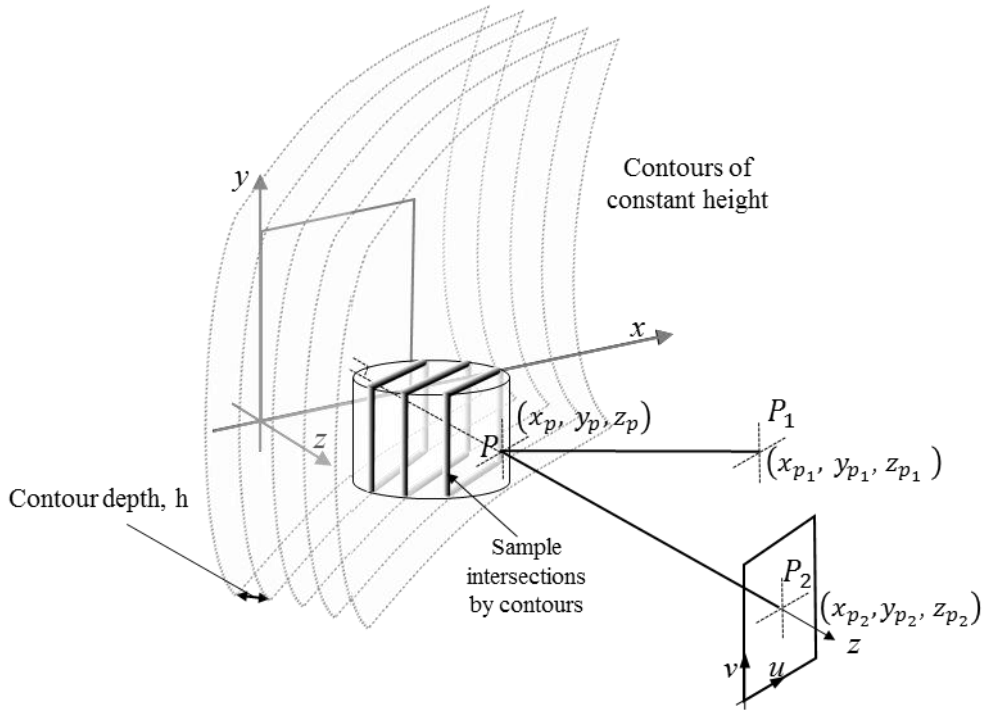


Figure 6-1 Three-dimensional geometrical representation of the two-wavelength optical setup. P_1 is the point of illumination, P_2 is the point of observation, P is an arbitrary point on the surface under investigation. Elliptical contours due to superposition of the two wavelength interferograms are shown that are intersecting the sample with contours of constant height.

Measurements of shape in the MWHI method require additional efforts and the phase does not guarantee the shape. Furlong et al. described the shape with respect to the constant

Optical Path Length (OPL), as shown in Figure 6-1, and described it in a Cartesian coordinate system as (Furlong & Pryputniewicz, 2000),

$$OPL = \sqrt{(x_p - x_{p_1})^2 + (y_p - y_{p_1})^2 + (z_p - z_{p_1})^2} - z_p, \quad (6-6)$$

where $x_{p_1}, y_{p_1}, z_{p_1}$ are the coordinates of the point of illumination P_1 , x_p, y_p, z_p represent an arbitrary point P on the sample, and $x_{p_2}, y_{p_2}, z_{p_2}$ represent the coordinates of point P_2 of the observation point at the CCD of the camera.

As shown schematically in Figure 6-1 planes of constant OPL intersect the sample shape as contours of constant height. This intersection is embedded in the interference phase $\Delta\gamma$ as (Furlong & Pryputniewicz, 2000),

$$\Delta\gamma_i(u, v) = \frac{2\pi}{\lambda_0} OPL - \frac{2\pi}{\lambda_i} OPL = \frac{2\pi}{\Lambda_i} OPL, \quad (6-7)$$

where, Λ is the synthetic wavelength or equivalent wavelength described as the beating frequency between the two wavelengths of the tune (Kreis, 2006; Ulf Schnars et al., 2015; Vest, 1979),

$$\Lambda_i = \frac{\lambda_0 \lambda_i}{|\lambda_i - \lambda_0|}. \quad (6-8)$$

The interference phase is measured using Eqn. (6-5) but the relation between the shape of the sample to the OPL require more information. Using a custom holographic camera calibration, the transformation required to describe the shape using the coordinates of the setup is possible. To ensure the shape is measured with respect to a flat plane (the (x, y) plane shown in Figure 6-1), telecentric lenses with negligible aberrations and collimated wavefronts are used (Furlong & Pryputniewicz, 2000). Combination of Eqn. (6-6), Eqn. (6-7), and Eqn. (6-8) results in,

$$z_p = \frac{[(x_p - x_{p_1})^2 + (y_p - y_{p_1})^2 + z_{p_1}^2 - (\Delta\gamma \frac{\Lambda}{2\pi} - z_{p_2})^2]}{2[z_{p_1} + (\Delta\gamma \frac{\Lambda}{2\pi} - z_{p_2})]}. \quad (6-9)$$

The holographic calibration provide the necessary unknowns of the right hand side of Eqn. (6-9) to determine the absolute shape along the z axis.

6.1.1 MWHI in the presence of wavefront and optical distortions

TM shape measurements from a close distance using an endoscopic configuration are accompanied by,

- Radial distortions,
- Wavefront elliptical or semi-elliptical distortions.

Because of these defects, the interference phase undergoes two transformations that depend on wavelength, setup geometries, and sample location. As a result of these transformations, the measurements are performed compared to a non-flat plane in a non-orthogonal coordinate system. One nonlinear transformations is due to elliptical wavefronts while the other is due to radial optics (i.e., endoscopic configuration) distortions. A change in the wavelength, setup geometries, optical configuration, and/or sample location will change the superposition of the two transformations making it hard to determine the shape information.

Kandulla et al. used numerical reconstruction of the elliptical wavefronts combined with conventional camera calibration methods to determine each of the two transformations independently (Kandulla et al., 2004). Then the numerically and experimentally measured modulo 2π phases of the reconstructed wavefronts were subtracted to remove the effects of nonlinear transformations from the interference phase $\Delta\gamma$. The numerical reconstruction is performed based on known sample distance and the assumption of elliptical wavefronts.

However, there are challenges in the application of such numerical reconstruction in the real world due to the following factors:

- 1 Accurate estimation of the sample distance is not always possible from the measured holograms. Specifically using an endoscope with large depth of field compared to the field of view, this problem may lead to uncertainties in the numerical estimations of the elliptical wavefront,
- 2 Due to the requirements of high-power illuminations in high-speed holographic shape and displacement measurements, it is not always possible to illuminate the sample with a fiber. In this case, the beam expansion may not follow the ideal case of a spherical wavefront due to the aberrations in the expansion lens. Numerical reconstructions of the holograms require accurate knowledge of the lens transfer function, which adds to the complications of this method.

6.1.2 Holographic flat surface calibration

As stated before, the calibration of the endoscopic MWHI measured shape depends on two independent transformations due to wavefront and optical distortions. In this Section, an experimental technique that compensates for elliptical wavefront distortions without the need for computer reconstruction of holograms is presented. The method relies on MWHI measurements of the wavefront at each wavelength compared to a flat surface held at a known distance (Bergström et al., 2011; Liu-Sheng & Sridhar, 1996; Thalmann & Dandliker, 1985).

As shown in Figure 6-2, a plate that is flatter than the desired sensitivity of the shape measurement is used as a calibration surface. Using a custom-made fixture the plate is

oriented at a known angle with respect to the camera axis, while maintained at a fixed distance relative to the imaging optics.

As shown in Figure 6-2, the estimated shape of the flat sample before compensation for distortions (schematically shown as a blue margin plane) is determined. The interference phase produced by the flat surface, holds two important information:

- 1 The elliptical wavefront distortions,
- 2 A regular phase change (or carrier) due to the orientation of the flat surface within the measurement device,

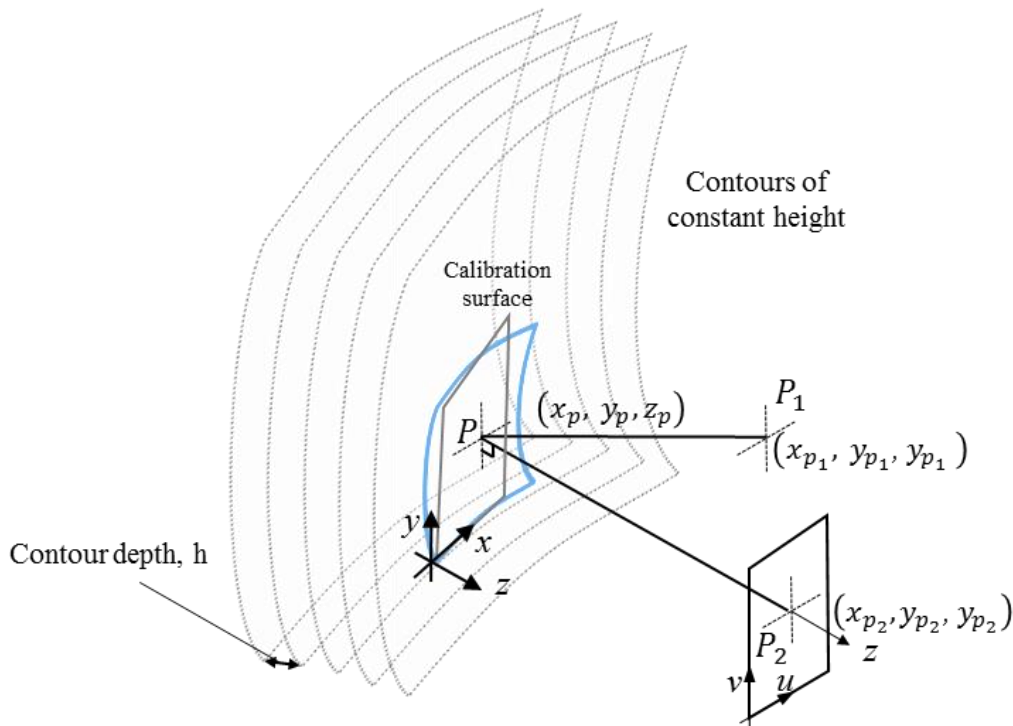


Figure 6-2 Schematic representation of the holographic flat surface calibration method. The uncalibrated shape of the flat surface is shown with the blue-bordered plane.

Since both the shape and the flat surface interference phases, are measured using the same set of wavelengths and through the same imaging optics (with the same distortions), the two modulo 2π phase maps are directly correlated without any coordinate transformation

or registration. As shown in Figure 6-3, the subtraction of $\Delta\gamma_R$ from the sample distorted interference phase $\Delta\gamma$ describes the shape in a coordinate system free from the wavefront distortions and the carrier. Furthermore, the flat surface interference phase provides the capability to remove the wavefront distortions independent of the optics distortions. Without this information, the wavefront and optics distortions are mixed with each other and they cannot be decomposed.

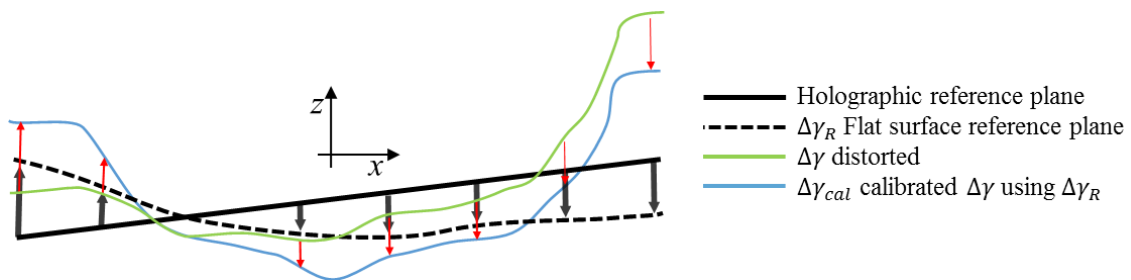


Figure 6-3 Two-dimensional schematic representation of the holographic flat surface calibration technique. Measuring the flat surface using the elliptical wavefronts, a non-flat distorted shape is determined and shown with dashed black lines. This is compared to a tilted coordinate system due to off axis illumination, which is shown with a thick black line. Subtraction of the black arrows (distorted shape of the flat sample) from any measurements result in removal of the distortions as well as the carrier from the measurements.

The last calibrations step is to transform the results from the camera coordinate system to the global coordinate system and if necessary remove the optical distortion (e.g., when an endoscope is used). While the shape is described relative to a constant optical path length plane, the requirements of measuring the illumination and observation coordinates for the shape measurements are not needed and the calibrated interference phase provides the shape by,

$$z_p = \frac{\Lambda_i}{4\pi} \Delta\gamma_{i_{cal}} , \quad (6-10)$$

where z_p is the coordinates of the sample surface in the global coordinate system free from the wavefront distortions.

6.1.3 Requirements of holographic flat surface calibration method

This method allows for an experimental holographic calibration procedure without the need for hologram reconstruction or inclusion of the illumination carrier effects as long as the following requirements are satisfied:

- 1- Knowledge of the wavelength, with sufficient accuracy and precision, is needed to repeat the same synthetic wavelengths of the calibration for the shape measurements.
- 2- Since the effects of wavefront distortions and carrier have small spatial frequency, the measured calibration data need to be free from any high spatial frequency features or noises.

The flat calibration measurements need to be performed only once for each illumination angle and/or optical configuration. Once it is done for a series of desired wavelengths the results can be used for multiple measurements. It should be noted that, if the depth of field is large compared to the ellipticity radius of the wavefront, it is better to position the flat surface closed to the location of the measured sample, while, in most of the TM measurements due to short depth of field (<5mm) a calibration is not necessary after sample relocation.

6.2 High-speed multi-resolution MWHI shape measurements

Due to technological limitations in the speed of tuning of the tunable lasers (i.e., <10 nm/s), holographic shape measurements using a single tunable laser have low temporal resolutions (i.e., <10 Hz). An option to perform high-speed MWHI is by rapidly switching between two or more laser sources coupled into a single fiber (Lu, 2012). However, this approach generates a small set of stable synthetic wavelengths and it significantly increases the cost

and complexity of the setup. When it comes to measurements on live samples, variable synthetic wavelengths can better define irregularities in the depth and shape of the TM.

One way to increase the speed in acquisition of shape in the MWHI method using a single laser is to perform phase sampling while the laser is being tuned. The interference phase between various states of transient variations of the wavelength provide a range of contour depths from millimeter to tens of micrometers to determine the sample shape with a variety of resolution ranges. If we can account for the predictable delays of the laser driver, the shape measurements can be performed in a fraction of a conventional MWHI measurement with the advantage of slicing the single tune onto many smaller wavelength increments. The key for such improvements is in the ability to perform accurate phase sampling in the presence of wavelength variations.

Although the synthetic wavelength can vary from micrometers to millimeters, the phase sampling is still sensitive to nanometer scale vibrations of the sample, and setup. Furthermore, as it will be described in the next Section, the temporal instabilities of the wavelength vary the optical path length similar to the nanometer-scale motions of the sample. The MWHI method has a more strict criteria compared to the HDH displacement measurement, discussed in Section 5.4, as sub-nanometer scale variations of the wavelength introduce unwanted non-uniform phase shifts in an off-axis configuration. Therefore, higher phase sampling rates compared to the displacements measurements are required for the shape measurements to compensate for additional noise induced by temporal wavelength instabilities.

6.2.1 High-speed phase sampling in presence of wavelength and sample noises

The benefits of performing the phase sampling during a single wavelength tune was discussed but the challenges in performing such a task have not yet been discussed. In Section 5.4 it was demonstrated how a camera exposure measures the intensity of a continuously varying hologram in an off-axis configuration at point (x, y) and time t_i is as,

$$I(x, y, t_i) = \frac{1}{\tau} \int_{t=t_i-\frac{\tau}{2}}^{t_i+\frac{\tau}{2}} I_{DC} + I_m \cos[\delta(t) + N(x, y, t) + \phi] dt, \quad (6-11)$$

where I_{DC} is the background intensity due to zero-order terms, I_m is a constant amplitude of the modulating term and ϕ is the random phase distribution as described in Eqn. (6-3).

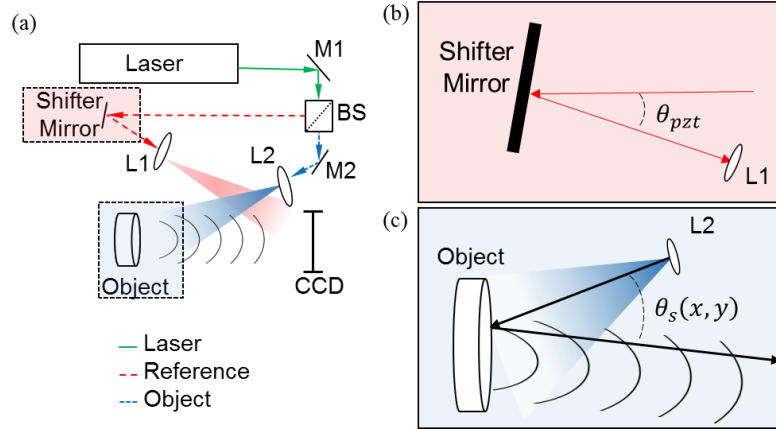


Figure 6-4 Off axis configuration parameters: (a) schematic representation of the setup; (b) enlarged pink area of panel (a), representing angle θ_{pzt} ; and (c) enlarged blue area of panel (a) representing the spatially varying angle $\theta_s(x, y)$ due to shape and off-axis illumination.

The functions $\delta(t)$ and $N(x, y, t)$ are phase shifter and the shifter noise functions, respectively, described as,

$$\delta(t) = D_{pzt}(t) \frac{2\pi}{\lambda(t)} (1 + \cos \theta_{pzt}), \quad (6-12)$$

$$N(x, y, t) = D_s(x, y, t) \frac{2\pi}{\lambda(t)} (1 + \cos(\theta_s(x, y))), \quad (6-13)$$

where D_{pzt} and D_s are displacements of the phase shifter actuator and sample at the point of interest, respectively and θ_{pzt} and θ_s are phase shifter and the sample off-axis angles, respectively (shown in Figure 6-4).

Combining Eqn. (6-11), (6-12), and (6-13), the hologram intensity is,

$$I(x, y, t_i) = I_{DC} + \frac{I_m}{\tau} \int_{t=t_i-\frac{\tau}{2}}^{t_i+\frac{\tau}{2}} \cos \left[\frac{2\pi}{\lambda(t)} (D_{pzt}(t)[\cos(\theta_{pzt}) + 1] + D_s(x, y, t)[\cos(\theta_s(x, y)) + 1]) + \phi \right] dt, \quad (6-14)$$

where the temporally stable parts are taken out of integration. Because of the wavelength dependency of the shifter noise function and phase shifter functions, wavelength variation during the camera exposures introduce an unwanted phase shift. In addition, due to spatially varied angle $\theta_s(x, y)$, the wavelength induced phase shifts are not spatially uniform.

To obtain a spatially uniform phase shifted hologram the velocity and amplitude of the motions of the phase shifter need to be sufficiently larger than the noises as well as wavelength variations. Since θ_{pzt} and θ_s are mostly constant during the exposure time, τ , the criteria for achieving a uniform applied shift are,

$$\frac{d(D_{pzt})}{dt} \gg \frac{\partial D_s}{\partial t}, \quad \frac{d(D_{pzt})}{dt} \gg \frac{\partial \lambda}{\partial t}, \quad D_{pzt} \gg D_s. \quad (6-15)$$

If the camera exposures are sufficiently shorter than the overall phase variations, it can be assumed that the effects of phase integration are minimal, therefore the intensity of the hologram is,

$$I(x, y, t) = I_{DC} + I_m \cos[\delta(t) + N(x, y, t) + \phi], \quad (6-16)$$

The next step is the quantification of the optical phase using temporal phase sampling. The intensities acquired at multiple states of the laser wavelength and phase shifts are,

$$\begin{aligned}
 I(x, y, t_0) &= I_{DC} + I_m \cos[\delta(t_0) + N(x, y, t_0) + \phi], \\
 I(x, y, t_1) &= I_{DC} + I_m \cos[\delta(t_1) + N(x, y, t_1) + \phi + \Delta\gamma_1], \\
 &\dots, \\
 I(x, y, t_n) &= I_{DC} + I_m \cos[\delta(t_n) + N(x, y, t_n) + \phi + \Delta\gamma_n].
 \end{aligned}
 \tag{6-17}$$

The terms $\Delta\gamma_1, \dots, \Delta\gamma_n$ are the phase variations due to wavelength variations. Depending on the speed of acquisition of the set of n phase shifted frames (i.e., $t_n - t_0$) with respect to the wavelength variations, two cases may occur:

Case 1- The wavelengths in Eqn. (6-17) are sufficiently close to each other that the very large synthetic wavelengths (>meters) are insensitive to sample shape and off-axis illumination. In this case, the resultant wavelength induced phase shifts are spatially uniform and they contribute to temporal variations in the applied shift, which is equivalent to phase sampling in presence of temporal noises. The HPCC method in case 1 can be utilized to determine the applied shift as discussed in Section 5.5.5.

Case 2- The wavelength variations in Eqn. (6-17) generate a synthetic wavelength sufficiently small to introduce a non-uniform phase shift, due to the (now unknown) sample shape and the carrier due to off-axis illumination. This behavior of wavelength induced phase shifts are equivalent to phase shifting in presence of spatiotemporal noises discussed in case 2 of the HPCC method in Section 5.5.6. Figure 6-5 shows a correlation map representing the phase shift between two holograms influenced by a wavelength variations of smaller than <0.02 nm. The two holograms were measured with the interval of $535 \mu\text{s}$. As shown in Figure 6-5-a the shape and off-axis illumination cause the bottom left region

of the correlation map to have different values, representing difference phase shift compared to the top right. The variations in correlation value across the surface result in a wide non-uniform distribution of correlation values in the histogram shown in Figure 6-5-b.

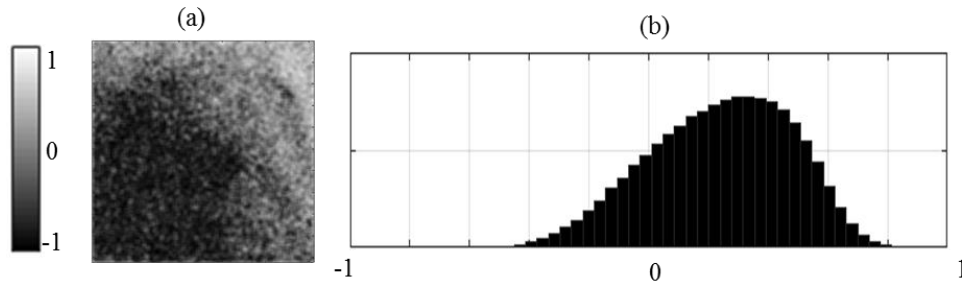


Figure 6-5 Representation of the spatially varied wavelength induced phase shifts: (a) correlation maps between two phase shifted holograms interfered by <0.02 nm wavelength variations captured in a period of $535\mu\text{s}$ during the wavelength tune; and (b) histogram of the gray scale values in panel (a) showing non uniform spatial phase shift. The sample is a human TM having a depth at the central region of $<2\text{mm}$.

6.2.2 Implementation of the high-speed MWHI method

By adjusting the speed of high-speed cameras compared to the wavelength variations it is possible to generate phase shifts with sufficiently higher temporal resolutions to maintain the spatially uniform applied shift criterion of case 1. Figure 6-6 illustrate the time line of the events in a set of high-speed MWHI measurements.

As shown in Figure 6-6, the shape measurements begin by sending a square pulse to the laser driver, which in turn drives the electronics and mechanics to alter the wavelength. The high-speed camera is armed to respond to each trigger signals by a burst of high-speed frames (i.e., $>40,000$ fps). A continuous ramp of phase shift is synchronized with the initiation of each trigger with the period slightly larger than the burst duration and amplitude sufficiently high to generate phase shifts with speed satisfying the case-1 criterion (previous Section). Therefore, each time the camera receives a trigger a set of

phase shifted holograms (i.e., <50 frames) at rates much faster than the wavelength variations (i.e., >60 times) is acquired. The bottom panel of Figure 6-6 schematically illustrate the phase sampling procedure. The bottom-left panel shows the PZT actuator displacements while the bottom right panel represent the generated phase shift.

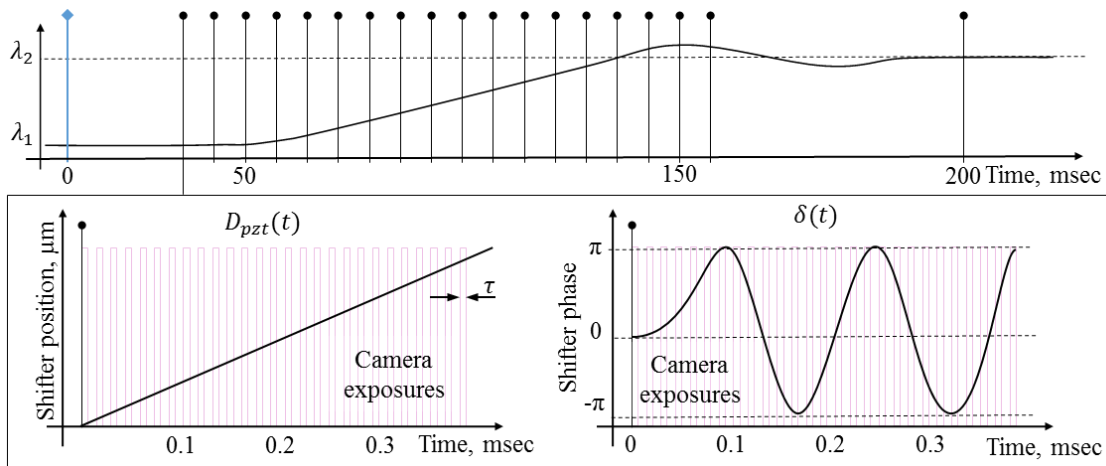


Figure 6-6 Schematic representation of the timeline of the events in a set of high-speed MWHI shape measurements. The blue diamond stem line in the top panel represent the initiation of a square pulse sent to the laser driver to alter the wavelength while the black line show the resultant wavelength variations having ~50 msec delay. Each of the circular stem lines indicate the initiation of a set of high-speed phase shifted frames as shown in the bottom panel. In each set a continuously linear phase shift (i.e., ramp) is performed by a duration of <500 μs and amplitude of several wavelengths to generate a few cycles

6.3 High-speed combinatorial MWHI shape measurements

Multi-resolution shape measurements (Section 6.2) provide a single contour depth at optimum resolution compared to sample depth and sensor resolution. The optimum resolution in this method is not always the maximum resolution since high-spatial frequency regions of the shape (i.e., areas with small curvature and surface discontinuities) cannot be quantified due to dense contour depths. Therefore, high-resolution contour maps as well as a large portion of the spatial domain are removed for the final shape. Furthermore, for further shape analysis such as determination of surface normals, it is

required to perform sufficient spatial filtering to remove any surface discontinuities that result in removal/variations of important parts of the shape. If the sample is stable during the wavelength ramp (i.e., within <100 msec), the measured surfaces with various resolutions across the ramp are in fact repetitions of the same measurement that can be combined to increase the shape resolution. Since any two wavelengths can be used to determine the shape, each set of MWHI measurements contain the following number of shape measurements,

$$C_2^k = \frac{k!}{2!(k-2)!} = \frac{k}{2}(k-1) \quad (6-18)$$

where k is the number of triggers that have sufficient wavelength variations to provide the shape with sufficient signal to noise ratio.

Overall, the procedure to extract a high-resolution shape by generating a shape database from a set of high-speed MWHI measurements is as follows:

- 1- Using the HPCC algorithm (Section 5.5), the frames corresponding to the desired phase shifts (i.e., $\pi i/2$, $i=0,1,2,\dots$.) are determined for each of the phase samplings (each black round stem in Figure 7-2 is a single phase sampling occurred in <500 μ s)
- 2- A shape database is constructed by analyzing all the possibilities of non-repeated combinations,
- 3- A phase map with smallest synthetic wavelength having minimum unwrapping discontinuities is chosen as the reference set,
- 4- Using the differences between the depth of the sample at two specific regions (i.e., window of 5 by 5 pixels) of each set compared to the reference set, all the shape database was scaled,

- 5- The scaled sets with very low signal to noise ratio (compared to the reference phase map) as well as the areas at each frame with large unwrapping errors are removed, such that all the accepted database represent the shape of the sample with different signal to noise ratio,
- 6- For each pixel a normal (or lognormal) distribution function is fitted on the measured data set,
- 7- The mean of the normal distribution (μ) corresponds to the sample high-resolution phase map with uncertainty within the width of the normal distribution (i.e., $\pm\sigma$).
- 8- Using the synthetic wavelength and calibration phase map of the reference set, the shape is scaled and calibrated to be free from any illumination distortions (as discussed in Section 6.1.2 of shape measurement Chapter)

After analysis of more than 400 measurements, about 210 accepted measurements were fitted to measure the high-resolution shape shown in Figure 7-6. The human postmortem TM shape was measured over the entire domain of the sensor free from any unwrapping errors due to sample discontinuities or phase deficiencies.

6.4 Shape and displacements measurement setup

A conventional lens with large numerical aperture and a near infrared coating was used to observe the sample. A tunable laser (Newport Velocity) with the tuning range of 770-790nm was used for shape measurements with linewidth of about 100 kHz with maximum power of <30 mW. A solid-state laser with wavelength of 532 nm, linewidth of <100 MHz, and power of >50 mW was used for the displacement measurements. Figure 6-7 shows the schematic view of the holographic shape and displacements measurement system. Each laser is divided onto two reference and object beams using two variable beam splitters for

each wavelength. After adjusting the beam-ratio of each laser, using kinematic mirrors and dichroic beam combiners the references and object beams are directed onto two beams as shown in Figure 6-7. The unified reference arm is equipped with a piezo Nano-positioner to perform phase shifting for both shape and displacement measurements using a single device. Each laser is equipped with a fast and automated mechanical shutter to rapidly switch between the two lasers.

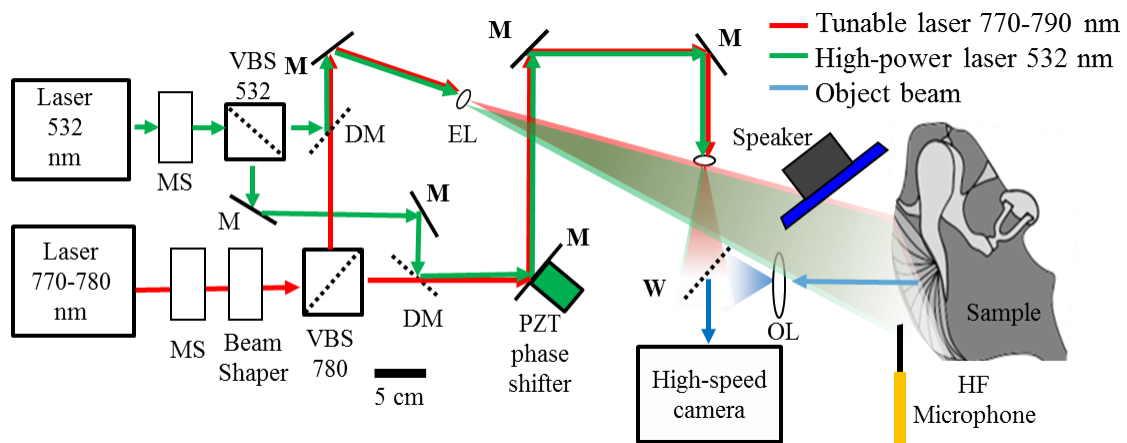


Figure 6-7 Schematic view of the shape and displacement measurement setup. MS - Mechanical Shutter, VBS - Variable Beam Splitter, DM Dichroic Mirrors, M- Mirror, W - Wedge beam combiner, OL -Objective Lens.

Overall, the following improvements were made on the HDH setup to implement the shape measurement system with minimum hardware modifications with identical sensitivity vector for both systems.

- 1 Variable beam splitters at each wavelength is used to control the object to reference intensity ratio for each laser,
- 2 Due to large difference between the two laser wavelengths, instead of conventional beam combining techniques a dichroic mirror with a cutoff frequency between the two wavelengths was used. While the dichroic coating acts as a mirror for one of the wavelengths, it transmits the other one efficiently and can act as a beam combiner,

- 3 Wedge beam combiner with ratio of 90:10 (reflectance/transmittance) used to maximize the object beam intensity efficiency for both of the wavelengths,
- 4 Coating of the lens and the wedge beam combiner were optimized to handle 400-800nm range.

6.5 Uncertainty analysis

Since the flat surface calibration method is also a holographic shape measurement, the uncertainty analysis should be based on Eqn.(6-9) which is rewritten here,

$$z_p = \frac{[(x_p - x_{p_1})^2 + (y_p - y_{p_1})^2 + z_{p_1}^2 - (\Delta\gamma \frac{\Lambda}{2\pi} - z_{p_2})^2]}{2[z_{p_1} + (\Delta\gamma \frac{\Lambda}{2\pi} - z_{p_2})]}, \quad (6-9)$$

The contour depth h (shown in Figure 6-2) is defined as the distance between two consecutive in-phase phase contours written as, (C. Furlong et al., 2006)

$$h = z_p - z'_p = \frac{[(x_p - x_{p_1})^2 + (y_p - y_{p_1})^2 + z_{p_1}^2 - (T)^2]}{2[z_{p_1} + T]} - \frac{[(x_p - x_{p_1})^2 + (y_p - y_{p_1})^2 + z_{p_1}^2 - (T')^2]}{2[z_{p_1} + T']}, \quad (6-19)$$

where,

$$T = \Delta\gamma \frac{\Lambda}{2\pi} - z_{p_2}, \quad T' = (\Delta\gamma + 2\pi k) \frac{\Lambda}{2\pi} - z_{p_2}. \quad (6-20)$$

Therefore, h is a function of

$$h = h(\Lambda, \Delta\gamma, x_{p_1}, y_{p_1}, z_{p_1}, x_p, y_p, z_{p_2}), \quad (6-21)$$

where, the last six terms are setup geometries while the first two are synthetic wavelength, and the measured phase. The uncertainty in measuring the contour depth is (C. Furlong et al., 2006),

$$\begin{aligned}
\delta h = & \left[\left(\frac{\partial h}{\partial \Lambda} \delta(\Lambda) \right)^2 + \left(\frac{\partial h}{\partial \Delta \gamma} \delta(\Delta \gamma) \right)^2 + \left(\frac{\partial h}{\partial x_{p_1}} \delta(x_{p_1}) \right)^2 + \right. \\
& \left. \left(\frac{\partial h}{\partial y_{p_1}} \delta(y_{p_1}) \right)^2 + \left(\frac{\partial h}{\partial z_{p_1}} \delta(z_{p_1}) \right)^2 + \left(\frac{\partial h}{\partial x_p} \delta(x_p) \right)^2 + \right. \\
& \left. \left(\frac{\partial h}{\partial y_p} \delta(y_p) \right)^2 + \left(\frac{\partial h}{\partial z_p} \delta(z_p) \right)^2 \right]^{1/2}, \tag{6-22}
\end{aligned}$$

where the operator δ denotes the uncertainty in measuring that parameter. Instead of calculating the overall uncertainty using bulky calculations, in here we focus on the main parameters affecting each part of Eqn. (6-22). Furthermore, the uncertainties in geometrical coordinates (the last six terms) have a zero-order effect in varying the contour depth. For example, the third term in Eqn. (6-22) after derivation become,

$$\frac{\partial h}{\partial x_{p_1}} \delta(x_{p_1}) = 2x_{p_1}(z_p - z'_p) \delta(x_{p_1}), \tag{6-23}$$

with all the terms as scalars. Therefore, because of large effects of the first two parameters in Eqn. (6-22), in the next Sections the effects of these two terms in the uncertainty of the contour depth are presented.

6.5.1 Synthetic wavelength

The uncertainty in measuring the contour depth $\delta(\Lambda)$ from Eqn. (6-8) is,

$$\Lambda_i = \frac{\lambda_1 \lambda_2}{|\lambda_2 - \lambda_1|}, \tag{6-8}$$

$$\delta(\Lambda) = \left[\left(\frac{\partial \Lambda}{\partial \lambda_1} \delta(\lambda_1) \right)^2 + \left(\frac{\partial \Lambda}{\partial \lambda_2} \delta(\lambda_2) \right)^2 \right]^{1/2}. \tag{6-24}$$

where $\delta(\lambda_1)$ and $\delta(\lambda_2)$ are the experimental uncertainties in measuring the wavelength (i.e., wavelength meter resolution). The uncertainty in the wavelength measurement is related to,

$$\delta(\Lambda) = \left[\left(\frac{\lambda_1 \lambda_{diff} - \lambda_1 \lambda_2}{\lambda_{diff}^2} \delta(\lambda_1) \right)^2 + \left(\frac{\lambda_2 \lambda_{diff} - \lambda_1 \lambda_2}{\lambda_{diff}^2} \delta(\lambda_2) \right)^2 \right]^{\frac{1}{2}} = \frac{(\lambda_1^4 \delta_{\lambda_2}^2 + \lambda_2^4 \delta_{\lambda_1}^2)}{(\lambda_{diff})^4}, \quad (6-25)$$

where the difference between the two wavelengths is called $\lambda_{diff} = \lambda_1 - \lambda_2$ pointing more directly at the Eqn. (6-8) pole at $\lambda_1 = \lambda_2$. In Eqn. (6-8) the closer the wavelengths, or λ_{diff} closer to zero, the larger the resultant synthetic wavelength Λ , the uncertainty variations near the pole are inverse quadratic due to λ_{diff}^4 . This requires highly accurate knowledge of wavelengths as λ_{diff} is closer to zero. For a tune of 1nm with $\lambda_1 = 780\text{nm}$, $\lambda_2 = 781\text{nm}$, and wavelength resolution of $\delta(\lambda_1) = \delta(\lambda_2) = 0.1 \text{ nm}$ the uncertainty in the measured synthetic wavelength is $\delta(\Lambda) \cong 3.7 \times 10^{-9} \text{ m}$ but for a tune of 0.1 nm it is $\delta(\Lambda) \cong 3.7 \times 10^{-5} \text{ m}$ which is four orders of magnitude larger.

6.5.2 Interference phase

Evaluation of the phase shifter uncertainties requires complex numerical models that were performed by other researchers and is not the focus of this Dissertation (de Groot & Deck, 1996; Malacara, 2007; Johannes Schwider, 1989; J. Schwider et al., 1983; Surrel, 1996; Ichirou Yamaguchi et al., 2006; B. Zhao & Surrel, 1995). Here, important parameters affecting the phase shifting resolution are briefly discussed. Overall, the following factors influence the recovered phase resolution:

- 1 Phase shifter error

- 2 Source stability
- 3 Spatial resolution
- 4 Vibration errors
- 5 Air turbulence
- 6 Detector nonlinearities, quantization errors, and interferometer optical errors

Due to technological improvements, the detector and quantization errors are small and they are not considered here. Also due to high-speed imaging, it can be considered that the effects of air turbulence are small. The vibration error effects has been already explained in the high-speed MWHI and HDH method. Below we discuss the main parameters affecting the interference phase quality in the high-speed MWHI method:

6.5.3 Phase shifter error

Since most of the phase shifting algorithms rely on least square methods to determine the interference phase (Greivenkamp, 1984) the more the number of phase shifted frames the more the applied shift resolution. Using the HPCC algorithm the applied shift at multiple frames during a single continuous phase shift can be detected and used to recover the phase with higher resolutions (i.e., >18 phase shifts for each wavelength within <500 μ s).

6.5.4 Laser source Stability

The stability of the laser source in frequency (i.e., wavelength) and intensity are very important in the phase shifting holographic interferometry. If the laser source is unstable, it will interfere with the fringe pattern contrast and stability causing reduction in accuracy of the recovered phase. If the intensity of the source varies, the phase shifts have different zero-order terms during the phase shifting process resulting in low phase contrast.

6.5.5 Spatial resolution

The maximum synthetic wavelengths range is in direct relationship with the number of fringes used to code the difference in depth of the sample (i.e., fringe density). The denser the quantifiable fringes, the higher the resolution of the measured shape. If a synthetic wavelength provide excessive fringe density compared to the spatial resolution the data is lost and phase cannot be recovered. Therefore, a balance between the spatial resolution and fringe density is essential in obtaining maximum shape resolution.

Furthermore, if a lensed holographic system is used, the shape measurement is also affected by the depth of field. As the holograms go out-of-focus, the Gaussian blur reduces the sensitivity of the holographic system resulting in low signal to noise ratio and lower quantifiable fringe density.

The simplified relation between the fringe density (governed by sensor resolution) to the minimum contour depth is shown in Figure 6-8. The observation angle, θ , which is the angle that the sensitivity vector forms with the surface normal at each point, has direct relationship with the contour depth (Figure 6-8), the smaller this angle, the shorter the contour depth. Determination of the minimum contour depth h to gain maximum shape resolution at each optical/sample configuration can be found by analyzing this criteria over the entire shape,

$$h \cong \frac{w}{\cos \theta} , \quad (6-26)$$

where w is the shortest quantifiable fringe width, and θ is the angle of observation. Since w is fixed and θ is varied across the sample, the synthetic wavelengths must be adjusted to not to exceed the maximum allowable contour depth. For any sample that has a depth, the angle of observation has a maximum at some point that can be taken as the basis for

estimation of the shortest contour depth to achieve optimum shape resolution. Using the proposed method with the passive adjustability of shape resolution (measuring the shape with a range of synthetic wavelengths), this optimum state of shape resolution can be achieved with much higher precision without the need of multiple experiments.

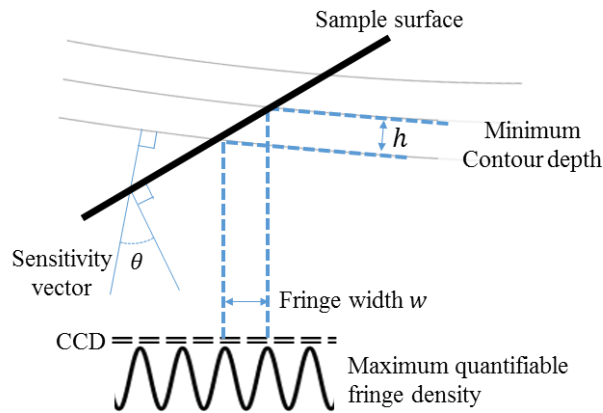


Figure 6-8 Schematic representation of the relation between the maximum quantifiable fringe density, maximum surface angle, and the minimum contour depth.

6.6 Validation of the shape measurements

Shape accuracy and precision are verified by National Institute of Standard and Technology (NIST) traceable gauges and custom made samples, respectively.

6.6.1 Shape resolution

The shape resolution was determined using the following procedure:

- 1- Shape of a NIST traceable ball (radius 5 ± 0.025 mm) is measured (Section 6.1.1)
- 2- Shape is calibrated using the flat surface calibration method (Section 6.1.16.1.2)
- 3- Utilizing well-known least square optimization methods a sphere is fit to the measured surface. An iterative optimization algorithm is used to minimize the errors in radius and coordinates of the center of the sphere for all points of the measured data cloud. The output of the algorithm is the center and radius of the

fitted sphere. The quality of this fit is reported by Root Mean Squared Error (RMSE) of the final fit.

- 4- Based on the center determined by the algorithm the radius of the part of the measured surface is compared against the nominal values provided by NIST to determine how close is the measured shape to the ideal sphere.

Figure 6-9 illustrates the measured shape using an open optics configuration in the two conditions before and after calibration. The color map in each case illustrates the spatial distribution of the errors on top of the shape using the described method in step 4. Table 6-1 presents the results obtained from this method in each case. The higher the resolution of the measured shape the lower the errors compared to the NIST nominal values. There are two errors presented in Table 6-1: the first error (i.e., Radius RMSE fit vs. measurement) shows the quality of the sphere fit algorithm while the second error (i.e., RMSE measurement vs. NIST) provides the shape resolution as described in step 4.

Table 6-1 The results of sphere fitting for determination of shape resolution.

	Calibrated	Uncalibrated
Center of the fit sphere [x,y,z] , mm	[4.91, 4.93, -4.78]	[5.16, 6.22, -5.19]
Radius of the fit sphere, mm	4.96	5.44
Radius RMSE ¹ fit vs. measurement, mm	0.013	0.037
RMSE measurement vs. NIST, mm	0.045	0.445

¹ Root Mean Squared Error (RMSE)

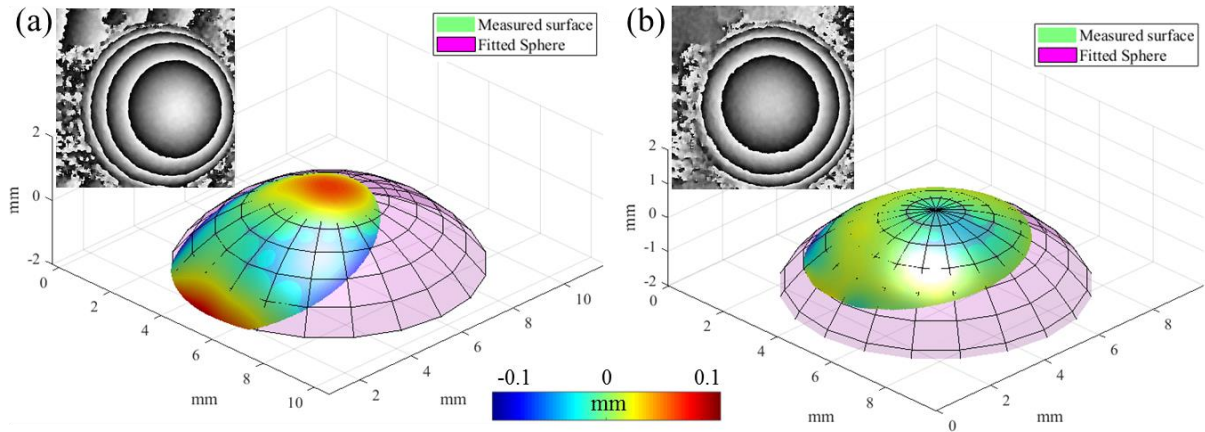


Figure 6-9 Spatial distribution of errors between the radius of the measured surface and the fitted sphere: (a) before the flat surface calibration; and (b) after the flat surface calibration. Top left of each panel is the modulo 2π interference phase before and after calibration respectively.

6.6.2 Shape repeatability

A custom sample was made to study the repeatability of the measurements under actual TM measuring conditions including a surface that can acoustically vibrate during the measurements as well as having a 3D shape similar to the TM. Figure 6-10 illustrates the mechanism used to adjust the depth of the sample as well as the view of the sample for the measurements presented in this Section.

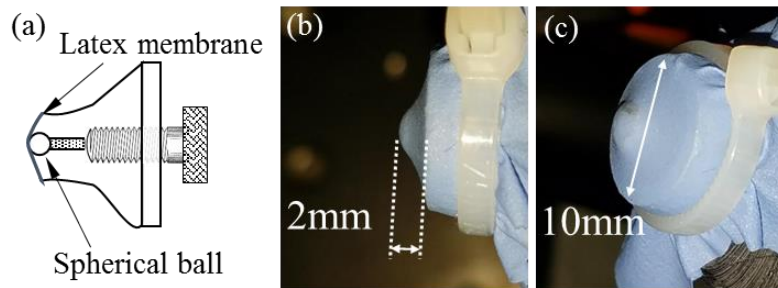


Figure 6-10 Custom made conical latex membrane to study the repeatability of the measurements: (a) the mechanism to make a 3D artificial membrane with adjustable depth; (b) side view for the measurements presented; and (c) isometric view showing the diameter of the sample.

Using five consecutive repeated measurements, the shape of the same sample was measured multiple times. The repeatability is studied by comparison of the uncalibrated wrapped and unwrapped phases having the maximum resolution (i.e., the synthetic wavelength having the largest tuning range).

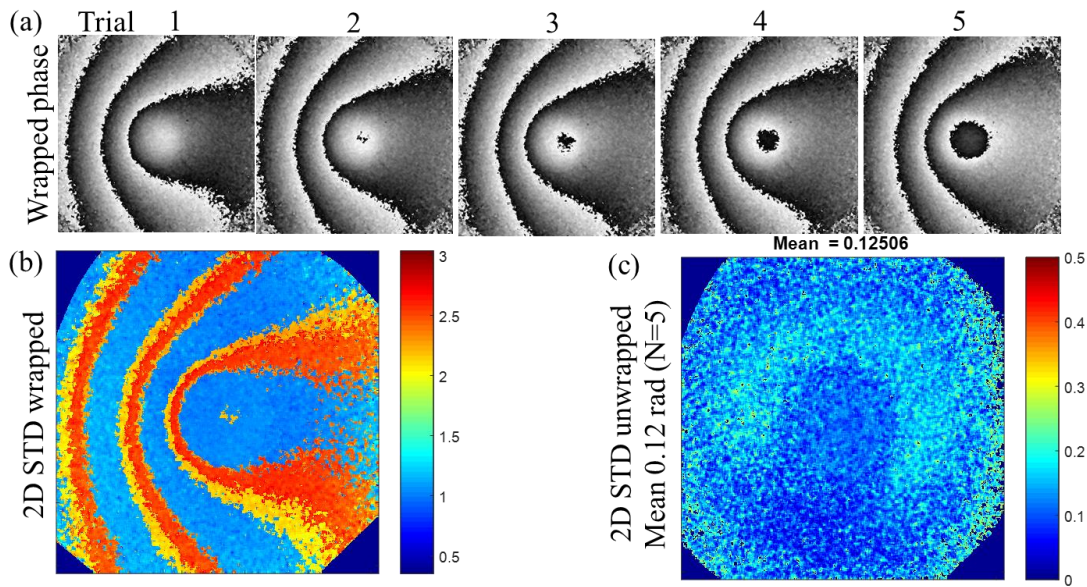


Figure 6-11 (a) the wrapped modulo 2π phase corresponding to each of the five consecutive shape measurements; (b) spatial distribution of the standard deviation of wrapped phase in all trials; and (c) spatial distribution of standard deviation of unwrapped phase of all trials. All units are in radians.

Based on these results the interference phase is quantified within ± 0.12 radians. Having a synthetic wavelength of 1.2 mm, the shape is measured with $\pm 115 \mu\text{m}$.

In this chapter two novel shape measurement methods are presented that can provide repeatable shape measurements with sufficient resolutions required for determination of surface normals as well as holographic sensitivity vector. The shape measurements were incorporated onto the displacement measurement satisfying all the design constraints. In the next section of the dissertation, the representative results of various applications of the developed HDH shape and displacement system are presented.

Part 3: Applications

7 High-speed holographic shape and transient response measurements of human tympanic membrane

In this Chapter, the results of high-speed digital holographic shape and displacements measurements on a human post mortem samples is presented to demonstrate the added measuring capabilities.

7.1 Setup specifications

Figure 7-1 shows the schematic view of the combined holographic shape and displacements measurement setup. A conventional lens with large numerical aperture and NIR coating was used to observe the sample. A tunable laser (Newport Velocity) with the tuning range of 770-790nm was used for shape measurements with linewidth of about 100 kHz with maximum power of <30 mW. A solid-state laser with wavelength of 532 nm, linewidth of <100 MHz, and power of ~50 mW was used for the displacement measurements. The lasers are divided into two sets of reference and illumination beams using two variable beam splitters for each wavelength. After adjusting the beam-ratio of each laser, the reference and illumination beams are directed into light paths with identical optical length for the two lasers as shown in Figure 7-1. The reference arm is equipped with a piezo Nano-positioner to perform phase shifting for both shape and displacements measurements. The object beam reflected back from the sample is combined with the reference using a 90:10 (reflection:transmission) broadband wedge beam combiner. Each laser is equipped with an automated mechanical shutter to rapidly switch between the two lasers (within <5 msec).

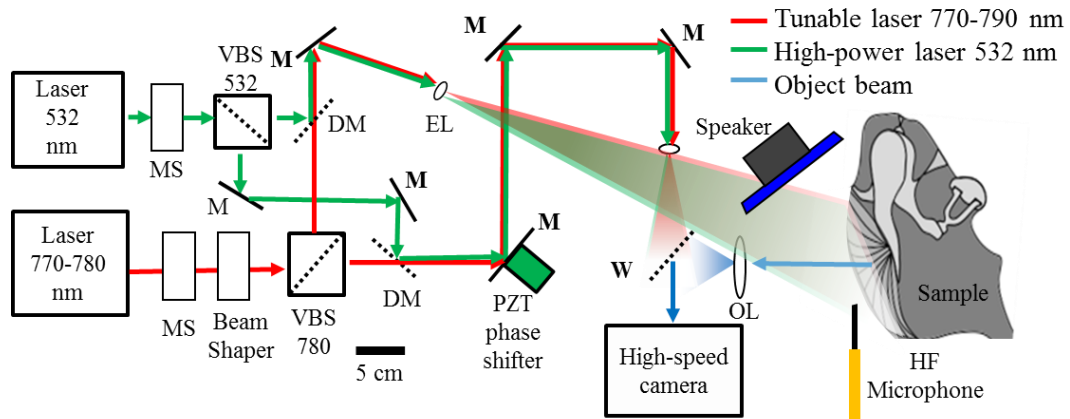


Figure 7-1 Schematic view of the shape and displacement measurement setup. MS - Mechanical Shutter, VBS - Variable Beam Splitter, DM Dichroic Mirrors, M- Mirror, W - Wedge beam combiner, OL -Objective Lens.

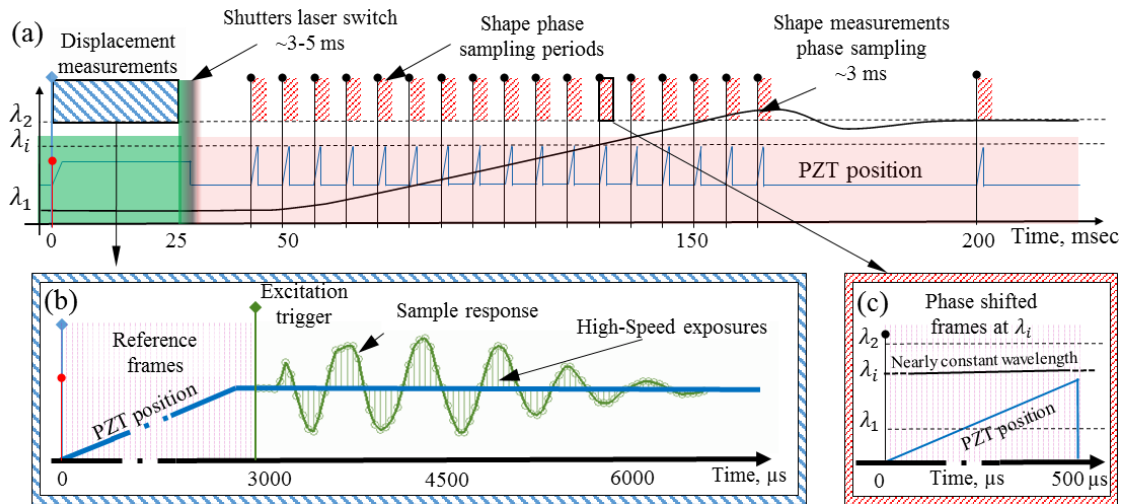


Figure 7-2 Timeline of the events in a set of shape and displacements measurements. The green and red background on the top panel represent the timing that each laser illuminate the sample. Green is for the 532 nm and red is for the infrared tunable laser. The round headed stems show the timing of camera triggers. The blue diamond stem represents the initiation of the laser tune, and the green diamond stem is the trigger to excite the sound source. The timing of the displacement measurement is shown with a dashed blue background. Bottom tight panel schematizes one of the continuous phase shifts to determine the phase of the wavefront sufficiently faster than laser wavelength variations.

7.2 Timeline

The timelines of the events in both shape and displacement measurements are shown in Figure 7-2. The high-power illumination shutter opens >100 msec before the

measurements to avoid any acoustic excitation due to the mechanical shutter while the camera is set to capture 25 msec of frames (@ 67 kHz). While the green laser illuminates the sample, the measurements sequence start with three simultaneous events: triggering of the NIR laser tuning, phase shifter ramp triggering, and camera trigger for the displacements measurements. This ordering is because of long (>50 msec) delay in the tunable laser response that allows for the entire displacements measurements to performed, before the tuning change starts. Once the camera receives the trigger (red round stem in Figure 7-2) for displacements measurements, it continuously save the holograms corresponding to displacement measurements (including reference and deformed frames) in 25ms.

The displacements measurements include capturing a set of reference holograms during a continuous phase shift (within, 3ms) followed by a broadband acoustic click (50 μ s square pulse, shown with a green diamond stem) to excite the membrane right after the phase shifter reaches its stable state. After 25ms, the piezo moves back to its original position while both the green and NIR laser shutters simultaneously close and open, respectively within less than 5ms. At the time of the shutters activation, the camera settings will change to allow for fewer frames per trigger during the shape phase sampling events (ramps initiated by black stems in Figure 7-2). Each of the 17 camera shape triggers are synchronized with a continuous phase shifting ramp of <500 μ s to allow for measurements of shape with various synthetic wavelengths across the ramp. After each phase sampling camera trigger (shown with black round stems in Figure 7-2.) a phase ramp is initiated and the camera gathers images at the desired wavelength increments. After the laser reaches the second wavelength, the last phase sampling is performed to finish a single set of

measurements by returning the tunable lasers, phase shifter, and shutters to their initial settings. Both shape and displacements measurements are performed within 200 msec and the entire measurement sequence is repeated at least three times. Further details of the shape and displacements measurements were discussed in Chapter 5 and 6, respectively.

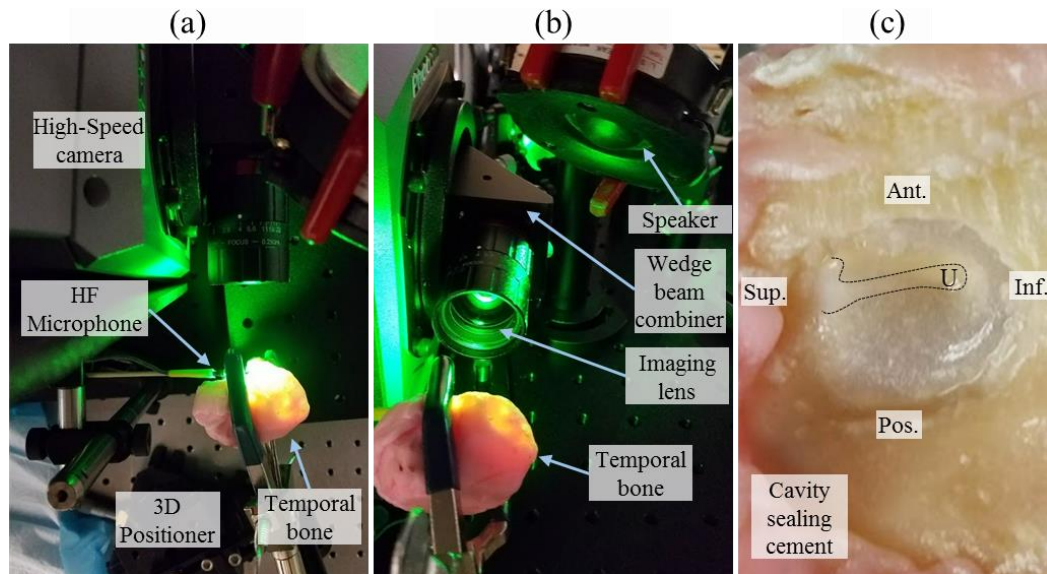


Figure 7-3 The sample, setup, and measuring instrumentations: (a) top view; (b) isometric view; and (c) the sample; a human post-mortem TM. The black contour shows the outline of the manubrium and umbo (shown with a U symbol).

7.3 Sample preparation

A fresh human post mortem sample was used for this study. The cartilaginous part and the boney part of the outer canal were removed to allow for larger view of the TM. The middle-ear cavity was opened to check the middle-ear ossicles healthiness and then it was sealed using silastic cement, though it was loose enough to allow equilibration of the internal pressure with the atmosphere (Figure 7-3-a). The lateral surface of the TM was sprayed with a thin layer of white face paint using a modified commercially available airbrush. To ensure the paint layer is sufficiently thin and uniform the airbrush was set to generate the finest particles while the sample was placed >10 cm away from the airbrush. The paint

layer was sufficiently thin that part of ossicles are still visible using white light illumination (Figure 7-3).

7.4 Multi-resolution MWHI shape measurements

Based on the results of sensitivity analysis using the numerical model (Section 4.4), the desired shape, and orientation measurements must satisfy two criteria,

- 1- Uniform resolution in all dimensions for accurate surface normal determination,
- 2- Sufficient resolution to measure surface normals after removal of surface discontinuities maintaining the smallest curvatures on the TM.

As discussed in detail in the shape measurements Chapter, the synthetic wavelength has direct relationship with the shape resolution. The farther the value of the two wavelengths of the double exposure hologram, the smaller the synthetic wavelength (Section 6.1). While the synthetic wavelength has inverse relationship with signal to noise ratio¹ and spatial resolution, TM measurements was performed with a synthetic wavelengths of about 1.5mm. Smaller synthetic wavelengths result in dense fringes at umbo region causing unwrapping problems.

Figure 7-4 show measured phase maps with various number of fringes across the field of view due to the recovery of phase with various synthetic wavelengths. The top panel in Figure 7-4 show the measured wavelengths in each of three consecutive trials during the first ten phase sampling triggers. Figure 7-4-b illustrates the various shape resolutions available from a choice of any two combinations out of 17 phase sampling sets measured

¹ The smaller the synthetic wavelength the higher the signal to noise ratio.

during a single tuning ramp. For simplicity each synthetic wavelength is hyphenated by the number of the wavelength samples used in the computation (i.e., a double exposure combination of phase sampling at λ_1 and λ_9 has synthetic wavelength $\Lambda_{1,9}$).

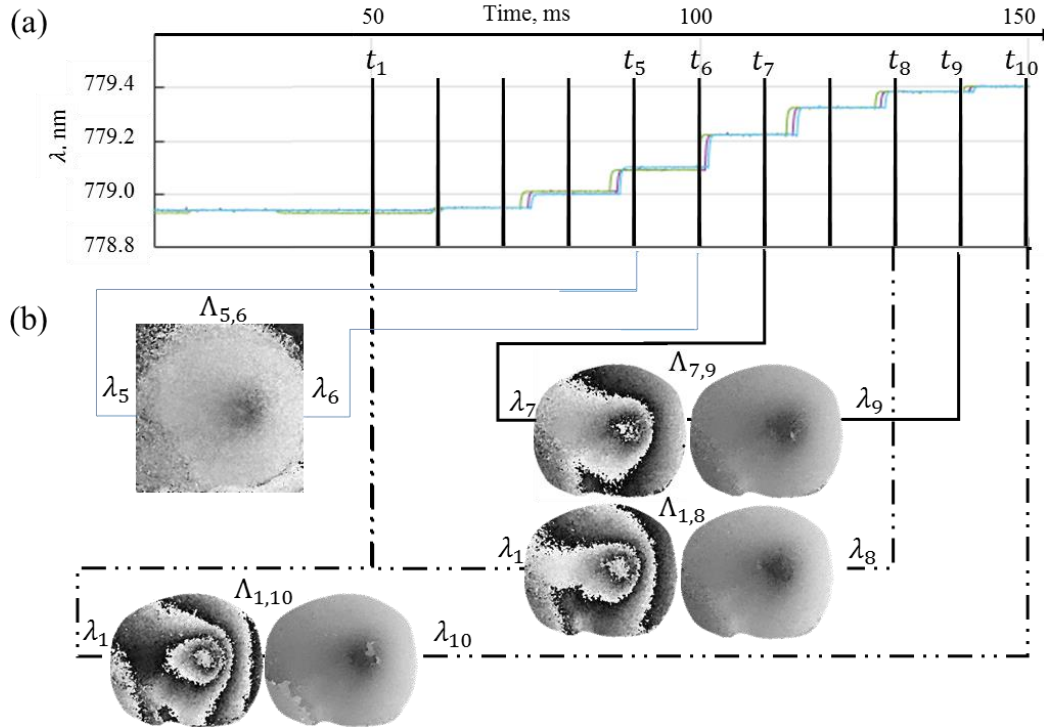


Figure 7-4 Representative phase maps showing the multiple resolution measuring capability: (a) timings of the wavelength variations with respect to the triggers. The wavelengths are numbered by their temporal sequence during the tuning ramp. There are no jumps in the actual wavelength tuning, the jumps observed in the wavelength readings are due to the low temporal resolution of the wavelength meter (<80 Hz); (b) wrapped and unwrapped phase maps taken with selected arbitrary combinations showing various number of fringes across the sample. Large synthetic wavelengths (i.e., $\Lambda_{5,6}$) provide phase maps that are relatively immune to shape discontinuities as well they may not require phase unwrapping procedures (there are no wrapped discontinuities). The smaller synthetic wavelength phase maps (i.e., $\Lambda_{1,10}$, $\Lambda_{1,8}$) provide shorter contour depth with higher signal to noise ratio to observe finer details of the surface, however they are more sensitive to surface discontinuities as in panel of $\Lambda_{1,10}$, the unwrapping error artifacts at the umbo and annulus region were formed due to denser fringes.

Using this capability the shape of TM can be measured with a resolution sufficient for many TM investigations. The range of various synthetic wavelengths provide the capability of obtaining the shape at an optimum contour depth (a synthetic wavelength that

provides the shape with maximum quantifiable fringe density) without multiple repetition of measurements. In case of unknown shape depth, multiple (>3) shape measurements are required to experimentally determine a value close to the optimum contour depth. Using the multi-resolution MWHI shape measurement, all the required information to extract the (i.e., the range of various synthetic wavelengths) is measured in a set of data that can be used to robustly measure the shape at the highest spatial resolution of the sensor. Figure 7-5 shows the measured shape having a resolution close to the optimum resolution of the sensor while only a single measurement was performed.

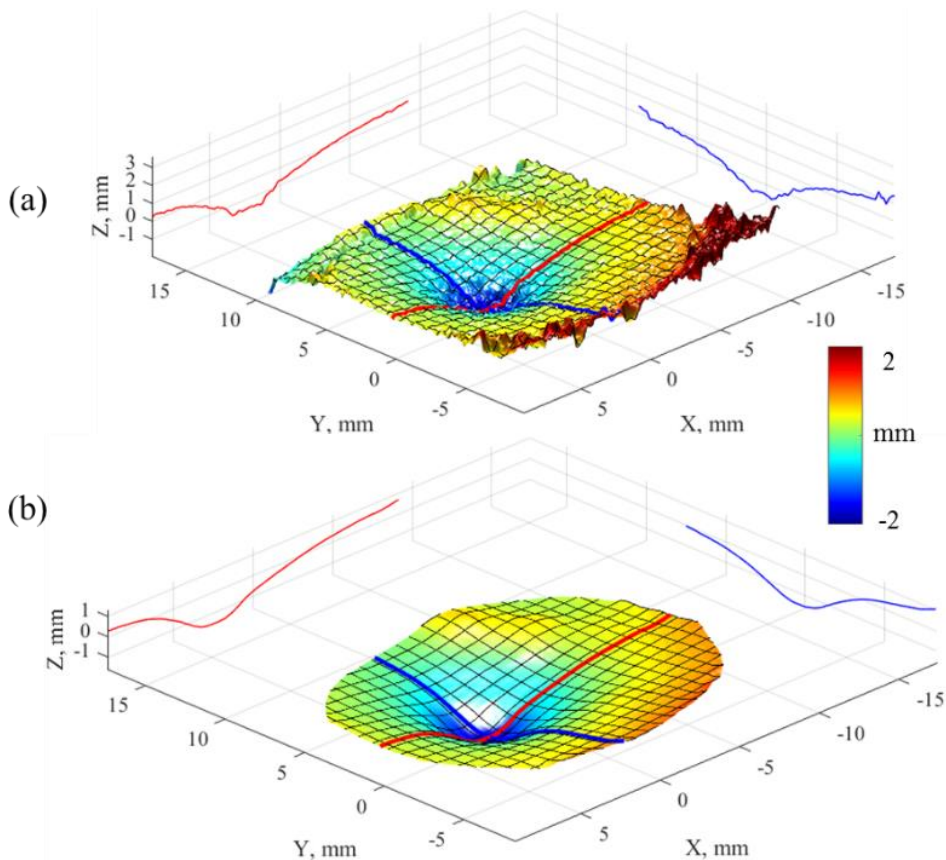


Figure 7-5 Results of reconstructing the shape from the phase map having synthetic wavelength $\Lambda_{1,8}$ (shown in Figure 7-4): (a) 3D representation of the shape after slight spatial filtering (averaging 3 by 3 pixels). The peripheral regions of the shape (part of annulus and temporal bone) show unwrapping errors as a result of shadows and sharp discontinuities between the temporal bone and pars tensa; and (b) TM shape, masked and spatially filtered (averaging 15 by 15 pixels), suitable for determination of surface normals.

After calibration and unwrapping process of the phase map determined by the synthetic wavelength $\Lambda_{1,8} = 1.28 \text{ mm}$ the shape was slightly filtered and shown in Figure 7-5-a. As stated before, the smaller synthetic wavelengths provide higher resolution but they are more sensitive to surface discontinuities. In order to use a single phase-map shape suitable for determination of surface normals, the areas with unwrapping artifacts are masked and the surface is spatially filtered (averaging or Gaussian spatial filter) to extract continuously differentiable smooth surface.

7.5 Combinatorial shape measurements

As determined in Section 4.7, the surface normals are highly sensitive to the surface noise and discontinuities of the surface requiring larger spatial filtering amplitudes prior to normal estimation. If shape resolution in any dimension is insufficient, the spatial filtering may remove the important details on the surface of TM that necessitates the need for higher shape resolution. To determine the shape and surface normals with sufficiently higher resolutions a new method to utilize the entire bandwidth of the high-speed shape measurements was used.

If the sample is stable during the wavelength ramp (i.e., within <100 msec), the measured surfaces with various resolutions across the ramp are in fact repetitions of the same measurement that can be combined to increase the shape resolution. The largest measured wavelength difference is used to determine the absolute depth of the sample eliminating the need for high-resolution wavelength measurements (see Section 6.5.1). As an example, phase map $\Lambda_{1,8}$ shown in Figure 7-4 is suitable for this purpose since the combination of the synthetic wavelength and measurement quality provide the shape depth with the least

uncertainty. This depth is used to scale all the other phase maps with larger synthetic wavelengths without the need for the knowledge of wavelength during the tuning ramp.

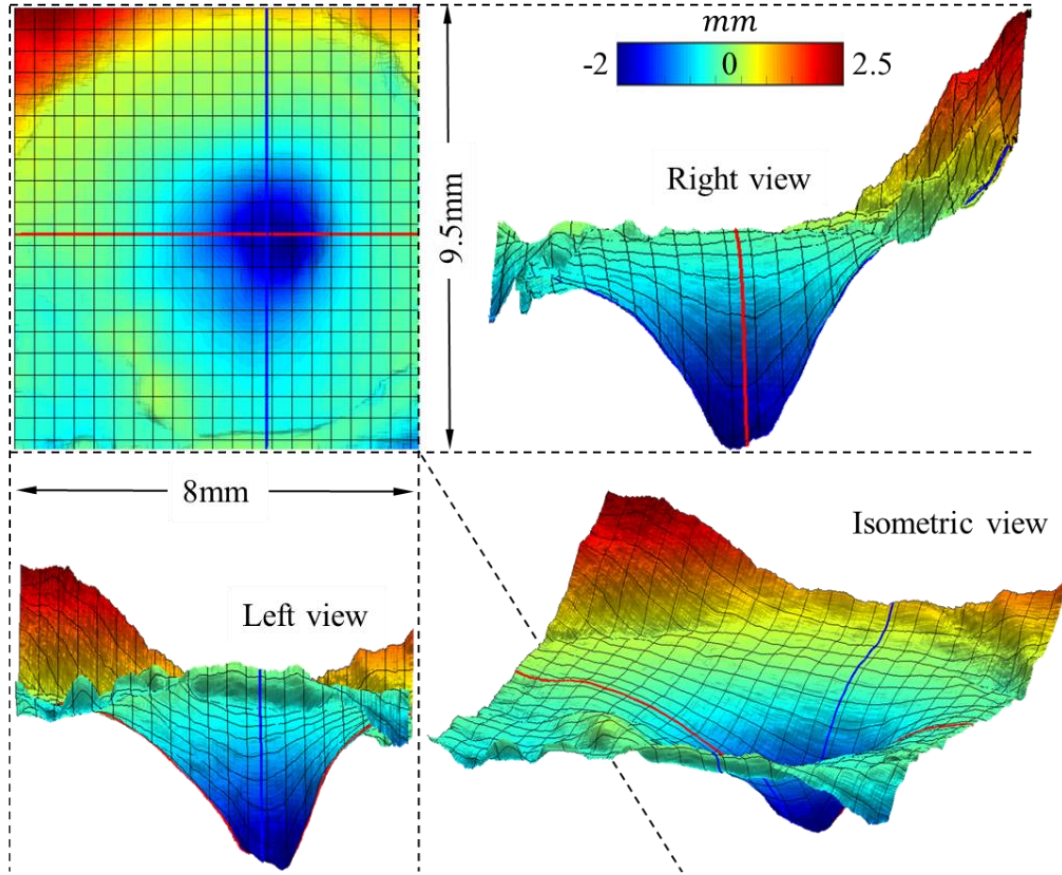


Figure 7-6 TM measured shape using the combinatorial MWHI method. Scaled and calibrated results are determined by fitting a normal distribution over >200 scaled measured shapes across the tuning ramp. The color bar represents the shape of the sample along the z-axis. The shape illustration in left and right view has a larger dimension along z-axis to show the shape at the umbo and annulus regions.

Overall, the procedure to extract a high-resolution shape by generating a shape database from a set of high-speed MWHI measurements is as follows:

- 1- Using the HPCC algorithm (Section 5.5), the frames corresponding to the desired phase shifts (i.e., $\pi/2$, $i=0,1,2,\dots$) are determined for each of the phase samplings (each black round stem in Figure 7-2 is a single phase sampling occurred in $<500\mu\text{s}$)

- 2- A shape database is constructed by analyzing all the possibilities of non-repeated combinations,
- 3- A phase map with smallest synthetic wavelength having minimum unwrapping discontinuities is chosen as the reference set,
- 4- Using the differences between the depth of the sample at two specific regions (i.e., window of 5 by 5 pixels) of each set compared to the reference set, all the shape database was scaled,
- 5- The scaled sets with very low signal to noise ratio (compared to the reference phase map) as well as the areas at each frame with large unwrapping errors are removed,
- 6- For each pixel a normal (or lognormal) distribution function is fitted on the measured data set,
- 7- The mean of the normal distribution (μ) corresponds to the sample high-resolution phase map with uncertainty within the width of the normal distribution (i.e., $\pm\sigma$).
- 8- Using the synthetic wavelength and calibration phase map of the reference set, the shape is scaled and calibrated to be free from any illumination distortions (as discussed in Section 6.1.2 of shape measurement Chapter)

After analysis of more than 400 measurements, about 210 accepted measurements were fitted to measure the high-resolution shape shown in Figure 7-6. The human postmortem TM shape was measured over the entire domain of the sensor free from any unwrapping errors due to sample discontinuities or phase deficiencies.

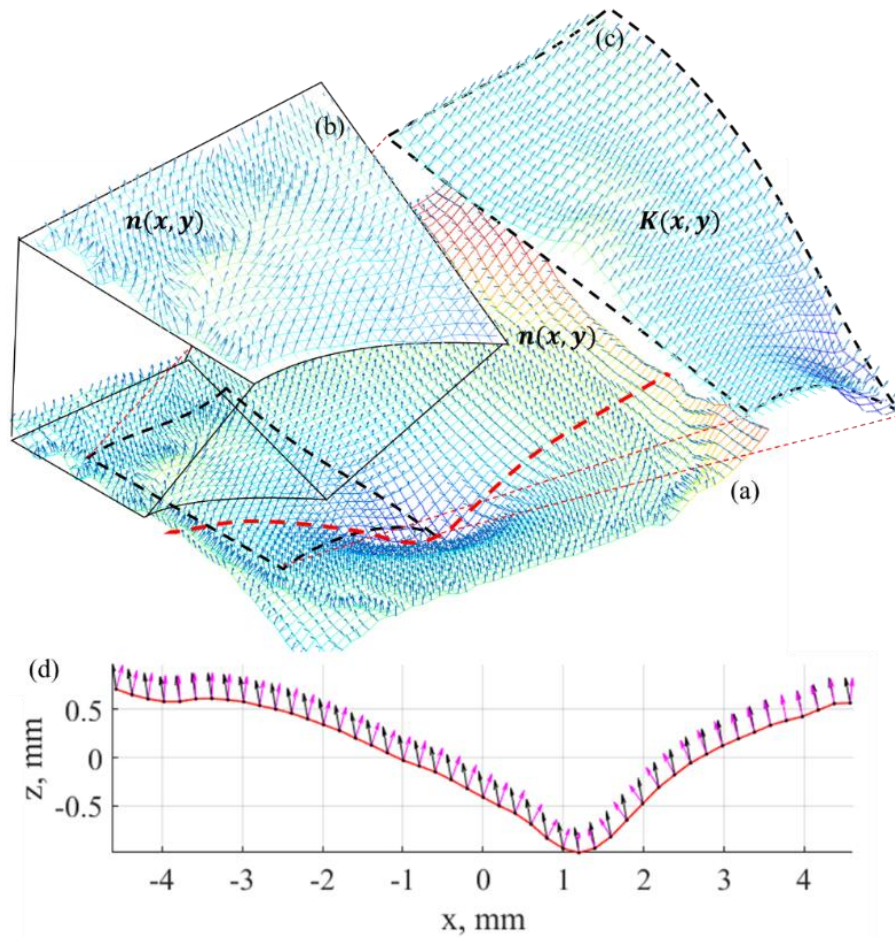


Figure 7-7 Distribution of 10 times down sampled surface normals (\mathbf{n}), and sensitivity vectors \mathbf{K} : (a) full-field surface normal distribution; (b) zoomed distribution of surface normals at the black line region of panel (a); (c) sensitivity vector distribution $\mathbf{K}(x, y)$ black dashed line region of panel (a); and (d) determined surface normals and sensitivity vector along the red line shown in panel (a). magenta vectors are the surface normals and black vectors are sensitivity vectors;

7.6 Surface normal and sensitivity vector measurements

Using the high-resolution shape by the combinatorial MWHI shape measurements, the surface normals are determined with minimum spatial filtering and over the entire field of view¹ of the sensor (without masking). To determine the surface normals, a Matlab internal

¹ Using a single set of wavelengths, the annulus region has unwrapping errors and need to be masked out that limits the field of view of both shape and displacements measurements.

function was used capable of determination of surface normals from a discrete three dimensional (in a Cartesian coordinate system) data cloud (Matlab, 1760).

Figure 7-7-a illustrates the distribution of determined surface normals across the measured TM shape (the illustration is down-sampled for better visualization). To better show the continuous distribution of surface normals a zoomed area of Figure 7-7-a is shown in Figure 7-7-b.

In the next step, using the setup geometries (coordinates of illumination/observation) and the measured shape, the sensitivity vector map is determined. The spatial variations of the distribution of sensitivity vector along the shape for the region of the TM shown with a dashed line in Figure 7-7-a, is shown in Figure 7-7-c. The surface normals and sensitivity vectors along the red dashed line shown in Figure 7-7-a are shown with magenta and black arrows respectively in Figure 7-7-d.

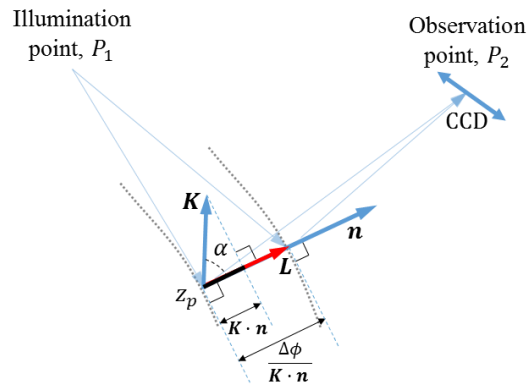


Figure 7-8 Schematics of out-of-plane displacements measurements by the sensitivity vector \mathbf{K} , and surface normal vector \mathbf{n} .

7.7 Determination of sensitivity multiplier

After calculation of the surface normal vector \mathbf{n} , which based on the thin shell theory is equivalent to the direction of the displacement vector (i.e., $\mathbf{L} = |\mathbf{L}| \cdot \mathbf{n}$), the magnitude of the surface-normal displacement are determined by,

$$|\mathbf{L}| = \frac{\Delta\phi}{\mathbf{K} \cdot \mathbf{n}}, \quad (7-1)$$

$$\eta = (\mathbf{K} \cdot \mathbf{n})^{-1}, \quad \Delta\phi \times \eta = |\mathbf{L}|, \quad (7-2)$$

where the sensitivity vector and the surface normals are as shown in Figure 7-8.

Using the surface-normal vector map (shown in Figure 7-7-a-b) and the sensitivity vector map (shown in Figure 7-7-c), the sensitivity multiplier (i.e., $\eta = \mathbf{n} \cdot \mathbf{K}$ in m/rad) at each point across the sample was computed and shown in Figure 7-9. This map is called sensitivity multiplier since it has the role of converting the light cycles to the amplitude of surface-normal displacements at each point using Eqn. (7-2).

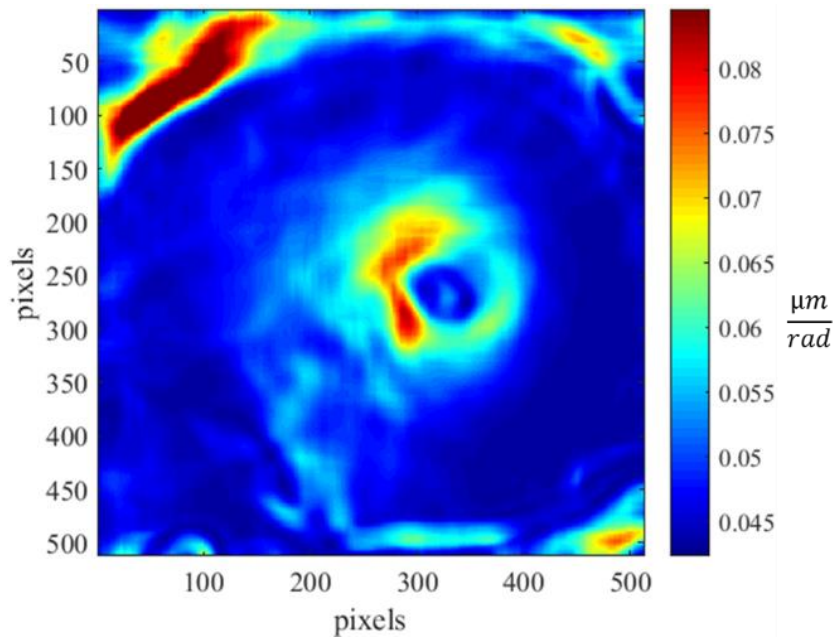


Figure 7-9 Spatial distribution of sensitivity multiplier $\eta(x, y)$ determined for displacements measurements laser wavelength of $\lambda = 532 \text{ nm}$. The deep blue region has the multiplier equivalent to parallel observation and illumination.

7.8 Displacements measurements results

The displacements measurements procedure was discussed in Chapter 5, in here a briefly summary of the experimental and analysis specifications are presented. Using the HPCC

method (Section 5.5) the best reference set corresponding to $\pi/2$ phase shift as well as a set of reference frames corresponding to a complete cycle of the phase shift was detected for determination of zero-order terms (Section 5.3.2). Figure 7-10 illustrates the output of the HPCC automated detection algorithm having a near sinusoidal phase variation along the continuous phase shift due to the ramp. The holograms of the correlation images as well as the smooth and harmonic phase variations suggest there are minimum environmental noises (similar to case-1 in Section 5.5.5).

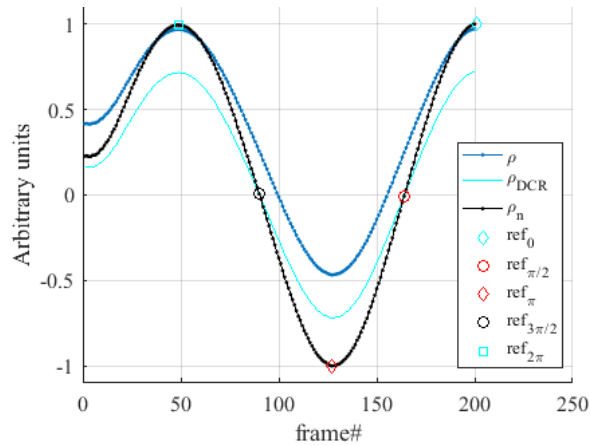


Figure 7-10 The output of the HPCC algorithm showing the applied shift across the ramp using the methods described in Section 5.5.

Having the knowledge of phase shift for each frame of the reference ramp, first the zero order terms are determined by temporal averaging over the frames of a complete cycle of phase shift (Section 5.3.2). To determine the modulo 2π interference phase $\Delta\phi$, the correlation coefficient between two $\pi/2$ reference frames and the deformed frames are calculated using Eqn. (5-15) as discussed in 5.2.3. Next, spatial discontinuities of the modulo 2π phase maps at each deformed state were removed using a fast unwrapping algorithm (Herráez et al., 2002). Finally, using the sensitivity multiplier map (Figure 7-9) determined using the shape, orientation, and setup geometries the displacements of the

sample at each point were measured from the unwrapped interference phase. Figure 7-11 show nine selected instances out of more than 1700 full field displacements measurement during a single TM transient response measurement.

Top panels in Figure 7-11, are the first three consecutive frames of the measurements showing the initial response of the membrane in response to sound. At this stage, nearly the entire surface of the TM, except small region posterior to manubrium, simultaneously respond to sound pressure variations. During the first $45\mu\text{s}$ (the first four panels), there has been minimum travelling waves observed as the same displacements pattern with increasing amplitude was repeated that makes it suitable for further investigations of acoustic to solid interaction. At this stage, because TM deforms mostly toward a single direction it is suitable to determine the TM and middle-ear stiffness factors.

Followed by this stage, the waves reflect from both the manubrium and the annulus forming complex superposition of travelling and standing waves. This stage minimum amount of excitation affects the TM response making it suitable for experimental modal analysis to determine mechanical properties of pars tensa.

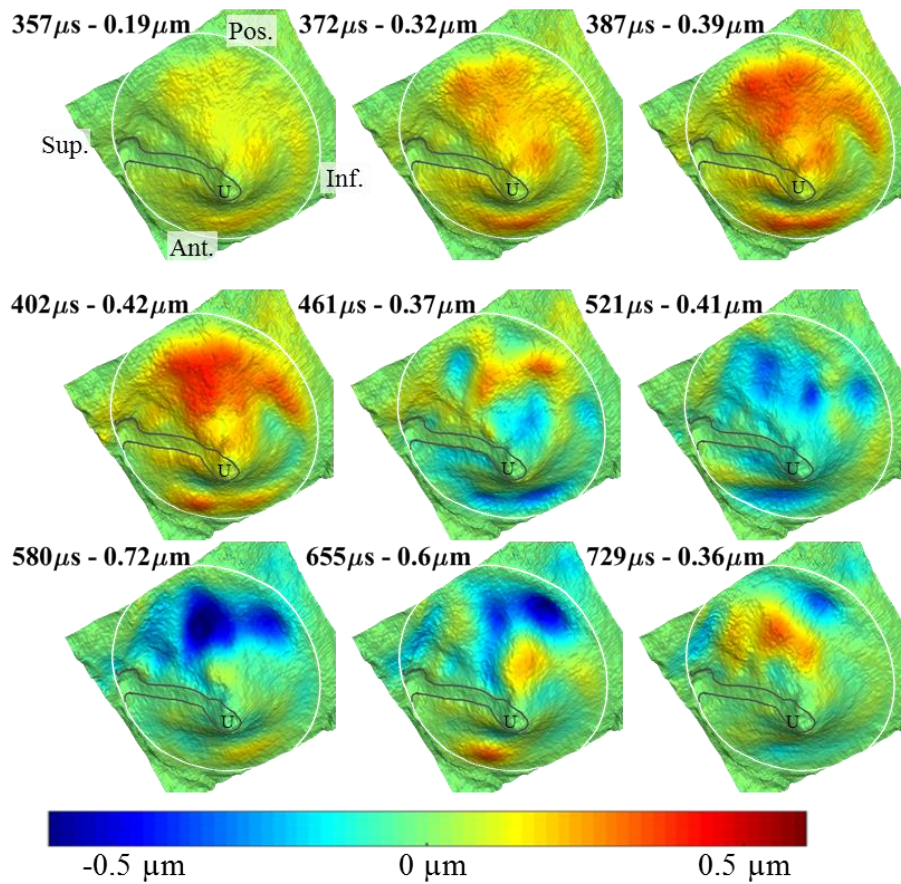


Figure 7-11 Nine temporal instances of the full-field of view normal displacements of the TM due to an acoustic click excitation superimposed on its shape. The color bar represents the actual amplitude of the calculated normal displacements. The displacements in the 3D plots are 1000 times exaggerated to be able to show them on top of the millimeter-scale shape. The number on top right of each panel show the maximum absolute displacements at that instance.

Figure 7-12 time waveforms at six selected regions across the TM for the three consecutive click measurements. All the trials are nearly on top of each other showing highly repeatable measuring capabilities having smaller than $\pm 10\text{nm}$ variations. Region 1 show the displacements at the umbo together with scaled microphone pressure readings. Regions two to five are displacements at posterior (Pos.), Anterior (Ant.), inferior (Inf.) and superior (Sup.) locations on the pars tensa while region six is on the pars flaccida. While the manubrium and umbo regions damp within less than a millisecond, the majority of pars tensa regions damp in about 3 msec.

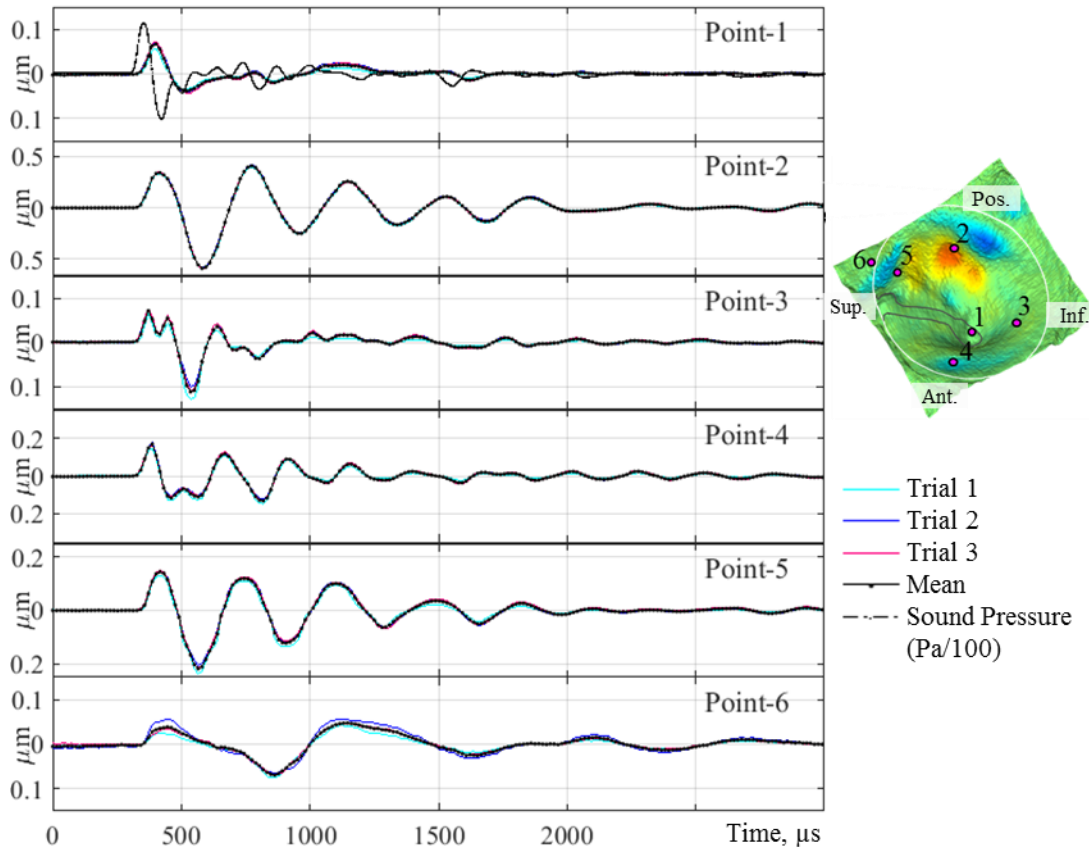


Figure 7-12 Time waveforms of six selected regions across the sample out of more than 200,000 data points. The location of each point (the center of a spatial averaged window of 5 pixels) with respect to the shape of the TM is shown on the top right panel. Calibrated sound pressure readings are shown on top of the waveform of point 1 (umbo displacements).

7.9 Significance of surface-normal displacement measurements

To determine the variations of the displacements after application of the spatially varied sensitivity vector for determination of normal displacements, the results are compared with the ones obtained by assumption of Parallel Illumination Observation (PIO) condition (i.e., $\eta = \frac{\lambda}{4\pi}$) to determine the errors. Figure 7-13 show the error maps between normal displacements of Figure 7-11 and the ones obtained under PIO conditions.

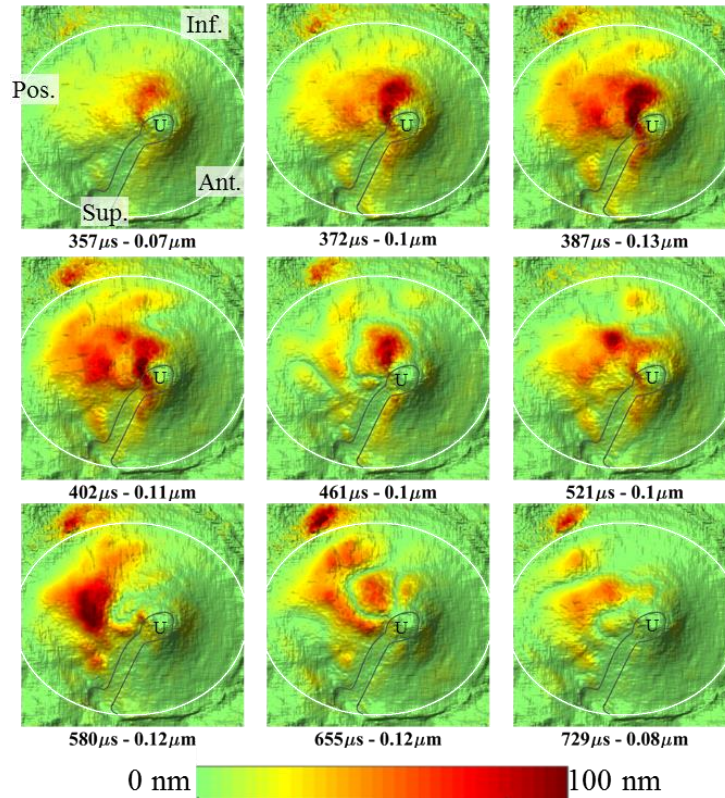


Figure 7-13 The spatiotemporal absolute differences between surface-normal displacements and the displacements determined under PIO assumptions. The maximum differences occur at 387 μ s with an amplitude \sim 138 nm.

As shown in Figure 7-13 the errors depend on the direction of the sensitivity vector as well as surface normals (related to shape and orientation). While the regions around umbo (shown with U in each panel) have the largest curvatures, as well as large displacements errors are larger around umbo. Because of angled illumination vector (from the left side of the sample), the left region posterior to umbo have the largest errors.

Because, the maximum errors depend on where the absolute value of displacements occur with respect to shape, orientation and setup geometries, the maximum errors are not temporally constant (although the same sensitivity multiplier map was used for all the holograms). By finding the location of maximum error at each time and using the normal displacements the temporal variations of the errors are determined. Figure 7-14 show the

error percentile (blue line scaled on the left vertical axis) together with temporal variations of the maximum spatial error (orange solid line) and normal displacements at the point of maximum errors (dashed solid lines) in nanometers.

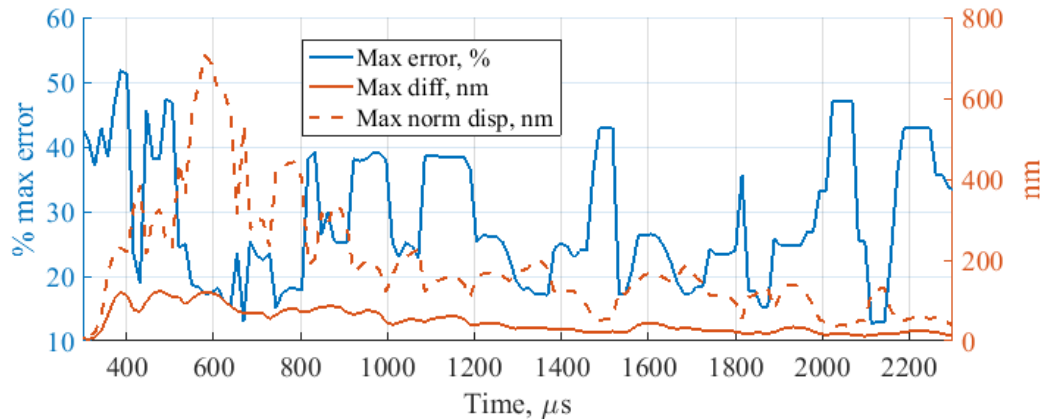


Figure 7-14 Temporal variations of errors induced by application of a PIO sensitivity vector with respect to the results obtain by application of spatially varied sensitivity vector and surface normals. The blue line shows the percentile between the two orange lines scaled on the right side of the panel in nanometers. The solid orange line shows the amplitude of maximum displacement errors at each hologram while the dashed orange line show the normal displacements measured at the same location.

The results show the initiation of the motions are accompanied by about 40% maximum error with a peak of 52% error at 387 μ s (top right panel of Figure 7-13). The maximum error amplitude is about 138nm and occurred at 595 μ s.

The spatiotemporal distribution of the errors together with the important regions they occur show the importance of shape measurements in parallel with displacement measurements to account for these variations. It should be noted again that the measurements presented in this Chapter were performed by using nearly collimated wavefronts, in the case of an endoscopic optical configuration the elliptical wavefronts can add to these spatially varied errors.

8 Milestones

In this Chapter, milestones in the developments of the high-speed holographic shape and displacement are presented in the form of peer-reviewed publications. Each publication addresses a step in the applications of the high-speed digital holography for the middle-ear research and clinical applications.

Section 8.1 presents one of the initial improvements to the high-speed holographic displacement measurement method that greatly increased measurement repeatability. Two published papers are presented in this section: the first paper focuses on the technical improvements and the second one presents the medical application of this method after enabling comparative study of multiple repeatable measurements.

Section 8.2 presents our first successful attempts in the use of high-speed holography *in vivo*. A chinchilla with a hearing frequency range close to humans was used for this study. Due to long and angled ear canal of chinchillas, the cartilaginous outer part of ear and a considerable portion of the bony canal was removed by surgery; however, still a small portion of the animal TM was observable using an open optics configuration. A custom-made holographic otoscope was designed and implemented to the HDH displacement measurement system that enabled illumination and observation inside the confined ear canal of the chinchilla. This holographic otoscope has the potential capability to observe the TM in adult humans. Representative results show highly repeatable measurements in live samples, as multiple measurements (N=6) show repeatable motions with absolute displacement error of <20 nm and <23 μ s temporal differences. The quantitative measurements of the transient response of TM on live samples, to the best of our knowledge, were the first in a live animal.

Section 8.3, presents the final methodological improvements on the temporal phase sampling methods that further enhance the capabilities of the HDH displacement measurement method. One of the first requirements of the 2+N HCI method is the spatiotemporal stability of the sample during the phase shifting process. Using the continuous phase sampling and methods such as HPCC, we demonstrated the open-loop capability to quantify the applied shift and to robustly compensate for the nonlinearities of the phase shifter as well as uncontrolled rigid body motions of the sample (e.g., Section 8.1, 8.2, and Section 5.5.5). However, in cases of continuous deformation, using this early version of the system (i.e., a TM in a noisy environment), spatially uniform applied shift during the continuous phase sampling can lead to erroneous results. This short unsubmitted report presented in this section (to be submitted to one of the relevant journals in the field of high-speed holography) describes the methodological improvements after applying the HPCC method for each pixels to reconstruct the spatially uniform phase shifted reference frame. Representative results on an in-vivo human skin under continuous pneumatic excitation are presented to show the added capabilities.

Section 8.4 describes the latest accepted conference proceeding that focuses on the design, developments, and manufacturing of the shape measurement method with the capability of working alongside the HDH displacement measurements (Chapter 5). The manuscript demonstrates the utility of HPCC methods in phase quantification in presence of continuous wavelength variations enabling multi-resolution shape measurements milliseconds prior to displacement measurements. The results presented in this paper, show the multi-resolution shape measurements has the capability to determine the shape at

near optimum resolution of the sensor by adjusting the contour depth with respect to each sample conditions.

Section 8.5 describes the latest development in the shape measurements, which is the high-speed high-resolution combinatorial shape measurements. Multi-resolution shape measurements presented in Section 8.4 (and Section 6.2) provide a single contour depth at optimum resolution of the sensor with respect to sample depth. The optimum resolution may not always be the maximum resolution since the high-spatial frequency regions of the shape (i.e., areas with significant curvature and local perturbations, e.g. those caused by the connection between the TM and the bone at the umbo) cannot be quantified due to dense contour depths at specific regions. Combinatorial MWHI shape measurements can measure the shape from the maximum spatial resolution contour depths while at the same time use the information from lower resolution contour depths to reduce the sensitivity of the measurements to surface discontinuities.

8.1 Continuous phase sampling and repeatability of the measurements

In this Section two papers are presented based on the same set of measurements:

In the first paper, methodological improvements in the high-speed digital holographic displacement measurements method are presented (Razavi et al., 2016a). These early improvements enabled repeatability in TM transient measurements by compensating for negative effects of the phase shifter positioner nonlinearities as well as spatially uniform vibrations of the sample. The first paper describes the improvements produced by replacing a phase step with continuous phase shifting to account for driver and setup nonlinearities. Instead of the HPCC algorithm, a phase-quality optimization algorithm was used to estimate the best set of reference frames in the 2+N HCI method. The phase-quality optimization algorithm depended on the zero order terms (Section 5.3.1) and its results were non-repeatable under specific conditions (i.e., inefficiency in determination of zero order terms).

The second paper in this section describes a comparative study on the TM response to local mechanical and global acoustic stimuli using high-speed holography. The two excitation modes provide distinct and complementary results to study the spatial variations in damping, stiffness and mass of the TM (Razavi et al., 2016b). Without repeatable measurements, the results in this paper could not be achieved. Due to superposition of multiple eigen modes and eigen frequencies, the TM transient response is a complex mixture of travelling and standing waves. Using the localized mechanical excitation, the spatial variations of mechanical properties can be investigated prior to the complex superposition of waves across the TM surface. Some of the videos of the results are available in the journal website (Razavi et al., 2016b).

8.1.1 Transient response of the eardrum Excited by localized mechanical forces

Chapter 4

Transient Response of the Eardrum Excited by Localized Mechanical Forces

P. Razavi, I. Dobrev, M. Ravicz, J.T. Cheng, C. Furlong, and J.J. Rosowski

Abstract The Tympanic Membrane (TM, eardrum) is the interface between the middle and outer ear and helps transform the variations in sound pressure in the ear canal into vibrations of the ossicles. However, the transient acoustic response of TM due to the complexity of wave interference, hinders the understanding of the motions. Therefore, to reduce this effect, local ($<1 \text{ mm}^2$ area) mechanical excitation rather than entire-surface acoustic loading is proposed. To focus on the initial stages of the evolution of motion, we have developed a high-speed digital holographic system based on local phase correlation method, enabling the acquisition of full-field displacements of the TM up to $10 \mu\text{s}$ temporal and 150 k points spatial resolution. A piezoelectric plunger equipped with a feedback load sensor excites the TM by a $50 \mu\text{s}$ click and the mechanical contact is guaranteed during the experiment by $>100 \mu\text{m}$ indentation of TM surface towards the camera. The results include characterization of wave travelling speed versus input force and localized mechanical properties, such as damping ratio, modal frequencies, and time constants. We expect that the results will lead to an improved understanding of the TM's localized material properties and modeling of the eardrum behavior.

Keywords Digital high-speed holography • Mechanical excitation • Otology • Transient response • Tympanic membrane

4.1 Introduction

Sound induced motions of the TM is the first stage of the hearing process, the TM transforms the sound energy into mechanical vibration in ossicles and causes the motion of hair cells in cochlea. Despite the past decades efforts of researchers, the complex motion of TM and its material properties have not yet been fully investigated [1–6]. Most of what is known of the transformation has been derived from measurements of the TM response to sound induced motion, however, most environmental sounds and speech contain acoustic transients such as click-like and chirp-like sounds. Based on our previous transient acoustic measurements, the motions start globally and are followed by complex motions that interfere, which limit the analysis and interpretation of their mechanics and extraction of mechanical properties [7, 11, 12, 13]. In this paper, we propose the use of our developed high speed digital holographic system and localized mechanical excitation to quantify the first stages of motion waves before their interference.

P. Razavi (✉)
Center for Holographic Studies and Laser micro-mechanics (CHSLT), Worcester, MA, USA
Mechanical Engineering Department, Worcester Polytechnic Institute, Worcester, MA, USA
e-mail: prazavi@wpi.edu

I. Dobrev
Center for Holographic Studies and Laser micro-mechanics (CHSLT), Worcester, MA, USA
University Hospital Zurich, Zurich, Switzerland

M. Ravicz • J.T. Cheng • J.J. Rosowski
Eaton-Peabody Laboratory, Massachusetts Eye and Ear Infirmary, Boston, MA, USA
Department of Otology and Laryngology, Harvard Medical School, Boston, MA, USA

C. Furlong
Center for Holographic Studies and Laser micro-mechanics (CHSLT), Worcester, MA, USA
Mechanical Engineering Department, Worcester Polytechnic Institute, Worcester, MA, USA
Eaton-Peabody Laboratory, Massachusetts Eye and Ear Infirmary, Boston, MA, USA
Department of Otology and Laryngology, Harvard Medical School, Boston, MA, USA

© The Society for Experimental Mechanics, Inc. 2016
S.A. Tekalur et al. (eds.), *Mechanics of Biological Systems and Materials, Volume 6*,
Conference Proceedings of the Society for Experimental Mechanics Series, DOI 10.1007/978-3-319-21455-9_4

31

We also report progress of our efforts to improve the capabilities of previously developed High-speed Digital Holographic System (HDHS), which utilizes a novel $2+N$ frame acquisition method based on hybrid spatio-temporal Local Correlation (LC) phase sampling approach [7–9]. The HDHS has the advantage of utilizing the temporal resolution of a high-speed camera without limiting its spatial resolution and the need of specialized optical setups [7, 10]. Automatic execution and synchronization of high-speed measurements is achieved by a custom control system. The high temporal (i.e., > 40 kHz) and spatial (i.e., > 150 k data points) measurement resolutions of the HDHS enable the investigation of the complex spatio-temporal behavior of the TM at a sufficient level of detail to further expand our knowledge of the hearing processes.

4.2 Methods

We have developed and implemented a novel high-speed $2+N$ frame acquisition method based on hybrid spatio-temporal local correlation (LC) phase sampling approach [8, 10], that allows quantification of the TM transient deformations by utilizing two reference frames, $I_{ref}, I_{ref+\pi/2}$, and N consecutive deformed frames, $(I_{def})_{i, i=1, 2, \dots, N}$, recorded before and throughout the evolution of an event, as shown in Fig. 4.1.

According to Fig. 4.1b, the $2+N$ frame acquisition method starts by recording two phase $\pi/2$ phase shifted reference frames, I_{ref} and $I_{ref+\pi/2}$, temporally separated to bypass the piezoelectric transducer (PZT) overshoot after the introduction of the phase shift [8]. While keeping the PZT at its $\pi/2$ position, a set of frames, $(I_{def})_{i, i=1, 2, \dots, N}$, i.e., deformed frames, are recorded at a rapid sampling rate (e.g., > 40 kHz) to capture the transient deformations of the TM. The corresponding spatio-temporal variation of the double-exposure optical phase change, $\phi(m, n, t)$, is quantified by correlating the intensities of each deformed and reference frames with

$$\phi(m, n, t) = \tan^{-1} \left[\frac{\rho(I_{ref}(m, n), I_{def}(m, n, t))}{\rho(I_{ref+\pi/2}(m, n), I_{def}(m, n, t))} \right], \quad (4.1)$$

where ρ is the Pearson's correlation coefficient for finite discrete sets having the recorded intensities as arguments and computed based on a spatial kernel (i.e., with dimensions of 3×3 or 5×5 pixels) centered around each measurement point, (m, n) , of a pair of reference and deformed frames [7, 8].

There is only one phase shift and the LC method is highly sensitive to the exact degree of the shifted phase. Furthermore, due to the physical constraints of the phase shifter device, as shown in Fig. 4.1b, the phase shifter experiences an overshoot and ringing after the $\pi/2$ phase shift. Additionally, there are other environmental factors such as room temperature and driver resolution which cause random inaccuracies in the phase shifter. To overcome the sensitivity of the LC method, we propose a continuous rather than a sudden phase shift in order to minimize the effect of position overshooting and randomness, as shown in Fig. 4.1c. In addition, by using a phase quality optimization algorithm, the frames corresponding to the best phase quality are chosen. This modification in the acquisition algorithm, has resulted in more repeatable and stable HDHS results. It has also eliminated the precision issues caused by nanometer errors introduced by the phase shifter and/or movements of other elements in the setup.

4.3 Representative Results

A post mortem human sample was characterized with the updated HDHS setup and with mechanical and acoustic stimuli. The TM was mechanically excited from the ossicular chain side and the middle ear was detached from the inner ear leaving some of the stabilizing ligaments and stapes intact. In this preparation, the sample maintains nearly all of its natural behavior during local excitation. A custom PZT actuator mounted on a three dimensional positioner excited the membrane locally at different regions, as shown in Fig. 4.1a. Due to the advantage of high-speed data acquisition, multiple sets of data can be acquired with negligible environmental effects, such that boundary condition effects, including changes in the sensitivity vector, sample dehydration, and excitation angle are negligible and the results are precise. Typical measurements consisting of at least 30 mechanical excitations at multiple locations and 12 acoustic excitations last less than 2 h. Representative results of individual acoustical and mechanical excitation measurements are presented.

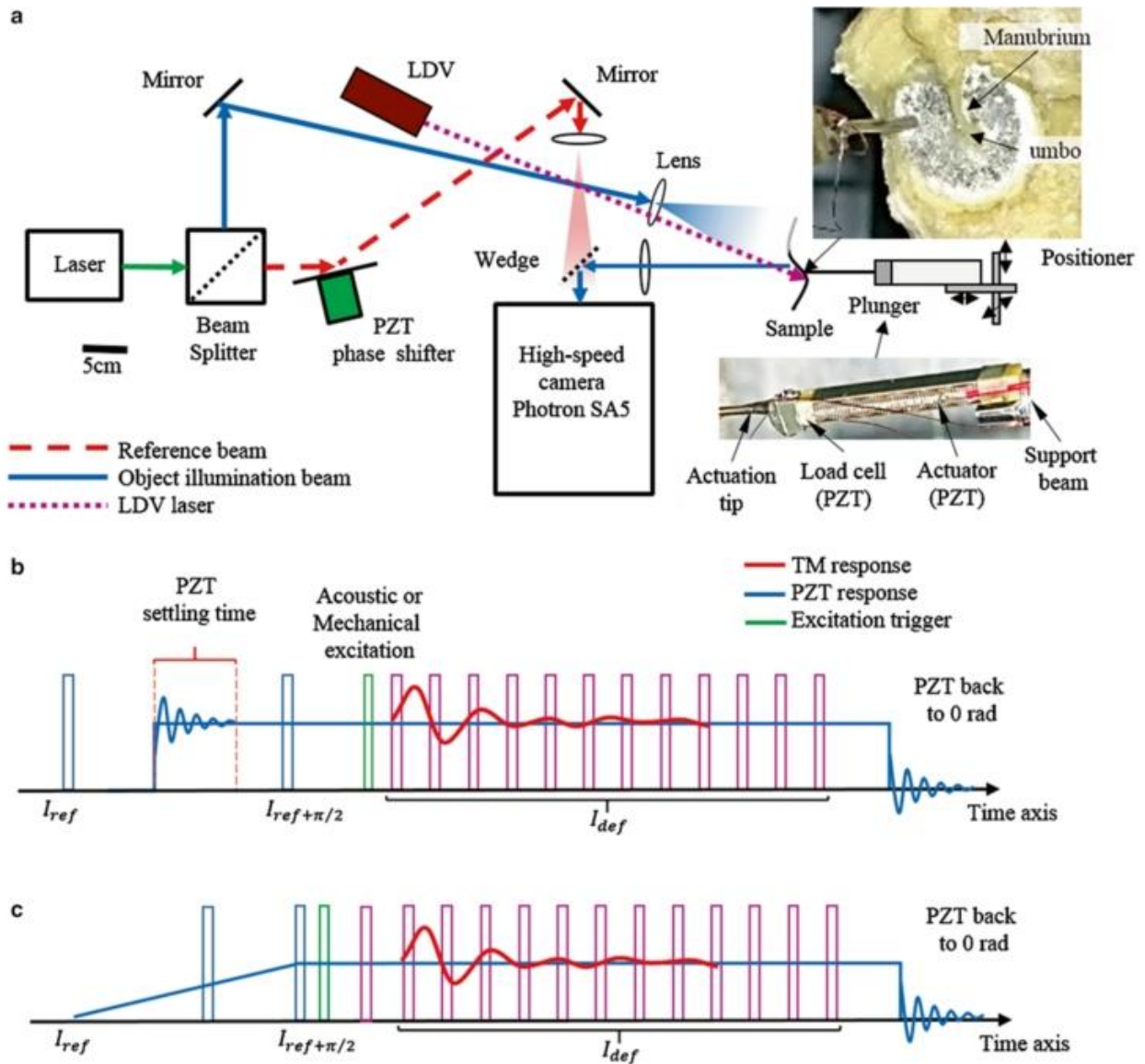


Fig. 4.1 Schematic representation of the HDHS and the acquisition timing diagrams: (a) HDHS setup showing the human TM sample subjected to localized excitation with a custom made plunger; (b) former timing diagram demonstrating the principle of operation of the high-speed $2+N$ frame acquisition method [7]; and (c) the modified continuous phase shifting method that reduces the effects of PZT oscillations at the beginning of data acquisition

4.3.1 Acoustic Excitation

The natural responses of the TM subjected to loading by acoustic clicks having a typical duration of $50 \mu\text{s}$ were investigated. The HDHS was used to measure the transient time waveform response of the TM at each point across the full-field-of-view, as shown in Fig. 4.2. Figure 4.2b depicts the deformations of the TM at six specific points of interest, including the umbo. Analysis of the deformations of the entire TM indicates that the maximum deformation occurs at $595 \mu\text{s}$ from the beginning of the acoustic excitation. At this state the manubrium and umbo experience their maximum deformations, which are followed by oscillations of other parts of the TM that include travelling waves as well as wave interference while the oscillations of the umbo are dampened rapidly. At the later stages of oscillations, the interpretation of the mechanics is challenging, typically $600\text{--}900 \mu\text{s}$ after the umbo reaches its maximum deformation.

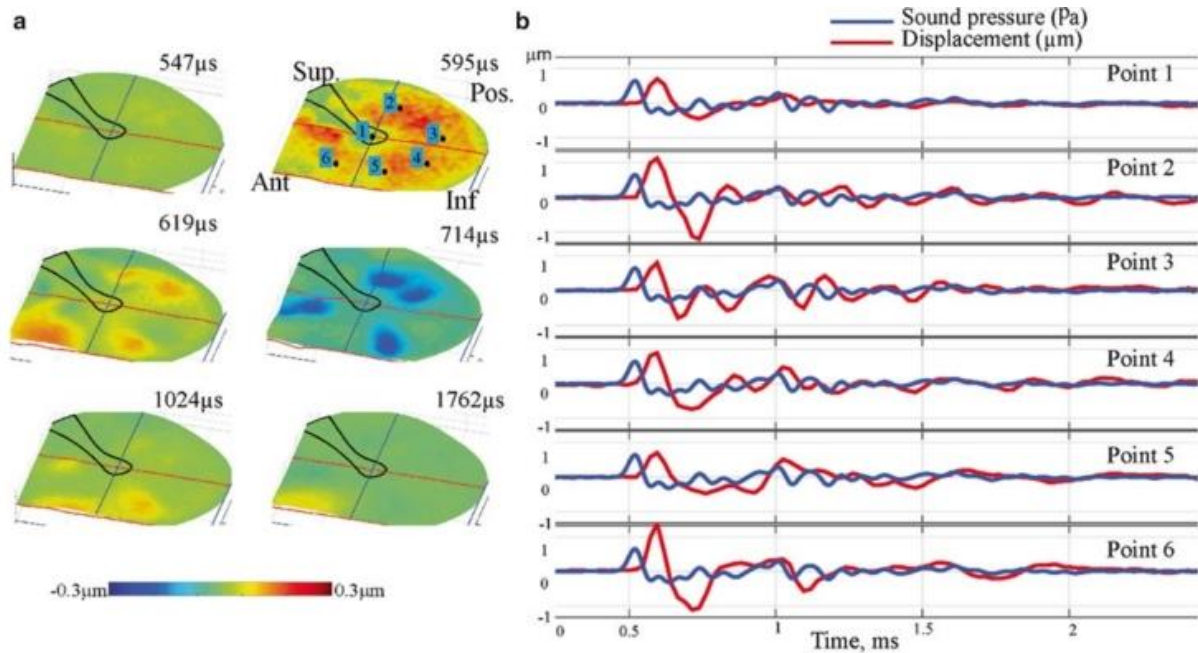


Fig. 4.2 Representative transient measurements of the TM subjected to acoustic excitation: (a) selected full-field motions at six temporal instances spanning the period from the beginning of the excitation to 1.7 ms; and (b) deformation and sound pressure vector at six specific points of interest as identified in (a) at 595 μ s

By analyzing the transient response of each 147 k points due to the impulse excitation, the natural frequencies and mode shapes up to 12 kHz can be calculated, including corresponding time constants, acoustic phase delay, mechanical damping, and local material properties. These characteristics are determined by analyzing the envelope of the decaying function in the time-displacement domain for every single point, as shown in Fig. 4.3.

4.3.2 Mechanical Excitation at Umbo

The role of the human tympanic membrane is to transform sound into mechanical energy and the umbo links the TM to the ossicular chain. Therefore, exciting the TM at the umbo location can help understand the energy transformation from the TM to the umbo and vice versa.

Figure 4.4 shows representative full-field measurements of transient deformations of the TM when mechanical excitation is applied at the umbo. The excitation was a 50 μ s square wave with amplitude of 500 mV and in order to maintain contact between the plunger and the TM during the measurements, the plunger was preloaded about 50 μ m into the surface of the TM. The results show that uniform deformation waves begin at the umbo and propagate around the manubrium to reach the TM ring. While the manubrium settles down after around 100 μ s the rest of the TM continues to oscillate for about 1.2 ms.

4.3.3 Mechanical Excitation at Other Regions

Following the mechanical excitation of the umbo, the TM was mechanically excited at other locations. To enable these measurements, the plunger was mounted on a three dimensional positioner to locate it at the following specific points of interest on the membrane, as shown in Fig. 4.5,

- a) posterior superior,
- b) posterior inferior,
- c) anterior inferior.

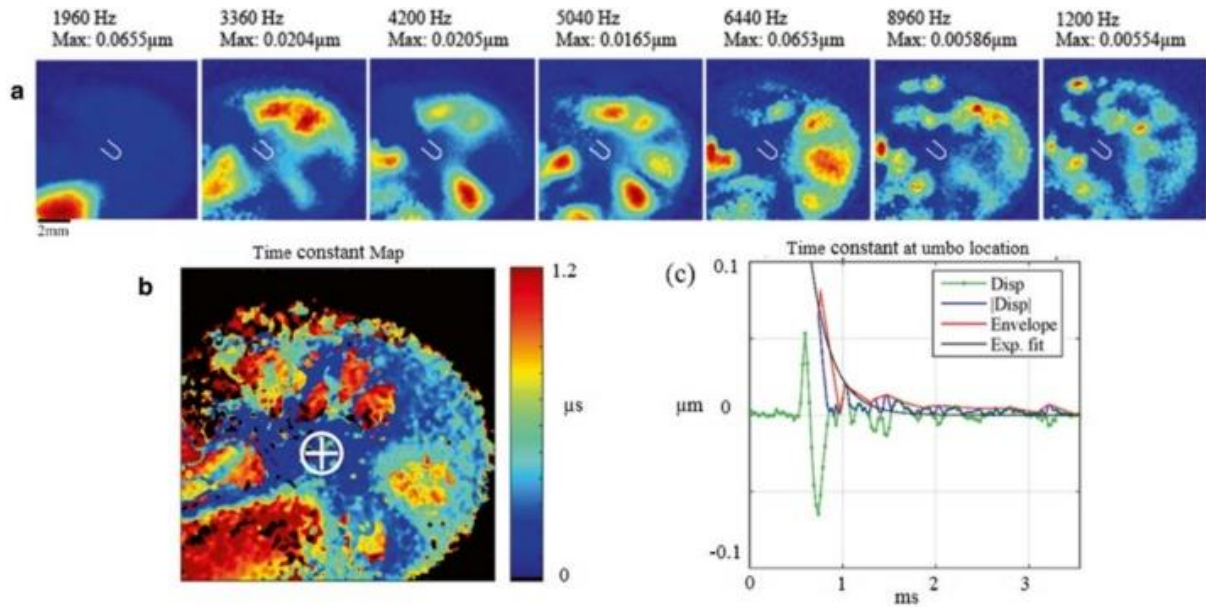


Fig. 4.3 Quantification of the acoustic stimuli results: (a) corresponding mode shapes, frequencies, and corresponding maximum displacements; (b) The time constant map of the full spatio-temporal motion, and; (c) time constant waveform at the umbo location marked by *circled plus* at part (b)

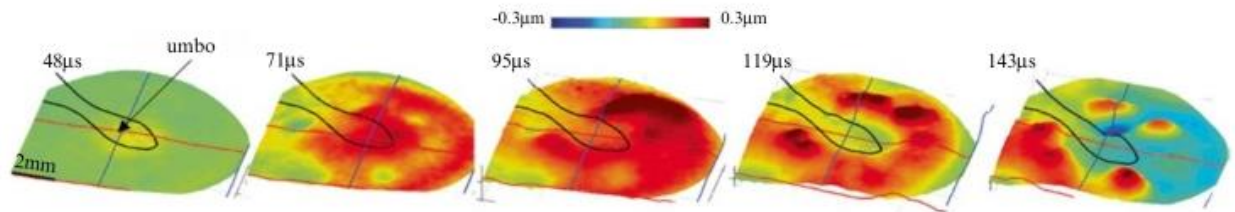


Fig. 4.4 Full-field of view displacement of the mechanical excitation at the umbo location

Figure 4.5 shows the mechanical response of the membrane from 71 to 167 μs , relative to the beginning of the excitation, for the three points of interest. We observed that after about 200 μs , the complexity of the motions increase to the point that their analysis and interpretation become cumbersome. Although we plan to investigate such complex motions in future works, some preliminary observations can be extracted from our current measurements. Specifically, for location (a), Fig. 4.3a, measurements indicate an overall higher amplitude of motions than at the other locations, (b) and (c), by about 0.2 μm . The motion starts clockwise with respect to the umbo as the center of rotation. We assume that the higher deformation is partially caused by a bony part of the manubrium located at the top left of the excitation, which stops the waves from moving counterclockwise. In this case all of the waves travel clockwise with a faster speed than at other locations. The arrows shown in Fig. 4.5 indicate the direction of wave propagation. The motion starts with a speed around 60–90 m/s and reaches the other side of the TM along the radial direction and it is followed by waves hitting the tympanic ring at the superior anterior quadrant and returning to the location of excitation. For locations (b) and (c), Fig. 4.5b–c, the motion spreads in both, clockwise and counterclockwise directions and the measured traveling wave speeds are around 40 m/s for location (b) and as low as 20 m/s for location (c). The maximum amplitude of displacement shows a reduction from location (a) to location (c). In all three locations, the manubrium undergoes reduced motions. The waves produced by mechanical excitation at the *pars tensa* of the TM tend to dissipate by interference rather than moving the umbo, which suggests that the TM dissipates local motions and filters them out. These measurements also suggest spatial variations of damping characteristics and mechanical properties across the TM surface. The shape of the deformations produced at the first moments of the mechanical impact as well as their temporal evolution can reveal the type of material model, e.g., isotropic or orthotropic, characterizing

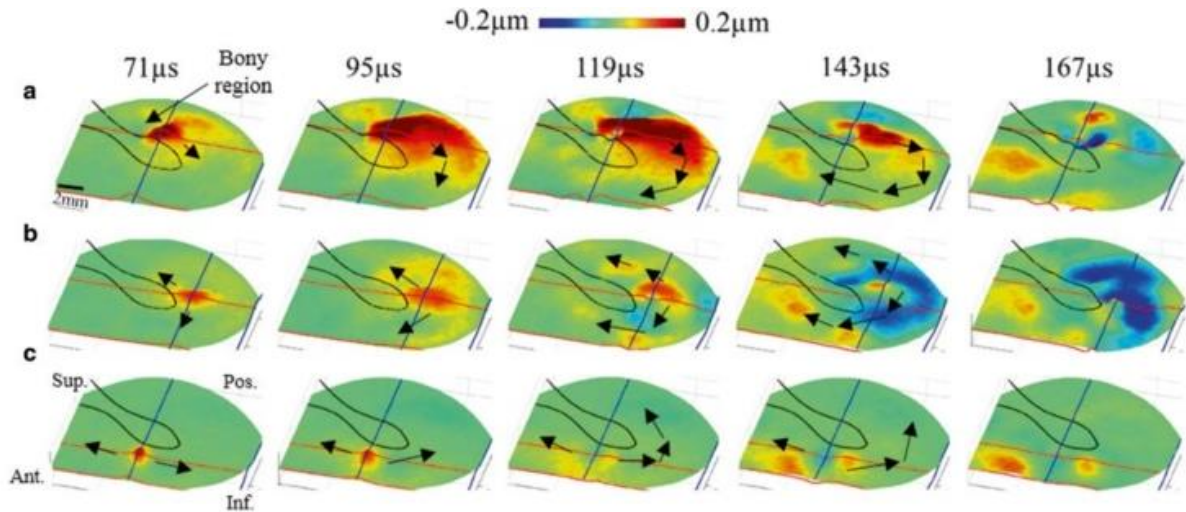


Fig. 4.5 Motion of the TM due to mechanical excitation at the three stated positions: (a) posterior anterior; (b) inferior posterior, and; (c) superior anterior (*Sup.* stands for superior, *Pos.* stands for posterior, *Inf.* stands for inferior and *Ant.* stands for anterior)

the material properties of the TM. Based on the measurements at locations (a) to (c) different wave propagation patterns and wave speeds can also suggest spatial variations of the thickness of the TM.

4.4 Conclusions and Future Work

Transient acoustic and mechanical excitation of the tympanic membrane are potential approaches to characterize the acousto-mechanical mechanical properties of the TM. There are a few available methods to characterize the transient nanometer scale motions of the TM with a sufficient temporal resolution throughout the audible range and with a spatial resolution to capture the complex motions that are developed during acoustic excitation. We have been developing high-speed digital holographic systems to measure transient events in the middle ear [7, 8]. In this paper, we report improvements to our novel HDHS system to further enhance its measuring accuracy and precision. By applying the updated HDHS to investigate acoustic (global) as well as mechanical (local) stimuli of the TM, we are able to capture the complex transient motions that are developed. Acoustic and mechanical transients provide distinct and complementary stimuli for the study of TM response. Further investigations includes analysis of the capabilities and the effectiveness of the two stimuli methods to determine TM properties such as spatial variations in dominant frequency, time constant, and wave propagation speeds. HDHS is enabling fundamental research on the initial transient dynamics of the TM, its relationship to the energy transfer into the middle-ear, and its connection to previous steady-state dynamics. HDHS will be further optimized for in-vivo applications in medical research and results will be reported in future publications.

Acknowledgements This work has been funded by the National Institute on Deafness and Other Communication Disorders (NIDCD), the National Institute of Health (NIH), the Massachusetts Eye and Ear Infirmary (MEEI), and the Mittal Fund. The authors should like to acknowledge the help of Morteza Khaleghi at the Center for Holographic Studies and Laser micro-mechaTronics (CHSLT) at Worcester Polytechnic Institute.

References

1. Rosowski, J.J., Cheng, J.T., Ravicz, M.E., Hulli, N., Hernandez-Montes, M., Harrington, E., Furlong, C.: Computer-assisted time-averaged holograms of the motion of the surface of the mammalian tympanic membrane with sound stimuli of 0.4–25 kHz. *Hear. Res.* **253**(1), 83–96 (2009)
2. Rosowski, J.J., Dobrev, I., Khaleghi, M., Lu, W., Cheng, J.T., Harrington, E., Furlong, C.: Measurements of three-dimensional shape and sound-induced motion of the chinchilla tympanic membrane. *Hear. Res.* **301**, 44–52 (2012). doi:10.1016/j.heares.2012.11.022

3. Khaleghi, M., Furlong, C., Ravicz, M., Cheng, J.T., Rosowski, J.J.: Three-dimensional vibrometry of the human eardrum with stroboscopic lensless digital holography. *J. Biomed. Opt.* **20**(5), 051028 (2015)
4. Puria, S., Allen, J.B.: Measurements and model of the cat middle ear: evidence of tympanic membrane acoustic delay. *JASA* **104**, 3463 (1998)
5. Tonndorf, J., Khanna, S.M.: Tympanic-membrane vibrations in human cadaver ears studied by time-averaged holography. *J. Acoust. Soc. Am.* **52**, 1221–1233 (1972)
6. Cheng, J.T., Hamade, M., Merchant, S.N., Rosowski, J.J., Harrington, E., Furlong, C.: Wave motion on the surface of the human tympanic membrane: Holographic measurement and modeling analysis. *JASA* **133**, 918 (2013)
7. Dobrev, I., Furlong, C., Rosowski, J.J., Cheng, J.T.: High-Speed Digital Holography for Transient Response of the Human Tympanic Membrane. *Adv. Opt. Methods Exp. Mech.* **3**, 337–342 (2015). doi:10.1007/978-3-319-06986-9_39
8. Dobrev, I., Furlong, C., Rosowski, J.J., Cheng, J.T., Harrington, E.J.: Implementation and evaluation of single frame recording techniques for holographic measurements of the tympanic membrane in-vivo. *Proc. SEM* **2013**(3), 85–95 (2014)
9. Georgas, P.J., Schajer, G.S.: Modulo-2pi phase determination from individual ESPI images. *Opt. Lasers Eng.* **50**(8), 1030–1035 (2012)
10. Pedrini, G., Osten, W., Gusev, M.E.: High-speed digital holographic interferometry for vibration measurement. *Appl. Opt.* **45**(15), 3456–3462 (2006)
11. Kemp, D.T.: Stimulated acoustic emissions from within the human auditory system. *JASA* **64**, 1386 (1978)
12. Puria, S.: Measurements of human middle ear forward and reverse acoustics: implications for otoacoustic emissions. *JASA* **113**, 2773 (2003)
13. Decraemer, W.F., Khanna, S.M., and Funnell, W.R.J.: Vibrations at a fine grid of points on the cat tympanic membrane measured with a heterodyne interferometer. In: *EOS/SPIE International Symposia on Industrial Lasers and Inspection, Conference on Biomedical Laser and Metrology and Applications*, 1999

8.1.2 Response of the human tympanic membrane to transient acoustic and mechanical stimuli: Preliminary results



Contents lists available at [ScienceDirect](http://www.sciencedirect.com)

Hearing Research

journal homepage: www.elsevier.com/locate/heares



Research paper

Response of the human tympanic membrane to transient acoustic and mechanical stimuli: Preliminary results



Payam Razavi ^a, Michael E. Ravicz ^{b, c, *}, Ivo Dobrev ^{a, 1}, Jeffrey Tao Cheng ^{b, c},
Cosme Furlong ^{a, c}, John J. Rosowski ^{b, c}

^a Center for Holographic Studies and Laser micro-mechaTronics, Worcester Polytechnic Institute, Worcester, MA, USA

^b Eaton-Peabody Laboratory of Auditory Physiology, Massachusetts Eye & Ear Infirmary, Boston, MA, USA

^c Harvard/MIT Division of Health Sciences and Technology, Cambridge, MA, USA

ARTICLE INFO

Article history:

Received 30 July 2015

Received in revised form

21 December 2015

Accepted 31 January 2016

Available online 12 February 2016

Keywords:

Tympanic membrane

Transient response

Click response

Mechanical impulse

Impulse response

Human

ABSTRACT

The response of the tympanic membrane (TM) to transient environmental sounds and the contributions of different parts of the TM to middle-ear sound transmission were investigated by measuring the TM response to global transients (acoustic clicks) and to local transients (mechanical impulses) applied to the umbo and various locations on the TM. A lightly-fixed human temporal bone was prepared by removing the ear canal, inner ear, and stapes, leaving the incus, malleus, and TM intact. Motion of nearly the entire TM was measured by a digital holography system with a high speed camera at a rate of 42 000 frames per second, giving a temporal resolution of $<24 \mu\text{s}$ for the duration of the TM response. The entire TM responded nearly instantaneously to acoustic transient stimuli, though the peak displacement and decay time constant varied with location. With local mechanical transients, the TM responded first locally at the site of stimulation, and the response spread approximately symmetrically and circumferentially around the umbo and manubrium. Acoustic and mechanical transients provide distinct and complementary stimuli for the study of TM response. Spatial variations in decay and rate of spread of response imply local variations in TM stiffness, mass, and damping.

© 2016 Elsevier B.V. All rights reserved.

1. Introduction

Though most characterizations of tympanic membrane (TM) response to sound have used steady-state tonal stimuli, most environmental sounds are transient in nature. Studies of TM motion in response to steady-state stimuli include, among others, Tonndorf and Khanna (1972), Khanna and Tonndorf (1972), Decraemer et al. (1989), and Cheng et al. (2010, 2013). In animals, an early holographic study (Dancer et al., 1975) examined guinea pig TM motion amplitude in response to acoustic transients, and de La Rochefoucauld et al. (2010) examined the gerbil middle ear response to clicks. Dobrev (2014) and Dobrev et al. (2014a) have demonstrated techniques to measure TM transient responses, but the complex response of the entire human TM to transients has not yet been studied in any detail.

As in most mammals, the human TM is attached to the tympanic ring along its edge and to the malleus manubrium at more central locations. Unlike in other mammals, the human TM is attached firmly to the manubrium at only two points: the umbo (extreme end of the manubrium) and the lateral process near the TM rim (e.g., Gea et al., 2010; De Greef et al., 2014). Between these two firm attachment locations is a thin epithelial fold, the plica mallearis, that attaches the TM to the manubrium (De Greef et al., 2016).

There is an ongoing debate about how different parts of the TM contribute to sound transmission to the middle ear with low- or high-frequency stimuli. For example, some have argued that the motion of the TM distant from the umbo contributes little to motion of the umbo (and the coupled ossicular chain and cochlea) at high frequencies (Tonndorf and Khanna, 1970, 1972; Shaw, 1977, 1982; Shaw and Stinson, 1981), while others suggest that the radial fibers within the TM help couple distant TM motions to the TM at all frequencies (O'Connor et al., 2008). The debate includes questions of how the response characteristics and mechanical properties of the TM may vary over its surface; for instance, the TM thickness and presumably its mass varies among regions (Van der

* Corresponding author. Eaton-Peabody Laboratory, Mass. Eye & Ear Infirmary, 243 Charles St., Boston MA 02114, USA.

E-mail address: mike_ravicz@meei.harvard.edu (M.E. Ravicz).

¹ Now at University Hospital Zürich, University of Zürich, Zürich, Switzerland.

Jeught et al., 2013), and different parts of the TM may have different natural frequencies (Fay et al., 2006).

Transients provide a means to investigate these ideas by determining how different parts of the TM contribute to middle-ear input. Sound stimuli activate the entire TM nearly identically and simultaneously (Ravicz et al., 2014), and motion of the umbo in response to acoustic transients (“clicks”) represents a summing of the contributions of the entire surface of the TM to umbo motion, where the contribution of different TM locations to the total umbo motion may vary with location and frequency. In contrast, mechanical transients (“pokes”) that directly stimulate only a discrete small region of the TM allow the assessment of how individual small regions contribute to the motion of the umbo. Transient stimulation also provides a rich data set for modeling, including the determination of best frequencies and damping along the membrane surface. Since transients contain many frequencies, TM responses to transients are amenable to modal analysis.

In this paper we investigate the response of the TM in a human cadaveric temporal bone to global transient stimuli (acoustic clicks) and to local transient stimuli (mechanical impulses) applied to several different locations on the TM. We present TM transient responses measured using a newly-developed high-speed holographic system capable of measuring TM motion over most of its surface with a temporal resolution of less than 24 μs (Dobrev et al., 2014a). We use this technique to acquire preliminary results with both clicks and pokes in the same bone to examine three questions: (1) How do TM responses to global and local transient excitation differ? (2) Do the mechanical properties of the TM differ among locations and, if so, how? (3) Do different parts of the TM contribute differently to umbo motion?

2. Methods

2.1. Preparation of specimens

A de-identified human temporal bone was collected by the Massachusetts Eye and Ear Infirmary and fixed for three weeks according to the method of Thiel (2002; Stieger et al., 2012).² The specimen was prepared by removing as much of the ear canal as possible, the inner ear, and the stapes to provide visual access to as much of the TM as possible. The TM, tympanic ring, and the malleus, incus, and their supporting ligaments were maintained (Fig. 1b, c). After preparation, the specimen was taken to the Center for Holographic Studies and Laser micro-mechaTronics at the Worcester Polytechnic Institute for holographic measurements. The lateral surface of the TM was painted with a zinc oxide (ZnO) solution to increase the reflectivity of the TM surface (Rosowski et al., 2009; Cheng et al., 2013). We have shown that neither the Thiel fixation nor the paint have a substantial effect on TM motion (Guignard et al., 2014; Cheng et al., 2013).

2.2. Stimuli and acoustic responses

Acoustic impulses (“clicks”) generated by a 50- μs square voltage pulse through a power amplifier (2100; NAD Electronics, Pickering, ON, Canada) were delivered to the lateral side of the TM by a loudspeaker (SB29RDC-C-4; SB Acoustics, Denmark) located about 12 cm laterally to the TM, at approximately 30° off axis. The click had a peak sound pressure of 10 Pa as measured by a microphone (ER-7; Etymotic Research, Elk Grove Village, IL, USA) positioned at the posterior TM rim (Fig. 1b). Examples of the voltage pulse and

resulting click waveform near the lateral TM surface are shown in Fig. 2a. Note that the (rarefaction) click waveform measured near the TM begins approximately 441 μs after the voltage pulse, due to the propagation time from the speaker to the TM. Irregularities in the click waveform after 500 μs are likely due to reflections off nearby structures. Because the middle ear was open, sound could reach the medial TM surface also, but the acoustic baffle action of the preparation and its mounting and the additional sound propagation distance to the medial TM reduced the significance of medial sound pressures on early TM responses.

Mechanical displacement impulses (“pokes”) in response to the same 50- μs square voltage pulse were delivered by a small actuator comprising a piezoelectric stack (PI P-882.51, Karlsruhe, Germany; 3 \times 2 \times 18 mm long) with a thin extension rod made of stainless steel hypodermic tubing (22 ga: 0.7 mm outer diameter (o.d.) \times 0.4 mm inner diameter (i.d.) \times 10 mm long) anchored in a 3 \times 2 \times 0.8 mm thick aluminum plate glued to the end of the piezoelectric stack to produce a contact area 0.7 mm in diameter. Pokes were delivered to the medial side of the TM at the umbo or at three other locations (Fig. 1c, d). The mechanical stiffness of the piezoelectric stimulator is very high, so the displacement amplitude of the poke stimulus was effectively the same among poke locations. The acoustic response to the poke was recorded by the microphone as described above. An example of the poke waveform is also shown in Fig. 2a. Spectra of these stimuli are shown in Fig. 2b. The spectral rolloff of the voltage stimulus at 20 kHz is consistent with the 50- μs voltage pulse width.

2.3. Measurement of TM motion

Motion of nearly the entire TM surface was measured by a high-speed digital holography system (Fig. 1a), which includes a continuous-wave (CW) 532 nm laser (SLIM-532, 50 mW; Oxixus, O’Fallon, MO, USA), variable ratio beam splitter, an optical phase shifter, a high-speed camera (SA5 1000 k; Photron, San Diego, CA, USA), and beam combining and imaging optics (Razavi et al., 2015a).

Digital holograms were recorded by splitting the laser into two beams, object and reference, by the use of a variable ratio beam splitter; see Fig. 1a. A reference/object beam power ratio of about two was used. The reference beam illuminated the camera detector, whereas the object beam was directed and expanded to illuminate the specimen. The irradiance that reflected off the specimen was captured by a telecentric lens and combined with the reference beam. The interference pattern of the two beams was digitized by the camera. Displacements of the TM toward the camera are described as in the positive direction.

High-speed acquisition was achieved by a novel high-speed 2 + N frame acquisition method (Razavi et al., 2015a) based on a hybrid spatio-temporal local correlation (LC) phase sampling approach (Dobrev et al., 2014a,b,c), that allows quantification of the TM transient deformations by utilizing two reference frames and N consecutive deformed frames recorded before and throughout the evolution of the event of interest. The high-speed camera capabilities allow for frame rates from 7000 frames per second (fps) at full resolution (i.e., 10⁶ pixels) to 10⁶ fps at reduced resolutions (i.e. 1000 pixels). For measurements of the TM transient motion presented in this paper, a trade-off was made by setting the camera at 384 \times 384 pixels and at 42 000 fps to achieve both (a) adequate spatial resolution (~22 μm per pixel) to resolve the complex deformation patterns of the TM and (b) adequate temporal resolution (<24 μs for 25 ms after the stimulus) to resolve the full hearing range bandwidth.

The amount of the TM we could measure was constrained by the field of view of the camera, which was limited by how completely

² The specimen was the left ear from a 71-year-old male and was frozen for approximately 2 years before being thawed and fixed.

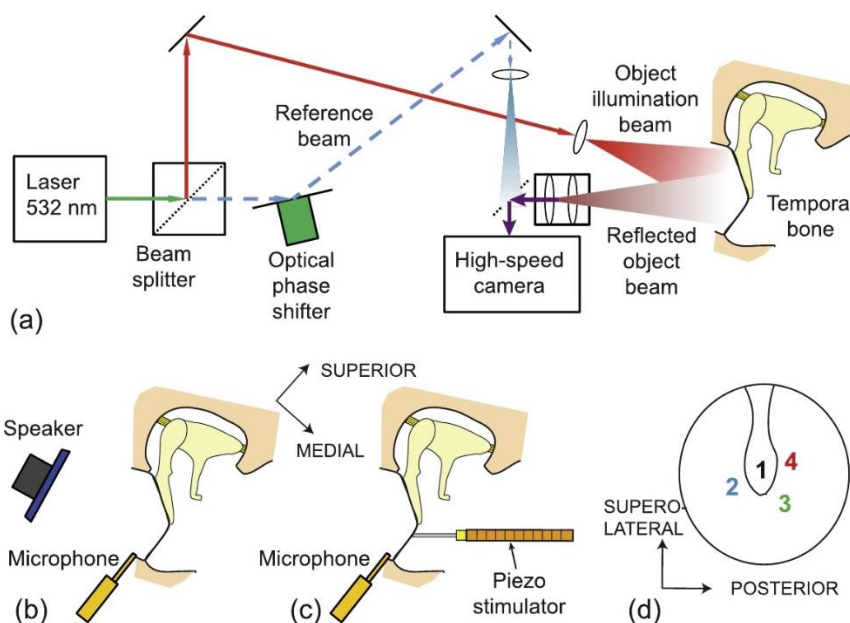


Fig. 1. (a) Schematic of high-speed laser holography system. A laser beam is split into reference (dashed) and object (solid) illumination beams. The object illumination beam reflects off the TM of the temporal bone specimen and creates an interference pattern with the reference beam in the high-speed camera. The stapes and cochlea were removed from the specimen, but the malleus and incus and their ligaments were preserved. (b) Acoustic clicks were delivered by a speaker near the lateral TM and measured by a microphone at the tympanic ring. (c) Mechanical pokes were delivered to the medial side of the TM by a piezoelectric stack actuator with extension located at the umbo (not shown) or at nearby locations (e.g., ~ 1.5 mm inferior to the umbo, shown here). (d) Schematic of TM showing poke locations.

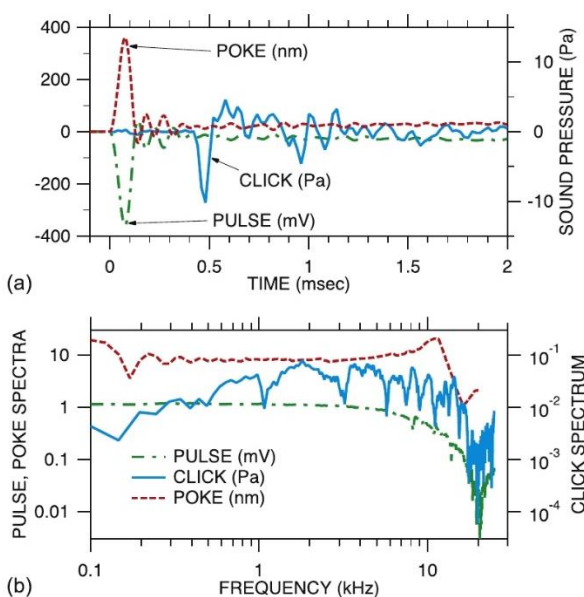


Fig. 2. (a) Waveforms of the acoustic click measured near the lateral TM surface (in Pa, solid, right axis), mechanical poke (in nm, dashed, left axis), and electrical pulse to speaker (mV, dot-dashed, left axis; electrical pulse to speaker was similar). (b) Spectral magnitudes of the waveforms in panel a.

we could expose the TM and by the focal length of the camera lens, all of which influenced the tradeoff between spatial and temporal resolution. Our choice of parameters provides sufficient field of view and spatial and temporal resolution for the measurements

and analyses described here. The displacement resolution and noise floor are about 10 nm.

3. Results

The results describe here are preliminary in nature, as they were obtained from one temporal bone. As such, they serve to illustrate the nature of transient responses observed and how they might be analyzed and interpreted. Measurements of poke responses were repeated after the bone had been removed, moistened, and replaced, with results very similar to those shown here.

3.1. Response to impulsive acoustic stimuli – clicks

Fig. 3a shows four maps of the displacement of the TM in response to an acoustic click. Each panel shows a map of the TM displacement at an instant in time after the click is produced by the speaker. Recall that the TM is a curved surface, so each panel shows the change in position of each visible point on the TM in response to the stimulus relative to the reference position (its position before the stimulus). The first panel (500 μ s) shows the TM at rest, before the TM has begun to respond to the click.³ Subsequent panels show the TM displacement at later instants in time relative to the reference state. (See video “Payam transient Fig. 3.mp4” in Supplemental Materials.)

Supplementary data related to this article can be found online at <http://dx.doi.org/10.1016/j.heares.2016.01.019>.

The entire visible TM responded nearly instantaneously to acoustic transient stimuli. For the initial response (571 μ s), the

³ This 500- μ s latency includes the acoustic propagation time from the speaker to the TM (see Fig. 2a).

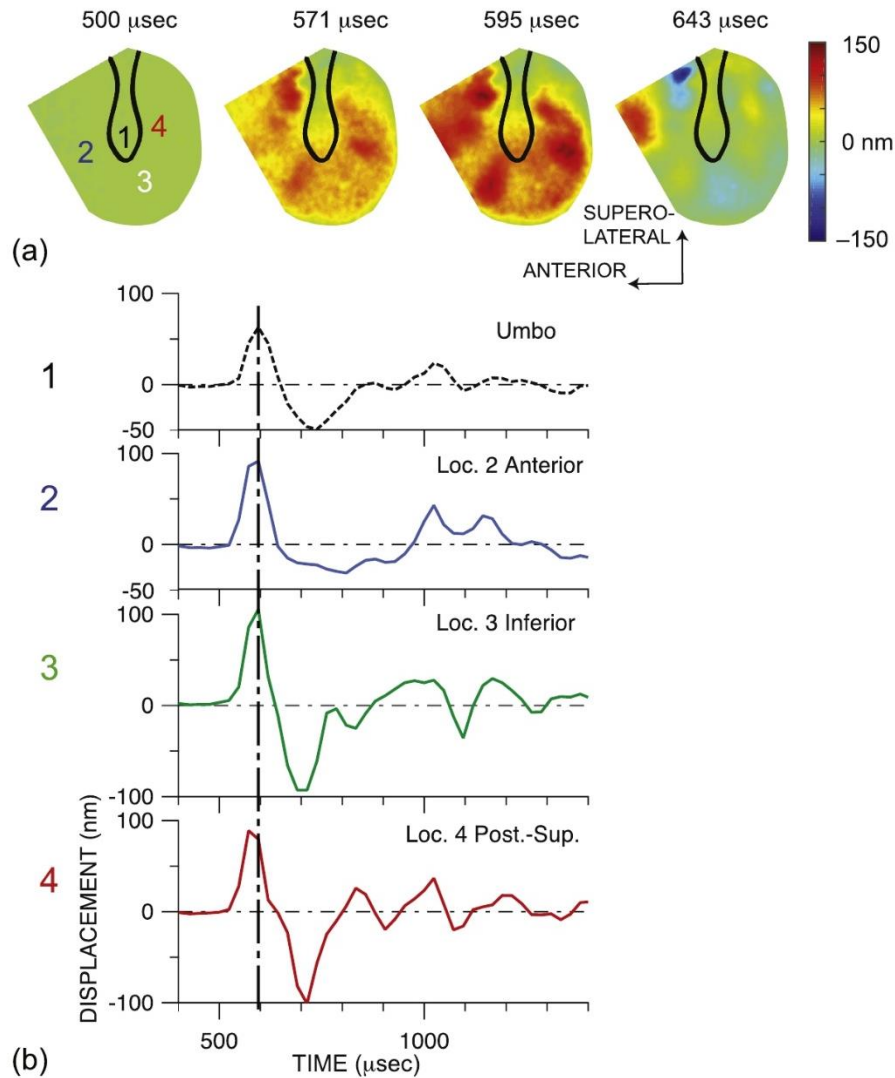


Fig. 3. (a) TM displacement maps at four representative instants following an acoustic rarefaction click: 500, 571, 595, 643 μ s. (b) Displacement waveforms at the umbo and three other TM locations (denoted 1, 2, 3, 4; see panel a) in response to an acoustic click. The response at each location is the mean over a 5×5 pixel array ($110 \times 110 \mu$ m) near the center of each numeral in panel (a). The vertical dot-dashed line shows the time of peak displacement response at the umbo (595 μ s). Positive displacement is toward the camera (laterally).

entire TM moved in phase, and the response peaked by about 595 μ s. By 643 μ s (about 95 μ s after the beginning of the response), a region anterior to the manubrium moved with substantial amplitude and with opposite phase to another area 1–2 mm posterior to it. After another 100 μ s or so (not shown), small areas of the TM moved with opposite phase. Because the middle ear was open, the click stimulus reached the medial side of the TM after a few hundred μ s and could have influenced later TM motion, but we saw no later uniform TM displacement that would be evidence of this. The early in-phase motion and higher motion amplitudes away from the umbo are consistent with previous observations (Dobrev, 2014; Dobrev et al., 2014a,b).

To facilitate comparisons of TM responses between stimulus type and location, we evaluate the TM response in more detail at a few locations of interest (first panel of Fig. 3a): Location 1 (Loc. 1) at the umbo, Loc. 2 1.6 mm anterior to the umbo, Loc. 3 1.5 mm

inferior, and Loc. 4 1.6 mm posterior and a little superior to the umbo. We compute the representative displacement at each of these locations as the mean of a 5×5 pixel array ($\sim 110 \times 110 \mu$ m) around the point about at the center of the numeral. The click-induced time waveforms of the TM displacement response at these locations are shown in Fig. 3b. The responses at all three locations on the TM (Locs. 2, 3, 4) began and peaked at about the same time (within the 24- μ s time resolution of our measurements), while the peak umbo response occurred slightly later (vertical line). The peaks of the waveforms at Locs. 2, 3, and 4 appear to be split between two time samples, which suggests that those peaks occurred about one-half sample ($\sim 12 \mu$ s) before the peak at the umbo. The amplitudes of these initial responses were smaller at the umbo than at other locations. At Loc. 4 (postero-superior to the umbo), the response 100–150 μ s later was of opposite sign and larger amplitude than the initial response.

3.2. Response to impulsive mechanical stimuli – “pokes”

3.2.1. At the umbo

Fig. 4a shows TM displacement maps of the response to a poke at the umbo. With this local stimulus, the TM responded first locally at the umbo (48 μ s), and the response spread approximately symmetrically and circumferentially around the umbo and manubrium (later panels). The time waveforms of TM displacement (Fig. 4b) at Locations 1, 2, 3, and 4 (as described in Fig. 3 above) show how the umbo response was maximal at 71 μ s (vertical line) and decayed monotonically and smoothly over the next 1000 μ s. The response peaked later at other

locations anterior, inferior, or postero-superior to the umbo (see Fig. 4a for map); and at Loc. 4 (postero-superior), the second response peak was larger than the first. By 143 μ s, anterior and posterior parts of the TM moved in opposite directions. As with acoustic clicks, the response was smaller at the umbo than at other locations. (See “Payam transient Fig. 4.mp4” in Supplemental Materials.)

Supplementary data related to this article can be found online at <http://dx.doi.org/10.1016/j.heares.2016.01.019>.

3.2.2. At other locations

Fig. 5 shows maps of TM displacement at three instants for

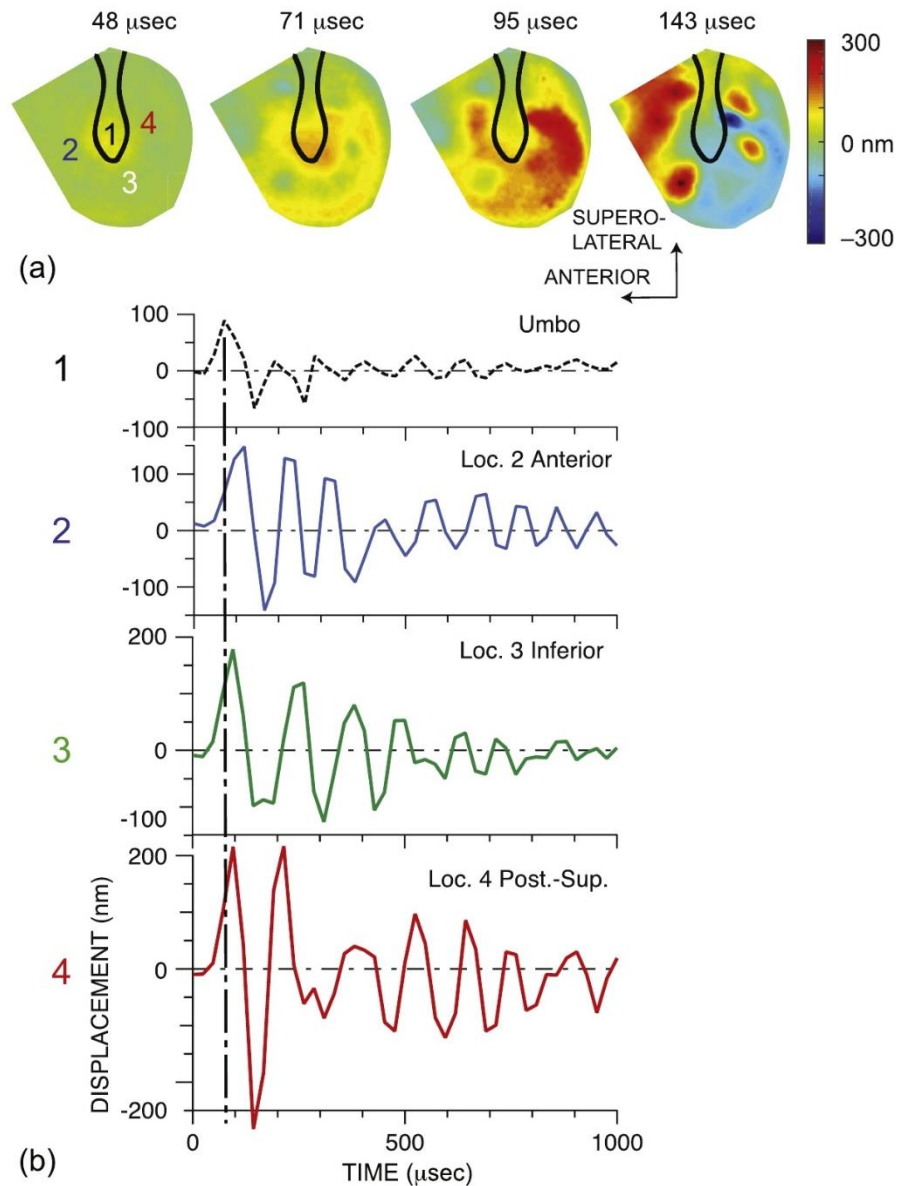


Fig. 4. (a) TM displacement maps at four consecutive instants following a mechanical poke at the umbo: 48, 71, 95, 143 μ s. (b) Displacement waveforms at umbo and three other TM locations (denoted 1, 2, 3, 4; see panel a) in response to a mechanical poke at the umbo. The response at each location is the mean over a 5×5 pixel array as described for Fig. 3. The vertical dot-dashed line shows the time of peak displacement response at the umbo (71 μ s).

identical pokes at the other stimulus locations: (a) Loc. 2 anterior, (b) Loc. 3 inferior, and (c) Loc. 4 superior–posterior to the umbo. With pokes at other locations, as with a poke at the umbo, the TM responded first locally at the site of stimulation, and the response spread approximately symmetrically and circumferentially around the umbo and manubrium. The first response at the poke location and the spread of the response are similar to previous observations (Dobrev, 2014). (See videos “Payam transient Fig. 5a.mp4”, “Payam transient Fig. 5b.mp4”, and “Payam transient Fig. 5c.mp4” in Supplemental Materials.)

Supplementary data related to this article can be found online at <http://dx.doi.org/10.1016/j.heares.2016.01.019>.

4. Discussion

4.1. Comparison of responses to global and local impulsive stimuli

In this section, we examine the response of the TM to global (acoustic clicks) and local stimuli (mechanical pokes) at the four locations described and discussed in Sec. 3 above (1, 2, 3, 4)

and at five additional locations for a more representative survey (2a, 2b, 3a, 3b, 4a). The locations are shown on a map of the TM in Fig. 6a and in order from antero-superior to postero-superior in Fig. 6b. The following figures in this section and the next display response properties at the TM locations in this order.

4.1.1. Timing and amplitude of responses to clicks and umbo pokes

The timing and amplitude of the first peak of the TM displacement response at different locations differed between a click stimulus and a poke at the umbo, as seen by comparing Figs. 3 and 4. Fig. 7 explores these response differences in more detail.

The timing of the first response peak (closed symbols) and the maximum response (open symbols) is shown for clicks and umbo pokes in Fig. 7a at each of the nine locations described in Fig. 6 above. For convenience and ease of comparison, the peak umbo response time to a click is aligned with the peak umbo response time to an umbo poke ($71 \mu\text{s}$ – see Fig. 4b).

Fig. 7a highlights differences and similarities in the TM

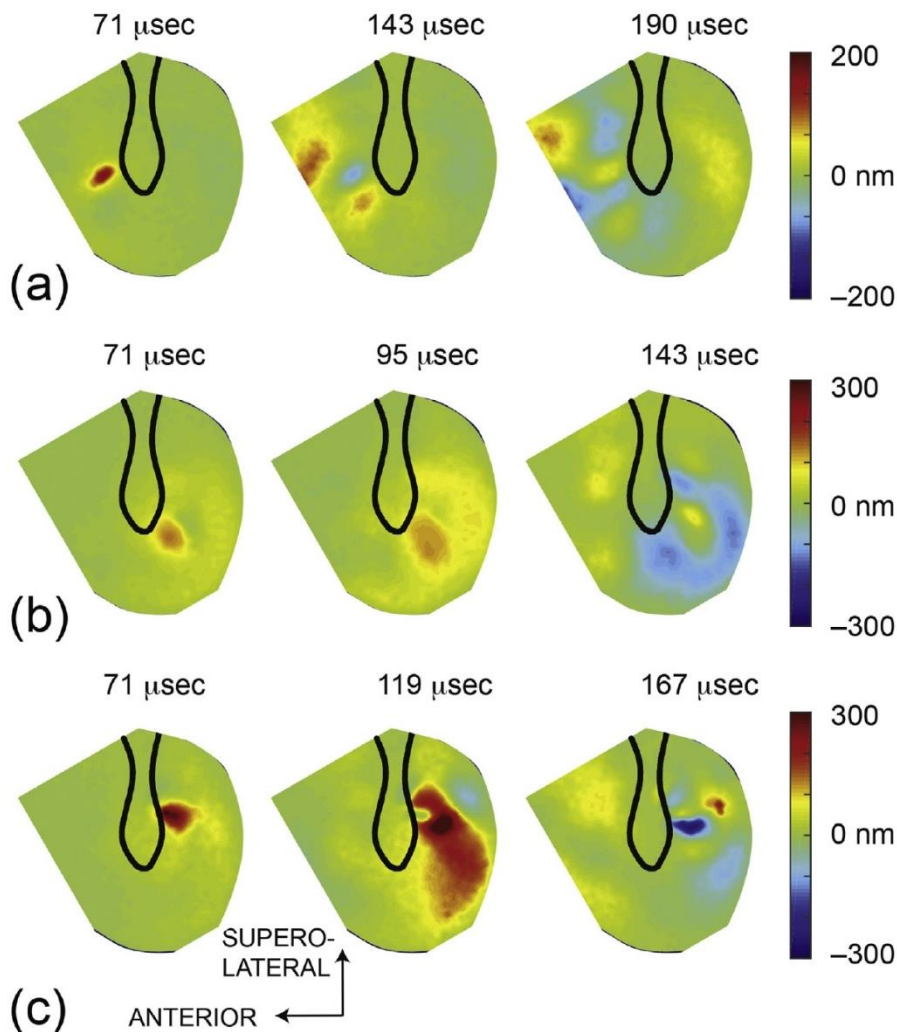


Fig. 5. TM displacement maps at various instants in response to a mechanical poke at (a) Loc. 2 anterior, (b) Loc. 3 inferior, and (c) Loc. 4 postero-superior to the umbo (see Fig. 4a).

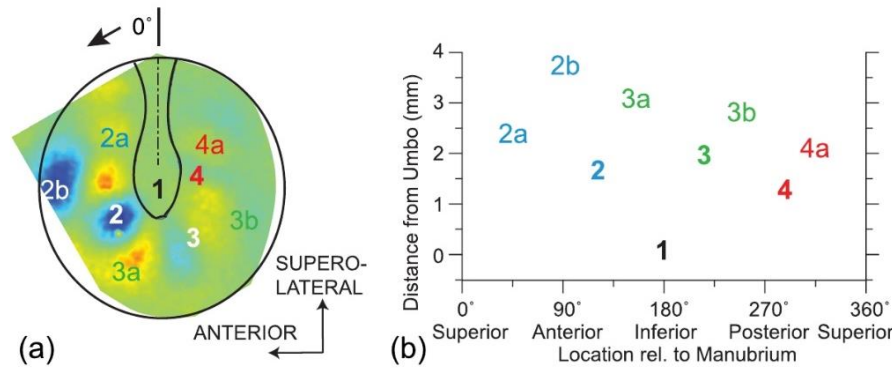


Fig. 6. (a) Outline of TM showing the 4 stimulus locations (1, 2, 3, 4) described in previous figures and 5 additional locations (2a, 2b, 3a, 3b, 4a) where TM displacement was evaluated. (b) Polar-coordinate representation of all 9 locations of interest. Horizontal axis: Azimuth from manubrium; vertical axis: radius from umbo.

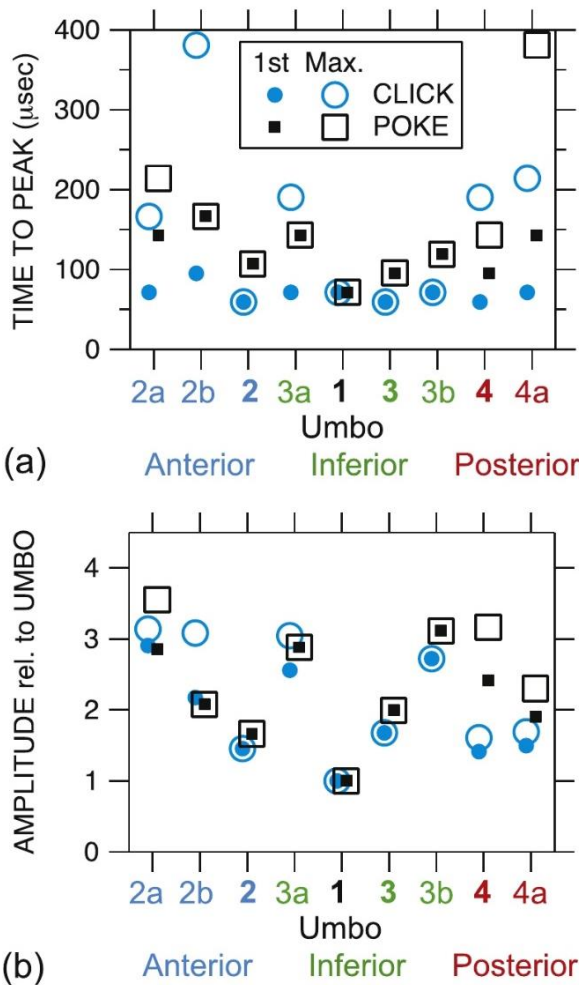


Fig. 7. (a) Time and (b) amplitudes of first response peak (filled symbols) and maximum response peak (open symbols), at each of the 9 locations where TM displacement was evaluated (over a 5×5 pixel array as described for Fig. 3), in order from antero-superior to postero-superior (as described in Fig. 6), for acoustic clicks (circles) and mechanical pokes at the umbo (squares). At locations with concentric symbols, the first response peak was the highest peak. For ease of comparison, click response times in (a) have been normalized to the umbo poke response time (71 μ s), and amplitudes in (b) have been normalized by the response amplitude at the umbo.

response to global (click) or local (poke) stimuli. (1) With click stimuli, the first response peak (filled circles) at most evaluation locations occurs at about the same time as the umbo (see Fig. 3). With umbo pokes (squares), the umbo responds first (see Fig. 4), and the response spreads radially and from more inferior to more superior locations: The locations closest to the umbo (2, 3, 4; see Fig. 6) respond next, and the locations most superior (2a, 4a) or further from the umbo (2b, 3a, 3b) respond later. (2) At locations inferior to the umbo (2, 3a, 3, 3b), the initial response peak to clicks and especially to pokes is also the maximum peak (open symbols), while at locations superior to the umbo (2a, 4a, 4b), the response builds over several hundred μ s.

The variations in the amplitudes of the first TM response peaks and maximum peaks with location, shown in Fig. 7b, show considerable commonalities between clicks and umbo pokes. For both stimuli, the response (normalized by umbo response) was smallest at the umbo (see Figs. 3, 4) and generally larger at locations further from the umbo (2a, 2b, 3a, 3b).

Fig. 7 also provides evidence of variations in mechanical coupling between different parts of the TM. The click and poke responses at the antero-superior and postero-superior locations (2a, 2b, 4, 4a) generally built up with time – the maximum displacement peak (open symbols) occurs later than the first peak – while at the other locations, the initial peak was the maximum. The buildup in response at these more superior locations suggests that motion of other parts of the TM contributed to the response at these locations, which in turn suggests that these locations were less tightly coupled to the umbo. The similarity in response characteristics among the other locations and the umbo suggests that these other locations have a tighter mechanical coupling to the umbo than the more superior locations.

4.1.2. Other aspects of click responses

As noted above and in Fig. 3, the peak umbo response to clicks occurs at 595 μ s, which is slightly later than other parts of the TM and about 100 μ s after the arrival of the click stimulus at the edge of the TM (476–500 μ s; see Fig. 2a). The 100 μ s delay between the click and the umbo displacement peak is of the same order of magnitude as the group delay observed previously between sound pressure near the umbo and umbo velocity (e.g., 68–92 μ s by Ravicz et al., 2004), attributed to the TM (32 μ s; O'Connor and Puria, 2008), or observed between ear-canal and cochlear sound pressures (83 μ s; Nakajima et al., 2009).

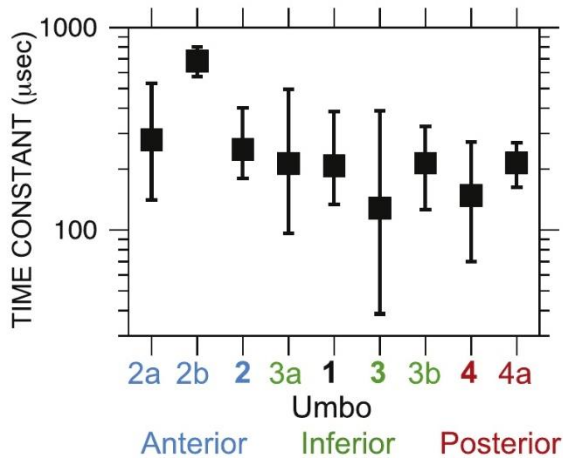


Fig. 8. Map of means (squares) and ranges of decay time constants (bars) at each of the 9 evaluation locations (Fig. 6), in order from anterior to posterior. Time constants were computed from responses to mechanical pokes at the umbo and the other three TM locations. Note logarithmic vertical scale.

4.2. Evidence of spatial variations in tympanic membrane mechanical properties

4.2.1. Decay time constants

The damping of the TM response is described by the decay time constant, defined as the time by which the response decays to $1/e$ of its maximum. Decay time constants were computed from the TM displacement waveforms at each of the nine locations in response to mechanical pokes by fitting a straight line to the logarithm of the rectified waveform between the initial peak and the first minimum.⁴ The means and ranges of the time constants are shown for the nine locations in Fig. 8. (Data at the poke location have been omitted, as the presence of the stimulator might affect the response decay.)

Though the range of decay time constants computed by this method was fairly large (about a factor of 20), the mean decay time constants computed from pokes at three or four locations were relatively uniform: Mean time constants generally varied between 150 and 250 μ s (squares) except at antero-superior Loc. 2b (680 μ s). The longer time constants observed at Locs. 2a and 2b suggest that TM mechanical damping may be lower in antero-superior parts of the TM than in other parts.

The values of (single) decay time constants we obtained by this fairly direct method are within the range of those (multiple) estimated from dynamic measurements on isolated TM samples (85, 5700 μ s; Zhang and Gan, 2013) or from finite-element models fit to TM responses to tones (6.6, 40, 255, 2500 μ s; De Greef et al., 2014) by less direct means. An advantage of our technique is that the effects of interactions between different TM regions excited by a global acoustic stimulus are minimized.

4.2.2. Response propagation velocities

Local wave propagation velocities along the TM surface were computed from poke response data at each of the nine evaluation

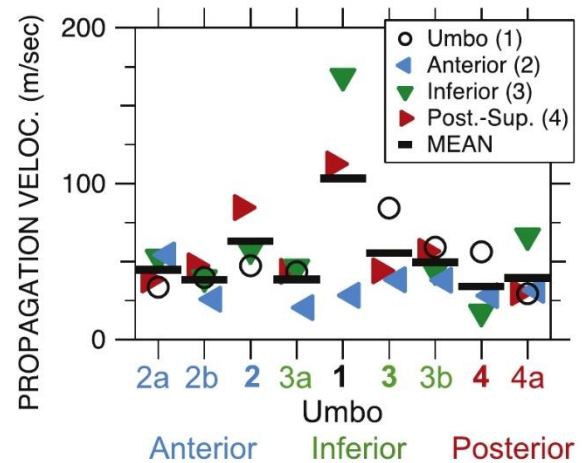


Fig. 9. Propagation velocities at locations of interest in response to mechanical pokes at various stimulus locations (see Fig. 6): umbo (1; open circles), anterior (2; left triangles), inferior (3; inverted triangles), and postero-superior (4; right triangles). Mean velocities at each location are shown by horizontal bars. Propagation velocities at poke locations for pokes at those locations were omitted.

locations. At each location, the propagation velocity was computed from the difference between the time of the first peak in the response at that location (Fig. 7) and the first response peak at the poke location, normalized by the linear distance between the evaluation location and the stimulus location from Fig. 6a. (For example, Fig. 6b shows linear distances between the evaluation locations and the umbo. Data at the poke locations for a poke at that location were omitted.) Fig. 9 shows the propagation velocity at each evaluation location from a poke at each stimulus location (symbols). For example: (a) the open circle at Loc. 4 indicates that a poke at the umbo produced a response at Loc. 4, 1.3 mm from the

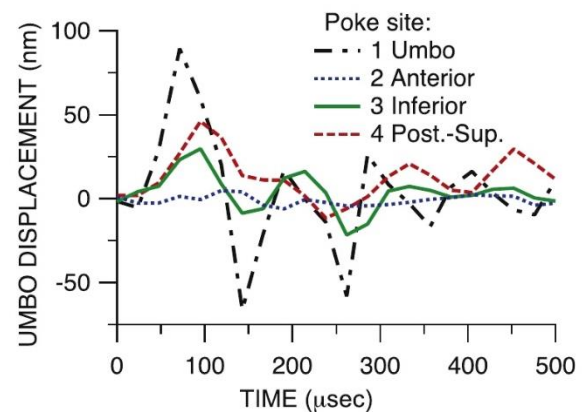


Fig. 10. Umbo displacement waveforms in response to a poke at the umbo or the three other TM stimulation locations.

umbo (Fig. 6b), whose initial peak was 24 μ s after the peak at the umbo, which implies a propagation velocity of 56 m/s between the umbo and Loc. 4; and (b) the right-facing triangle at Loc. 2 indicates that the initial response peak at Loc. 2 from a poke at Loc. 4 (3.0 mm away) occurred 36 μ s after the peak at Loc. 4, which implies a

⁴ The rectified waveforms generally showed several minima at different latencies from the initial peak (as in Dobrev, 2014, Fig. 13.10), which suggests that a full description of the TM viscoelastic behavior should include several time constants (e.g., De Greef et al., 2014). For simplicity, we examined only the decay to the first minimum.

Table 1

Amplitudes and latencies of first response peaks at Locations 1, 2, 3, and 4 to an umbo poke compared to umbo first response peak amplitudes and latencies in response to pokes at Locations 1, 2, 3, and 4.

Location	Displacement peak at Loc. from poke at umbo		Displacement peak at umbo from poke at Loc.	
	Displacement (nm)	Latency (μ s)	Displacement (nm)	Latency (μ s)
1 (umbo)	90	0	90	0
2 (anterior)	150	36	<10	59
3 (inferior)	180	24	30	12
4 (postero-superior)	220	24	46	24

propagation velocity of 85 m/s between Loc. 4 and Loc. 2.⁵ The means of these velocities at each location, computed from pokes at each of the stimulus locations, are also shown in Fig. 9 by the short horizontal lines.

The propagation velocities computed by this method ranged from 18 m/s (at Loc. 4 for a poke at Loc. 3) to 170 m/s (at the umbo for a poke at Loc. 3), but 80% of the velocities were between 26 and 67 m/s with a mean of 43 m/s. Velocities were highest from the inferior and postero-superior poke locations (Locs. 3, 4) to the umbo and anterior Loc. 2. Pokes at Loc. 3 (inferior; inverted triangles) generally produced the highest velocities to the other TM locations (62 m/s average among the other 8 locations), and pokes at Loc. 2 (anterior; left triangles) generally produced the lowest velocities (average 33 m/s). These velocity estimates are similar to those estimated from clicks (24 m/s; Dobrev, 2014) and a factor of 5–10 higher than traveling-wave velocities estimated from displacements measured with steady-state acoustic stimuli (tones; 3–13 m/s; Cheng et al., 2013). The propagation velocity is determined by the local mechanical properties, the local mass and stiffness (e.g., Fletcher, 1992); and the stiffness may be influenced by the local TM curvature. The variations in propagation velocities to and from different locations suggest that TM mechanical properties can vary over the TM.

4.3. Contribution of different TM locations to umbo displacement

Mechanical stimuli applied locally can also reveal the contribution of different parts of the TM to umbo response. Umbo displacement waveforms in response to pokes at different TM locations are shown in Fig. 10. The umbo response amplitude to a TM poke differed by poke location: The response was largest from a poke at the umbo, while a poke at Loc. 3 or Loc. 4 also produced a substantial response. In contrast, the response to a poke at anterior Loc. 2 was considerably smaller and barely distinguishable from noise.

The umbo displacements produced by pokes at these three TM poke locations were not well correlated with the response of those locations to a poke at the umbo, which can be seen in Table 1. An umbo poke produced the highest response at Loc. 4, and a poke at Loc. 4 produced the highest umbo response among the TM poke locations (except for the umbo itself). In contrast, an umbo poke produced large displacements at Locs. 2 and Loc. 3 that were larger than the umbo response, while a poke at Loc. 2 produced almost no umbo response. (The amplitude of the poke stimulus was effectively constant among poke locations, as mentioned in Sec. 2.2.) The large responses at Locs. 3 and 4 to an umbo poke and robust umbo response to pokes at Locs. 3 and 4 support the suggestion in Sec.

⁵ It should be kept in mind that the approximately 12- μ s timing resolution (24- μ s frame interval + half-cycle adjustment for response peaks split between samples) places a distance-related limitation on the precision of velocity estimates: For instance, the 12- μ s resolution limits the precision of the 56 m/s estimate of the velocity between the umbo and Loc. 4 1.3 mm away to about 30 m/s.

4.1.1 above that the inferior and posterior poke locations were fairly well coupled to the umbo. The low umbo response to a poke at Loc. 2 and the relatively long response latency between Loc. 2 and the umbo support the suggestion that the anterior poke location was less well coupled to the umbo.

The results from pokes at only three TM locations provide intriguing insights into the mechanical coupling between different parts of the TM and the relative contributions of different parts of the TM to the umbo response in the case of acoustic stimulation. Further work in this area is likely to be fruitful and may contribute to a rethinking of the best location on the TM for ossicular prostheses to couple sound energy efficiently from the TM to the inner ear.

5. Conclusions

1. Acoustic and mechanical transients provide distinct and complementary stimuli for the study of TM dynamics.
2. Systematic spatial variations in response time and amplitude, decay, and rate of spread of response imply the existence of local variations in TM stiffness, mass, damping, and coupling between different TM regions.
3. Knowledge of how these TM mechanical properties vary over the TM can influence the design of TM and ossicular prostheses.

Acknowledgments

We thank Nima Maftoon for helpful discussions and the staffs of CHSLT at the Worcester Polytechnic Institute and the Eaton-Peabody Lab. Funded by NIDCD R01 DC008642, the Massachusetts Eye & Ear Infirmary, the Worcester Polytechnic Institute, and the Mittal Fund.

References

- Cheng, J.T., Aarnisalo, A.A., Harrington, E., Hernandez-Montes, M. de S., Furlong, C., Merchant, S.N., Rosowski, J.J., 2010. Motion of the surface of the human tympanic membrane measured with stroboscopic holography. *Hear. Res.* 263, 66–77.
- Cheng, J.T., Hamade, M., Harrington, E., Furlong, C., Merchant, S.N., Rosowski, J.J., 2013. Wave motion on the surface of the human tympanic membrane: holographic measurement and modeling analysis. *J. Acoust. Soc. Am.* 133, 918–937.
- Dancer, A.L., Franke, R.B., Smigielleski, P., Albe, F., Fagot, H., 1975. Holographic interferometry applied to the investigation of tympani-membrane displacements in guinea pig ears subjected to acoustic impulses. *J. Acoust. Soc. Am.* 58, 223–228.
- De Greef, D., Aernouts, J., Aerts, J., Cheng, J.T., Horwitz, R., Rosowski, J.J., Dirckx, J.J.J., 2014. Viscoelastic properties of the human tympanic membrane studied with stroboscopic holography and finite element modeling. *Hear. Res.* 312, 69–80.
- De Greef, D., Goyens, J., Pintelon, I., Bogers, J.-P., Van Rompaey, V., Hamans, E., Van de Heyning, P., Dirckx, J.J.J., 2016. On the connection between the tympanic membrane and the malleus. *Hear. Res.* (this issue).
- de La Rochefoucauld, O., Kachroo, P., Olson, E.S., 2010. Ossicular motion related to middle ear transmission delay in gerbil. *Hear. Res.* 270, 158–172.
- Decraemer, W.F., Khanna, S.M., Funnell, W.R.J., 1989. Interferometric measurement of the amplitude and phase of tympanic membrane vibrations in cat. *Hear. Res.* 38, 1–18.
- Dobrev, I.T., 2014. Full-field Vibrometry by High-speed Digital Holography for Middle-ear Mechanics. Ph.D. dissertation. Worcester Polytechnic Institute, 245 pp.

- Dobrev, I., Furlong, C., Cheng, J.T., Rosowski, J.J., 2014a. Full-field transient vibrometry of the human tympanic membrane by local phase correlation and high-speed holography. *J. Biomed. Opt.* 19 (9), 096001.
- Dobrev, I., Furlong, C., Cheng, J.T., Rosowski, J.J., 2014b. Optimization of a lensless digital holographic microscope system for transient measurements of the human tympanic membrane. *Exp. Mech.* <http://dx.doi.org/10.1007/s11340-014-9945-4>.
- Dobrev, I., Furlong, C., Cheng, J.T., Harrington, E.J., Rosowski, J.J., 2014c. Implementation and evaluation of single frame recording techniques for holographic measurements of the tympanic membrane. In: Jin, Helena, Sciammarella, Cesar, Yoshida, Sanichiro, Lamberti, Luciano (Eds.), *In-vivo Advancement of Optical Methods in Experimental Mechanics*, vol. 3. Springer International Publishing, ISBN 9783319007670, pp. 85–92.
- Fay, J.P., Puria, S., Steele, C.R., 2006. The discordant eardrum. *Proc. Nat. Acad. Sci.* 103, 19743–19748.
- Fletcher, N.H., 1992. *Acoustic Systems in Biology*. Oxford Univ. Press, New York, p. 333.
- Gea, S.L.R., Decraemer, W.F., Funnell, W.R.J., Dirckx, J.J.J., Maier, H., 2010. Tympanic membrane boundary deformations derived from static displacements observed with computerized tomography in human and gerbil. *J. Assoc. Res. Otolaryngol.* 11, 1–17. Erratum in *J. Assoc. Res. Otolaryngol.* 11, 525.
- Guignard, J., Fullerton, B.C., Rosowski, J.J., Cheng, J.T., 2014. Unpublished data.
- Khanna, S.M., Tonndorf, J., 1972. Tympanic-membrane vibrations in cats studied by time-averaged holography. *J. Acoust. Soc. Am.* 51, 1904–1920.
- Nakajima, H.H., Dong, W., Olson, E.S., Merchant, S.N., Ravicz, M.E., Rosowski, J.J., 2009. Differential intracochlear sound pressure measurements in normal human temporal bones. *J. Assoc. Res. Otolaryngol.* 10, 23–36.
- O'Connor, K.N., Puria, S., 2008. Middle-ear circuit model parameters based on a population of human ears. *J. Acoust. Soc. Am.* 123, 197–211.
- O'Connor, K.N., Tam, M., Blevins, N.H., Puria, S., 2008. Tympanic membrane collagen fibers: a key to high-frequency sound conduction. *Laryngoscope* 118, 483–490.
- Ravicz, M.E., Rosowski, J.J., Merchant, S.N., 2004. Mechanisms of hearing loss resulting from middle-ear fluid. *Hear. Res.* 195, 103–130.
- Ravicz, M.E., Cheng, J.T., Rosowski, J.J., 2014. Sound pressure distribution within the human ear canal and models: forward stimulation. *J. Acoust. Soc. Am.* 136 (6), 3132–3146.
- Razavi, P., Dobrev, I., Ravicz, M., Cheng, J.T., Furlong, C., Rosowski, J.J., 2015a. Transient response of the eardrum excited by localized mechanical forces. In: Tekalur, Arjun, Srinivasan, Zavattieri, Pablo, Korach, Chad S. (Eds.), *Mechanics of Biological Systems and Materials*, 6. Springer International Publishing, pp. 31–37. ISBN: 10.1007/978-3-319-21455-9_4.
- Rosowski, J.J., Cheng, J.T., Ravicz, M.E., Hulli, N., Harrington, E.J., Hernandez-Montes, M.S., Furlong, C., 2009. Computer-assisted time-averaged holography of the motion of the surface of the tympanic membrane with sound stimuli of 0.4 to 25 kHz. *Hear. Res.* 253, 83–96.
- Shaw, E.A.G., 1977. Eardrum representation in middle-ear acoustical networks. *J. Acoust. Soc. Am.* 62 (Suppl. 1), S12.
- Shaw, E.A.G., 1982. The 1979 Rayleigh medal lecture: the elusive connection. In: Gatehouse, R.W. (Ed.), *Localization of Sound*. Amphora, Groton, CT.
- Shaw, E.A.G., Stinson, M.R., 1981. Network concepts and energy flow in the human middle ear. *J. Acoust. Soc. Am.* 69 (Suppl. 1), S43.
- Stieger, C., Candrea, C., Kompis, M., Herrmann, G., Pfiffner, F., Widmer, D., Arnold, A., 2012. Laser Doppler vibrometric assessment of middle ear motion in Thiel-embalmed heads. *Otol. Neurotol.* 33, 311–318.
- Thiel, W., 2002. Ergänzung für die Konservierung ganzer Leichen nach W. Thiel. *Ann. Anat.* 184, 267–269.
- Tonndorf, J., Khanna, S.M., 1970. The role of the tympanic membrane vibrations in middle ear transmission. *Ann. Otol.* 79, 743–753.
- Tonndorf, J., Khanna, S.M., 1972. Tympanic-membrane vibrations in human cadaver ears studied by time-averaged holography. *J. Acoust. Soc. Am.* 52, 1221–1233.
- Van der Jeught, S., Dirckx, J.J.J., Aerts, J.R.M., Bradu, A., Podoleanu, A.G., Buytaert, J.A.N., 2013. Full-field thickness distribution of human tympanic membrane obtained with optical coherence tomography. *J. Assoc. Res. Otolaryngol.* 14, 483–494.
- Zhang, X., Gan, R.Z., 2013. Dynamic properties of human tympanic membrane based on frequency-temperature superposition. *Ann. Biomed. Eng.* 41, 205–214.

8.2 In-vivo displacement measurements

The paper presented in this Section, describes our first successful measurements of the transient motions of a live mammalian TM using the proposed high-speed displacement measurement method described in Chapter 5 (Razavi et al., 2017a). This paper describes the state of holographic system prior to the developments of the high-speed MWHI shape measurements.

A costume-made otoscope was designed and incorporated onto the optical head of the high-speed holographic system to enable illumination and observation of a chinchilla TM with a larger field of view without complete removal of the boney part of the ear canal. This paper presents, to the best of our knowledge for the first time, the full-field transient response of a live chinchilla TM that shows the potential of the high-speed holographic measurements in determination of detailed response of TM in live samples. We also studied the difference in acoustically induced transient response of TM in live and post-mortem conditions.

The developments presented in Chapter 5 was the key milestone that enabled the measurements of nanometer-scale displacements in presence of the large (submillimeter) physiological motions. Although the HPCC algorithm was not used for these measurements, another relatively robust method based on phase quality determined the best reference frames from the continuous phase shifted reference holograms.

8.2.1 High-speed holography for in-vivo measurement of acoustically induced motions of mammalian tympanic membrane

Chapter 11

High-Speed Holography for In-Vivo Measurement of Acoustically Induced Motions of Mammalian Tympanic Membrane

Payam Razavi, Jeffrey Tao Cheng, Cosme Furlong, and John J. Rosowski

Abstract Measurements of human Tympanic Membrane (TM, eardrum) motions require nanometer and microsecond spatio-temporal resolutions while maintaining a field-of-view of about one centimeter. Previously, we have developed holographic methods to successfully measuring continuous and transient responses of post-mortem TM's. To expand our capabilities to in-vivo measurements, it is necessary to overcome such challenges as the influence of submillimeter physiological motions as well as the confined location of the TM. We are developing novel High-speed Digital Holographic Methods (HDHM) in combination with recently developed image and data processing algorithms to overcome such challenges. Our developments have unique capabilities that utilize the full spatio-temporal resolution of high-speed cameras (i.e., >147,000 points at >42,000 fps) to measure nanometer-scale TM motions in the audible range (0.02–20 kHz). We present preliminary holographic measurements made on an anesthetized chinchilla in a controlled anechoic chamber in-vivo and in-vitro. To the best of our knowledge, these data are reported for the first time and establish the potential of HDHM as a hearing research and clinical tool to further expand our understanding of the human hearing processes.

Keywords High-speed digital holography • In-vivo measurements • Middle ear mechanics • Transient acoustic excitation • Tympanic membrane

11.1 Introduction

The transformation of sound energy in mammalian middle ear to mechanical vibrations in inner ear is not yet well understood, while it is essential for understanding the hearing processes and diagnosis of middle ear diseases [1, 2]. TM is the interface between the middle and outer ear and transforms sound energy into mechanical vibrations of the ossicles. It is confined at the end of the ear canal and has a conical shape of about 1–3 mm depth and about 8 mm diameter in humans. TM is thin (50–150 μm) and consists of three distinct layers: mucosal, epidermis, and fibrous [2, 3]. Understanding the transformation of sound energy requires accurate measurement of the full-Field Of View (FOV) spatio-temporal motions, shape, and ultrastructure [3]. In addition, measurements of the TM motions are challenging because of required nano-meter displacement and micro-second temporal resolutions, while maintaining a FOV of about six orders of magnitude larger than its motions (~ 8 mm) [4].

Available quantitative clinical TM diagnostics tools such as tympanometry and Laser Doppler Vibrometry (LDV) lack full-field measuring capabilities. Holographic methodologies are powerful nondestructive testing tools that have been used in the past to enable full-FOV measurements of the vibrating patterns of the TM surface [5–7]. Løkberg et al. used electronic

P. Razavi (✉)

Center for Holographic Studies and Laser micro-mechaTronics (CHSLT), Worcester Polytechnic Institute, Worcester, MA, USA

Mechanical Engineering Department, Worcester Polytechnic Institute, Worcester, MA, USA

e-mail: prazavi@wpi.edu

J.T. Cheng • J.J. Rosowski

Eaton-Peabody Laboratory, Massachusetts Eye and Ear Infirmary, Boston, MA, USA

Department of Otolaryngology, Harvard Medical School, Boston, MA, USA

C. Furlong

Center for Holographic Studies and Laser micro-mechaTronics (CHSLT), Worcester Polytechnic Institute, Worcester, MA, USA

Mechanical Engineering Department, Worcester Polytechnic Institute, Worcester, MA, USA

Eaton-Peabody Laboratory, Massachusetts Eye and Ear Infirmary, Boston, MA, USA

Department of Otolaryngology, Harvard Medical School, Boston, MA, USA

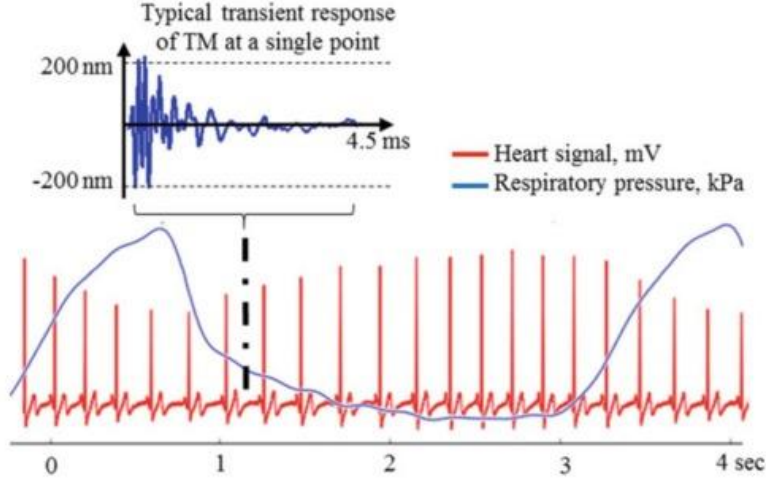
© The Society for Experimental Mechanics, Inc. 2017

C.S. Korach et al. (eds.), *Mechanics of Biological Systems and Materials, Volume 6*,

Conference Proceedings of the Society for Experimental Mechanics Series, DOI 10.1007/978-3-319-41351-8_11

75

Fig. 11.1 Typical timing diagram of heartbeat and respiratory signals together with typical transient response of TM measured at a single point and produced by an acoustic click



speckle pattern interferometry (ESPI) to obtain preliminary qualitative measurements of vibration of human TM in-vivo [8]. Previously, we have developed various holographic methods to measure steady state and transient responses of post-mortem TM's [4, 9–13]. However, measurements in live ears are adversely affected by physiological in-vivo motions due to respiration, blood circulation, and muscle motion [8]. To expand our capabilities to in-vivo measurements, it is necessary to overcome the following challenges:

- The influence of submillimeter physiological motions (i.e., breathing, heartbeat, tremor etc.) while measuring motions with nano-meter resolution, as illustrated in Fig. 11.1.
- Access to and orientation of the TM within the external ear necessitating a large depth of focus.
- Technological challenges, such as increases in the speed of measurements without compromising spatial resolution and measuring sensitivity.

11.2 Methods

To overcome the challenges mentioned above we advanced our holographic tools and developed High-speed Digital Holographic Methods (HDHM) to capture the transient motion of the TM at high frequencies (i.e., >10 kHz) nearly free from low frequency physiological motions. We have developed and implemented high-speed $2 + N$ frame acquisition methods based on hybrid spatio-temporal Local Correlation (LC) phase sampling approach that allows for quantification of the TM transient deformations by utilizing two reference frames, $I_{ref}, I_{ref+\pi/2}$, and N consecutive deformed frames, $(I_{def})_i$, $i \in 1, 2 \dots N$, recorded before and throughout the evolution of an event [9], shown in Fig. 11.2.

The timing diagram of the events occurring during measurements is shown in Fig. 11.2a. By use of continuous phase shifting method and developed phase quality optimization algorithm, two frames with $\pi/2$ phase shift is chosen from hundreds of the reference holograms to extract the exact undeformed state of the TM. Next, the sample desired excitation occurs. At the same time, while keeping the PZT at its $\pi/2$ position, a series of high-speed (e.g., >40 kHz) holograms $(I_{def})_i$, $i \in 1, 2 \dots N$, measure the TM motions [11]. The corresponding spatio-temporal variation of the double-exposure optical phase change, $\phi(m, n, t)$, is quantified by correlating the intensities of each deformed and reference frames with

$$\phi(m, n, t) = \tan^{-1} \left[\frac{\rho(I_{ref}(m, n), I_{def}(m, n, t))}{\rho(I_{ref+\pi/2}(m, n), I_{def}(m, n, t))} \right] \quad (11.1)$$

where ρ is the Pearson's correlation coefficient for finite discrete sets having the recorded intensities as arguments and computed based on a spatial kernel (e.g., with dimensions of 3×3 or 5×5 pixels) centered around each measurement point, (m, n) , of a pair of reference and deformed frames [9, 14]. Measuring accuracy of HDHM has been verified with Laser Doppler Vibrometry [9].

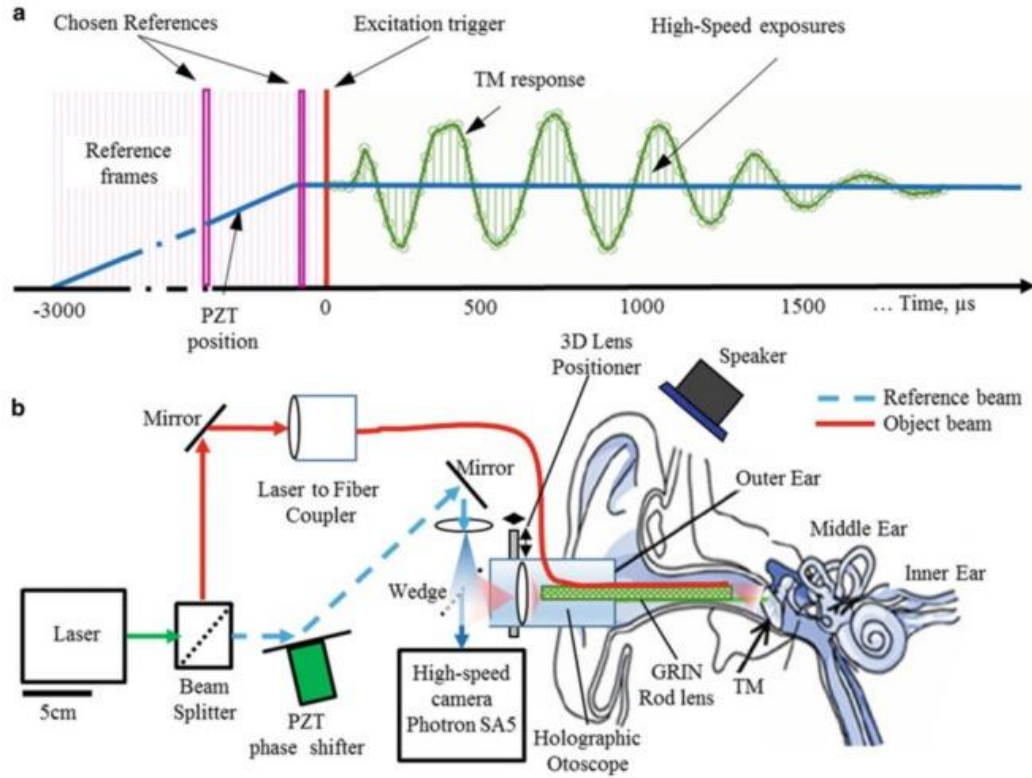


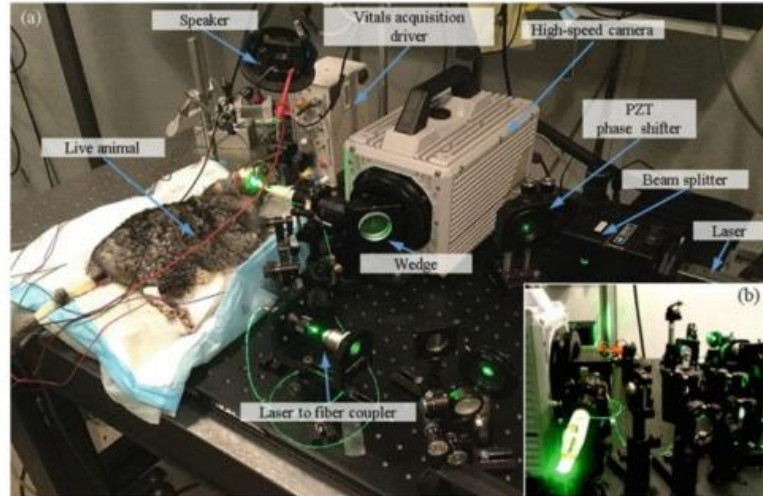
Fig. 11.2 Schematic representation of the HDHS and the acquisition timing diagrams: (a) timing diagram demonstrating the principle of operation of the high-speed $2 + N$ frame acquisition method [7]; and (b) schematic representation of the developed high-speed holographic system equipped with a custom-made otoscope. Illumination and observation inside the ear canal is performed by fiber optics and a GRIN INdex (GRIN) rod lens, respectively. The otoscope has a relatively large depth of focus, which is sufficient to measure motions of the cone-shaped TM

11.3 Experimental Setup

A portable setup with remotely controlled capabilities was realized at Worcester Polytechnic Institute (WPI) and moved inside a double-walled sound booth located in the facilities of the Massachusetts Eye and Ear Infirmary (MEEI). The HDHM setup includes a high-speed camera (Photron SA-5), a CW laser (532 nm, 50 mW), variable beam splitter, beam combiner wedge, mirrors, beam expanders, piezoelectric phase shifter, laser to fiber coupler and a holographic otoscope, as shown in Fig. 11.3. The laser beam is split into reference and illumination beams by use of a beam splitter. The illumination beam, after being coupled into a fiber optic waveguide, irradiates the TM through the ear canal. The object beam and the reference beam are combined at the CCD camera by use of the wedge. The sample is excited by a speaker (placed within 15 cm of the TM surface) with 50 μs square pulses that produce an acoustic click. The sound pressure variations at the surface of the TM are measured by a probe microphone. During the measurements, cooling fans associated with the laser and camera systems are switched off. All the measurements were repeated thrice consecutively with 100 ms intervals to investigate the repeatability of the motions under various environmental conditions.

All animal procedures were approved by the Massachusetts Eye and Ear Animal Care Committee. Chinchillas were anesthetized and remained so throughout the in-vivo measurements. The cartilaginous and bony part of ear canals were resected to expose the majority of the TM surface and the middle ear cavity was vented, but otherwise intact. The TM was painted with a thin layer of ZiO solution for improved reflectivity. After a series of in-vivo measurements, the animal was euthanized and measurements repeated without repositioning the animal.

Fig. 11.3 HDHM setup during live animal measurements: (a) opto-mechanical components inside a double-walled sound booth; and (b) view of the otoscope head



11.4 Representative Results

We report preliminary results of acoustically induced transient response of a chinchilla under two excitation amplitudes and two conditions: in-vivo and post-mortem.

11.4.1 Quantitative Full-Field-of-View In-Vivo Measurements

Two sets of three consecutive experiments were performed at two excitation levels for each of the pre- and post-mortem conditions. Figure 11.4 shows eight temporal instances of the normalized mean ($N = 6$) of these measurements together with the motions at six specific locations across the TM. Despite large physiological motions, highly repeatable measurements were recorded. In addition, a linear response of the TM under different loading conditions was observed.

11.4.2 Comparison of Pre- and Post-mortem Response of the TM in the time domain

We observed similarities and differences between live and post-mortem measurements, including:

- The motions in both live and post-mortem cases are very similar, including the size and location of motion maxima at the beginning of the response to the click (see the $143 \mu\text{s}$ panels in Fig. 11.5a), but the patterns diverge somewhat as time progresses (see the differences in magnitude and number of local maxima and minima at $1171 \mu\text{s}$).
- Similar conclusion can be drawn looking at the temporal response of selected location on the TM surface, Fig. 11.5b.
- Similar comparison of the time waveform of the displacements at different TM locations suggest the average decay time of the displacement is increased postmortem.
- The large increases in the decay time of the displacements seen post-mortem are consistent with post-mortem changes in the damping provided by the cochlear load.
- Maximum peak-to-peak motions of the membrane surface is increased by about 20 % in post-mortem condition.

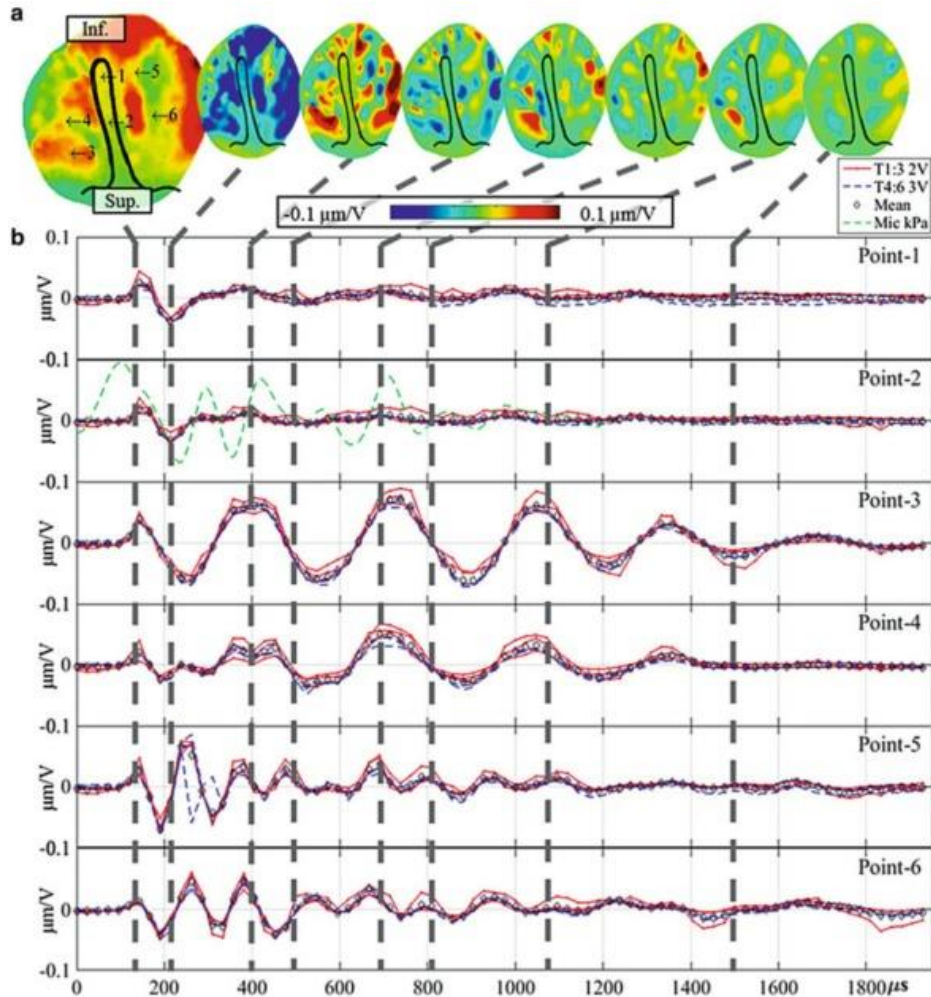


Fig. 11.4 In-vivo measurement results up to 1.8 ms; (a) mean ($N = 6$) displacement maps taken at eight temporal instances between 143 and 1500 μs . The color bar codes instantaneous displacements between $\pm 0.1 \mu\text{m/V}$. The map at 143 μs shows the umbo peak motion and the numbers and arrows indicate six locations where displacement versus time waveforms are plotted in (b). Point-1 is at the umbo, and the manubrium is outlined in black; (b) displacement waveforms at six locations normalized by the stimulus voltage are illustrated. At each location, six individual measurements at two different stimulus voltages (T1-3: 2 V and T4-6: 3 V) are plotted together with the corresponding mean, shown by open diamond. The sound pressure waveform recorded by the microphone is shown in green in the panel of point-2

11.4.3 Comparison of Pre- and Post-mortem Response of the TM in the Frequency Domain

FFT analyses were performed on the displacement waveforms at each point on the TM surface to define maps of the displacement magnitude, as shown in Fig. 11.6, at the frequencies with prominent spectral peaks obtained from the mean of the FFTs, as marked by circles in Fig. 11.7. After analysis of the results, the following was observed:

- The displacement maps show more spatially complex shapes with lower amplitudes in the in-vivo condition.
- The similarities of the frequencies of peak displacements in pre- and post mortem conditions suggest minimal changes in the mass and stiffness of the middle ear.

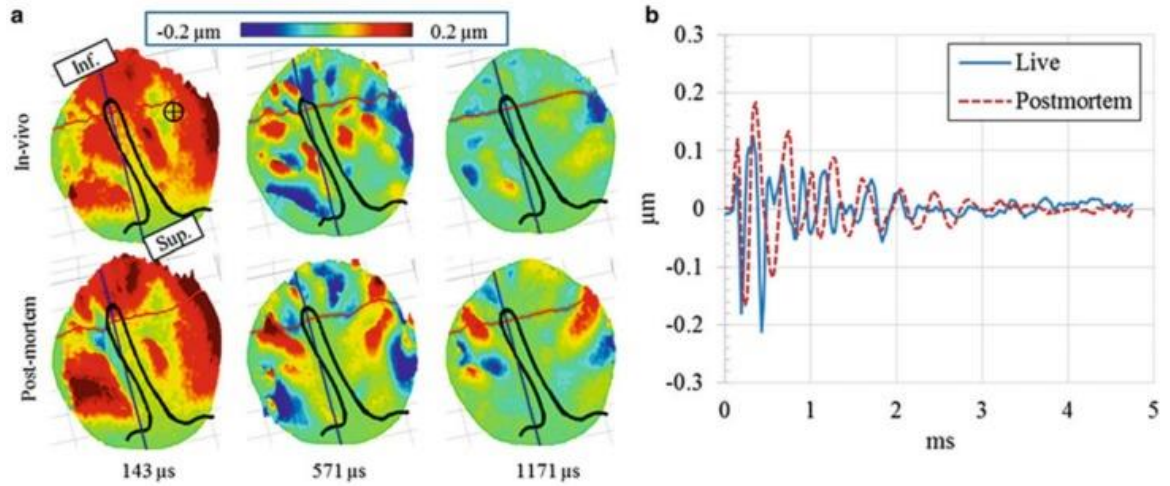


Fig. 11.5 Comparison of live and post-mortem spatio temporal evolution of motions in a chinchilla TM: (a) three temporal instances of full-FOV motions of the sample; and (b) temporal comparison of motions at the location shown with *circled plus* in (a)

Fig. 11.6 Maps of the displacement magnitudes at the spectral peaks isolated from Fig. 11.7 and identified by *open circle*

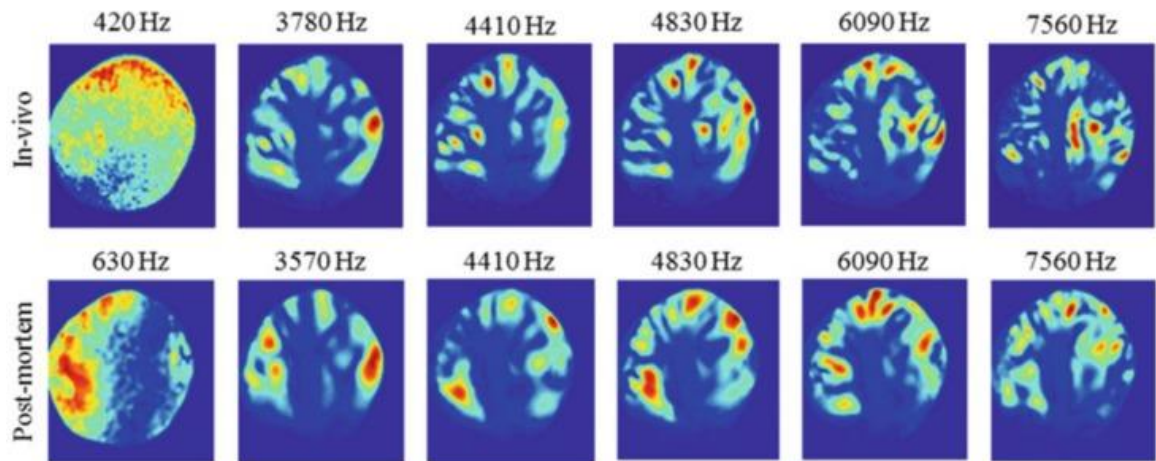
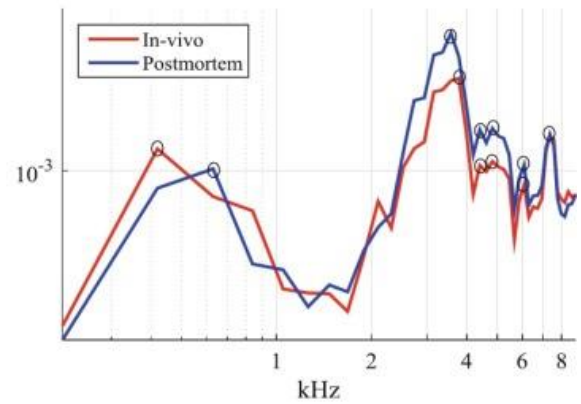


Fig. 11.7 Comparison of live and post-mortem spatio-temporal mean of the FFTs of the displacement waveform at each point. Selected spectral peaks are shown by *open circle*

11.5 Conclusions and Future Work

We report preliminary quantitative measurements of TM motions in full-FOV in a live animal. Our techniques provide high temporal (i.e., $<23.8 \mu\text{s}$) and spatial (i.e., $>100 \text{ k}$ data points) resolutions with nano-meter (i.e., $<15 \text{ nm}$) displacement sensitivity in the presence of physiological and environmental noises. We observed similarities and differences in the response of the TM in live and post-mortem conditions. The preliminary results establish the potential of HDHM as a hearing research and clinical tool to expand our understanding of human hearing. Future work includes the analysis together with the interpretation of the live and post-mortem measurements for further understanding of hearing function and potential medical applications. Fundamental research work will be focused on the initial transient dynamics of the TM, its relationship to the energy transfer into the middle ear, and its connection to previous steady-state dynamics research done by our group and others. In addition, further improvements of the opto-mechanical design of the holographic otoscope will be performed.

Acknowledgements This work has been funded by the National Institute on Deafness and Other Communication Disorders (NIDCD), the National Institute of Health (NIH), the Massachusetts Eye and Ear Infirmary (MEEI), NSF MRI program award: CMMI-1428921, and the Mital Fund. The authors would like to acknowledge contributions of Nima Maftoon, Melissa McKinnon, and Michael E. Ravicz from the MEEI and Ivo Dobrev and Koohyar Pooladvand from the CHSLT at the Worcester Polytechnic Institute.

References

1. Rosowski, J.J., Cheng, J.T., Ravicz, M.E., Hulli, N., Hernandez-Montes, M., Harrington, E., Furlong, C.: Computer-assisted time-averaged holograms of the motion of the surface of the mammalian tympanic membrane with sound stimuli of 0.4–25 kHz. *Hear. Res.* **253**, 83–96 (2009)
2. Decraemer, W., Funnell, W.: Anatomical and mechanical properties of the tympanic membrane. In: *Chronic Otitis Media: Pathogenesis-Oriented Therapeutic Management*, pp. 51–84. Kugler Publications, The Netherlands (2008)
3. Van der Jeught, S., Dirckx, J.J.J., Aerts, J.R.M., Bradu, A., Podoleanu, A.G., Buytaert, J.A.N.: Full-field thickness distribution of human tympanic membrane obtained with optical coherence tomography. *J. Assoc. Res. Otolaryngol.* **14**, 483–494 (2013)
4. Khaleghi, M., Cheng, J.T., Furlong, C., Rosowski, J.J.: In-plane and out-of-plane motions of the human tympanic membrane. *J. Acoust. Soc. Am.* **139**, 104–117 (2016)
5. Khanna, S.M., Tonndorf, J.: Tympanic membrane vibrations in cats studied by time-averaged holography. *J. Acoust. Soc. Am.* **51**, 1904–1920 (1972)
6. Tonndorf, J., Khanna, S.M.: Tympanic-membrane vibrations in human cadaver ears studied by time-averaged holography. *J. Acoust. Soc. Am.* **52**, 1221–1233 (1972)
7. del Socorro Hernández-Montes, M., Furlong, C., Rosowski, J.J., Hulli, N., Harrington, E., Cheng, J.T., Ravicz, M.E., Santoyo, F.M.: Optoelectronic holographic otoscope for measurement of nano-displacements in tympanic membranes. *J. Biomed. Opt.* **14**, 034023-034023-9 (2009)
8. Løkberg, O., Hagmoen, K., Gundersen, T.: Vibration measurement of the human tympanic membrane-in vivo. *Acta Otolaryngol.* **89**, 37–42 (1980)
9. Dobrev, I., Furlong, C., Cheng, J.T., Rosowski, J.J.: Full-field transient vibrometry of the human tympanic membrane by local phase correlation and high-speed holography. *J. Biomed. Opt.* **19**, 96001 (2014)
10. Razavi, P., Ravicz, M.E., Dobrev, I., Cheng, J.T., Furlong, C., Rosowski, J.J.: Response of the human tympanic membrane to transient acoustic and mechanical stimuli. *Hear. Res.* (2016). doi:10.1016/j.heares.2016.01.019
11. Razavi, P., Dobrev, I., Ravicz, M., Cheng, J.T., Furlong, C., Rosowski, J.J.: Transient response of the eardrum excited by localized mechanical forces. In: Tekalur, S.A., Zavattieri, P., Korach, C.S. (eds.) *Mechanics of Biological Systems and Materials*, Volume 6, pp. 31–37. Springer, Cham (2016)
12. Khaleghi, M., Furlong, C., Cheng, J., Rosowski, J.: Characterization of acoustically-induced forces of the human eardrum. In: Tekalur, S.A., Zavattieri, P., Korach, C.S. (eds.) *Mechanics of Biological Systems and Materials*, Volume 6, pp. 147–154. Springer, Cham (2016)
13. Khaleghi, M., Furlong, C., Cheng, J., Rosowski, J.: Thin-shell behavior of mammalian tympanic membrane studied by digital holography. In: Barthelat, F., Korach, C., Zavattieri, P., Prorok, B.C., Grande-Allen, K.J. (eds.) *Mechanics of Biological Systems and Materials*, Volume 7, pp. 19–25. Springer, Cham (2015)
14. Georgas, P.J., Schajer, G.S.: Modulo-2pi phase determination from individual ESPI images. *Opt. Lasers Eng.* **50**, 1030–1035 (2012)

8.3 Robust high-speed temporal phase sampling

In conventional holographic measurements, vibration isolation optical tables, controlled environmental and excitation conditions, are a necessary part of the measurements. One of the first requirements of the 2+N HCI method is the spatiotemporal stability of the sample during the phase shifting process. Using the continuous phase sampling and methods such as HPCC we demonstrated the possibility of determining the applied shift robustly by compensating for the nonlinearities of the phase shifter as well as sample rigid body motions (e.g., Section 8.1, 8.2, and Section 5.5.5). When it comes to a sample that is continuously deforming (i.e., a TM in a noisy environment), the repeatability of the 2+N HCI method is greatly degraded if the sample undergoes a non-uniform spatial phase shift. The short report presented in this section (to be submitted to one of the relevant journals in the field of high-speed holography) describes the methodological improvements after applying the HPCC method for each pixels to reconstruct the spatially uniform phase shifted reference frame. In this report, we briefly present how the developments of Chapter 5 can enable high-speed holography on samples with uncontrolled displacements that vary in space and time. The proposed method enhances the applications of high-speed holography for a broader range of samples that may not satisfy the environmental stability requirements of conventional holographic interferometry methods. Furthermore, this method also can relax the requirements of having a controlled excitation as the phase sampling can be done at any time during the continuous motions of the sample.

8.3.1 Noise immune high-speed holographic vibrometry

Abstract: A new temporal phase sampling method is presented that is immune to uncontrolled spatiotemporal object and setup vibrations. Temporal scan of a continuous phase shift provides the feedback to reconstruct spatially uniform phase shifted holograms.

1. Introduction

Quantification of interference phase require temporal or spatial phase sampling. Spatial phase sampling methods use a fraction of the spatial resolution (Kakue et al., 2011), while the temporal phase samplings sacrifice the temporal resolution. While a high-speed camera (>10 kHz) is designed to have large pixels for increased light sensitivity, they have lower spatial resolutions compared to conventional cameras (i.e., <1 Megapixels at >20 kHz). For many applications, it is desired to maintain both spatial and temporal resolutions. To address this need, we previously proposed a hybrid 2+N High-speed phase Correlation Interferometry (HCI) method to separate the temporal phase shift from the sample response (Ivo Dobrev et al., 2014a; Razavi et al., 2017c). This method requires a stable sample during the phase shift as well as a controlled excitation to enable transient response measurements. If the sample has large deformations during the phase shifting period, the applied phase shifts are not spatially uniform resulting in corrupted interference phase.

2. Method

The correlation (i.e., Pearson's) coefficient (ρ) between a small kernel (a group of pixels) centered at the same point (x,y) of reference I_{ref} and deformed I_{def} holograms provides the interference phase $\Delta\phi$ by ,

$$\rho(I_{ref}(x,y), I_{def}(x,y)) = \frac{(1+r(x,y))^2 + 4r \cos(\Delta\phi(x,y))}{(1+r(x,y))^2 + 4r}, \quad (1)$$

where r is the beam intensity ratio described as, $r(x,y) = I_o(x,y)/I_r(x,y)$, where I_o and I_r are the intensities of reference and object beams. Depending on the value of the interference phase, the correlation has a range between $\rho_{min} = (r-1)^2/((r+1)^2 + 4r)$ and $\rho_{max} = 1$. In actual measurements due to sensor and speckle noise the range of the correlation slightly shifts making the correlation range to be $[\rho_{min} - \epsilon, 1 - \epsilon]$ (Schmitt & Hunt, 1997). Quantification of the interference phase $\Delta\phi$ from Eqn. 1 requires:

- 1- The knowledge of the spatially varied ratio $r(x,y)$ which is not trivial due to the sensor noise effects
- 2- Resolving the sign ambiguity due to even cosine function (i.e., $\cos -\Delta\phi = \cos\Delta\phi$)

By capturing a series of continuously phase shifted high-speed holograms with at least a complete cycle of phase shift, the correlation coefficient between a reference frame (e.g., $t=t_0$) and the other phase shifted frames provide a harmonically repeating signal showing all the possible outcomes of the correlation at the specific pixel, that we call *correlation signal* - P. While we are interested in determining the phase value from the correlation results, the range of P at each pixel is adjusted to [-1 1] to remove the effect of spatially varying intensity ratio $r(x,y)$, in other words,

$$\cos(\Delta\phi(x,y,t_0,t_i)) = [(P(x,y)/a_2(x,y)) - a_1(x,y)] = P_{sc}(x,y,t_i), \quad (2)$$

where a_1 and a_2 are two constants determined by P to map its range from $[\rho_{min} - \epsilon, 1 - \epsilon]$ to $[-1,1]$ as shown in Fig.1, while the phase amplitude is determined by taking the arccosine of P_{sc} . For example, the frames having $P_{sc}=0$ has $\pi(2i-1)/2, i \in \mathbb{N}$ phase difference.

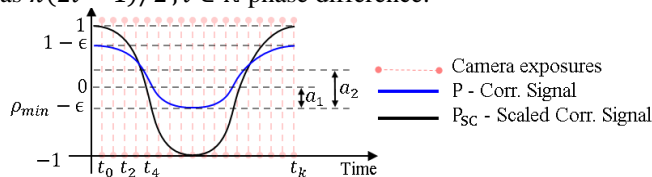


Fig.1. Schematics of the scaling of the correlation range from $[\rho_{min} - \epsilon, 1 - \epsilon]$ to $[-1,1]$ using a_1 and a_2 . To resolve the sign ambiguity taking the advantage of high-speed imaging, a temporal scan is performed from the reference frame- t_0 to frame- t_i determining the sign and number of cycles. This method provides the interference phase as long as the phase shifter can produce at least a complete cycle of phase shift in presence of spatiotemporal sample induced ones with sufficient temporal resolutions (i.e., >12 frames per cycle).

Although this method can directly find the interference phase, we use it as a feedback to determine the state of temporal phase shift at each pixel to account for spatiotemporally non-uniform sample/setup induced phase shifts. The scaled correlation signal at each pixel is determined (Fig. 2.a) while using an automated algorithm the timings (temporal instances of frames) at each point having a desired phase shift (i.e., $\pi/2$) are found. To show the concept, the results of an experiment on a latex membrane is shown in Fig.2.b. The sample was spatiotemporally deformed by a steady state tonal stimulation over the entire experiment length. The temporal distribution of the frames having $\pi/2$ phase shift with respect to the frame at $t=t_0$ was determined and shown in Fig 2.b.

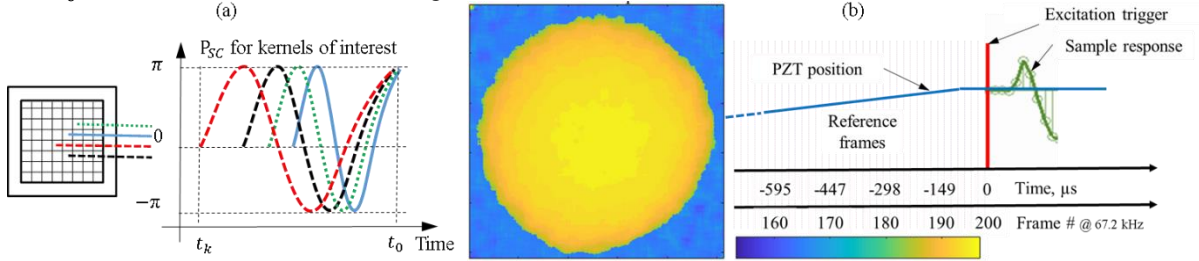


Fig.2. (a) schematic representation of determining P_{sc} for each pixel; and (b) the results of an experiment on latex membrane showing the capability of determining the distribution of frames having $\pi/2$ phase shift.

Using the information from the frames map of Fig 2.b, where each pixel describes the frame number with $\pi/2$ applied shift, we can reconstruct a new $\pi/2$ reference 'frame' in which the intensity of each pixel equals that of the corresponding pixel at the frame determined by the map of Fig 2.b. To show the difference between a reconstructed hologram and an intact one their subtraction in percentile of the sensor bit depth is shown in Fig.3.a. This reconstructed hologram is used in the 2+N correlation interferometric method to accept sample motions during the phase sampling period that widely increase the applicability of this method.

3. Results

These improvements made it possible to measure displacements on live samples undergoing large continuous deformations while the excitation may not be under control. Figure 3.c show response of an unmounted human skin (the person just put his arm in front of the camera) due to a continuous puff of air over the entire measurement.

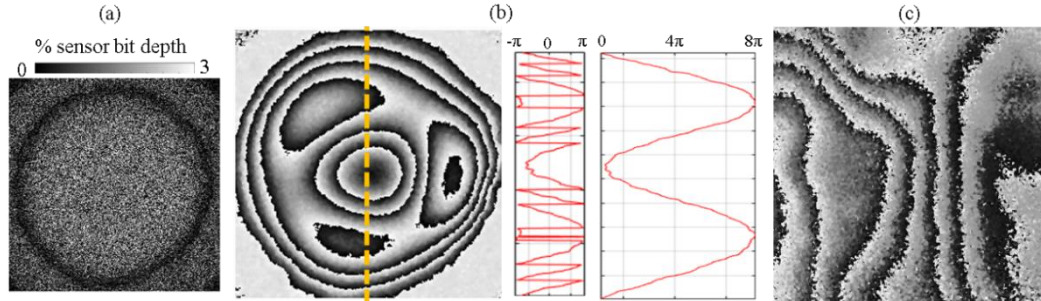


Fig.3. (a) subtraction of the reconstructed hologram with a camera frame; (b) wrapped phase using the reconstructed reference in the 2+N HCI method of the artificial sample of Fig.2.b; and (c) in-vivo human skin deformations in response to a continuous air flow demonstrating the phase sampling capability on moving samples.

4. References

- [1] T. Kakue, et al., "High-speed phase imaging by parallel phase-shifting digital holography," *Opt. Lett.* - 36, pp. 4131-4133 (2011).
- [2] P. Razavi, C. Furlong, and J. D. Trolinger, "Full-Field Digital Holographic Vibrometry for Characterization of High-Speed MEMS," in *Advancement of Optical Methods in Experimental Mechanics: (Experimental and Applied Mechanics, FL, 2017)*, pp. 41-47.
- [3] I. Dobrev, C. Furlong, J. T. Cheng, and J. J. Rosowski, "Full-field transient vibrometry of the human tympanic membrane by local phase correlation and high-speed holography," *JBO* - 19, pp. 096001-096001, (2014).
- [4] D. R. Schmitt and R. W. Hunt, "Optimization of fringe pattern calculation with direct correlations in speckle interferometry," *Appl. Opt* 36, pp. 8848-8857, (1997)

8.4 High-speed multi-resolution shape and displacement measurements

This section describes the methodological and hardware developments of the high-speed shape measurement method. The paper presented in this section is accepted for the proceeding of the 2018 Society of Experimental Mechanics (SEM, 75th anniversary, July 2018). The utility of the HPCC methods in phase quantification in the presence of continuous wavelength variations enabled multi-resolution shape measurements to be made milliseconds before displacement measurements. The results presented in this paper, show the multi-resolution shape measurements has the capability to determine the shape at near optimum resolution of the sensor by adjusting the contour depth with respect to each sample conditions.

The design of the high-speed measurement system enabled adding shape measurement capability without sacrificing any of the advantages of the high-speed holographic displacement measurement method. Using the unique hardware design, two lasers with different properties are used in a single measurements series using the same imaging optics so that nearly the same optical axis and sensitivity vector are used for both displacement and shape measurements. The hardware design allows for replacements of the imaging optics by an endoscope without any major modifications, to enable future endoscopic shape and displacements measurements. Furthermore, the high-speed multi-resolution MWHI (Section 6.2) shape measurements described in this paper provide the shape at the optimum contour depth in a single measurement. In a sample with unknown absolute depth, conventional MWHI methods require multiple lengthy measurements or multiple independent laser sources.

8.4.1 High-speed shape and transient response measurements of TM

High-speed shape and transient response measurements of tympanic membrane

Payam Razavi^{1,2}, Haimi, Tang^{1,2}, Nima Maftoon^{3,4}, Jeffrey Tao Cheng^{3,4},
John J. Rosowski^{3,4}, and Cosme Furlong^{1,2,3,4}

¹ Center for Holographic Studies and Laser micro-mechaTronics (CHSLT),

² Mechanical Engineering Department, Worcester Polytechnic Institute, Worcester, MA USA

³ Eaton-Peabody Laboratory, Massachusetts Eye and Ear, Boston, MA USA

⁴ Department of Otology and Laryngology, Harvard Medical School, Boston, MA USA

Abstract

We are developing a High-speed Digital Holographic (HDH) system to measure acoustically induced transient displacements of live mammalian Tympanic Membrane (TM) for research and clinical applications. To date, the HDH can measure one-dimensional displacements along one sensitivity vector. However, TM shape is also needed for some applications. Furthermore, because of the TM's tent-like shape and angled orientation inside the ear canal, 1-D measurements need to be combined with measurements of the shape and orientation of the TM to determine the true surface normal (out-of-plane) displacements. To enable shape measurements capabilities into our HDH, a tunable laser (linewidth <300 kHz, 770.2-790 nm, <8 nm/s) is incorporated in tandem with the single frequency (linewidth <100 MHz, 532.3 nm) laser that is used for displacement measurements in order to define a common sensitivity vector. Interferograms gathered with continuous high-speed optical phase sampling and wavelength tuning allow the reconstruction of the TM shape with <50 μm and <120 μm measuring resolution and repeatability, respectively. With our modified HDH, shape measurements are followed by transient displacement measurements (>67 kHz, <15 nm spatiotemporal resolutions) in response to broadband acoustic click excitations (50 μs duration). Both shape and displacement measurements can be made within less than 150 ms, which enable measurements under disturbances introduced by breathing and heartbeat. Therefore, enabling potential future measurements in vivo. Representative shape and displacement measurements capabilities are demonstrated on human temporal bones under normal and pathological conditions.

Keywords: endoscopic, holographic interferometry, multiple wavelength, shape measurement, transient response, tympanic membrane.

1. Introduction

The displacements at each point of the surface in a holographic interferometric measurement of deformation, give rise to the optical path length difference. The optical path length in an off-axis configuration is shown in Fig. 1-a, as the summation of the magnitudes of the blue *path-vectors* $\mathbf{r}_1, \mathbf{r}_2$. The *propagation-vectors* ($\mathbf{k}_1, \mathbf{k}_2$) along each path-vector show the direction of the light array with an amplitude of $2\pi/\lambda$ (wave number, k) such that their dot product with the corresponding path-vector (e.g., $\mathbf{r}_1 \cdot \mathbf{k}_1$) provides the optical path length in cycles of light (phase cycles) [1].

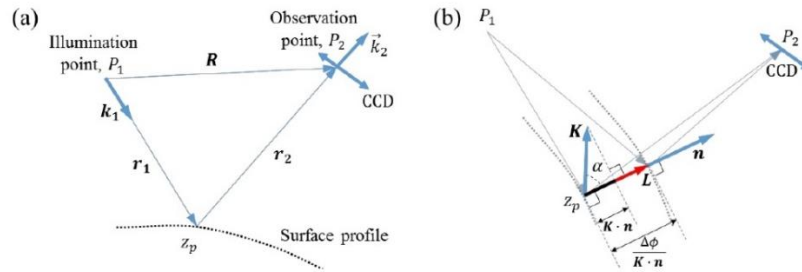


Fig. 1. Nomenclature for fringe analysis: (a) schematic representation of optical path length from observation to a point on the sample surface to a point of observation on the CCD; and (b) schematics of out-of-plane displacements measurements relation to the interference phase $\Delta\phi$, sensitivity vector \mathbf{K} , displacements vector \mathbf{L} , and the surface normals \mathbf{n} in a thin-shell.

In most of holographic applications, the lengths of path vectors are in the order of centimeters to meters while the displacements are in the order of nanometers to micrometers, therefore, the optical path length difference is related to the displacements by,

$$\Delta\phi = \mathbf{K} \cdot \mathbf{L}, \quad \mathbf{K} = \mathbf{k}_2 - \mathbf{k}_1, \quad (1)$$

where \mathbf{K} is the sensitivity vector, \mathbf{L} is the displacements vector, and $\Delta\phi$ is the interference phase. Since the displacements vector has three unknowns, at least three independent sensitivity vectors (i.e., 3D holography) are needed to determine displacements. Other way to retrieve the displacements is by determining the direction of the displacements vector \mathbf{L} . Based on our previous studies and verifications, TM has a thin-shell structure that the out-of-plane component of the displacements along the surface normal are the dominant displacements direction [2], therefore, the displacement vector can be decomposed to its magnitude and surface normal (i.e., $\mathbf{L} = |\mathbf{L}| \cdot \mathbf{n}$), and consequently, we can rewrite Eqn. (1) as,

$$|\mathbf{L}| = \frac{\Delta\phi}{\mathbf{K} \cdot \mathbf{n}} = \frac{\Delta\phi}{|\mathbf{K}| \cos(\alpha)}, \quad (2)$$

where the surface normal \mathbf{n} , sensitivity vector \mathbf{K} , and the angle α , which is the angle between the two vectors, are shown schematically in Fig.1-b. It should be noted that, the holographic measurements of the Tympanic Membrane (TM, eardrum) inside the ear canal require about 10-15 millimeter working distance, which is large compared to the millimeter scale spatial variations of the optical path length due to shape and orientation of the TM. This phenomenon produces a spatially varying sensitivity vector that can generate errors in displacements as large as 50%. In this paper, we present a novel high-speed digital holographic shape measurement method incorporated into our high-speed holographic displacement measurement system to measure the TM shape and orientation in-situ. Knowledge of shape helps to account for the spatial variations of the sensitivity vector to determine surface-normal displacements from 1-D holographic measurements.

2. Methods

2.1. High-speed digital holographic interferometry

We have previously developed and implemented a High-speed Digital Holographic (HDH) method that instantaneously measures the full-field (>200,000 points at 67,200 Frames Per Seconds (FPS)) transient displacements of the TM in response to pulsed acoustical and mechanical excitations [3-5]. To measure the transient response of TM in-vivo, an adaptive phase sampling holographic method was developed to compensate for the effects of large in-vivo physiological motions using high-speed continuous phase sampling [1].

2.2. Shape measurements requirements

The development of the shape measurement system was performed with the aim of satisfying all of the following functional requirements:

1. Utilizing the same imaging optics as the ones of High-speed Digital Holographic Displacement measurement system
2. Measurements under small triangulation volumes of the ear canal
3. Adjustable shape resolution to account for TM shape depth variations
4. Uniform and sufficient axial and lateral shape resolutions to accurately determine surface normals
5. Short intervals (<seconds) between displacements and the shape measurements to maintain the same coordinate system for both measurements
6. High-speed shape measurements to reduce the effects of in-vivo physiological motions

Meeting these functional requirements in one method is not a trivial task. Many of the methods that have been previously applied to TM shape measurements are inappropriate. For example, structured light projection [6, 7] requires large triangulation angles compared to the ear canal's confined volume while others that are capable of single shot in-vivo endoscopic measurements [8] require high-resolution sensors (>10 Megapixels) and specialized optics that are incompatible with the HDH system.

2.3. Multiple Wavelengths Holographic Interferometry (MWHI)

MWHI shape measurement method uses a tunable laser source, which can vary the illumination wavelength during repeated sets of phase-shifted holograms. While the Optical Path Length (OPL) is constant (i.e., stationary sample), the variations of the wavelength generates contours of constant height due to sample shape. The relation between the interference phase $\Delta\gamma$, the constant OPL, and the tuned set of wavelengths at each hologram exposures (i.e., λ_1 to λ_2) is described by,

$$\Delta\gamma = \frac{2\pi}{\lambda_1} OPL - \frac{2\pi}{\lambda_2} OPL = \frac{2\pi}{\Lambda} OPL, \quad (3)$$

where Λ is the synthetic or equivalent wavelength determined by,

$$\Lambda = \frac{\lambda_1 \lambda_2}{\lambda_1 - \lambda_2}. \quad (4)$$

To determine the shape, additional calibration efforts are required to transform the interference phase $\Delta\phi$ onto a coordinate system that OPL provide the shape of the sample [9, 10] along the camera axis (z in Fig. 2) by,

$$z_p(x, y) = \frac{\Lambda}{4\pi} \Delta\gamma_c(x, y), \quad (5)$$

where $\Delta\phi_c$ is the calibrated phase and z_p is the z component of point P corresponding to the shape of the sample.

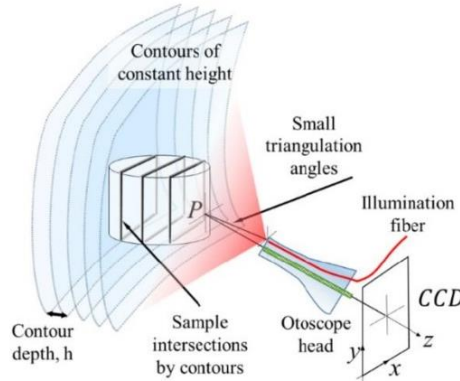


Fig. 2. Schematic representation of contours of constant depth (h) in the MWHI shape measurements method intersecting the sample shape.

2.4. High-speed multi-resolution MWHI method

In order to increase the speed of acquisition without utility of multiple lasers, a new technique was used. By performing phase samplings at a temporal resolution much higher than the phase shift noises introduced by sample or wavelength variations, we managed to quantify the interference phase (i.e., $\Delta\gamma$) during a laser tune. This achievement significantly increase the speed of acquisition by removing the delays required for the laser wavelength stability. Furthermore, this technique provides the shape over a continuous range of contour depths that enables the shape measurements performed at an optimum contour depth (a synthetic wavelength that provides the shape with maximum quantifiable fringe density) without multiple repetition of measurements. While the shape depth is unknown at least multiple (>3) shape measurements are required to experimentally determine a value close to the optimum contour depth but using the proposed method, all the required information to extract the shape is measured in a single set of data in a duration of a single frame of a conventional camera (i.e., 20 Hz). The shape of the sample can be extracted robustly at the highest possible spatial resolution of the sensor.

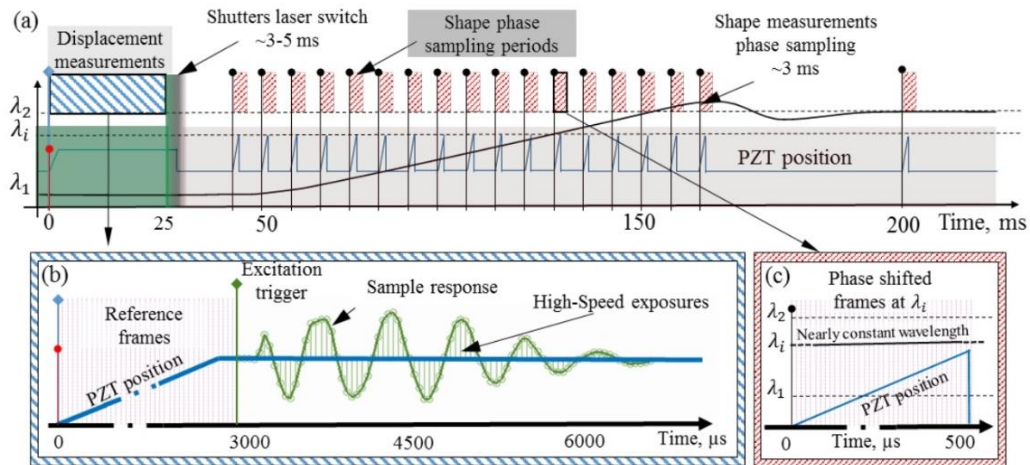


Fig. 3 (a) timeline of the events in a set of shape and displacements measurements. The color of the background shows which laser illuminate the sample; (b) the timeline of the events during the displacements measurements; and (c) one of the 17 high-speed phase samplings performed to save the phase shifted wavefronts with nearly constant wavelength with respect to tuning speed.

2.5. Timeline of high-speed shape and displacement measurements

Fig. 3 illustrates the timeline of the shape and displacement measurement with a total duration of about 200 msec. The displacements measurements are performed in less than 25 msec and shown in figure 2.3.b, while one of the discrete high-speed phase sampling for the shape measurements is shown in figure 2.3.c. Both shape and displacement measurements are

performed at 67,200 frames per second temporal resolution. As shown in figure 2.3.b, the displacement measurements start by capturing a set of reference holograms during a continuous phase shift (within 3ms) followed by a broadband acoustic click (a 50 μ s square pulse). After 25ms, the piezo moves back to its original position, the shutters are set to switch to the variable wavelength laser. Each of the 17 shape phase sampling triggers are synchronized with a continuous ramp of the PZT positioner to allow for quantitative phase imaging while the tunable laser slowly varies the illumination wavelength. The last phase sampling is performed after the wavelength reaches its final value. Both shape and displacement measurements are repeated three times.

2.6. Experimental setup

Different lasers were used for shape and displacement measurements: A 780 \pm 10 nm tunable laser for shape and a highly stable CW 532 nm laser for displacements. As shown in FIGFIG, using variable beam splitters (VBS), each laser is divided into reference and illumination beams. To maintain the same observation vector for both measurements, the lasers are guided onto the same illumination and reference axis using dichroic mirrors (DM). The beam reflected from the sample (object beam) is combined with the reference using a wideband wedge to form an interference pattern on the sensor of the high-speed camera. Each laser is equipped with an automated mechanical shutters (MS) to switch between the lasers rapidly (<5 msec).

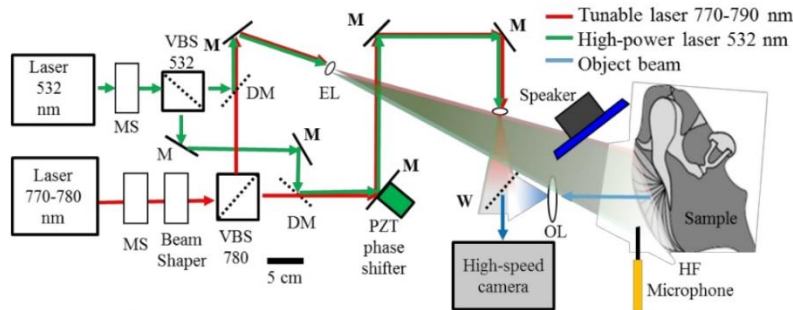


Fig. 4 Schematic representation of the shape and displacements measurements setup. Variable Beam Splitters (VBS) are to balance the intensity ratio between the reference and object at different wavelengths. Mechanical shutters (MS), Dichroic Mirror (DM), Wedge (W), Expansion Lens (EL), Objective Lens (OL).

3. Representative results

3.1. Sample preparation

A fresh non-fixed human post mortem temporal bone was used for these measurements. The cartilaginous and bony parts of the ear canal were removed to provide a larger view of the TM. The middle-ear cavity was opened to check the middle ear ossicles healthiness and then it was sealed using the sealing cement. A small vent was installed to equilibrate the static pressure within the middle ear. The sample was sprayed with a thin layer of white face paint using a modified commercially available airbrush. To ensure the paint layer is sufficiently thin and uniform the airbrush was set to generate the finest particles while the sample was placed >10 cm away from the airbrush. The paint layer was sufficiently thin that part of ossicles are still visible under white light illumination.

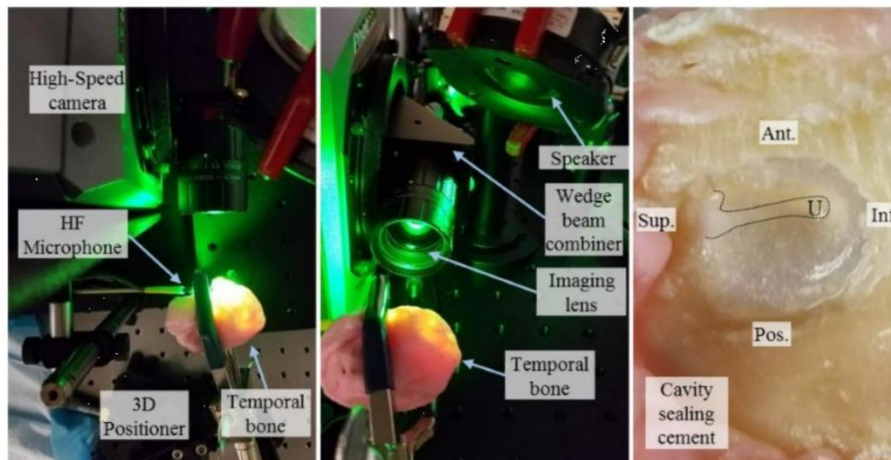


Fig. 5. The left two pictures show the setup, measuring instrumentations and the sample; and the right panel is a photograph of the human post-mortem TM. The black contour shows the outline of the manubrium and umbo (shown with U symbol).

3.2. Representative shape and displacement measurements

Shape and acoustically induced transient displacements of the human post-mortem TM is measured by the proposed multi-resolution high-speed MWHI method and the 2+N high-speed correlation interferometry. Using an optimization approach based on phase quality, out of tens of shape at varied resolutions, an optimum resolution phase-map (i.e., having the maximum phase quality and fringe density) was chosen to be used for determination of surface-normals and sensitivity vectors. Fig. 6-a show the optimum resolution (in this case with a synthetic wavelength of $\Lambda \cong 1.2$ mm) modulo 2π phase maps reconstructed at the optimum synthetic wavelength. Fig. 6-b shows the wrapped phase after the calibration procedure (i.e., using a flat surface calibration method), and Fig. 6-c illustrates the shape after spatial filtering and masking procedure. Filtering and masking are performed to remove any surface discontinuities that may interfere with the surface normal determination. The colorbar quantifies the shape of the sample along the z-axis.

Having the information from the coordinates at each point on the TM together with the setup geometries, i.e., the coordinates of the observation and the illumination points, the spatial distribution of the surface normals and the sensitivity vectors are computed. Fig. 6-d illustrates the surface normals (magenta arrows) and sensitivity vectors (black arrows) distribution along a single selected line intersection of the TM surface passing through the umbo (i.e., the red line shown in Fig. 6-c). It is clearly visible how the angle α vary spatially across the field of view. In the next step, using Eqn. 2, a sensitivity multiplier map is computed from the surface-normal and sensitivity vectors at each point, where, the sensitivity multiplier is a 2D scalar map with the resolution of the sensor to convert the interference phase from cycles to the corresponding surface-normal displacements.

Having the sensitivity map, the acoustically induced TM transient response surface-normal displacements are determined from the interference phase measured by the 2+N high-speed local phase correlation method [3]. Fig. 6-e illustrates 3D maps representing the shape and normal-displacements at nine selected temporal instances out of 1700 consecutive measurements (25 ms, @ 67200 FPS) during the TM transient response due to a broadband acoustic click.

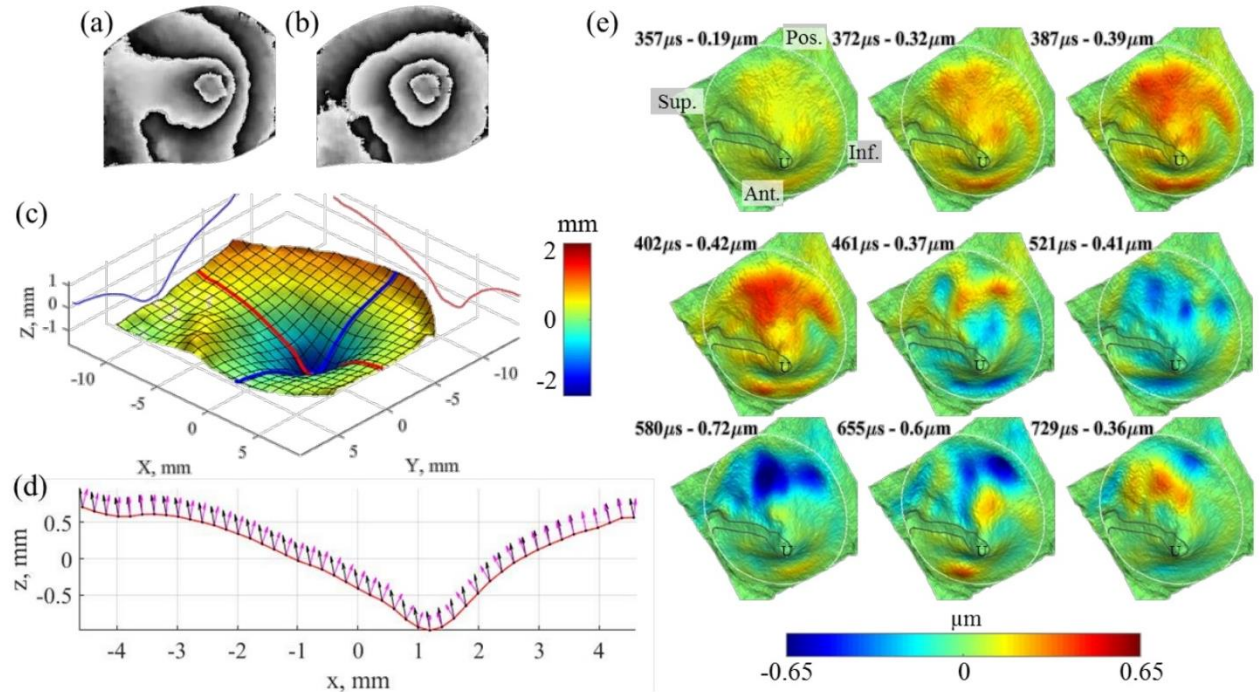


Fig. 6 results of shape and transient response measurements of a human post-mortem sample: (a) wrapped interference phase $\Delta\gamma$; (b) wrapped interference phase after flat surface calibration $\Delta\gamma_c$; (c) 3D shape and orientation of the TM after it was unwrapped, scaled, spatially filtered, and masked. The shape of the red and blue lines are shown in the y-z and x-z planes and the colorbar represent the depth of the sample along z-axis; (d) determined surface normals and sensitivity vectors along the red line shown in panel (c). The magenta vectors represent surface normals and black vectors represent calculated sensitivity vectors at selected points; and (e) 3D representation of the TM transient response surface normal displacements due to an acoustic click (50 μ s square pulse). The nanometer-scale displacements are 1000 times exaggerated and shown on top of millimeter-scale shape. The manubrium of the malleus is shown with a black line and U represents the umbo.

3.3. Discussion

The results show the TM response from the very first moments of acoustic to solid interaction, the complex travelling and standing surface waves, and up to complete dissipation of the vibrations across the entire surface of the TM. The first four consecutive frames of the measurements in Fig. 6-e show the initial response of the membrane as the sound waves start to move the TM mostly along a single direction while there have been minimum travelling waves observed. We call this stage of the response “initiation” and has many applications for determination of TM stiffness, the determination of overall volume change, etc. After the initiation stage, while the umbo and manubrium motions are nearly damped, the waves reflect from both the manubrium and the annulus and they form complex superposition of travelling and standing waves across the TM (“Surface wave superposition stage”). TM response at this stage is temporally separated from the excitation, making it suitable for methods such as experimental modal analysis to determine mechanical properties, damping etc. The last stage of the response includes the TM vibration at one of the primary mode shapes, until the motions are completely damped out (dissipation stage).

4. Conclusions and future work

To improve our high-speed displacement measurement capabilities, a high-speed holographic shape measurement method is developed to measure TM shape parameters (i.e., curvature, dimensions, etc.) as well as to compensate for geometrically induced spatial variations of the sensitivity vector. These improvements provide large range of measuring capabilities to evaluate insitu and near instantaneous (<200 ms) TM displacements and shape along near six orders of magnitude different resolution ranges (from millimeters to nanometers). The results establish the potential of the high-speed multi-resolution MWHI shape measurements to operate in parallel with high-speed holographic displacement measurements within a fraction of a second that can help to reduce the effects of in-vivo physiological motions. Furthermore, the knowledge of shape and orientation makes the displacements measurements independent of direction of observation, which facilitates comparison of measurements after the specimen is moved. The results also can help to better interpret the TM transient response either by accurate measurements of speed and trajectory of the travelling waves or by use of finite element or experimental modal analysis. Finally, the TM shape parameters such as curvature, area, etc. have direct clinical diagnostic values that can be used for rehabilitation surgeries as well as development of personalized grafts and artificial TMs. Future work includes the analysis of the data gathered from several human samples and development of miniaturized optical head to enable in-vivo measurements inside the ear canal.

5. Acknowledgements

This work has been funded by the National Institute on Deafness and Other Communication Disorders (NIDCD), the National Institute of Health (NIH), and the Massachusetts Eye and Ear (MEE). The authors would like to acknowledge contributions from other members of the CHSLT at the Worcester Polytechnic Institute.

6. References

- [1] C. M. Vest, "Holographic interferometry," New York, John Wiley and Sons, Inc., 1979. 476 p., vol. 1, 1979.
- [2] M. Khaleghi, J. T. Cheng, C. Furlong, and J. J. Rosowski, "In-plane and out-of-plane motions of the human tympanic membrane," *J. Acous. Soc. Am.*, vol. 139, pp. 104-17, Jan 2016.
- [3] P. Razavi, J. T. Cheng, C. Furlong, and J. J. Rosowski, "High-Speed Holography for In-Vivo Measurement of Acoustically Induced Motions of Mammalian Tympanic Membrane," in *Mechanics of Biological Systems and Materials*, Volume 6: Proceedings of the 2016 Annual Conference on Experimental and Applied Mechanics, Cham, 2017, pp. 75-81.
- [4] I. Dobrev, C. Furlong, J. T. Cheng, and J. J. Rosowski, "Full-field transient vibrometry of the human tympanic membrane by local phase correlation and high-speed holography," *J. Biomed. Opt.*, vol. 19, pp. 096001-096001, 2014.
- [5] P. Razavi, M. E. Ravicz, I. Dobrev, J. T. Cheng, C. Furlong, and J. J. Rosowski, "Response of the human tympanic membrane to transient acoustic and mechanical stimuli," *Hear. Res.*, vol. 340, pp. 15-24, Oct 2016.
- [6] S. Van der Jeught and J. J. J. Dirckx, "Real-time structured light-based otoscopy for quantitative measurement of eardrum deformation," *J. Biomed. Opt.*, vol. 22, pp. 016008-016008, 2017.
- [7] J. J. Dirckx and W. F. Decraemer, "Optoelectronic moire projector for real-time shape and deformation studies of the tympanic membrane," *J. Biomed. Opt.*, vol. 2, pp. 176-185, 1997.
- [8] N. Bedard, T. Shope, A. Hoberman, M. A. Haralam, N. Shaikh, J. Kovačević, et al., "Light field otoscope design for 3D in vivo imaging of the middle ear," *Biomed. Opt. Express*, vol. 8, pp. 260-272, 2017/01/01 2017.
- [9] J. Kandulla, B. Kemper, S. Knoche, and G. von Bally, "Two-wavelength method for endoscopic shape measurement by spatial phase-shifting speckle-interferometry," *Appl. Opt.*, vol. 43, pp. 5429-5437, 2004/10/10 2004.
- [10] C. Furlong and R. J. Pryputniewicz, "Absolute shape measurements using high-resolution optoelectronic holography methods," *Opt. Eng.*, vol. 39, p. 216, 2000.

8.5 High-resolution combinatorial MWHI shape measurements

The developments of a combinatorial MWHI shape measurement method is the subject of this un-submitted abstract. Multi-resolution shape measurements presented in the previous paper (and Section 6.2) provide a single contour depth at optimum resolution of the sensor with respect to sample depth. The optimum resolution may not be the maximum resolution since high-spatial frequency regions of the shape (i.e., areas with small curvature and surface discontinuities) may not be quantifiable due to too dense contour depths. Therefore, high-resolution contour maps as well as a large portion of the spatial domain are removed for the final shape. Furthermore, for further shape analysis such as determination of surface normals, it is required to perform sufficient spatial filtering to remove any surface discontinuities that may include removal of important details of the shape.

Using the combinatorial shape measurements, instead of using a single phase map, the entire spatiotemporal domain of the measurements are used by computing a large database from any non-repeated combinations of the measured phase samplings. The entire database is scaled as discussed in Section 6.3. From the denser contour depths the regions with excessive fringe density are used to increase the shape resolution while from the lower resolution phase maps the sensitivity of the method to surface discontinuities are reduced. Furthermore, because a normal distribution is fit at each pixel the data is free from the effects of sensor and speckle noise enabling higher spatial resolution over the entire sensor.

8.5.1 Full-field surface profilometry using temporal domain high-speed multi-wavelength holography

Abstract

Shape resolution in Multiple Wavelength Holographic Interferometry (MWHI) is determined by the synthetic wavelength, the spatial resolution of the sensor, and measuring dimensions. In this paper, a new method is presented to perform temporal phase sampling during the period of a single laser tune to generate phase maps with a wide range of synthetic wavelengths corresponding to sample shape with a range of resolutions. While the short synthetic wavelengths phase maps are immune to surface discontinuities the longer ones contribute to the high-resolution surface details with high signal to noise ratio. In less than 100 msec, while the sample is highly stable and the laser is being continuously tuned, tens of rapid phase samplings (continuous phase shifts in $<500 \mu\text{s}$ at $>67 \text{ kHz}$) are performed, each containing the phase with slightly varied wavelength. Since the sample is highly stable during rapid measurements, hundreds of shape phase maps with different or repeated resolutions is extracted by choosing any two non-repeated combinations from the phase samplings (e.g., for 30 phase samplings there are $C_2^{30} = 435$ dataset). After scaling each phase map using the longest synthetic wavelength, a normal distribution is fitted at each pixel to determine the surface profile with an accuracy beyond the limitations of the MWHI method nearly free from surface noise suitable for full-field-of-view profilometry.

Keywords: holographic interferometry, phase sampling, multiple wavelengths, extended resolutions.

Conclusions and future work

A non-destructive non-contact measuring instrument was developed to enable nearly instantaneous shape and displacements measurements of the mammalian TM suitable for hearing research and clinical applications. This development provides unprecedented details about the shape and motions of the TM in response to various types of stimulation that can help to better understand the function of TM in the hearing processes.

Using the developed methodologies presented in Chapter 5, the influence of large submillimeter scale physiological motions were compensated by use of a robust open-loop temporal phase sampling mechanism to accurately and precisely measure the nanometer-scale TM displacements of a live sample. Preliminary measurements of chinchilla TMs and human skin in-vivo show the clinical applicability of this method. The methodologies presented in this Chapter also build the cornerstone of the holographic shape measurements by enabling quantitative phase sampling during the transient variations of the laser wavelengths.

The shape measurement capabilities were designed from scratch with the main goal of accounting for spatial variations of the sensitivity vector due to shape and orientation of the TM. The shape measuring capacity was incorporated into the holographic displacements measurements without sacrificing any of its functionalities. Using the same illumination and observation optics and by maintain the same optical path for both systems the measured shape can be directly used for surface-normal displacements computations without any additional registration efforts. Using the multi-resolution capability, in a single measurement all the necessary information to extract the shape at the optimum contour depth with respect to the sample depth and spatial resolution of the camera is measured that

can bring highly repeatable high-resolution shape measurements. Furthermore, the novel method of the combinatorial shape measurements provide unprecedented spatial resolution with less sensitivity to surface discontinuities to determine the surface normals with minimum need for spatial filtering.

The ultimate goal of this system is to perform in-vivo high-speed holographic shape and displacement measurements inside the ear canal using an endoscopic configuration. This goal was achieved with the developments presented in this Dissertation that enabled direct holographic measurements using the proper holographic endoscope (otoscope). As an example, the shape measurements was equipped with the proper calibrations to remove the elliptical illumination and optical aberrations in a future endoscopic configuration. Furthermore, the application of spatially varied sensitivity vector as well as the uncertainty analysis in each chapter were aimed to predict and account for the endoscopic holographic measuring conditions.

The improvements and developments presented in this Dissertation can open new doors by expanding the available bioinstrumentation for hearing research and diagnosis applications. The future works include but not limited to the following items:

- **Improvements in available TM models:** High-speed shape and full-field transient displacement measurements, provide the necessary information to test the performance of available TM models. One of the main advantages of this method is the very short time between the shape and displacements measurement that minimizes the temporal variations of material properties (i.e., due to decay, dehydration, etc.) as well as shape.
- **Development of a shape independent TM transient response database:** The shape parameters (i.e., curvature, area, diameter, etc.), can be used to normalize different

displacement parameters derived from the surface normal displacements to better correlate the differences between different TM's or different conditions of the TM (i.e., normal versus pathological). New parameters, such as speed of travelling waves normalized by surface curvature, area of TM normalized by maximum initial displacements can better correlate the response of different samples with different geometries.

- **TM diagnosis purposes:** Our preliminary investigations using high-speed holography as a diagnostic for middle-ear infections (otitis media) detected different levels of the fluid in contact with TM (Razavi et al., 2017b). This research can be further expanded to provide detailed information about the TM response in normal and pathological conditions.

Currently myringotomy and ossiculoplasty surgeries are performed without benefiting from measurements of the TM displacements before and after surgeries. Quantification of the performance of such surgeries require quantitative full-field shape and displacements measurements.

- **Experimental modal analysis:** The method proposed is suitable to extract comparative differences of the TM mechanical properties under various normal and pathological conditions (Maftoon et al., 2017). Further research in this field can include the shape and normal-displacements for higher accuracy and inclusion of surface curvature in determination of TM complex Eigen modes and Eigen frequencies.
- **Development of additively manufactured grafts and artificial TM's:** Our former developments using digital holography has been used for characterization of additively manufactured live biological tissues using steady state stimuli (J. T. Cheng et al., 2010;

Maftoon et al., 2018). Iterative optimization of manufacturing parameters can be done with the aim of producing grafts and artificial TMs having the shape and acoustically induced transient displacements close to the human TM's.

- **Miniaturization of the imaging and illumination optics:** The future goal of the developments performed in this Dissertation is to use high-speed holography as a clinical diagnosis tool that can help middle-ear diagnosis and rehabilitation surgeries. Design and manufacturing of miniaturized and ergonomic optics that can illuminate and observe the TM inside the limited volume of the ear canal while maintaining the requirements of holography is one of the main parts of the future works. Recent improvements in additive manufacturing of miniaturized optics (i.e., printing a lens or any diffractive element at the end effector of the fiber), and fiber optics bundling technologies (>40,000 fibers) allow the development of a miniaturized flexible endoscope satisfying the holographic measurements requirements.
- **Application to other fields:** The developments performed in this Dissertation can benefit other fields as well as the middle-ear. This system has been previously used for testing and characterization of the surface of MEMS devices such as deformable mirrors, and electroactive polymers (Rasmussen et al., 2016; Razavi et al., 2017c; Razavi et al., 2015; Trolinger et al., 2016). This system has the potential to be used for other organs of body (from cells to large organs such as skin), and many areas in industry that require high-resolution non-destructive non-contact full-field sensors.

References

- Abramson, N. (1983). Light-in-flight recording: high-speed holographic motion pictures of ultrafast phenomena. *Appl. Opt.*, 22(2), 215-232. doi:10.1364/AO.22.000215
- Aernouts, J., Aerts, J. R., & Dirckx, J. J. (2012). Mechanical properties of human tympanic membrane in the quasi-static regime from in situ point indentation measurements. *Hear. Res.*, 290(1-2), 45-54. doi:10.1016/j.heares.2012.05.001
- Akondi, V., Vohnsen, B., & Marcos, S. (2016). Virtual pyramid wavefront sensor for phase unwrapping. *Appl. Opt.*, 55(29), 8363-8367. doi:10.1364/AO.55.008363
- Awatsuji, Y., Sasada, M., & Kubota, T. (2004). Parallel quasi-phase-shifting digital holography. *Appl. Phys. Lett.*, 85(6), 1069-1071. doi:doi:<http://dx.doi.org/10.1063/1.1777796>
- Bedard, N., Shope, T., Hoberman, A., Haralam, M. A., Shaikh, N., Kovačević, J., . . . Tošić, I. (2017). Light field otoscope design for 3D in vivo imaging of the middle ear. *Biomed. Opt. Express*, 8(1), 260-272. doi:10.1364/BOE.8.000260
- Bergström, P., Rosendahl, S., Gren, P., & Sjö Dahl, M. (2011). *Shape verification using dual-wavelength holographic interferometry*.
- BIPM, I., IFCC, I., IUPAC, I., & ISO, O. (2008). Evaluation of measurement data—guide for the expression of uncertainty in measurement. JCGM 100: 2008. *Citado en las*, 167.
- Buunen, T., & Vlaming, M. (1981). Laser-Doppler velocity meter applied to tympanic membrane vibrations in cat. *The Journal of the Acoustical Society of America*, 69(3), 744-750.
- Chang, E. W., Kobler, J. B., & Yun, S. H. (2011). Triggered optical coherence tomography for capturing rapid periodic motion. *Sci. Rep.*, 1, 48.
- Cheng, J. T., Aarnisalo, A. A., Harrington, E., Hernandez-Montes Mdel, S., Furlong, C., Merchant, S. N., & Rosowski, J. J. (2010). Motion of the surface of the human tympanic membrane measured with stroboscopic holography. *Hear. Res.*, 263(1-2), 66-77. doi:10.1016/j.heares.2009.12.024
- Cheng, T., Dai, C., & Gan, R. Z. (2007). Viscoelastic Properties of Human Tympanic Membrane. *Ann. Biomed. Eng.*, 35(2), 305-314. doi:10.1007/s10439-006-9227-0
- Creath, K. (1985). Phase-shifting speckle interferometry. *Appl. Opt.*, 24(18), 3053-3058. doi:10.1364/AO.24.003053
- Dancer, A. L., Franke, R. B., Smigielski, P., Albe, F., & Fagot, H. (1975). Holographic interferometry applied to the investigation of tympanic-membrane displacements in guinea pig ears subjected to acoustic impulses. *The Journal of the Acoustical Society of America*, 58(1), 223-228. doi:doi:<http://dx.doi.org/10.1121/1.380649>
- Danti, S., Mota, C., D'alessandro, D., Trombi, L., Ricci, C., Redmond, S. L., . . . Moroni, L. (2015). Tissue engineering of the tympanic membrane using electrospun PEOT/PBT copolymer scaffolds: A morphological in vitro study. *Hearing, Balance and Communication*, 13(4), 133-147.
- Davila, A., Huntley, J. M., Kaufmann, G. H., & Kerr, D. (2005). High-speed dynamic speckle interferometry: phase errors due to intensity, velocity, and speckle decorrelation. *Appl. Opt.*, 44(19), 3954-3962. doi:10.1364/AO.44.003954
- De Greef, D., Buytaert, J. A. N., Aerts, J. R. M., Van Hoorebeke, L., Dierick, M., & Dirckx, J. (2015). Details of human middle ear morphology based on micro-CT

- imaging of phosphotungstic acid stained samples. *J. Morphol.*, 276(9), 1025-1046. doi:10.1002/jmor.20392
- de Groot, P. J., & Deck, L. L. (1996). Numerical simulations of vibration in phase-shifting interferometry. *Appl. Opt.*, 35(13), 2172-2178. doi:10.1364/AO.35.002172
- Decraemer, W., & Funnell, W. (2008). Anatomical and mechanical properties of the tympanic membrane. *Chronic otitis media: Pathogenesis-oriented therapeutic management*, 51-84.
- Del Socorro Hernández-Montes, M., Furlong, C., Rosowski, J. J., Hulli, N., Harrington, E., Cheng, J. T., . . . Santoyo, F. M. (2009). Optoelectronic holographic otoscope for measurement of nano-displacements in tympanic membranes. *J. Biomed. Opt.*, 14(3), 034023-034023-034029. doi:10.1117/1.3153898
- Deng, Z., Wu, J., Qiu, J., Wang, J., Tian, Y., Li, Y., & Jin, Y. (2009). Comparison of porcine acellular dermis and dura mater as natural scaffolds for bioengineering tympanic membranes. *Tissue Engineering Part A*, 15(12), 3729-3739.
- Dirckx, J. J., & Decraemer, W. F. (1997). Optoelectronic moire projector for real-time shape and deformation studies of the tympanic membrane. *J. Biomed. Opt.*, 2(2), 176-185. doi:10.1117/12.268966
- Dobbert, M., & Schrijver, B. (2014). *Uncertainty Propagation for Measurements with Multiple Output Quantities*. Paper presented at the Proceedings of the 2014 NCSL International Workshop and Symposium.
- Dobrev, I., Furlong, C., Cheng, J. T., & Rosowski, J. J. (2014a). Full-field transient vibrometry of the human tympanic membrane by local phase correlation and high-speed holography. *J. Biomed. Opt.*, 19(9), 096001-096001. doi:10.1117/1.JBO.19.9.096001
- Dobrev, I., Furlong, C., Cheng, J. T., & Rosowski, J. J. (2014b). Full-field transient vibrometry of the human tympanic membrane by local phase correlation and high-speed holography. *BIOMEDO*, 19(9), 96001. doi:10.1117/1.JBO.19.9.096001
- Dobrev, I., Furlong, C., Cheng, J. T., & Rosowski, J. J. (2015). Optimization of a Lensless Digital Holographic Otoscope System for Transient Measurements of the Human Tympanic Membrane. *Experimental Mechanics*, 55(2), 459-470. doi:10.1007/s11340-014-9945-4
- Fay, J., Puria, S., Decraemer, W. F., & Steele, C. (2005). Three approaches for estimating the elastic modulus of the tympanic membrane. *J. Biomech.*, 38(9), 1807-1815. doi:<http://dx.doi.org/10.1016/j.jbiomech.2004.08.022>
- Feng, B., & Gan, R. Z. (2004). Lumped parametric model of the human ear for sound transmission. *Biomechanics and Modeling in Mechanobiology*, 3(1), 33-47. doi:10.1007/s10237-004-0044-9
- Ferrazzini, M. (2003). *Virtual middle ear: a dynamic mathematical model based on the finite element method*. ETH Zurich.
- Flanagan, J. L. (2013). *Speech analysis synthesis and perception* (Vol. 3): Springer Science & Business Media.
- Funnell, W. R. J., & Laszlo, C. A. (1978). Modeling of the cat eardrum as a thin shell using the finite-element method. *The Journal of the Acoustical Society of America*, 63(5), 1461-1467. doi:<http://dx.doi.org/10.1121/1.381892>

- Furlong, C., Gouverneur, I., & Rodgers, M. (2006). *Development of scalable optoelectronic methodologies for characterization of surface shape and deformation*. Paper presented at the Society of Experimental Mechanics.
- Furlong, C., & Pryputniewicz, R. J. (2000). Absolute shape measurements using high-resolution optoelectronic holography methods. *Opt. Eng.*, 39(1), 216.
- Gan, R. Z., Nakmali, D., Ji, X. D., Leckness, K., & Yokell, Z. (2016a). Mechanical damage of tympanic membrane in relation to impulse pressure waveform—A study in chinchillas. *Hear. Res.*, 340, 25-34.
- Gan, R. Z., Nakmali, D., Ji, X. D., Leckness, K., & Yokell, Z. (2016b). Mechanical damage of tympanic membrane in relation to impulse pressure waveform – A study in chinchillas. *Hear. Res.*, 340, 25-34.
doi:<http://dx.doi.org/10.1016/j.heares.2016.01.004>
- Geisler, C. D. (1998). *From sound to synapse: physiology of the mammalian ear*: Oxford University Press, USA.
- Georgas, P. J., & Schajer, G. S. (2012). Modulo-2pi phase determination from individual ESPI images. *Optics and Lasers in Engineering*, 50(8), 1030-1035.
doi:<http://dx.doi.org/10.1016/j.optlaseng.2012.03.005>
- Ghiglia, D. C., & Pritt, M. D. (1998). *Two-dimensional phase unwrapping: theory, algorithms, and software* (Vol. 4): Wiley New York.
- Greivenkamp, J. E. (1984). Generalized Data Reduction For Heterodyne Interferometry. *Opt. Eng.*, 23(4), 234350-234350-. doi:10.1117/12.7973298
- Hariharan, P. (1984). *Optical Holography: Principles, Techniques, and Applications* Cambridge U. Press, Cambridge, UK, 1984, 207.
- Herráez, M. A., Burton, D. R., Lalor, M. J., & Gdeisat, M. A. (2002). Fast two-dimensional phase-unwrapping algorithm based on sorting by reliability following a noncontinuous path. *Appl. Opt.*, 41(35), 7437-7444. doi:10.1364/AO.41.007437
- Jackson, R. P., Chlebicki, C., Krasieva, T. B., & Puria, S. (2008). *Multiphoton microscopy imaging of collagen fiber layers and orientation in the tympanic membrane*. doi: 10.1117/12.774353 retrieved from <http://dx.doi.org/10.1117/12.774353>
- Jones, R., & Wykes, C. (1983). *Holographic and Speckle Interferometry: A Discussion of the Theory, Practice, and Application of the Techniques*: Cambridge University Press.
- Kakue, T., Endo, Y., Nishitsuji, T., Shimobaba, T., Masuda, N., & Ito, T. (2017). Digital holographic high-speed 3D imaging for the vibrometry of fast-occurring phenomena. *Sci. Rep.*, 7(1), 10413.
- Kakue, T., Yonesaka, R., Tahara, T., Awatsuji, Y., Nishio, K., Ura, S., . . . Matoba, O. (2011). High-speed phase imaging by parallel phase-shifting digital holography. *Opt. Lett.*, 36(21), 4131-4133. doi:10.1364/OL.36.004131
- Kandulla, J., Kemper, B., Knoche, S., & von Bally, G. (2004). Two-wavelength method for endoscopic shape measurement by spatial phase-shifting speckle-interferometry. *Appl. Opt.*, 43(29), 5429-5437. doi:10.1364/AO.43.005429
- Khaleghi, M. (2015). *Development of Holographic Interferometric Methodologies for Characterization of Shape and Function of the Human Tympanic Membrane*. Worcester Polytechnic Institute.

- Khaleghi, M., Cheng, J. T., Furlong, C., & Rosowski, J. J. (2016). In-plane and out-of-plane motions of the human tympanic membrane. *J. Acous. Soc. Am.*, *139*(1), 104-117. doi:10.1121/1.4935386
- Khaleghi, M., Guignard, J., Furlong, C., & Rosowski, J. J. (2015). Simultaneous full-field 3-D vibrometry of the human eardrum using spatial-bandwidth multiplexed holography. *J. Biomed. Opt.*, *20*(11), 111202. doi:10.1117/1.JBO.20.11.111202
- Khaleghi, M., Lu, W., Dobrev, I., Cheng, J. T., Furlong, C., & Rosowski, J. J. (2013). *Digital holographic measurements of shape and three-dimensional sound-induced displacements of tympanic membrane.*
- Khanna, S. M., & Tonndorf, J. (1972). Tympanic Membrane Vibrations in Cats Studied by Time-Averaged Holography. *The Journal of the Acoustical Society of America*, *51*(6B), 1904-1920. doi:doi:<http://dx.doi.org/10.1121/1.1913050>
- Kozin, E. D., Black, N. L., Cheng, J. T., Cotler, M. J., McKenna, M. J., Lee, D. J., . . . Remenschneider, A. K. (2016). Design, fabrication, and in vitro testing of novel three-dimensionally printed tympanic membrane grafts. *Hear. Res.*, *340*, 191-203.
- Kreis, T. (2006). *Handbook of holographic interferometry: optical and digital methods*: John Wiley & Sons.
- Kuypers, L. C., Decraemer, W. F., & Dirckx, J. J. J. (2006). Thickness Distribution of Fresh and Preserved Human Eardrums Measured with Confocal Microscopy. *Otol. Neurotol.*, *27*(2), 256-264. doi:10.1097/01.mao.0000187044.73791.92
- Lauterborn, W., & Ebeling, K. J. (1977). High-speed holography of laser-induced breakdown in liquids. *Appl. Phys. Lett.*, *31*(10), 663-664. doi:doi:<http://dx.doi.org/10.1063/1.89495>
- Lim, D. (1970). Human tympanic membrane: an ultrastructural observation. *Acta Otolaryngol.*, *70*(3), 176-186.
- Liu-Sheng, W., & Sridhar, K. (1996). Shape measurement using additive - subtractive phase shifting speckle interferometry. *Measurement Science and Technology*, *7*(12), 1748.
- Lokberg, O. (1980). Electronic Speckle Pattern Interferometry. *Physics in Technology*, *11*(1), 16-22.
- Lu, W. (2012). *Development of a multi-wavelength lensless digital holography system for 3D deformations and shape measurements of tympanic membranes.* Worcester Polytechnic Institute.
- Maftoon, N., Black, N. L., Razavi, P., Furlong, C., Remenschneider, A. K., Lewis, J. A., . . . Cheng, J. T. (2018, 02/09/2018). *Audio-frequency characterization of biomaterials for hearing prostheses.* Paper presented at the Association for Research in Otolaryngology, 41st annual midwinter meeting, San Diego, CA.
- Maftoon, N., Razavi, P., Cheng, J. T., Ravicz, M., Furlong, C., & Rosowski, J. J. (2017, 02/2017). *Modal holography detects middle ear fluid.* Paper presented at the Association for Research in Otolaryngology Baltimore, MD.
- Malacara, D. (2007). *Optical shop testing* (Vol. 59): John Wiley & Sons.
- Matlab, U. s. G. (1760). *The mathworks. Inc., Natick, MA, 1992.*
- Millerd, J. E., Brock, N. J., Hayes, J. B., North-Morris, M. B., Novak, M., & Wyant, J. C. (2004). *Pixelated phase-mask dynamic interferometer.*

- Møller, A. R. (1963). Transfer Function of the Middle Ear. *The Journal of the Acoustical Society of America*, 35(10), 1526-1534.
doi:doi:<http://dx.doi.org/10.1121/1.1918742>
- Parker, R. J., & Jones, D. G. (1988). Holography In An Industrial Environment. *Opt. Eng.*, 27(1), 270155-270155-. doi:10.1117/12.7976642
- Pedrini, G., Osten, W., & Gusev, M. E. (2006). High-speed digital holographic interferometry for vibration measurement. *Appl. Opt.*, 45(15), 3456-3462.
doi:10.1364/AO.45.003456
- Pedrini, G., Zou, Y. L., & Tiziani, H. J. (1995). Digital double-pulsed holographic-interferometry for vibration analysis. *Journal of Modern Optics*, 42(2), 367-374.
doi:10.1080/09500349514550321
- Pérez-López, C., Torre-Ibarra, M. H. D. I., & Santoyo, F. M. (2006). Very high speed cw digital holographic interferometry. *Opt. Express*, 14(21), 9709-9715.
doi:10.1364/OE.14.009709
- Photron. (2018). FastCam SA-Z. Retrieved from <https://photron.com/fastcam-sa-z/>
- Rabbitt, R. D., & Holmes, M. H. (1986). A fibrous dynamic continuum model of the tympanic membrane. *The Journal of the Acoustical Society of America*, 80(6), 1716-1728. doi:doi:<http://dx.doi.org/10.1121/1.394284>
- Rasmussen, L., Sandberg, E., Albers, L. N., Rodriguez, S., Gentile, C. A., Meixler, L. D., . . . Liffland, S. (2016). *Ras Labs-CASIS-ISS NL experiment for synthetic muscle: resistance to ionizing radiation*.
- Razavi, P., cheng, J. T., Furlong, C., & Rosowski, J. J. (2017a). *High-Speed Holography for In-Vivo Measurement of Acoustically Induced Motions of Mammalian Tympanic Membrane*. Paper presented at the Mechanics of Biological Systems and Materials, Volume 6: Proceedings of the 2016 Annual Conference on Experimental and Applied Mechanics, Cham.
- Razavi, P., Cheng, J. T., Maftoon, N., Ravicz, M. E., Rosowski, J. J., & Furlong, C. (2017b, 09/02/2017). *Characterization of Acoustically Induced Transient Response of Tympanic Membrane Under Normal and Pathological Conditions*. Paper presented at the Association for Research in Otolaryngology, 40th annual midwinter meeting
- Razavi, P., Dobrev, I., Ravicz, M., Cheng, J. T., Furlong, C., & Rosowski, J. J. (2016a). Transient Response of the Eardrum Excited by Localized Mechanical Forces. In S. A. Tekalur, P. Zavattieri, & C. S. Korach (Eds.), *Mechanics of Biological Systems and Materials, Volume 6* (pp. 31-37): Springer International Publishing.
- Razavi, P., Furlong, C., & Trolinger, J. D. (2017c). Full-Field Digital Holographic Vibrometry for Characterization of High-Speed MEMS. In S. Yoshida, L. Lamberti, & C. Sciammarella (Eds.), *Advancement of Optical Methods in Experimental Mechanics, Volume 3: Proceedings of the 2016 Annual Conference on Experimental and Applied Mechanics* (pp. 41-47). Cham: Springer International Publishing.
- Razavi, P., Khaleghi, M., & Furlong, C. (2015, 24/08/2015). *High-speed digital holographic MEMS inspection instrument*. Paper presented at the SPECKLE 2015: VI International Conference on Speckle Metrology.
- Razavi, P., Ravicz, M. E., Dobrev, I., Cheng, J. T., Furlong, C., & Rosowski, J. J. (2016b). Response of the human tympanic membrane to transient acoustic and

- mechanical stimuli: Preliminary results. *Hear. Res.*, 340, 15-24.
doi:10.1016/j.heares.2016.01.019
- Rosowski, J. J. (1994). Outer and Middle Ears. In R. R. Fay & A. N. Popper (Eds.), *Comparative Hearing: Mammals* (pp. 172-247). New York, NY: Springer New York.
- Rosowski, J. J. (1996). Models of External- and Middle-Ear Function. In H. L. Hawkins, T. A. McMullen, A. N. Popper, & R. R. Fay (Eds.), *Auditory Computation* (pp. 15-61). New York, NY: Springer New York.
- Rosowski, J. J., Cheng, J. T., Ravicz, M. E., Hulli, N., Hernandez-Montes, M., Harrington, E., & Furlong, C. (2009). Computer-assisted time-averaged holograms of the motion of the surface of the mammalian tympanic membrane with sound stimuli of 0.4-25 kHz. *Hear. Res.*, 253(1-2), 83-96.
doi:10.1016/j.heares.2009.03.010
- Rosowski, J. J., Dobrev, I., Khaleghi, M., Lu, W., Cheng, J. T., Harrington, E., & Furlong, C. (2013). Measurements of three-dimensional shape and sound-induced motion of the chinchilla tympanic membrane. *Hear. Res.*, 301, 44-52.
doi:10.1016/j.heares.2012.11.022
- Schmitt, D. R., & Hunt, R. W. (1997). Optimization of fringe pattern calculation with direct correlations in speckle interferometry. *Appl. Opt.*, 36(34), 8848-8857.
doi:10.1364/AO.36.008848
- Schnars, U. (1994). Direct phase determination in hologram interferometry with use of digitally recorded holograms. *Journal of the Optical Society of America a-Optics Image Science and Vision*, 11(7), 2011-2015. doi:10.1364/josaa.11.002011
- Schnars, U., Falldorf, C., Watson, J., Jüptner, W., SpringerLink, & Springer, L. e. E. (2015). *Digital Holography and Wavefront Sensing: Principles, Techniques and Applications* (Vol. 2nd 2015.;2;2nd 2015;). Berlin, Heidelberg: Springer Berlin Heidelberg.
- Schnars, U., Hartmann, H. J., & Juptner, W. P. O. (1995). *Digital recording and numerical reconstruction of holograms for nondestructive testing* (Vol. 2545).
- Schnars, U., & Juptner, W. (1994a). Direct recording of holograms by a ccd target and numerical reconstruction. *Appl. Opt.*, 33(2), 179-181.
- Schnars, U., & Juptner, W. P. O. (1994b). Digital recording and reconstruction of holograms in hologram interferometry and shearography. *Appl. Opt.*, 33(20), 4373-4377.
- Schwider, J. (1989). Phase shifting interferometry: reference phase error reduction. *Appl. Opt.*, 28(18), 3889-3892. doi:10.1364/AO.28.003889
- Schwider, J., Burow, R., Elssner, K. E., Grzanna, J., Spolaczyk, R., & Merkel, K. (1983). Digital wave-front measuring interferometry: some systematic error sources. *Appl. Opt.*, 22(21), 3421-3432. doi:10.1364/AO.22.003421
- Stasche, N., Foth, H.-J., Hörmann, K., Baker, A., & Huthoff, C. (1994). Middle Ear Transmission Disorders—Tympanic Membrane Vibration Analysis by Laser-Doppler-Vibrometry. *Acta Oto-Laryngol.*, 114(1), 59-63.
doi:10.3109/00016489409126017
- Surrel, Y. (1996). Design of algorithms for phase measurements by the use of phase stepping. *Appl. Opt.*, 35(1), 51-60.

- Takeda, M., Ina, H., & Kobayashi, S. (1982). Fourier-transform method of fringe-pattern analysis for computer-based topography and interferometry. *J. Opt. Soc. Am.*, 72(1), 156-160. doi:10.1364/JOSA.72.000156
- Thalmann, R., & Dandliker, R. (1985). *Holographic Contouring Using Electronic Phase Measurement*.
- Timoshenko, S. P., & Woinowsky-Krieger, S. (1959). *Theory of plates and shells*: McGraw-hill.
- Tonndorf, J., & Khanna, S. M. (1972). Tympanic-Membrane Vibrations in Human Cadaver Ears Studied by Time-Averaged Holography. *The Journal of the Acoustical Society of America*, 52(4B), 1221-1233. doi:doi:<http://dx.doi.org/10.1121/1.1913236>
- Trolinger, J. D., Hess, C. F., Razavi, P., & Furlong, C. (2016). *Digital holographic interferometry for characterizing deformable mirrors in aero-optics*.
- Van der Jeught, S., & Dirckx, J. J. J. (2017). Real-time structured light-based otoscopy for quantitative measurement of eardrum deformation. *J. Biomed. Opt.*, 22(1), 016008-016008. doi:10.1117/1.JBO.22.1.016008
- Vest, C. M. (1979). *Holographic interferometry*. New York, John Wiley and Sons, Inc., 1979. 476 p., 1.
- Volandri, G., Di Puccio, F., Forte, P., & Carmignani, C. (2011). Biomechanics of the tympanic membrane. *J. Biomech.*, 44(7), 1219-1236. doi:<http://dx.doi.org/10.1016/j.jbiomech.2010.12.023>
- Yamaguchi, I., Ida, T., & Yokota, M. (2006). *Surface shape measurement by phase-shifting digital holography with dual wavelengths*.
- Yamaguchi, I., & Zhang, T. (1997). Phase-shifting digital holography. *Opt. Lett.*, 22(16), 1268-1270. doi:10.1364/ol.22.001268
- Yu, Q., Fu, S., Yang, X., Sun, X., & Liu, X. (2004). Extraction of phase field from a single contoured correlation fringe pattern of ESPI. *Opt. Express*, 12(1), 75-83. doi:10.1364/OPEX.12.000075
- Zhao, B., & Surrel, Y. (1995). Phase shifting: six-sample self-calibrating algorithm insensitive to the second harmonic in the fringe signal. *OPTICAL ENGINEERING-BELLINGHAM-INTERNATIONAL SOCIETY FOR OPTICAL ENGINEERING-*, 34, 2821-2821.
- Zhao, F., Wada, H., Koike, T., Ohyama, K., Kawase, T., & Stephens, D. (2002). Middle Ear Dynamic Characteristics in Patients with Otosclerosis. *Ear Hear.*, 23(2), 150-158.
- Zwislocki, J. (1962). Analysis of the Middle-Ear Function. Part I: Input Impedance. *The Journal of the Acoustical Society of America*, 34(9B), 1514-1523. doi:doi:<http://dx.doi.org/10.1121/1.1918382>

Appendix A. Phase correlation interferometry: derivations of mathematics

This Chapter presents the detailed derivations of the developments presented in Chapter 5¹ of this Dissertation:

$$I_{ref} = I_r + I_o + 2\sqrt{I_r I_o} \cos(\theta), \quad (A - 1)$$

$$I_{def} = I_r + I_o + 2\sqrt{I_r I_o} \cos(\theta + \Delta\phi). \quad (A - 2)$$

Pearson's product-moment coefficient

$$\rho = \frac{\langle I_{ref} I_{def} \rangle - \langle I_{ref} \rangle \langle I_{def} \rangle}{[\langle I_{ref}^2 \rangle - \langle I_{ref} \rangle^2]^{\frac{1}{2}} [\langle I_{def}^2 \rangle - \langle I_{def} \rangle^2]^{\frac{1}{2}}}, \quad (A - 3)$$

where operator $\langle \rangle$ resembles the expected value that is equivalent to the weighted average for any random variables. The correlation coefficient can be evaluated by noting that (Wykes, appendix E)

- I_{ref} , I_{def} and θ are independent variables, which means $\langle X, Y \rangle = \langle X \rangle \langle Y \rangle$.
- $\langle I^2 \rangle = 2\langle I \rangle^2$

Assume θ is uniform distributed and $\Delta\phi$ is constant, therefore

$$\langle \cos\theta \rangle = \frac{1}{2\pi} \int_{-\pi}^{\pi} \cos\theta \cdot d\theta = 0, \quad (A - 4)$$

$$\langle \cos(\theta + \Delta\phi) \rangle = \frac{1}{2\pi} \int_{-\pi}^{\pi} \cos(\theta + \Delta\phi) \cdot d\theta = 0 \quad (A - 5)$$

$$\langle \cos^2\theta \rangle = \frac{1}{2\pi} \int_{-\pi}^{\pi} \cos^2\theta \cdot d\theta = \frac{1}{2}, \quad (A - 6)$$

¹ The derivations presented in this Appendix were obtained together with Mr. Haimi Tang.

$$\begin{aligned}
\langle \cos(\theta + \Delta\phi) \cos\theta \rangle &= \frac{1}{2\pi} \int_{-\pi}^{\pi} \cos(\theta + \Delta\phi) \cos\theta \cdot d\theta \\
&= \frac{1}{2\pi} \int_{-\pi}^{\pi} (\cos\theta \cos\Delta\phi - \sin\theta \sin\Delta\phi) \cos\theta \cdot d\theta \\
&= \frac{1}{2\pi} \int_{-\pi}^{\pi} (\cos\theta \cos\Delta\phi) \cos\theta \cdot d\theta - \frac{1}{2\pi} \int_{-\pi}^{\pi} (\sin\theta \sin\Delta\phi) \cos\theta \cdot d\theta \\
&= \frac{1}{2\pi} \cos\Delta\phi \int_{-\pi}^{\pi} (\cos\theta) \cos\theta \cdot d\theta - \frac{1}{2\pi} \sin\Delta\phi \int_{-\pi}^{\pi} (\sin\theta) \cos\theta \cdot d\theta \\
&= \frac{1}{2\pi} \cos\Delta\phi \int_{-\pi}^{\pi} \cos^2\theta \cdot d\theta - \frac{1}{2\pi} \sin\Delta\phi \int_{-\pi}^{\pi} \frac{1}{2} \sin 2\theta \cdot d\theta \\
&= \frac{1}{2\pi} \cos\Delta\phi \pi - 0 = \frac{\cos(\Delta\phi)}{2} \tag{A-7}
\end{aligned}$$

$$\langle \cos^2(\theta + \Delta\phi) \rangle = \frac{1}{2\pi} \int_{-\pi}^{\pi} \cos^2(\theta + \Delta\phi) \cdot d\theta = \frac{1}{2}, \tag{A-8}$$

A.1 General speckle correlation case with intensity ratio r

Using the Pearson's product-moment coefficient, Eqn. (B-3)

$$\rho = \frac{\langle I_{ref} I_{def} \rangle - \langle I_{ref} \rangle \langle I_{def} \rangle}{\left[\langle I_{ref}^2 \rangle - \langle I_{ref} \rangle^2 \right]^{\frac{1}{2}} \left[\langle I_{def}^2 \rangle - \langle I_{def} \rangle^2 \right]^{\frac{1}{2}}}, \tag{A-3}$$

Let the reference and object intensities have the following relation,

$$\frac{I_{ref}}{I_{def}} = \frac{I}{rI} = \frac{1}{r}, \tag{A-9}$$

where r is called reference object intensity ratio. Therefore, the hologram intensities are,

$$I_{ref} = (r + 1)I + 2\sqrt{r}I \cos\theta, \tag{A-10}$$

$$I_{def} = (r + 1)I + 2\sqrt{r}I \cos(\theta + \Delta\phi). \tag{A-11}$$

Performing the same calculation to measure the correlation based on the intensities:

$$\langle I_{ref} I_{def} \rangle = \langle \left((r + 1)I + 2\sqrt{r}I \cos\theta \right) \left((r + 1)I + 2\sqrt{r}I \cos(\theta + \Delta\phi) \right) \rangle$$

$$\begin{aligned}
&= \langle (r+1)^2 I^2 \rangle + \langle 2\sqrt{r}(r+1)I^2 \cos(\theta + \Delta\phi) \rangle + \langle 2\sqrt{r}(r+1)\cos\theta \rangle \\
&\quad + \langle 4rI^2 \cos(\theta + \Delta\phi)\cos\theta \rangle \\
&= (r+1)^2 \langle I^2 \rangle + 4r \langle I^2 \rangle \langle \cos(\theta + \Delta\phi)\cos\theta \rangle, \tag{A-12}
\end{aligned}$$

$$\begin{aligned}
\langle I_{ref} \rangle \langle I_{def} \rangle &= \langle (r+1)I + 2\sqrt{r}I\cos\theta \rangle \cdot \langle (r+1)I + 2\sqrt{r}I\cos(\theta + \Delta\phi) \rangle \\
&= (r+1)^2 \langle I \rangle^2 = \frac{(r+1)^2}{2} \langle I^2 \rangle, \tag{A-13}
\end{aligned}$$

$$[\langle I_{ref}^2 \rangle - \langle I_{ref} \rangle^2]^{\frac{1}{2}} = \left[\frac{(r+1)^2}{2} \langle I^2 \rangle + 4r \langle I^2 \rangle \langle \cos^2\theta \rangle \right]^{\frac{1}{2}}, \tag{A-14}$$

$$[\langle I_{def}^2 \rangle - \langle I_{def} \rangle^2]^{\frac{1}{2}} = \left[\frac{(r+1)^2}{2} \langle I^2 \rangle + 4r \langle I^2 \rangle \langle \cos^2(\theta + \Delta\phi) \rangle \right]^{\frac{1}{2}}, \tag{A-15}$$

Therefore using Eqn. (B-12) to (B-15),

$$\begin{aligned}
\rho &= \frac{(r+1)^2 \langle I^2 \rangle + 4r \langle I^2 \rangle \langle \cos(\theta + \Delta\phi)\cos\theta \rangle - \frac{(r+1)^2}{2} \langle I^2 \rangle}{\left[\frac{(r+1)^2}{2} \langle I^2 \rangle + 4r \langle I^2 \rangle \langle \cos^2\theta \rangle \right]^{\frac{1}{2}} \cdot \left[\frac{(r+1)^2}{2} \langle I^2 \rangle + 4r \langle I^2 \rangle \langle \cos^2(\theta + \Delta\phi) \rangle \right]^{\frac{1}{2}}} \\
&= \frac{\langle I^2 \rangle \left[\frac{(r+1)^2}{2} + 4r \frac{\cos(\Delta\phi)}{2} \right]}{\langle I^2 \rangle \left[\frac{(r+1)^2}{2} + 4r \frac{1}{2} \right]^{\frac{1}{2}} \cdot \left[\frac{(r+1)^2}{2} + 4r \frac{1}{2} \right]^{\frac{1}{2}}} = \frac{(r+1)^2 + 4r \cos(\Delta\phi)}{(r+1)^2 + 4r}, \tag{A-16}
\end{aligned}$$

A.2 Equal intensity ratio (r=1)

Let the intensity ratio $r = 1$, therefore,

$$I_{ref} = 2I + 2I\cos\theta, \tag{A-17}$$

$$I_{def} = 2I + 2I\cos(\theta + \Delta\phi), \tag{A-18}$$

$$\begin{aligned}
\langle I_{ref} I_{def} \rangle &= \langle (2I + 2I\cos\theta)(2I + 2I\cos(\theta + \Delta\phi)) \rangle \\
&= \langle 4I^2 \rangle + \langle 4I^2 \cos(\theta + \Delta\phi) \rangle + \langle 4I^2 \cos\theta \rangle + \langle 4I^2 \cos(\theta + \Delta\phi)\cos\theta \rangle
\end{aligned}$$

$$\begin{aligned}
&= \langle 4I^2 \rangle + \langle 4I^2 \rangle \langle \cos(\theta + \Delta\phi) \rangle + \langle 4I^2 \rangle \langle \cos\theta \rangle + \langle 4I^2 \rangle \langle \cos(\theta + \Delta\phi) \cos\theta \rangle \\
&= \langle 4I^2 \rangle + \langle 4I^2 \rangle \cdot 0 + \langle 4I^2 \rangle \cdot 0 + \langle 4I^2 \rangle \langle \cos(\theta + \Delta\phi) \cos\theta \rangle \\
&= 4\langle I^2 \rangle + 4\langle I^2 \rangle \langle \cos(\theta + \Delta\phi) \cos\theta \rangle, \tag{A-19}
\end{aligned}$$

$$\begin{aligned}
\langle I_{ref} \rangle \langle I_{def} \rangle &= \langle 2I + 2I \cos\theta \rangle \cdot \langle (2I + 2I \cos(\theta + \Delta\phi)) \rangle \\
&= (\langle 2I \rangle + \langle 2I \cos\theta \rangle) \cdot (\langle 2I \rangle + \langle 2I \cos(\theta + \Delta\phi) \rangle) \\
&= (\langle 2I \rangle + \langle 2I \rangle \langle \cos\theta \rangle) \cdot (\langle 2I \rangle + \langle 2I \rangle \langle \cos(\theta + \Delta\phi) \rangle) \\
&= \langle 2I \rangle^2 = 2\langle I^2 \rangle, \tag{A-20}
\end{aligned}$$

$$[\langle I_{ref}^2 \rangle - \langle I_{ref} \rangle^2]^{\frac{1}{2}} = [2\langle I^2 \rangle + 4\langle I^2 \rangle \langle \cos^2\theta \rangle]^{\frac{1}{2}}, \tag{A-21}$$

$$[\langle I_{def}^2 \rangle - \langle I_{def} \rangle^2]^{\frac{1}{2}} = [2\langle I^2 \rangle + 4\langle I^2 \rangle \langle \cos^2(\theta + \Delta\phi) \rangle]^{\frac{1}{2}} \tag{A-22}$$

Therefore, using Eqn. (B-19) to (B-22),

$$\rho = \frac{4\langle I^2 \rangle + 4\langle I^2 \rangle \frac{\cos(\Delta\phi)}{2} - 2\langle I^2 \rangle}{\left[2\langle I^2 \rangle + 4\langle I^2 \rangle \frac{1}{2}\right]^{\frac{1}{2}} \cdot \left[2\langle I^2 \rangle + 4\langle I^2 \rangle \frac{1}{2}\right]^{\frac{1}{2}}} = \frac{1 + \cos(\Delta\phi)}{2}, \tag{A-23}$$

A.3 Zero order terms were removed

Assume the zero order terms are removed, the intensities will take the form of:

$$I_{ref} = 2\sqrt{r}I \cos\theta, \tag{A-24}$$

$$I_{def} = 2\sqrt{r}I \cos(\theta + \Delta\phi), \tag{A-25}$$

Therefore,

$$\begin{aligned}
\langle I_{ref} I_{def} \rangle &= \langle (2\sqrt{r}I \cos\theta)(2\sqrt{r}I \cos(\theta + \Delta\phi)) \rangle \\
&= 4r\langle I^2 \rangle \langle \cos(\theta + \Delta\phi) \cos\theta \rangle, \tag{A-26}
\end{aligned}$$

$$\langle I_{ref} \rangle \langle I_{def} \rangle = \langle 2\sqrt{r}I \cos\theta \rangle \cdot \langle (2\sqrt{r}I \cos(\theta + \Delta\phi)) \rangle = 0, \quad (\text{A} - 27)$$

$$[\langle I_{ref}^2 \rangle - \langle I_{ref} \rangle^2]^{\frac{1}{2}} = [4r \langle I^2 \rangle \langle \cos^2\theta \rangle]^{\frac{1}{2}}, \quad (\text{A} - 28)$$

$$[\langle I_{def}^2 \rangle - \langle I_{def} \rangle^2]^{\frac{1}{2}} = [4r \langle I^2 \rangle \langle \cos^2(\theta + \Delta\phi) \rangle]^{\frac{1}{2}}, \quad (\text{A} - 29)$$

Therefore, using Eqn. (B-26) to (B-29), the correlation coefficient of Eqn. (B-3) takes the form of,

$$\begin{aligned} \rho &= \frac{4r \langle I^2 \rangle \langle \cos(\theta + \Delta\phi) \cos\theta \rangle}{[4r \langle I^2 \rangle \langle \cos^2\theta \rangle]^{\frac{1}{2}} \cdot [4r \langle I^2 \rangle \langle \cos^2(\theta + \Delta\phi) \rangle]^{\frac{1}{2}}} \\ &= \frac{\frac{\cos(\Delta\phi)}{2}}{\left(\frac{1}{2}\right)^{\frac{1}{2}} \cdot \left(\frac{1}{2}\right)^{\frac{1}{2}}} = \cos(\Delta\phi), \end{aligned} \quad (\text{A} - 30)$$